Novel Hybrid Multipolar RF Cavities for Transverse Beam Manipulations

Laurence Wroe
Linacre College

Thesis submitted in fulfillment of the requirements for the degree of
Doctor of Philosophy at the University of Oxford

Michaelmas Term, 2022

Abstract

This thesis describes the development and application of a method for tailoring the profile of electromagnetic fields in RF cavities for use in particle accelerators. This so-called azimuthal modulation method (AMM) is underpinned by an analytic expression of the basis of the electromagnetic modes in closed RF cavities whose cross-sections vary with the azimuth. This basis is derived and the notation $\{M\}\eta p$ is introduced to describe the azimuthal, radial and longitudinal form of the modes.

The scope of the AMM for designing realisable cavities is explored. The underlying reasons for the limitations on the range of magnitudes and orientations of multipoles that can be supported by azimuthally modulated cavities are derived and discussed.

This understanding provides the foundation for the latter half of the thesis where numerous applications of the AMM are presented. First, the AMM is used to construct a prototype cavity that supports a 3 GHz mode which could be used for the simultaneous acceleration and focusing of a particle beam. Experimental testing supported the multipolar content of the mode being as designed. Second, the AMM is applied to create RF cavities which support modes free from unwanted multipoles generated by power couplers and tuning pins. An example design of an RF structure which incorporates a single-slot power coupler and supports an accelerating mode free from dipole, quadrupole, sextupole and octupole components is analysed. Third, the AMM is used to design RF cavities that support modes tailored for the off-axis traversal of particle beams. An example optimisation of an accelerating field that remains as flat as possible along the horizontal is presented. Finally, the AMM also finds application in the creation of musical drums. This concept inspired an outreach workshop that was designed and delivered to showcase this research to 11-14 year-old school students.

To Granny, Grandad, Janny and Bruce.

Acknowledgements

Thank you first and foremost to my global supervisory team of Rob Apsimon, Manjit Dosanjh and Suzie Sheehy. It's not always been simple organising meetings, especially when there's four different time zones involved, but I am really looking forward to catching up with you all in person. Rob, I've really enjoyed this project which is no doubt thanks to your boundless (or infinitely spiralling perhaps...?) support and enthusiasm. I'm very thankful to have had your excellent technical knowledge readily available with your virtual door always open for discussions. Manjit, I'm very grateful for you overseeing both me and the project and to have had your expert guidance and advice. I look forward to seeing you regularly at CERN! And Suzie, it has been five and a half years since we first met to discuss Masters projects - I'm so thankful for all your support and efforts since then, not least for persuading me to come back to Oxford!

On a more local level, it has been a pleasure presenting this work to Shinji Machida, JB Lagrange, David Kelliher and Chris Rogers at RAL. Your insightful observations, suggestions and most importantly enthusiasm have all really helped me! Not to forget The Angels, Max and Jake, too: although the enthusiasm was usually more focused at the pub on a Friday evening rather than meetings on a Monday morning...

Thank you to those at the JAI and the University, particularly Alfons, Tim, Kim and Sue as well as the Funky Drums team of Jake, Beth, Sean and Aniq. And to friends who have made these few years very fun!

Cheers also to the Lewises. Suzanne and Zach, I've loved spending time with you and look forward to many more days trudging around Oxford! And to Mickey, you coached me much more than just football.

And thank you to all the Wroes, Martins and Vineses for their love and support. Mum, Dad, Ray, Jacob, Gab, Nat and Luke: I hope you all manage to get this far into reading the thesis at least...!

Finally to H. I didn't (nor did my supervisors!) expect to be submitting this thesis from Rainbow Beach after two and a half months of travelling. I wouldn't have done it any differently though - and I promise that I will actually do some planning now!

Contents

List of Figures

Chapter 1

Introduction

The number and application of particle accelerators has multiplied ever since Cockroft and Walton developed an early particle accelerator that, in 1932, delivered proton beams up to 700 keV to perform artificial nuclear disintegrations [1, 2]. Nowadays, there are over 100 particle accelerators and laboratories used for high-energy research [3]. Our current largest and highest-energy is the 27 km circumference Large Hadron Collider (LHC) which accelerates protons and ions to energies up to 7 TeV and 2.67 TeV per nucleon respectively [4]. These accelerators, however, represent just a small fraction of the total number worldwide. A conservative estimate places the total at over 40,000 as of 2020 [5], with 44% used for curing or relieving the symptoms of cancerous tumours via radiotherapy and 41% for doping and altering semiconductor materials via ion implantation [6].

Nonetheless, there is demand for more particle accelerators. There are over 20 concepts for colliders [7] that could complement or exceed the discovery reach of the LHC. Such machines would shed light on physics beyond the Standard Model which is inherently incomplete, for example it does not describe gravity, but has not been contradicted at the 5σ level by any LHC experiment [8]. These accelerators would need to push energy, luminosity or intensity frontiers and examples include the FCC

[9], CLIC [10], ILC [11] and CePC [12]. Additional accelerators are also needed to push social frontiers too: more than 50% of cancer patients in low and middle income countries lack access to radiotherapy treatment compared to under 10% in Europe [13, 14]. It was estimated in 2015 that a further 12,600 megavoltage machines are required to meet radiotherapy demands by 2035 [15, 16].

These frontiers are pushed by undertaking accelerator physics research, such as that documented in this thesis. The Livingston plot in Fig. 1.1, for example, shows that new acceleration concepts and innovative technological upgrades continually push the energy frontier. Here, particle energy is defined as the energy equivalent of a travelling proton that collides with a stationary proton to reach the same centre of mass energy. Each line represents a different acceleration concept, while the points on the line represent different accelerators themselves.

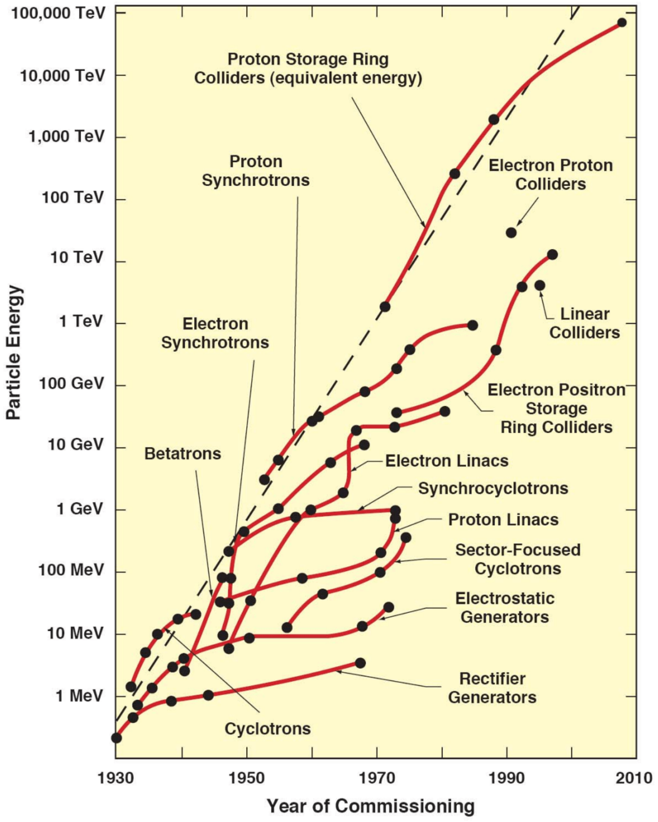

Figure 1.1: Livingstone plot showing particle energies achieved by accelerators against time. Reproduced from [17].

This thesis describes investigations and applications of tailoring the electromagnetic modes within radiofrequency (RF) cavities. In this introduction the motivation for the undertaken research is detailed. It begins with a brief overview of classical electromagnetism, which forms the foundations of this study, in Sec. 1.1. Subsequently, different types of RF particle accelerators and their underlying physics are discussed in Sec. 1.2. The transverse beam dynamics of such machines are then reviewed in Sec. 1.3, with the applications for RF cavities that affect such dynamics discussed. This introduction is concluded in Sec. 1.4 with an outline of the subsequent chapters that comprise the thesis.

1.1 Classical Electromagnetism

Particle accelerators are machines that use electromagnetic fields to control and propel beams of charged particles to high energies. A comprehensive summary of electrodynamic principles was first given in the 1860s when Maxwell wrote down a set of equations that unified the electric and magnetic forces. Cast in Heaviside's differential form, Maxwell's equations in vacuum are

$$\text{Gauss's law:} \qquad \nabla \cdot \vec{E} = 0, \tag{1.1}$$

$$\text{Gauss's law for magnetism:} \qquad \nabla \cdot \vec{B} = 0, \tag{1.2}$$

$$\text{Maxwell-Faraday equation:} \qquad \nabla \times \vec{E} = -\frac{\partial \vec{B}}{\partial t}, \tag{1.3}$$

$$\text{Ampère-Maxwell equation:} \qquad \nabla \times \vec{B} = \epsilon_0 \mu_0 \frac{\partial \vec{E}}{\partial t}, \tag{1.4}$$

where $\vec{E}$ denotes the electric field, $\vec{B}$ the magnetic field and ϵ_0 and μ_0 are the permittivity and the permeability of free space respectively [18]. The latter relate to the speed of light in vacuum as

$$c = \frac{1}{\sqrt{\mu_0 \epsilon_0}}. \tag{1.5}$$

The four Maxwell equations describe the generation of electromagnetic fields from charges and currents. Coupling them with the Lorentz force that describes the force $\vec{F}$ exerted on a particle of charge e traversing an electromagnetic field at a velocity $\vec{v}$

$$\vec{F} = e(\vec{E} + \vec{v} \times \vec{B}), \tag{1.6}$$

forms the foundation of classical electromagnetism.

We also note that that these five equations can be recast in terms of the magnetic vector potential $\vec{A}$ defined as

$$\vec{B} = \nabla \times \vec{A}, \tag{1.7}$$

and the electric scalar potential Φ given by

$$\vec{E} = -\nabla\Phi - \frac{\partial \vec{A}}{\partial t}. \tag{1.8}$$

Additionally, the energy gained from a particle traversing an electromagnetic field can be calculated from the Lorentz force as

$$W = -\int \vec{F} \cdot d\vec{l} = -e \int \vec{E} \cdot d\vec{l}. \tag{1.9}$$

1.2 Radiofrequency Particle Accelerators

The earliest particle accelerators used static, high-voltage potentials to accelerate particles to energies in direct proportion to the voltage. The maximum energy obtained is therefore limited by the maximum voltage that can be sustained which, in practice, is limited to the MV order because of the electrical breakdown of insulating materials [19].

This limitation is overcome by RF particle accelerators that use time-varying electromagnetic fields to accelerate bunches of particles in components such as RF cavities. In such designs, the beam is arranged into bunches that arrive at the accelerating component when the field has the correct polarity for acceleration.

RF accelerating structures are still limited to a maximum electric field E_{max} before their breakdown rate becomes impractically high. In the case of room-temperature copper cavities, the maximum electric field was found in the 1950s to be well-modelled by the Kilpatrick criterion

$$f = 1.64 E_{\text{max}}^2 e^{-8.5/E_{\text{max}}} \text{ [MHz]}, \tag{1.10}$$

where f is the frequency of the field [20, 21]. Since then, new criteria [22, 23] have been proposed to model the breakdown limit of modern normal conducting (NC) RF cavities, and structures have been designed that reach $E_{\text{max}} \sim 100$ MV/m [24].

Whereas RF cavities are used in RF particle accelerators to accelerate, magnets are typically used to control the transverse beam dynamics. This is because the maximum field of accelerator magnets is $B_{\text{max}} \sim 15$ T compared to $E_{\text{max}} \sim 100$ MV/m for RF cavities. Putting these values into the Lorentz force Equation 1.6, we find

$$B_{\text{max}} \beta c \gg E_{\text{max}}, \tag{1.11}$$

for high-β particles. That is, the magnetic forces that can be physically realised and exerted on particles in accelerators far exceeds that of electric forces.

With separate forces used to *accelerate* (where we define accelerate in this thesis to be acceleration in the longitudinal direction to higher energies) and *manipulate* (where we define manipulate in this thesis to be transverse manipulations for control) beams, RF particle accelerators come in various designs including the cyclotron, synchrotron and linear accelerator.

1.2.1 Cyclotrons

In a cyclotron, particles produced by a source at the centre of the machine continually spiral outwards due to their interaction with a magnetic field and repeated acceleration from a time-varying electric field. For particles in the non-relativistic limit, the RF frequency must equal the cyclotron frequency

$$f_c = \frac{eB}{2\pi m}, \tag{1.12}$$

where B is the magnitude of the magnetic field perpendicular to the plane the particle is travelling in and m is the particle rest mass [17].

At relativistic speeds, Eqn. 1.12 breaks down and the synchronicity between the RF and cyclotron frequency is lost. Solutions to this problem [25] include synchrocyclotrons that vary the accelerating frequency as

$$f(r) = \frac{1}{2\pi\sqrt{(m/eB)^2 + (r/c)^2}}, \tag{1.13}$$

where r is radial displacement, and isochronous cyclotrons that vary the magnetic field as

$$B(r) = \frac{m}{e\sqrt{(1/2\pi f)^2 - (r/c)^2}}. \tag{1.14}$$

Though modern cyclotrons are limited to lower energies than other technologies, their compactness is advantageous. They find application in proton beam therapy [26] as well as in the production of medical radionuclides for which there were almost 1,500 worldwide in 2020 [27].

1.2.2 Synchrotrons

Synchrotrons contrast the cyclotron design by constraining accelerating particles to a fixed, closed, circular path of radius ρ through the use of a time-varying magnetic field. Early designs were weak focusing which focus the beam in the vertical direction y by introducing a field gradient that, providing it satisfies

$$0 < \frac{-\rho}{B}\frac{\partial B_y}{\partial r} < 1, \tag{1.15}$$

also results in beams of different orbital offsets in the horizontal direction x converging on each other, as per Fig. 1.2. Despite this net focusing, the energy reach of weak focusing machines is limited by the orbital deviations increasing with the machine radius which requires magnets with ever larger apertures.

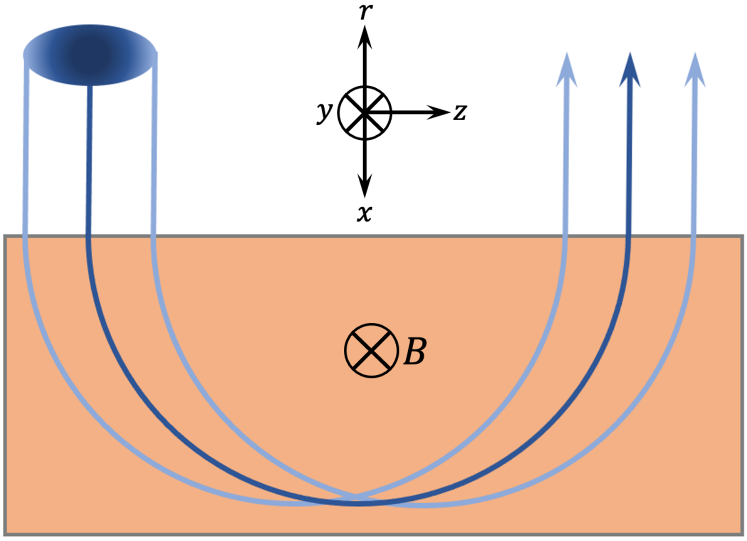

Figure 1.2: Weak focusing of a particle bunch.

Alternating gradient, or strong-focusing, accelerators overcome this limitation by alternately placing focusing and defocusing magnets to converge beams in both transverse directions [28]. Its implementation in particle accelerators has led to machines being constructed out of separate components of specialised functions, such as different m-pole magnets for different manipulations.

In alternating gradient synchrotrons, the bending magnetic field ramps as

$$B\rho = \frac{pc}{e}, \tag{1.16}$$

such that the orbital radius remains fixed as the particle momentum p increases. Outside of the ultrarelativistic limit, the RF frequency must also ramp too in order to compensate for the increasing particle velocity and ensure synchronicity. The energy reach is limited by the physical space that the accelerator can be built in and the strength of dipole fields that can be physically realised. Electron synchrotrons are also further limited by synchrotron radiation losses P_γ that scale as

$$P_\gamma \propto \frac{E^4}{\rho}, \tag{1.17}$$

where E is the energy of particles in the beam [18].

Alternating gradient synchrotrons provide the template for our modern, high-energy, large-scale colliders and synchrotron light sources. 37 of the latter are used worldwide to generate brilliant X-rays for structural analysis on atomic-scales [3].

1.2.3 Linear Accelerators

Linear accelerators (linacs) are single-pass machines that accelerate particles along a straight beamline from a source at one end to a target at the other. For acceleration, radiofrequency quadrupole (RFQ) or drift-tube linac (DTL) cavity structures are typically used at low-β ($\beta < 0.5$), whereas RF cavities are typically used at high-β [29].

Though less compact than their circular counterparts, linacs require relatively few dipole magnets and have no losses from synchrotron radiation. Their energy reach is limited by the physical space and the maximum gradient of the accelerating field.

Applications of linacs include the generation of X-rays and electrons for radiotherapy treatment, as injectors for higher-energy accelerators (such as LINAC4 which begins the chain of accelerators that feeds the LHC [30]) and for particle physics experiments (such as the SLAC electron accelerator which was used to find evidence of the internal structure within protons and neutrons [31, 32]).

1.3 Transverse Beam Dynamics

As well as acceleration, RF cavities find applications in manipulating particle beams. To motivate and discuss these, the transverse beam dynamics of particles traversing an alternating gradient accelerator composed of dipoles and quadrupoles are first analysed. Afterwards, the uses of higher order magnets, including sextupoles and octupoles, combined function magnets and RF cavities are discussed.

1.3.1 Magnetic Multipolar Expansion

In alternating gradient accelerators, the particles are kept tight to an ideal reference orbit by a set of magnets that form the magnetic lattice of the accelerator. Such systems are best analysed using the Frenet-Serret coordinate system shown in Fig. 1.3. Here a point P is defined with respect to the the reference orbit vector $\vec{r_0}$ that is a function of s, the path length along the reference orbit from an initial point, as well as to the horizontal $\vec{x}$ and vertical $\vec{y}$ displacements from the reference orbit. The unit vector $\hat{s}$ is tangential to the reference orbit.

The basis of the magnetic field in the absence of an electric potential, $\Phi = 0$, and consisting solely of transverse components can be written

$$B_y + iB_x = B_0 \sum_{m=1}^{\infty} (a_m + ib_m) \left(\frac{x + iy}{R_0} \right)^{m-1}, \tag{1.18}$$

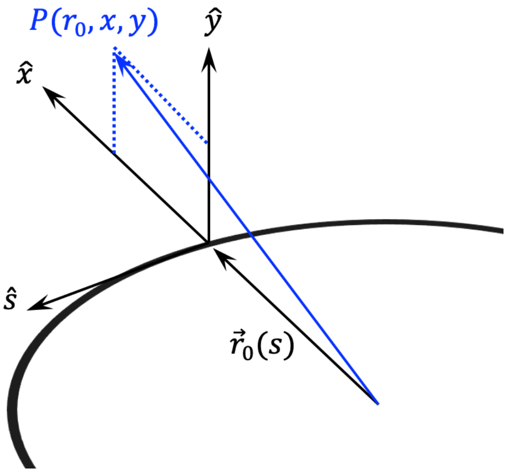

Figure 1.3: Frenet-Serret coordinate system.

as shown by [33]. Here B_0 and R_0 are a reference field and radius that remove any dimension from the normal b_m and skew a_m multipolar coefficients.

These multipolar coefficients can be calculated as

$$b_m = \frac{1}{(m-1)!}\frac{R_0^{m-1}}{B_0}\frac{\partial^{m-1}B_x}{\partial x^{m-1}}\bigg|_0, \qquad a_m = \frac{1}{(m-1)!}\frac{R_0^{m-1}}{B_0}\frac{\partial^{m-1}B_y}{\partial x^{m-1}}\bigg|_0, \tag{1.19}$$

where the notation $|_0$ indicates the differential term is evaluated at $x = y = 0$. The $m = 1$ multipolar coefficients are referred to as the dipole coefficients, the $m = 2$ as quadrupole, $m = 3$ as sextupole, $m = 4$ as octupole, $m = 5$ as decupole and so on. These coefficients determine the azimuthal structure of the magnetic field, as can be seen by transforming Eqn. 1.18 to polar coordinates

$$B_r = B_0 \sum_{m=1}^{\infty} \left[b_m \cos(m\theta) + a_m \sin(m\theta)\right] \left(\frac{r}{R_0}\right)^{m-1}, \tag{1.20}$$

$$B_\theta = B_0 \sum_{m=1}^{\infty} \left[a_m \cos(m\theta) - b_m \sin(m\theta)\right] \left(\frac{r}{R_0}\right)^{m-1}. \tag{1.21}$$

We note here that the change of transverse momentum of a test charge with velocity $\vec{v} = v_z\hat{z}$ that traverses an m-pole magnetic field of length L under the assumption that its velocity remains constant throughout the field and there are no fringe fields is

$$\Delta\vec{p}_{\perp}(r,\theta) = e\begin{pmatrix} -B_\theta \\ B_r \end{pmatrix} L = -ec_m\frac{B_0}{R_0^{m-1}}r^{m-1}\begin{pmatrix} \cos\left(m\theta-\Phi_m\right) \\ -\sin\left(m\theta-\Phi_m\right) \end{pmatrix} L. \tag{1.22}$$

This is calculated by integrating the Lorentz force Equation 1.6 and the multipolar magnitude c_m and orientation Φ_m are defined as $b_m = c_m\cos\left(\Phi_m\right)$ and $a_m = c_m\sin\left(\Phi_m\right)$.

1.3.2 Hill's Equation

The transverse motion of on-momentum particles $p = p_0$ in an accelerator lying in the horizontal plane and comprised of ideal dipole and quadrupole magnetic fields is governed by Hill's equation

$$x'' + K_x(s)x = 0, \qquad\qquad y'' + K_y(s)y = 0, \tag{1.23}$$

where the prime denotes differentiation with respect to s [18]. The focusing functions are defined as

$$K_x(s) = 1/\rho^2 + \frac{1}{\rho B_d}\frac{\partial B_y(s)}{\partial x}, \qquad\qquad K_y(s) = -\frac{1}{\rho B_d}\frac{\partial B_y(s)}{\partial x}, \tag{1.24}$$

where the magnetic rigidity is defined as $\rho B_d = p_0/e$ for bending fields B_d.

Alternating gradient accelerators satisfy

$$\left|\frac{\rho}{B_d}\frac{\partial B_y}{\partial r}\right| \gg 1. \tag{1.25}$$

In such a case, Hill's Equation 1.23 shows that focusing and defocusing quadrupoles must be placed alternately to focus the beam, where a focusing quadrupole is defined as focusing in the horizontal whilst defocusing in the vertical. Otherwise if, for example, only focusing quadrupoles were used such that $\partial B_y(s)/\partial x$ is positive for all s, the beam would oscillate in the x-direction but exponentially blow up in the y.

One design procedure for alternately placing the focusing and the defocusing quadrupoles is called *FODO*. Here the lattice is built out of repeated, identical FODO cells that each consist of a focusing (FO) quadrupole followed by a drift region then a defocusing (DO) quadrupole followed by another drift. Components such as dipoles and RF cavities can then be placed in the drift regions.

If repeated cells are used, a periodic condition over a cell of length L is imposed on the focusing functions, $K_{x,y}(s+L) = K_{x,y}(s)$. In such a case, the solutions to the Hill's Equation 1.23 for $K_{x,y} > 0$ are [25, 34]

$$x = \sqrt{\beta_x(s)\epsilon_x}\cos(\phi_x(s) - \phi_0), \qquad y = \sqrt{\beta_y(s)\epsilon_y}\cos(\phi_y(s) - \phi_0). \tag{1.26}$$

Without loss of generality, we discuss the horizontal component only and forgo the use of any subscripts. Thus in this parameterisation, the β function is an oscillatory function that relates to the transverse size of the beam as $\sigma = \sqrt{\beta(s)\epsilon}$, where ϵ is a constant called the emittance. The phase function ϕ relates to the β function as

$$\phi(s) = \int_0^s \frac{1}{\beta(s)} ds. \tag{1.27}$$

We define the tune in a circular machine as the number of betatron oscillations a particle undergoes per turn

$$Q = \frac{1}{2\pi} \oint_C \frac{1}{\beta(s)} ds, \tag{1.28}$$

where C is the circumference of the machine. Correspondingly, we define the cell tune $\nu = Q/N$ as the phase advances along each of the N cells that comprise the lattice.

1.3.3 Emittance

Differentiating the LHS of Eqn. 1.26 with respect to s gives the angle relative to the designed momentum, or divergence, as

$$x'(s) = -\frac{\sqrt{\varepsilon}}{\sqrt{\beta(s)}} \left\{ \alpha(s)\cos(\phi(s) - \phi_0) + \sin(\phi(s) - \phi_0) \right\}, \tag{1.29}$$

where we define

$$\alpha(s) = -\frac{1}{2}\beta'(s), \tag{1.30}$$

with the prime denoting differentiation with respect to s. If we further define

$$\gamma(s) = \frac{1 + \alpha^2(s)}{\beta(s)}, \tag{1.31}$$

then we can show that

$$\gamma(s)x^2(s) + 2\alpha(s)x(s)x'(s) + \beta(s)x'^2(s) = \epsilon. \tag{1.32}$$

Namely, the LHS is equal to the emittance, a constant, for all s.

Equation 1.32 defines an ellipse in (x, x') phase space with area $\pi\epsilon$, as shown in Fig. 1.4. The invariance of the phase space area is a consequence of the Hamiltonian evolution of the beam and Liouville's theorem which states, more generally, that the volume of the beam in 6D (x, x', y, y', z, z') phase space is conserved under evolution in s. As a result, the magnetic fields within the lattice can only manipulate the beam such that the product of its size with its divergence remains constant. To reduce the emittance and thus the beam size, non-conservative forces must interact with the beam. Techniques developed to achieve this include radiation damping and stochastic cooling.

In practice, the particles in a beam will not be uniformly distributed throughout

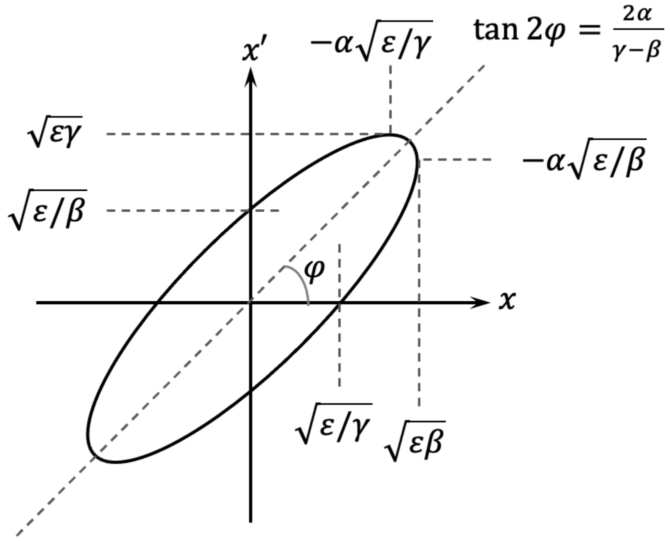

Figure 1.4: Phase space ellipse.

phase space. One such consequence is that the spatial profile of the beam is not well characterised by Eqn. 1.32 and so RMS emittances may be used instead. These are defined

$$\epsilon_{\text{RMS}} = \sqrt{\langle x^2 \rangle \langle x'^2 \rangle - \langle x \cdot x' \rangle^2}, \tag{1.33}$$

where $\langle x^2 \rangle$ and $\langle x'^2 \rangle$ are the variances in the positions and angles of the particles and $\langle x \cdot x' \rangle$ is the position-angle covariance between particles in the beam [35].

1.3.4 Dispersion

The momentum spread of the particles δp about the reference momentum also creates dispersion which is defined as

$$D(p, s) = \frac{\delta x(s)}{\delta p/p_0}, \tag{1.34}$$

where δx is the deviation from the reference orbit. Dispersion arises because particles of different energies undergo different orbits and it causes larger beam sizes.

1.3.5 Chromaticity

A finite momentum spread also modifies the quadrupole term in Hill's Equation 1.23 to

$$\frac{e}{p}\frac{\partial B_z(s)}{\partial x}\bigg|_0 \simeq \frac{1}{B_d\rho}\left(1-\frac{\delta p}{p_0}\right)\frac{\partial B_z(s)}{\partial x}\bigg|_0. \tag{1.35}$$

The effective focusing function is therefore weaker for particles of a larger energy but stronger for particles of a smaller energy. This is a chromatic aberration which creates an unwanted spread in the cell tune and can lead to beam loss [36]. Chromaticity is thus defined as

$$\xi(p) = \frac{\Delta\nu}{\delta p/p_0}, \tag{1.36}$$

where $\Delta\nu$ is the tune spread.

The unwanted chromatic effect from quadrupoles can be corrected by placing sextupoles with field gradient

$$\frac{\partial^2 B_z}{\partial x^2} = -\frac{1}{D}\frac{L_Q}{L_S}\frac{\partial B_z}{\partial x}, \tag{1.37}$$

adjacent to each quadrupole. Here, D is the dispersion function and L_Q and L_S are the lengths of the quadrupoles and sextupoles. These sextupoles kick off-centre particles in proportion to the square of their displacement, thus acting like a quadrupole with a focusing strength that is proportional to the displacement. As the reference orbit of off-momentum particles is displaced by $D\delta p/p_0$, the sextupoles correct for the chromaticity [37].

In practice, sextupoles are designed with much greater strengths than Eqn. 1.37 so that chromaticity is still reduced but with fewer sextupoles in the lattice.

1.3.6 Higher Order Magnets

Octupoles may be incorporated into the lattice to artificially induce a tune spread and generate Landau damping for the stabilisation of beams [38, 39].

Furthermore, construction or positioning errors of m-pole magnets can be corrected for by the use of higher order magnets. For example, octupole magnets can be incorporated into accelerator design to correct for octupolar errors in quadrupole fields [40] and decupole magnets to correct for decupolar errors generated in dipole fields [41].

1.3.7 Combined Function Magnets

Combined function magnets that incorporate the functions of multiple m-pole fields into one component are well investigated. For example, combined sextupole-dipole corrector magnets are installed in the LHC [42] and combined quadrupole-dipole magnets have been installed in several synchrotron light sources [43, 44, 45].

1.3.8 RF Cavities

RF cavities can also be operated in different m-pole-like modes that can manipulate particle beams analogously to m-pole magnets. The main advantages of using RF cavities over magnets are their relatively compact designs and ability to support fields that oscillate over the length scale of a particle bunch.

One such example are deflecting cavities that operate in dipolar, TM_{110}-like modes. These are used to exert a transverse kick on particle beams and have multiple applications depending upon the phase of RF used. For example, the LHS plot of Fig. 1.5 shows that a particle bunch is kicked transversely when the centre of the bunch is synchronised to pass through the deflecting cavity on-crest. Such kicking cavities have been designed to separate a single particle beam into multiple beams [46, 47, 48], provide longitudinal diagnostic measurements on particle beams such as measuring emittance [49], control electron beams in free-electron lasers by acting as emittance exchangers [50] and compress X-ray pulses in synchrotron light sources [51].

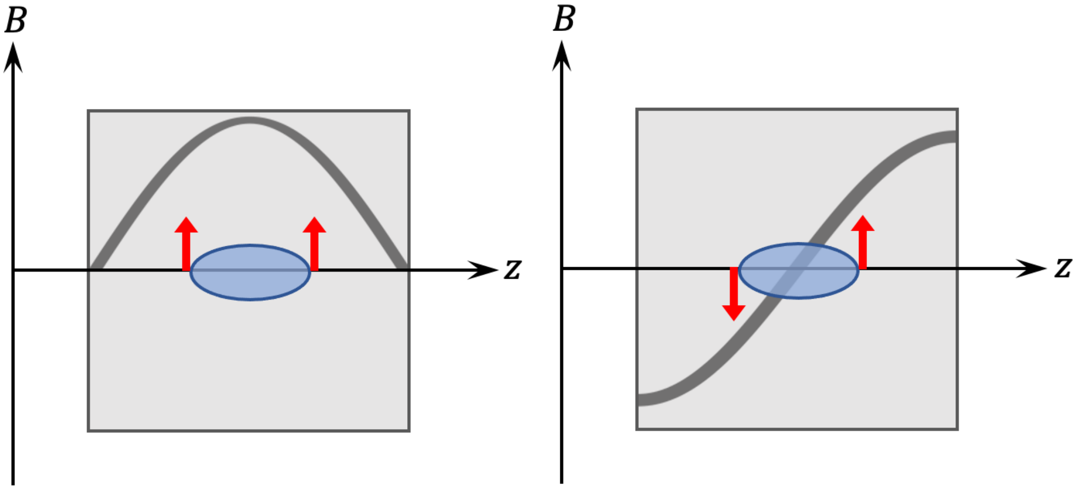

Figure 1.5: The forces imparted on a particle bunch travelling along the z-axis by the sinusoidally varying magnetic field in a deflecting cavity when phased to kick (left) or rotate (right). The forces are represented by the red arrows, the particle bunches by the blue ovals, the magnetic fields by the black lines and the cavities by the grey boxes. Note that the forces are perpendicular to the orientation of the magnetic field.

The RHS plot of Fig. 1.5 shows that a particle bunch is rotated when the centre of the bunch is synchronised to pass through the deflecting cavity at the zero-crossing. Such rotating cavities have been designed to measure longitudinal bunch lengths by rotating bunches onto a fixed transverse axis before imaging [52] and perform 3D charge-density measurements by varying the orientation of the transverse axis onto which the bunches are rotated [53].

An additional subset of cavities that operate at the zero-crossing are crab cavities. These are used to control the luminosity in particle colliders by varying the crossing angle of two colliding bunches [54]. For example, the reduction in luminosity resulting from a finite crossing angle for a Gaussian distributed bunch is

$$R_\Phi = \frac{1}{\sqrt{(1+\Phi^2)}}, \tag{1.38}$$

where $\Phi = \sigma_z\phi/\sigma_x$ with σ_z the bunch length, σ_x the transverse beam size and ϕ the half crossing angle at the interaction point [55]. Figure 1.6 shows how crab cavities can rotate the bunches for maximal overlap at the interaction point for maximal luminosity. These cavities have been commissioned and operated at KEKB [56, 57] and two different designs are scheduled for installation as part of the High-Luminosity LHC upgrade [58, 59].

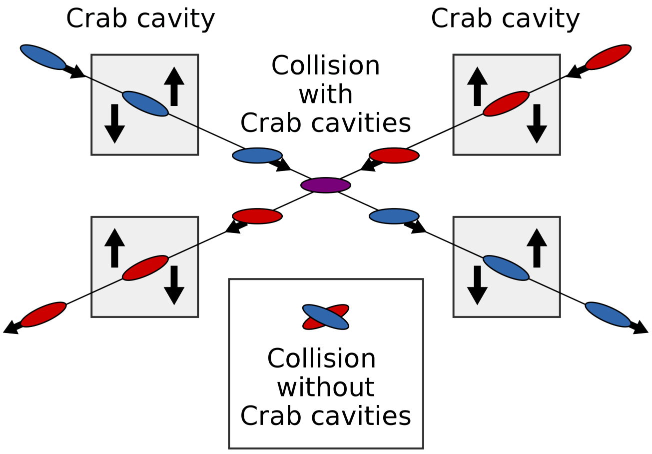

Figure 1.6: Improving the overlap of colliding beams with crab cavities. Reproduced from [60].

RF cavities that operate in different m-pole-like modes are also being explored for application in particle accelerators. For example, RF cavities which operate in quadrupolar, TM_{210}-like modes may be used for Landau damping transverse beam instabilities in the HL-LHC [61].

1.4 Thesis Outline

Having motivated and given examples of the uses of RF cavities in both accelerating and manipulating particle beams, this thesis proceeds to investigate a method for tailoring the electromagnetic modes within RF cavities. This begins in Chapter 2 where the basis of the electromagnetic fields inside closed azimuthally modulated cavities is derived. From this basis, the forms of the accelerating and manipulating modes in a pillbox cavity are found. They are analysed to determine their effect on the electrodynamics of on-axis beams that traverse them. This, and a discussion of the figures of merit of RF cavities, provides the basis for evaluating the tailored modes and their corresponding azimuthally modulated structures in subsequent chapters.

Chapter 3 begins with an analysis of two methods that introduce desired multipoles into an accelerating mode but in an uncontrolled manner. This motivates the azimuthal modulation method (AMM) which determines the azimuthually modulated cavity cross-sections that support desired modes by ensuring boundary conditions are satisfied. The AMM is outlined and the scope and limitations of its application are explored by an analysis of example modes composed of a monopole and a transverse multipole as well as those composed of two transverse multipoles. Concepts are introduced to describe the different properties of these modes and the azimuthally modulated cavities that support them. These concepts are extended to the design of cavities that support tailored modes of any multipolar content.

In Chapter 4, the results of experimental testing of an azimuthally modulated cavity are analysed. The chapter begins with an outline of the bead pull technique that is used to measure the electromagnetic fields in RF cavities and informed the decision to design and test an azimuthally modulated RF cavity that supports a 3 GHz mode which accelerates and focuses simultaneously. Simulation results are presented to show how power couplers were incorporated into the design such that the desired multipolar content of the mode is still attained. Experimental results from characterising the prototype are compared to simulation and the results of experimental bead pull testing analysed.

In Chapter 5, the AMM is applied to remove the unwanted transverse multipoles generated from incorporating power couplers into RF cavity designs. As an example, a structure is designed that incorporates a single-slot power coupler and supports an accelerating mode free of dipolar, quadrupolar, sextupolar and octupolar transverse multipoles. The effects of tuning RF cavities by deformation via one-way tuning pins on the mode is also analysed. The AMM is then applied to design RF cavities that anticipate and negate the average transverse multipoles caused by tuning pins.

In Chapter 6, the AMM is used to design RF cavities with tailored off-axis fields. For example, RF cavities are designed that have fields that vary as polynomials of the form x^m along the horizontal. Additionally, a procedure for optimising the field to vary as close to x^m given a spatial constraint on the cavity size is outlined. As an example, optimisation process is used to specifically design an RF cavity for application in a cyclotron. The generalisation of the method for designing fields that vary in any desired polynomial form is briefly discussed.

In Chapter 7, an overview is given of an outreach workshop called Funky Drums and Particle Accelerators that was designed to engage 11-14 year-old students with science. This workshop was inspired by the comparable physics that underlies both the electromagnetic modes in azimuthally modulated RF cavities and the vibrational modes of azimuthally modulated drums. The design of such drums is discussed as well as how they, and other experimental equipment, were used in the workshop.

Finally, the thesis is concluded in Chapter 8 by summarising and concluding the main results presented in each chapter. Future directions of this research are also discussed.

Chapter 2

Introduction to RF Cavities

An RF cavity is a type of resonator consisting of a metallic structure that confines electromagnetic fields of microwave wavelengths. The 3D shape of the cavity governs the spectrum of resonant frequencies and the corresponding spatial distributions of the electromagnetic standing waves, or modes, formed.

RF cavities are incorporated into particle accelerators such that a specific mode can be excited for either the acceleration or manipulation of a beam. This chapter provides an overview of the underlying physics of RF cavities, which underpins the research presented in the remainder of this thesis. It begins with a derivation of the mathematical form of electromagnetic standing waves in general RF cavities in Sec. 2.1. Specific boundary conditions are then applied in Sec. 2.2 to derive the electromagnetic basis of the modes in closed azimuthally modulated cavities. The electrodynamics of a particle beam traversing electromagnetic modes is reviewed in Sec. 2.3. Afterwards, the discussion is reduced to pillbox cavities in Sec. 2.4 where the electrodynamics of their different modes are reviewed and related to applications in particle accelerators. Essential and desired modifications that are made to the pillbox cavity design in order to optimise its figures of merit and incorporate it into a particle accelerator are then discussed in Sec. 2.5.

2.1 Electromagnetic Modes in RF Cavities

2.1.1 Vector Helmholtz Equation

Assuming an evacuated RF cavity, the electromagnetic fields inside it must satisfy the vacuum form of Maxwell's equations as given by Eqns. 1.1-1.4. From these and the vector identity

$$\nabla \times \nabla \times \vec{E} = \nabla(\nabla \cdot \vec{E}) - \nabla^2 \vec{E}, \tag{2.1}$$

one can derive that the electric field inside the RF cavity must satisfy the homogeneous wave equation

$$\nabla^2 \vec{E} - \frac{1}{c^2}\frac{\partial^2 \vec{E}}{\partial t^2} = 0. \tag{2.2}$$

Additionally, if the RF cavity is made of perfect electrically conducting material then the electric field must also satisfy the boundary condition

$$\hat{n} \times \vec{E} = 0, \tag{2.3}$$

where $\vec{n}$ is the normal vector perpendicular to the RF cavity surface at a given point.

We assume that both Eqn. 2.2 and Eqn. 2.3 are satisfied by an infinite number of standing wave modes and that each mode l has harmonic time-dependence with a distinct angular frequency ω_l and phase offset ξ_l such that

$$\vec{E}(\vec{r}, t) = \sum_l \vec{E}^{(l)}(\vec{r}) e^{-i(\omega_l t + \xi_l)}. \tag{2.4}$$

Inserting Eqn. 2.4 into Eqn. 2.2, we find that the spatial component of the electric field of each individual mode must satisfy the vector Helmholtz equation

$$\nabla^2 \vec{E}^{(l)}(\vec{r}) + k_l^2 \vec{E}^{(l)}(\vec{r}) = 0, \tag{2.5}$$

where $k_l = \omega_l / c$ is the wavenumber of the mode.

In subsequent analysis, we consider each mode independently and forgo the use of the superscript (l).

2.1.2 Cylindrical Coordinates

RF cavities used in particle accelerators often have cylindrical symmetry and so it is common to express the vector Helmholtz equation in cylindrical coordinates.

The cylindrical coordinate system is defined in Fig. 2.1 with the coordinates of a point P defined by (r, θ, z), where r is the Euclidean distance from the z-axis to P, θ is the azimuthal angle between the positive x-axis and the projection of P on the xy-plane, and z is the longitudinal displacement from the xy-plane to the point P. The correspondence between cylindrical and Cartesian coordinates is thus

$$x = r\cos(\theta), \qquad y = r\sin(\theta), \qquad z = z. \tag{2.6}$$

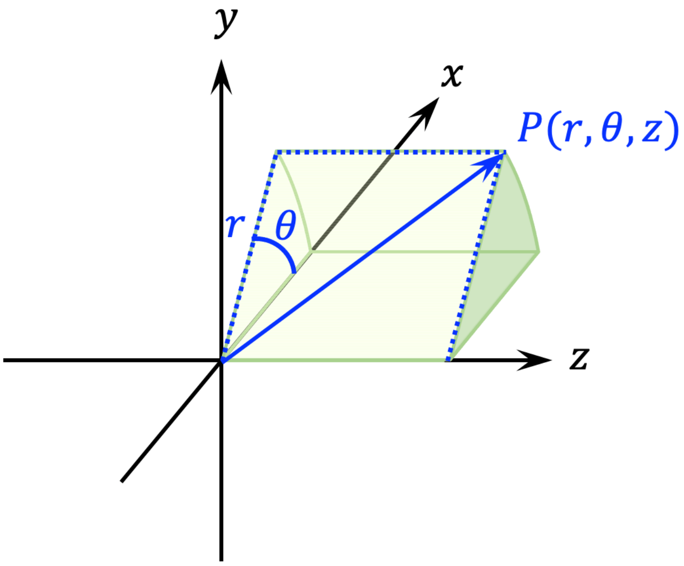

Figure 2.1: Cylindrical coordinate system.

Writing out each component of the vector Helmholtz Eqn. 2.5 in the cylindrical coordinate system gives

$$\frac{\partial^2 E_r}{\partial r^2} + \frac{1}{r}\frac{\partial E_r}{\partial r} + \frac{1}{r^2}\frac{\partial^2 E_r}{\partial \theta^2} + \frac{\partial^2 E_r}{\partial z^2} + \left(k_l^2 - \frac{1}{r^2}\right) E_r - \frac{2}{r^2}\frac{\partial E_\theta}{\partial \theta} = 0, \tag{2.7}$$

$$\frac{\partial^2 E_\theta}{\partial r^2} + \frac{1}{r}\frac{\partial E_\theta}{\partial r} + \frac{1}{r^2}\frac{\partial^2 E_\theta}{\partial \theta^2} + \frac{\partial^2 E_\theta}{\partial z^2} + \left(k_l^2 - \frac{1}{r^2}\right) E_\theta + \frac{2}{r^2}\frac{\partial E_r}{\partial \theta} = 0, \tag{2.8}$$

$$\frac{\partial^2 E_z}{\partial r^2} + \frac{1}{r}\frac{\partial E_z}{\partial r} + \frac{1}{r^2}\frac{\partial^2 E_z}{\partial \theta^2} + \frac{\partial^2 E_z}{\partial z^2} + k_l^2 E_z = 0. \tag{2.9}$$

Equations 2.7-2.9 are a set of coupled PDEs for which explicit, analytical solutions can be found.

2.1.3 Solving for the Electric Field

The Longitudinal Component

Equation 2.9 can be solved for the longitudinal component of the electric field by using the method of separation of variables. To do so, we substitute

$$E_z(r, \theta, z) = R(r)\Theta(\theta)Z(z), \tag{2.10}$$

into Eqn. 2.9 and divide through by $E_z(r, \theta, z)$ to get

$$\frac{1}{R}\frac{d^2 R}{dr^2} + \frac{1}{rR}\frac{dR}{dr} + \frac{1}{r^2\Theta}\frac{d^2\Theta}{d\theta^2} + k_l^2 = -\frac{1}{Z}\frac{d^2 Z}{dz^2}. \tag{2.11}$$

Since the LHS of Eqn. 2.11 only depends on r and θ whereas the RHS only depends on z, both sides can be equated to a constant. Denoting this constant as k^2 and equating it to the RHS of Eqn. 2.11 gives

$$\frac{d^2 Z}{dz^2} = -k^2 Z. \tag{2.12}$$

This has solutions that we choose to express in the complex exponential form as

$$Z = A_k e^{ikz} + B_k e^{-ikz}, \tag{2.13}$$

where A_k and B_k are constants and $k \in \mathbb{R}$ such that evanescent solutions are ignored.

Having solved for the form of Z, we now equate the LHS of Eqn. 2.11 to k^2 and rearrange it to

$$\frac{r^2}{R}\frac{d^2R}{dr^2} + \frac{r}{R}\frac{dR}{dr} + (k_l^2 - k^2) = -\frac{1}{\Theta}\frac{d^2\Theta}{d\theta^2}. \tag{2.14}$$

Similar to before, both sides can be equated to a constant because the LHS solely has dependence on r whereas the RHS only has dependence on θ. Denoting this constant as m^2 and equating it to the RHS of Eqn. 2.14 gives

$$\frac{d^2\Theta}{d\theta^2} = -m^2\Theta. \tag{2.15}$$

This has solutions that we choose to express in the trigonometric form as

$$\Theta = C_m \cos(m\theta) + D_m \sin(m\theta), \tag{2.16}$$

where C_m and D_m are constants and $m \in \mathbb{Z}$ because the electric field must be azimuthally periodic in 2π.

Having solved for the form of Θ, we now equate the LHS of Eqn. 2.14 to m^2 and rearrange it to

$$r^2\frac{d^2R}{dr^2} + r\frac{dR}{dr} + \left[(k_l^2 - k^2)^2 r^2 - m^2\right] R = 0. \tag{2.17}$$

This is the specific form of the well-studied Bessel's differential equation

$$x^2\frac{d^2y}{dx^2} + x\frac{dy}{dx} + (x^2 - \alpha^2)y = 0, \tag{2.18}$$

where α, known as the order of the Bessel function [62], is a real integer. Equation 2.18

has two linearly independent solutions because it is second-order and linear. In the case that $x \geq 0$, these are the Bessel functions of the first kind $J_\alpha(x)$ and the Bessel functions of the second kind $Y_\alpha(x)$, which can be expressed as

$$J_\alpha(x) = \sum_{q=0}^{\infty} \frac{(-1)^q}{q!(\alpha+q)!} \left(\frac{x}{2}\right)^{2q+\alpha}, \qquad Y_\alpha(x) = \lim_{q \to \alpha} \frac{J_q(x)\cos(q\pi) - J_{-q}(x)}{\sin(q\pi)}. \tag{2.19}$$

In the case that $x < 0$, the two solutions are the modified Bessel functions of the first kind $I_\alpha(x)$ and the modified Bessel functions of the second kind $K_\alpha(x)$, which can be expressed as

$$I_\alpha(x) = i^{-\alpha} J_\alpha(ix) = \sum_{q=0}^{\infty} \frac{1}{q!(\alpha+q)!} \left(\frac{x}{2}\right)^{2q+\alpha}, \qquad K_\alpha(x) = \lim_{q \to \alpha} \frac{\pi}{2} \frac{I_{-q}(x) - I_q(x)}{\sin(q\pi)}. \tag{2.20}$$

Figure 2.2 plots the four Bessel functions given by Eqns. 2.19-2.20 for five integer orders $\alpha = 0, 1, 2, 3$ and 4. We see that the Bessel functions of the first kind and second kind oscillate about zero. We introduce the notation j_{mn} to represent the n^{th} root of the Bessel function of the first kind of order m and likewise introduce y_{mn} to represent the roots of the Bessel function of the second kind. There are an infinite number of roots for each order and their values can be calculated numerically or looked up in tables [62]. In contrast, the modified Bessel functions of the first and second kind have no roots (ignoring any trivial roots at argument zero) because they positive for all positive arguments.

The general solution to Eqn. 2.17 therefore has the form

$$R(r) = \begin{cases} a_m J_m(\kappa_l r) + b_m Y_m(\kappa_l r), & k_l^2 \geq k^2; \\ c_m I_m(\kappa_l r) + d_m K_m(\kappa_l r), & \text{otherwise}, \end{cases} \tag{2.21}$$

where a_m, b_m, c_m and d_m are all constants and $\kappa_l^2 = |k_l^2 - k^2|$.

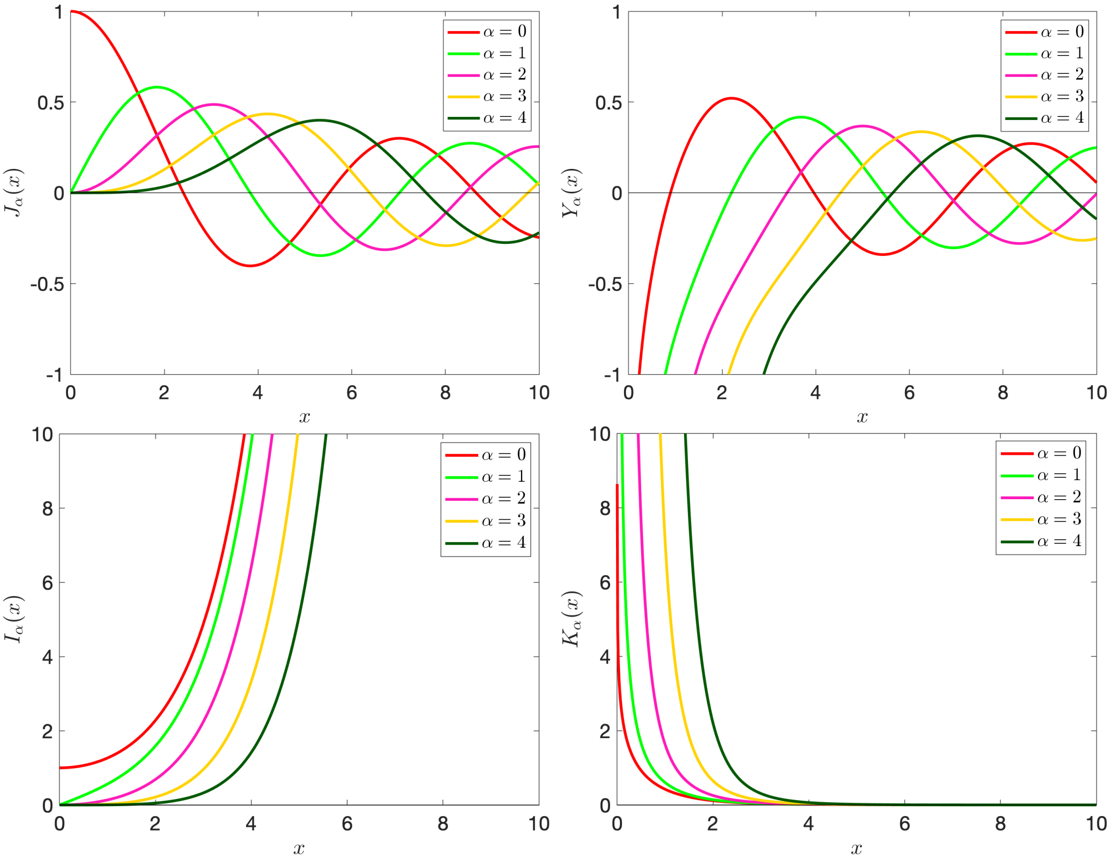

Figure 2.2: Plots of the Bessel functions of the first kind (top left), second kind (top right), modified first kind (bottom left) and modified second kind (bottom right).

The physical solution simplifies in the case of the electric field in an RF cavity absent of any charges. First, the $Y_m(x)$ and $K_m(x)$ solutions are both unphysical because they are infinite when the argument is null and the electric field must be finite at the cavity centre. Second, the $I_m(x)$ solutions (also known as the irrotational modes [63]) are disregarded because all orders diverge with increasing argument and the tangential component of the electric field must be zero at the cavity surfaces in the absence of any charges inside the cavity. In such a case, the physical solution therefore simplifies to

$$R(r) = \begin{cases} a_m J_m\left(\kappa_l r\right), & k_l^2 \geq k^2; \\ 0, & \text{otherwise.} \end{cases} \tag{2.22}$$

We can now substitute the solutions for R, Θ and Z as given by Eqns. 2.22, 2.16 and 2.13 into Eqn. 2.10 and express the longitudinal component of the electric field for a given value of $k \leq k_l^2$ and $m \in \mathbb{Z}^{0+}$ as

$$E_z(r,\theta,z) = a_m J_m\left(\kappa_l r\right)\left(C_m \cos\left(m\theta\right) + D_m \sin\left(m\theta\right)\right)\left(A_k e^{ikz} + B_k e^{-ikz}\right). \qquad (2.23)$$

Here only the real component of the electric field is physical.

The electric field in Eqn. 2.23 is degenerate with respect to both k and m. Therefore, we can sum over all their values and express the solution to Eqn. 2.9 as

$$E_z(\vec{r}) = \int_{-k_l}^{k_l} \frac{dk}{\sqrt{2\pi}} e^{ikz} \left\{ \tilde{e}_0(k) J_0(\kappa_l r) + \sum_{m=1}^{\infty} J_m(\kappa_l r)\left[\tilde{e}_m(k)\cos\left(m\theta\right) + \tilde{f}_m(k)\sin\left(m\theta\right)\right]\right\}. \qquad (2.24)$$

In this form, $\tilde{e}_m(k)$ and $\tilde{f}_m(k)$ are functions that explicitly depend on k and they are referred to as the normal and skew multipolar coefficients respectively. They determine the azimuthal form of the longitudinal electric field, much like the multipolar coefficients of the magnetic field discussed in Sec. 1.3.1. In this case, however, the multipolar coefficients have the same dimensions as the electric field.

The Radial and Azimuthal Components

The radial (Eqn. 2.7) and azimuthal (Eqn. 2.8) components of the vector Helmholtz equation are more complex to solve as they constitute a pair of coupled PDEs. They can, however, be decoupled with the use of Eqn. 1.1 and solved to find [64]

$$\begin{aligned} E_r(\vec{r}) = \int_{-k_l}^{k_l} \frac{dk}{\sqrt{2\pi}} e^{ikz}\left(-\frac{ik}{\kappa_l}\right)\Bigg\{ & \tilde{e}_0(k) J_1(\kappa_l r) + \\ & \sum_{m=1}^{\infty}\Bigg[\left(\tilde{e}_m(k) J_{m+1}(\kappa_l r) + \tilde{\beta}_m(k)\frac{J_m(\kappa_l r)}{\kappa_l r}\right)\cos\left(m\theta\right) + \\ & \left(\tilde{f}_m(k) J_{m+1}(\kappa_l r) + \tilde{\alpha}_m(k)\frac{J_m(\kappa_l r)}{\kappa_l r}\right)\sin\left(m\theta\right)\Bigg]\Bigg\}, \end{aligned} \qquad (2.25)$$

$$E_\theta(\vec{r}) = \int_{-\infty}^{\infty} \frac{dk}{\sqrt{2\pi}} e^{ikz} \left(\frac{ik}{\kappa_l}\right) \Bigg\{ \tilde{f}_0(k) J_1(\kappa_l r) + \sum_{m=1}^{\infty} \Bigg[\left(\tilde{f}_m(k) J_{m+1}(\kappa_l r) + \tilde{\alpha}_m(k) \left(\frac{J_m(\kappa_l r)}{\kappa_l r} - \frac{1}{m} J_{m-1}(\kappa_l r) \right) \right) \cos(m\theta) - \left(\tilde{e}_m(k) J_{m+1}(\kappa_l r) + \tilde{\beta}_m(k) \left(\frac{J_m(\kappa_l r)}{\kappa_l r} - \frac{1}{m} J_{m-1}(\kappa_l r) \right) \right) \sin(m\theta) \Bigg] \Bigg\}. \quad (2.26)$$

Here $\tilde{\beta}_m(k)$ and $\tilde{\alpha}_m(k)$ are functions that explicitly depend on k and have the same dimensions of the electric field, much like $\tilde{e}_m(k)$ and $\tilde{f}_m(k)$. However, they only contribute to the form of the radial and azimuthal components of the electric field.

2.1.4 Solving for the Magnetic Field

Equations 2.24-2.26 give the basis for the radial, azimuthal and longitudinal components of the electric field in a general RF cavity.

A similar method could be used to solve the vector Helmholtz equation for the magnetic field in cylindrical coordinates by applying the corresponding boundary condition for the magnetic field that

$$\hat{n} \cdot \vec{B} = 0. \quad (2.27)$$

A quicker method, however, is to relate the magnetic field to the electric field by integrating Eqn. 1.4

$$\vec{B}(\vec{r}, t) = -\int \nabla \times \vec{E}(\vec{r}, t) dt, \quad (2.28)$$

and then substituting in Eqn. 2.4 to find

$$\vec{B}(\vec{r}) = \frac{1}{i\omega_l} \nabla \times \vec{E}(\vec{r}). \quad (2.29)$$

In cylindrical coordinates, Eqn. 2.29 is

$$\vec{B}(\vec{r}) = -\frac{i}{\omega_l}\left(\left(\frac{1}{r}\frac{\partial E_z}{\partial \theta} - \frac{\partial E_\theta}{\partial z}\right)\hat{r} + \left(\frac{\partial E_r}{\partial z} - \frac{\partial E_z}{\partial r}\right)\hat{\theta} + \frac{1}{r}\left(\frac{\partial (rE_\theta)}{\partial r} - \frac{\partial E_r}{\partial \theta}\right)\hat{z}\right), \tag{2.30}$$

from which the basis of the magnetic field is simply found by substituting in E_z, E_r and E_θ as given by Eqns. 2.24-2.26. The inclusion of i in Eqn. 2.30 indicates that the magnetic field is π out of phase with the electric field.

2.2 Modes in Closed Azimuthally Modulated RF Cavities

Having derived the basis of the electromagnetic modes in a general RF cavity, we now seek the basis in closed azimuthally modulated RF cavities.

Such a cavity is shown in Fig. 2.3. It has an *azimuthally modulated* cross-section defined by the function $r_0(\theta)$ that gives the radial distance from the origin to the *cavity wall* as a function of the azimuthal angle. The cross-section is orientated in the xy-plane and extruded by length L along the z-direction to form the cavity wall. The cavity wall is centred on the origin and it is closed at each end by perpendicular, flat surfaces called the *end-caps*. It is assumed to be made out of perfect electrically conducting material and its volume assumed to exist under vacuum.

An azimuthally modulated cavity (that we assume closed unless stated otherwise) is therefore made up of three surfaces: the cavity wall and two end-caps. The general boundary condition of the electric field, $\hat{n} \times \vec{E} = 0$ as given by Eqn. 2.3, then becomes

$$E_\theta(r_0(\theta), \theta, z) = E_z(r_0(\theta), \theta, z) = 0, \tag{2.31}$$

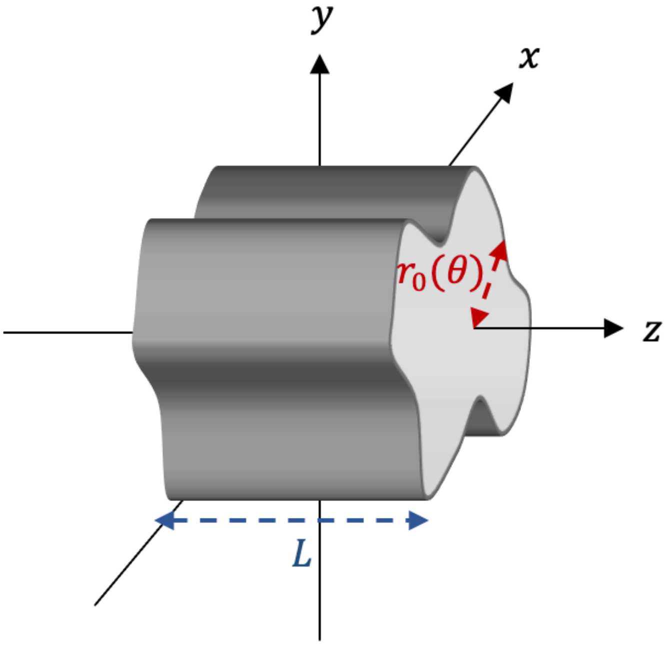

Figure 2.3: A closed azimuthally modulated RF cavity of longitudinal length L and azimuthally modulated cross-section $r_0(\theta)$.

on the cavity wall and

$$E_r(r, \theta, \pm L/2) = E_\theta(r, \theta, \pm L/2) = 0, \tag{2.32}$$

on the end-caps.

These explicit boundary conditions can be applied to the general basis of the electric field given by Eqns. 2.24-2.26 to determine the basis in azimuthally modulated cavities.

2.2.1 End-Cap Boundary Condition

Imposing the end-cap boundary condition given by Eqn. 2.32 on the radial component of the electric field stated in Eqn. 2.25 gives

$$\begin{aligned} E_r(r,\theta,\pm L/2) = \int_{-k_l}^{k_l} \frac{dk}{\sqrt{2\pi}} e^{\pm ikL/2} \left(-\frac{ik}{\kappa_l}\right) \Bigg\{ \tilde{e}_0(k) J_1(\kappa_l r) + \\ \sum_{m=1}^{\infty} \Bigg[\left(\tilde{e}_m(k) J_{m+1}(\kappa_l r) + \tilde{\beta}_m(k) \frac{J_m(\kappa_l r)}{\kappa_l r} \right) \cos(m\theta) + \\ \left(\tilde{f}_m(k) J_{m+1}(\kappa_l r) + \tilde{\alpha}_m(k) \frac{J_m(\kappa_l r)}{\kappa_l r} \right) \sin(m\theta) \Bigg] \Bigg\} = 0. \quad (2.33) \end{aligned}$$

The physical solution is solely the real component of Eqn. 2.33 and thus we require

$$\sin\left(\frac{kL}{2}\right) = 0, \quad (2.34)$$

because the end-cap boundary condition must be satisfied for all r and θ. Therefore only certain values of $k = k_p$ are allowed where

$$\frac{k_p L}{2} = p\pi, \quad (2.35)$$

with $p \in \mathbb{Z}$ and $k_p \leq k_l$. We note that an identical result follows from the end-cap boundary condition using the azimuthal component of the electric field.

This finding can be imposed on the general basis of the electric field using

$$\int_{-k_l}^{k_l} \frac{dk}{\sqrt{2\pi}} f(k) \delta(k - k_p) = f(k_p). \quad (2.36)$$

Doing so and only taking the real component for the physical solution, Eqns. 2.24-2.26

become

$$\begin{aligned}E_r(\vec{r}) = \sum_{\{k_p\}} \Bigg(\frac{k_p}{\kappa_{lp}} \sin(k_p z) \Bigg\{ \tilde{e}_0(k_p) J_1(\kappa_{lp} r) + \sum_{m=1}^{\infty} \Bigg[\Bigg(\tilde{e}_m(k_p) J_{m+1}(\kappa_{lp} r) + \\ \tilde{\beta}_m(k_p) \frac{J_m(\kappa_{lp} r)}{\kappa_p r} \Bigg) \cos(m\theta) + \Bigg(\tilde{f}_m(k_p) J_{m+1}(\kappa_{lp} r) + \tilde{\alpha}_m(k_p) \frac{J_m(\kappa_{lp} r)}{\kappa_{lp} r} \Bigg) \sin(m\theta) \Bigg] \Bigg\} \Bigg),\end{aligned} \tag{2.37}$$

$$\begin{aligned}E_\theta(\vec{r}) = -\sum_{\{k_p\}} \Bigg(\frac{k_p}{\kappa_{lp}} \sin(k_p z) \Bigg\{ \tilde{f}_0(k_p) J_1(\kappa_{lp} r) + \sum_{m=1}^{\infty} \Bigg[\Bigg(\tilde{f}_m(k_p) J_{m+1}(\kappa_{lp} r) + \\ \tilde{\alpha}_m(k_p) \Bigg(\frac{J_m(\kappa_{lp} r)}{\kappa_{lp} r} - \frac{J_{m-1}(\kappa_{lp} r)}{m} \Bigg) \Bigg) \cos(m\theta) - \Bigg(\tilde{e}_m(k_p) J_{m+1}(\kappa_{lp} r) + \\ \tilde{\beta}_m(k_p) \Bigg(\frac{J_m(\kappa_{lp} r)}{\kappa_{lp} r} - \frac{J_{m-1}(\kappa_{lp} r)}{m} \Bigg) \Bigg) \sin(m\theta) \Bigg] \Bigg\} \Bigg),\end{aligned} \tag{2.38}$$

$$\begin{aligned}E_z(\vec{r}) = \sum_{\{k_p\}} \Bigg(\cos(k_p z) \Bigg\{ \tilde{e}_0(k_p) J_0(\kappa_{lp} r) + \sum_{m=1}^{\infty} J_m(\kappa_{lp} r) \big[\tilde{e}_m(k_p) \cos(m\theta) + \\ \tilde{f}_m(k_p) \sin(m\theta) \big] \Bigg\} \Bigg),\end{aligned} \tag{2.39}$$

where the sum is over the set of all allowed values of k_p and we define

$$\kappa_{lp} = \sqrt{k_l^2 - k_p^2} = \sqrt{k_l^2 - \left(\frac{2p\pi}{L} \right)^2}. \tag{2.40}$$

Equations 2.37-2.39 can be written in a more compact form. First, we forgo expressing the sum over k_p. We do so because, as can be seen by rearranging Eqn. 2.40 to

$$\omega_l = \sqrt{\kappa_{lp}^2 + \left(\frac{2p\pi}{L} \right)^2}, \tag{2.41}$$

the resonant frequencies of the different modes in a given azimuthally modulated cavity vary with p, and so can be considered independently. Additionally, we use the Bessel relations [62]

$$\frac{2m}{x}J_m(x) = J_{m-1}(x) + J_{m+1}(x), \qquad 2\frac{dJ_m(x)}{dx} = J_{m-1}(x) - J_{m+1}(x), \tag{2.42}$$

to re-express the basis as

$$E_r(\vec{r}) = \frac{k_p}{\kappa_p}\sin(k_p z)\sum_{m=0}^{\infty}\left(\tilde{g}_m J_{m+1}(\kappa_p r)\cos(m\theta - \phi_m) + \tilde{\gamma}_m\frac{J_m(\kappa_p r)}{\kappa_p r}\cos(m\theta - \psi_m)\right), \tag{2.43}$$

$$E_\theta(\vec{r}) = \frac{k_p}{\kappa_p}\sin(k_p z)\sum_{m=0}^{\infty}\left(\tilde{g}_m J_{m+1}(\kappa_p r)\sin(m\theta - \phi_m) - \tilde{\gamma}_m\frac{J'_m(\kappa_p r)}{m}\sin(m\theta - \psi_m)\right), \tag{2.44}$$

$$E_z(\vec{r}) = \cos(k_p z)\sum_{m=0}^{\infty}\tilde{g}_m J_m(\kappa_p r)\cos(m\theta - \phi_m), \tag{2.45}$$

where we drop the subscript l from κ_p and define

$$\begin{gathered}\tilde{e}_m = \tilde{g}_m\cos\phi_m, \qquad \tilde{f}_m = \tilde{g}_m\sin\phi_m, \\ \tilde{\beta}_m = \tilde{\gamma}_m\cos\psi_m, \qquad \tilde{\alpha}_m = \tilde{\gamma}_m\sin\psi_m, \\ \phi_0 = \gamma_0 = \psi_0 = 0.\end{gathered} \tag{2.46}$$

In such a form, $\tilde{g}_m$ is called the *multipolar magnitude* because it determines the magnitude of the azimuthal form of the longitudinal electric field. It is always positive because $\tilde{g}_m = \sqrt{\tilde{e}_m^2 + \tilde{f}_m^2}$. The parameter ϕ_m gives the angle of the multipolar component relative to the horizontal such that $\phi_m = 0$ is a normal multipolar field and $\phi_m = \pi/2$ is a skew multipolar field. The parameters γ and ψ are defined similarly but they only influence the form of the radial and azimuthal components of the electric field.

2.2.2 Cavity Wall Boundary Condition

Imposing the cavity wall boundary condition on the longitudinal component of the electric field in Eqn. 2.45 gives

$$E_z(r_0(\theta), \theta, z) = \cos(k_p z) \sum_{m=0}^{\infty} \tilde{g}_m J_m(\kappa_p r_0(\theta)) \cos(m\theta - \phi_m) = 0, \tag{2.47}$$

and on the azimuthal component gives

$$\begin{aligned} E_z(r_0(\theta), \theta, z) = \frac{k_p}{\kappa_p} \sin(k_p z) \sum_{m=0}^{\infty} \Bigg(&\tilde{g}_m J_{m+1}(\kappa_p r_0(\theta)) \sin(m\theta - \phi_m) - \\ &\tilde{\gamma}_m \frac{J'_m(\kappa_p r_0(\theta))}{m} \sin(m\theta - \psi_m) \Bigg) = 0. \end{aligned} \tag{2.48}$$

We can solve Eqns. 2.47-2.48 to show that the form of the electromagnetic modes in azimuthally modulated cavities fall into one of two subsets: *transverse electric* (TE) or *transverse magnetic* (TM).

TE Modes

Equation 2.47 is trivially solved by

$$\tilde{g}_m = 0. \tag{2.49}$$

Such modes are defined as transverse electric because the longitudinal component of the electric field is zero throughout the cavity.

Substituting Eqn. 2.49 into Eqn. 2.48, the cavity wall boundary condition on the azimuthal component simplifies to

$$0 = -\sin(k_p z) \frac{k_p}{\kappa_p} \sum_{m=0}^{\infty} \tilde{\gamma}_m \frac{J'_m(\kappa_p r_0(\theta))}{m} \sin(m\theta - \psi_m). \tag{2.50}$$

Let us assume that Eqn. 2.50 is only solved for a set $\{M\}$ of integers for which the coefficients $\tilde{\gamma}_m$ are non-zero

$$\tilde{\gamma}_m = \begin{cases} \tilde{\gamma}_M, & m \in \{M\}; \\ 0, & \text{otherwise.} \end{cases} \tag{2.51}$$

The azimuthally modulated cross-section is then defined by

$$\kappa_p r_0^{(\eta)}(\theta) = j'_{\{M\}\eta}(\theta), \tag{2.52}$$

where $j'_{\{M\}\eta}(\theta)$ is a notation introduced to represent the roots to Eqn. 2.50. Here we introduce η to denote the order of the solution for a given $\{M\}$. We choose η because it is visually similar to n which we used earlier to denote n^{th} root of the m^{th} order Bessel functions j_{mn}.

Inserting Eqn. 2.49 and Eqn. 2.51 into Eqns. 2.43-2.45 thus gives the form of the electric field of a TE mode in an azimuthally modulated cavity as

$$E_r(r,\theta,z) = \sin(k_p z)\frac{k_p}{\kappa_p^2 r}\sum_{\{M\}}\tilde{\gamma}_M J_M(\kappa_p r)\cos(M\theta - \psi_M), \tag{2.53}$$

$$E_\theta(r,\theta,z) = -\sin(k_p z)\frac{k_p}{\kappa_p}\sum_{\{M\}}\frac{1}{M}\tilde{\gamma}_M J'_M(\kappa_p r)\sin(M\theta - \psi_M), \tag{2.54}$$

$$E_z(r,\theta,z) = 0, \tag{2.55}$$

where κ_p explicitly relates to the cavity cross-section via Eqn. 2.52.

The corresponding form of the magnetic field of a TE mode can then be calculated using Eqn. 2.30 to find

$$B_r(r,\theta,z) = \frac{i}{\omega_l}\cos(k_p z)\frac{k_p^2}{\kappa_p}\sum_{\{M\}}\tilde{\gamma}_M J'_M(\kappa_p r)\sin(M\theta - \psi_M), \tag{2.56}$$

$$B_\theta(r,\theta,z) = -\frac{i}{\omega_l}\cos{(k_p z)}\frac{k_p^2}{\kappa_p^2 r}\sum_{\{M\}}\tilde{\gamma}_M J_M(\kappa_p r)\cos{(M\theta - \psi_M)}, \tag{2.57}$$

$$B_z(r,\theta,z) = -\frac{i}{\omega_l}\sin{(k_p z)}k_p\sum_{\{M\}}\frac{1}{M}\tilde{\gamma}_M J_M(\kappa_p r)\sin{(M\theta - \psi_M)}. \tag{2.58}$$

TM Modes

Equation 2.47 also has non-trivial solutions. Let us assume it is only solved by a set $\{M\}$ of integers for which the coefficients $\tilde{g}_m$ are non-zero

$$\tilde{g}_m = \begin{cases} \tilde{g}_M, & m \in \{M\}; \\ 0, & \text{otherwise.} \end{cases} \tag{2.59}$$

This then defines the azimuthally modulated cross-section as

$$\kappa_p r_0^{(\eta)}(\theta) = j_{\{M\}\eta}(\theta). \tag{2.60}$$

Inserting Eqn. 2.59 into Eqn. 2.48, the boundary condition for the azimuthal component of the electric field on the cavity wall becomes

$$\begin{split} 0 = \sin{(k_p z)}\frac{k_p}{\kappa_p}\Bigg(\sum_{\{M\}}\tilde{g}_M J_{M+1}\left(\kappa_p r_0^{(\eta)}(\theta)\right)\sin{(M\theta - \phi_M)} + \\ \sum_{m=0}^{\infty}\tilde{\gamma}_m\left(\frac{1}{m}J_{m+1}\left(\kappa_p r_0^{(\eta)}(\theta)\right) - \frac{1}{\kappa_p r}J_m\left(\kappa_p r_0^{(\eta)}(\theta)\right)\right)\sin{(m\theta - \psi_m)}\Bigg). \end{split} \tag{2.61}$$

The constraint between the resonant frequency of the mode and the cross-section in Eqn. 2.60 requires the non-zero $\tilde{\gamma}_m$ terms to be of the same order as $\tilde{g}_m$

$$\tilde{\gamma}_m = \begin{cases} \tilde{\gamma}_M, & m \in \{M\}; \\ 0, & \text{otherwise,} \end{cases} \tag{2.62}$$

and the orientation of the multipolar magnitudes to be equal

$$\psi_M = \phi_M. \tag{2.63}$$

Inserting Eqns. 2.62-2.63 into Eqn. 2.61 gives

$$0 = \sin{(k_p z)} \frac{k_p}{\kappa_p} \sum_{\{M\}} (\tilde{g}_M + \frac{1}{M}\tilde{\gamma}_M) J_{M+1}(\kappa_p r_0^{(\eta)}(\theta)) \sin{(M\theta - \phi_M)}. \tag{2.64}$$

This is only satisfied for all θ and z if

$$\tilde{\gamma}_M = -M\tilde{g}_M. \tag{2.65}$$

Inserting Eqn. 2.59, Eqns. 2.62-2.63 and Eqn. 2.65 into Eqns. 2.43-2.45 thus gives the form of the electric field of a TM mode in an azimuthally modulated cavity as

$$E_r(r,\theta,z) = -\sin{(k_p z)} \frac{k_p}{\kappa_p} \sum_{\{M\}} \tilde{g}_M J_M'(\kappa_p r) \cos{(M\theta - \phi_M)}, \tag{2.66}$$

$$E_\theta(r,\theta,z) = \sin{(k_p z)} \frac{k_p}{\kappa_p^2 r} \sum_{\{M\}} M\tilde{g}_M J_M(\kappa_p r) \sin{(M\theta - \phi_M)}, \tag{2.67}$$

$$E_z(r,\theta,z) = \cos{(k_p z)} \sum_{\{M\}} \tilde{g}_M J_M(\kappa_p r) \cos{(M\theta - \phi_M)}, \tag{2.68}$$

where κ_p explicitly relates to the cavity cross-section via Eqn. 2.60.

The corresponding form of the magnetic field of a TM mode can again be calculated using Eqn. 2.30 to find

$$B_r(r,\theta,z) = \frac{i}{\omega_l} \cos{(k_p z)} \frac{\kappa_p^2 + k_p^2}{\kappa_p^2 r} \sum_{\{M\}} M\tilde{g}_M J_M(\kappa_p r) \sin{(M\theta - \phi_M)}, \tag{2.69}$$

$$B_\theta(r,\theta,z) = \frac{i}{\omega_l} \cos{(k_p z)} \frac{\kappa_p^2 + k_p^2}{\kappa_p} \sum_{\{M\}} \tilde{g}_M J_M'(\kappa_p r) \cos{(M\theta - \phi_M)}, \tag{2.70}$$

$$B_z(r, \theta, z) = 0. \tag{2.71}$$

Such modes are defined as transverse magnetic because the longitudinal component of the magnetic field is zero throughout the cavity.

2.2.3 Nomenclature of Modes

From Eqns. 2.53-2.58 and Eqns. 2.66-2.71, we see that all TE and TM modes in an azimuthally modulated cavity are defined analytically by the parameters:

- {M}: the set of integers for which $\tilde{g}_m$ (or $\tilde{\gamma}_m$) is non-zero. It specifies the orders of multipoles contained within the mode.
- $\tilde{g}_M$ ($\tilde{\gamma}_M$): the multipolar magnitudes that specify the magnitude of the multipoles contained within the mode.
- ϕ_M (ψ_M): the orientation of the multipolar components, with respect to the horizontal.
- η: the order of the solution for a given $\{M\}$.
- ω_l: the frequency of the mode.
- p: the longitudinal order of the mode.

We therefore introduce the nomenclature of TE$_{\{M\}\eta p}$ and TM$_{\{M\}\eta p}$ to represent the modes supported by azimuthally modulated cavities.

2.3 Electrodynamics in RF Cavities

Having derived the mathematical form of the modes supported by azimuthally modulated cavities, here we analyse mathematically how electromagnetic fields can be used to accelerate and manipulate beams in particle accelerators.

To simplify the analysis, a number of assumptions are made. We assume that that particle beams enter and exit the closed azimuthally modulated RF cavities *on-axis*; that is the beam has some transverse profile but its centroid travels along the z-axis where $r = 0$. Furthermore, we assume the cavity is sufficiently *thin* that the properties of the beam (velocity, energy and momentum) can be treated as constant whilst it traverses the mode. Additionally, we assume that all particles in the beam have a negligible transverse velocity such that the velocity of each particle is $\vec{v} = v_z\hat{z}$ throughout the cavity. We also ignore any space charge effects and assume that the beam is composed of infinitesimally small test charges that have a negligible effect on the field itself. We also assume the validity of the Panofsky-Wenzel theorem to analyse the transverse beam dynamics.

The results derived here are subsequently applied in Sec. 2.4 to analyse the different modes in a closed pillbox cavity and motivate the different applications of different modes. Such cavities, however, are not realistic for application in particle accelerators because they do not, for example, include beam pipes or power couplers. Their incorporation is thus discussed in Sec. 2.5.

2.3.1 Longitudinal Electrodynamics

The change in longitudinal momentum of a test charge traversing an azimuthally modulated RF cavity supporting a single, harmonic electromagnetic mode of frequency ω_l is

$$\Delta p_z(r,\theta) = \int_{-L/2}^{L/2} \frac{e}{v_z(\vec{r})} \left(E_z(\vec{r}) + \left(\vec{v}(\vec{r}) \times \vec{B}(\vec{r}) \right)_z \right) e^{-i(\omega_l t + \xi_l)} dz, \tag{2.72}$$

as determined from the Lorentz force Eqn. 1.6.

The position of a particle is given by $z(t) = v_z t$ throughout the cavity because the cavity is assumed thin and any transverse velocity of the particle is neglected. The longitudinal component of the cross-product term in Eqn. 2.72 is thus zero and so the change in longitudinal momentum simplifies to

$$\Delta p_z(r,\theta) = \frac{e}{v_z}\int_{-L/2}^{L/2} E_z(\vec{r})\cos{(\omega_l t + \xi_l)}dz. \tag{2.73}$$

Here we have taken the real component and thus chosen the specific phase of RF whereby $t = 0$ and $\xi_l = 0$ correspond to a maximum longitudinal electric field. This specific phase of RF is adopted throughout this thesis to allow for consistent comparison.

The longitudinal component of the electric field in an azimuthally modulated RF cavity is an even function with respect to changes in z for both TE and TM modes, as shown in Eqn. 2.55 and Eqn. 2.68. Therefore, if we expand the cosine term in Eqn. 2.73 and substitute for $t = z/v_z$ to get

$$\Delta p_z(r,\theta) = \frac{e}{v_z}\int_{-L/2}^{L/2} E_z(r,\theta,z)\left(\cos\left(\omega_l\frac{z}{v_z}\right)\cos{(\xi_l)} - \sin\left(\omega_l\frac{z}{v_z}\right)\sin{(\xi_l)}\right)dz, \tag{2.74}$$

we can subsequently neglect any contribution from the $\sin{(\omega_l z/v_z)}$ term because it is an odd function.

Equation. 2.73 therefore becomes

$$\Delta p_z(r,\theta) = \frac{e}{v_z}\cos{(\xi_l)}\int_{-L/2}^{L/2} E_z(\vec{r})\cos{(\omega_l t)}dz, \tag{2.75}$$

which we re-express as

$$\Delta p_z(r,\theta) = \frac{e}{v_z}\cos{(\xi_l)}V_z(r,\theta), \tag{2.76}$$

where the longitudinal voltage is defined as

$$V_z(r,\theta) = \int_{-L/2}^{L/2} E_z(\vec{r})\cos{(\omega_l t)}dz. \tag{2.77}$$

We also introduce the concept of the longitudinal transit time factor

$$T_z(r,\theta) = \frac{V_z(r,\theta)}{V_z^{\mathrm{max}}}, \tag{2.78}$$

where the maximum on-axis longitudinal voltage is

$$V_z^{\mathrm{max}} = \int_{-L/2}^{L/2} E_z^{\mathrm{max}} dz, \tag{2.79}$$

and the maximum on-axis longitudinal electric field is

$$E_z^{\mathrm{max}} = E_z(0,0,z). \tag{2.80}$$

We also define the effective length

$$\begin{aligned} L_{\mathrm{eff}}^{p} &= \int_{-L/2}^{L/2} \cos\left(\frac{2p\pi}{L}z\right)\cos\left(\frac{\omega_l}{v_z}z\right)dz = \\ &= 2\frac{\frac{\omega_l}{v_z}\cos(p\pi)\sin\left(\frac{\omega_l}{v_z}\frac{L}{2}\right) - \frac{2p\pi}{L}\sin(p\pi)\cos\left(\frac{\omega_l}{v_z}\frac{L}{2}\right)}{\left(\frac{\omega_l}{v_z}\right)^2 - \left(\frac{2p\pi}{L}\right)^2}. \end{aligned} \tag{2.81}$$

In the case that the longitudinal electric field is independent of z then

$$V_z(r,\theta) = E_z(r,\theta)L_{\mathrm{eff}}^{0}, \tag{2.82}$$

and so

$$T_z(r,\theta) = \frac{E_z(r,\theta)}{V_z^{\mathrm{max}}}L_{\mathrm{eff}}^{0}, \tag{2.83}$$

where

$$L_{\mathrm{eff}}^{0} = \frac{2v_z}{\omega_l}\sin\left(\frac{\omega_l}{v_z}\frac{L}{2}\right). \tag{2.84}$$

2.3.2 Transverse Electrodynamics

A similar method starting from the Lorentz force could be used to determine change in transverse momentum. However, it would be more complex as it requires the use of all six components of the electromagnetic field.

Under our assumptions a far simpler equation exists that requires knowledge of just one of the six components of the electromagnetic field to determine the change in transverse momentum. This is the Panofsky-Wenzel theorem, first derived in 1956 [65].

The Panofsky-Wenzel Theorem

The derivation begins with re-expressing the Lorentz force Eqn. 1.6 in terms of the magnetic vector potential and in the absence of an electric scalar potential as

$$\frac{d\vec{p}}{dz}v_z = e\left(-\frac{\partial\vec{A}}{\partial t} + \vec{v}\times\nabla\times\vec{A}\right). \tag{2.85}$$

The cross product term in Eqn. 2.85 is then substituted for using the vector identity

$$\vec{v}\times\nabla\times\vec{A} = (\nabla\vec{A})\cdot\vec{v} - (\vec{v}\cdot\nabla)\vec{A}, \tag{2.86}$$

the definition of the total derivative is used to substitute for the partial derivative term as

$$\frac{\partial\vec{A}}{\partial t} = \frac{d\vec{A}}{dt} - (\vec{v}\cdot\nabla)\vec{A}, \tag{2.87}$$

and the particle velocity term is substituted with

$$\vec{v} = \vec{v}_z + v_z\frac{\vec{p}_\perp}{p_z}, \tag{2.88}$$

such that Eqn. 2.85 becomes

$$\frac{d\vec{p}}{dz} = \frac{e}{v_z}\left(-\frac{d\vec{A}}{dt} + (\nabla\vec{A})\cdot\vec{v}\right) = e\left(-\frac{d\vec{A}}{dz} + \nabla A_z + (\nabla\vec{A})\cdot\frac{\vec{p}_\perp}{p_z}\right). \tag{2.89}$$

If only the transverse components of Eqn. 2.89 are considered, then it becomes

$$\frac{d\vec{p}_\perp}{dz} = -e\frac{d\vec{A}_\perp}{dz} + e\nabla_\perp A_z + e\frac{p_\perp}{p_z}\nabla_\perp\left(\vec{A}\cdot\hat{p}_\perp\right). \tag{2.90}$$

Integrating Eqn. 2.90 between the ends of the RF cavity gives the exact change in transverse momentum of a particle that traverses it. Doing so and imposing the boundary condition that the transverse component of the magnetic vector potential is zero at the edges of the RF cavity, simplifies Eqn. 2.90 to

$$\Delta\vec{p}_\perp = e\int_{-L/2}^{L/2}\nabla_\perp A_z dz + e\int_{-L/2}^{L/2}\frac{p_\perp}{p_z}\nabla_\perp(\vec{A}_\perp\cdot\hat{p}_\perp)dz. \tag{2.91}$$

Finally, the Panofsky-Wenzel theorem is derived by making the assumption

$$\int_{-L/2}^{L/2}\nabla_\perp A_z dz \gg \int_{-L/2}^{L/2}\frac{p_\perp}{p_z}\nabla_\perp(\vec{A}_\perp\cdot\hat{p}_\perp), \tag{2.92}$$

which is valid provided $A_z \neq 0$, the initial velocity of the test charge is along z and the cavity is thin. Assuming Eqn. 2.92 and using $E_z = -\partial A_z/\partial t = i\omega_l A_z$, Eqn. 2.91 becomes the Panofsky-Wenzel theorem

$$\Delta\vec{p}_\perp(r,\theta) = -i\frac{e}{\omega_l}\int_{-L/2}^{L/2}\nabla_\perp E_z(\vec{r},t)dz. \tag{2.93}$$

The theorem thus states that of the six components that define an electromagnetic field, only E_z is required to determine the change in transverse momentum of the test charge.

Change in Transverse Momentum

Using the Panosky-Wenzel theorem gives the change in transverse momentum of a test charge traversing an azimuthally modulated RF cavity supporting a single, harmonic electromagnetic mode of frequency ω_l as

$$\Delta\vec{p}_\perp(r,\theta) = -\frac{e}{\omega_l}\int_{-L/2}^{L/2} \nabla_\perp \left(E_z(\vec{r})\sin\left(\omega_l t + \xi_l\right)\right) dz, \tag{2.94}$$

where the real component has been taken.

Similar to determining the change in longitudinal momentum in Sec. 2.3.1, the sine term in Eqn. 2.94 can be expanded and the contribution from the odd $\sin\left(\omega_l z/v_z\right)$ term neglected. Doing so and also swapping the order of the differential and integral gives

$$\Delta\vec{p}_\perp(r,\theta) = -\frac{q}{\omega_l}\sin\left(\xi_l\right)\nabla_\perp \left(\int_{-L/2}^{L/2} E_z(\vec{r})\cos\left(\omega_l t\right) dz\right), \tag{2.95}$$

which we re-express as

$$\Delta p_\perp(r,\theta) = -\frac{q}{v_z}\sin\left(\xi_l\right)V_\perp(r,\theta), \tag{2.96}$$

where the transverse voltage is defined as

$$V_\perp(r,\theta) = \frac{v_z}{\omega_l}\nabla_\perp \left(\int_{-L/2}^{L/2} E_z(\vec{r})\cos\left(\omega_l t\right) dz\right). \tag{2.97}$$

We also introduce the concept of transverse transit time factor

$$T_\perp(r,\theta) = \frac{V_\perp(r,\theta)}{V_\perp^{\max}}, \tag{2.98}$$

where the maximum on-axis transverse voltage is

$$V_\perp^{\max} = \frac{v_z}{\omega_l}\int_{-L/2}^{L/2} \mathcal{E}_z^{\max} dz, \tag{2.99}$$

and the maximum on-axis transverse gradient of the longitudinal electric field is

$$\mathcal{E}_z^{\max} = \nabla_\perp E_z(r,\theta,z)\bigg|_{r=0} . \tag{2.100}$$

In the case that the longitudinal electric field is independent of z then

$$V_\perp(r,\theta) = \frac{v_z}{\omega_l}\nabla_\perp E_z(r,\theta)L_{\text{eff}}^0, \tag{2.101}$$

and so

$$T_\perp(r,\theta) = \frac{v_z}{\omega_l}\frac{\nabla_\perp E_z(r,\theta)}{V_\perp^{\max}}L_{\text{eff}}^0, \tag{2.102}$$

where L_{eff}^0 is defined in Eqn. 2.84.

2.3.3 Discussion

Two complementary equations have been derived in Eqn. 2.76 and Eqn. 2.96 which respectively give the change in longitudinal and transverse momenta of a test charge traversing an RF cavity. Equation 2.76 states that the greatest change in longitudinal momentum occurs when the test charge enters *on-crest* (whereby $\xi_l = 0, \pi$) and when the longitudinal voltage is maximised. In contrast, Eqn. 2.96 shows that the greatest change in transverse momentum occurs when the particle beam enters at the *zero-crossing* (whereby $\xi_l = \pi/2, 3\pi/2$) and when the transverse voltage is maximised. The particle beam must therefore enter the RF cavity *off-crest* (whereby $\xi_l \neq 0, \pi/2, \pi, 3\pi/2$) to change both the longitudinal and transverse momentum simultaneously.

We now use these two complementary equations to analyse the longitudinal and transverse electrodynamics of the different modes in closed pillbox cavities.

2.4 Pillbox Cavities

Pillbox cavities are the well-studied subset of azimuthally modulated cavities with a constant, circular cross-section of radius r_0. Figure 2.4 shows such a pillbox cavity.

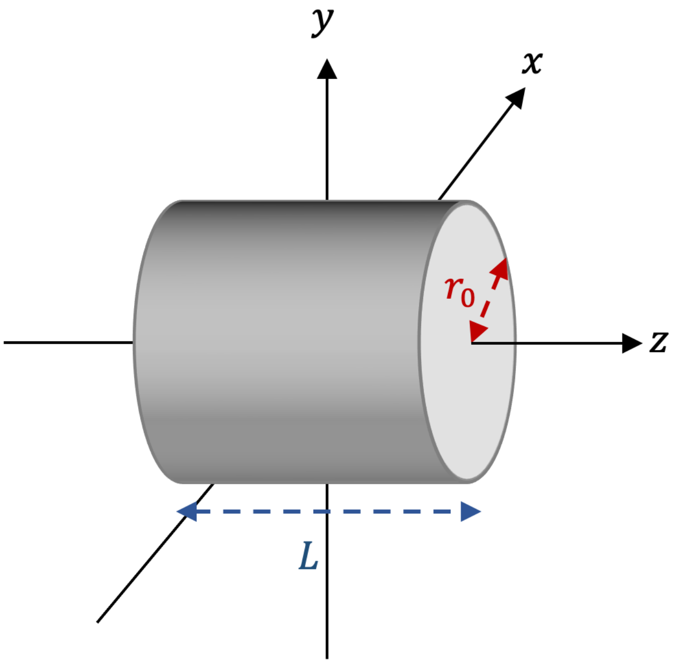

Figure 2.4: A pillbox RF cavity of longitudinal length L and circular cross-section of radius r_0.

2.4.1 TE$_{mnp}$ Modes

The cavity wall boundary condition on the azimuthal component of the electric field for a TE mode in a pillbox cavity, as given by Eqn. 2.50, must be satisfied for all angles θ. The only possible solutions are those of a single multipolar component

$$\tilde{\gamma}_m = \begin{cases} \tilde{\gamma}_M, & m = M; \\ 0, & \text{otherwise.} \end{cases} \tag{2.103}$$

In this case, Eqn. 2.52 becomes

$$\kappa_p r_0 = j'_{M\eta} \qquad \rightarrow \qquad \omega_l = c\sqrt{\left(\frac{j'_{M\eta}}{r_0}\right)^2 + \left(\frac{2p\pi}{L}\right)^2}, \tag{2.104}$$

thus relating the frequency of the mode and the cavity radius to the η^{th} root of the differentiated Bessel function of order M.

The TE modes in a cavity pillbox can therefore be simply denoted as $\text{TE}_{M\eta p}$ or, to match the literature, TE_{mnp}. Using the latter notation, the basis of the TE_{mnp} modes supported by a pillbox cavity is

$$E_r(r,\theta,z) = \sin(k_p z)\frac{k_p}{\kappa_p^2 r}\tilde{\gamma}_m J_m(\kappa_p r)\cos(m\theta - \psi_m) \tag{2.105}$$

$$E_\theta(r,\theta,z) = -\sin(k_p z)\frac{k_p}{\kappa_p}\frac{1}{m}\tilde{\gamma}_m J'_m(\kappa_p r)\sin(m\theta - \psi_m), \tag{2.106}$$

$$E_z(r,\theta,z) = 0. \tag{2.107}$$

$$B_r(r,\theta,z) = \frac{i}{\omega_l}\cos(k_p z)\frac{k_p^2}{\kappa_p}\tilde{\gamma}_m J'_m(\kappa_p r)\sin(m\theta - \psi_m), \tag{2.108}$$

$$B_\theta(r,\theta,z) = -\frac{i}{\omega_l}\cos(k_p z)\frac{k_p^2}{\kappa_p^2 r}\tilde{\gamma}_m J_m(\kappa_p r)\cos(m\theta - \psi_m), \tag{2.109}$$

$$B_z(r,\theta,z) = -\frac{i}{\omega_l}\sin(k_p z)k_p\frac{1}{m}\tilde{\gamma}_m J_m(\kappa_p r)\sin(m\theta - \psi_m), \tag{2.110}$$

which is equivalent to the literature [18, 66].

The absence of any longitudinal electric field means that, under our assumptions made, there is no change in longitudinal momentum as per Eqn. 2.76 nor any change in transverse momentum as per Eqn. 2.93 of a particle beam traversing a TE mode. Although TE modes do find applications in particle accelerators in situations where our assumptions do not apply [67], we solely focus on TM modes in the remainder of this thesis.

2.4.2 TM$_{mnp}$ Modes

The cavity wall boundary condition on the longitudinal component of the electric field for a TM mode in a pillbox cavity requires the modes to have distinct frequencies

$$\kappa_p r_0 = j_{M\eta} \qquad \rightarrow \qquad \omega_l = c\sqrt{\left(\frac{j_{M\eta}}{r_0}\right)^2 + \left(\frac{2p\pi}{L}\right)^2}, \tag{2.111}$$

and that each mode is solely composed of a single multipolar component. Again using the notation TM$_{mnp}$, these modes have the form

$$E_r(r,\theta,z) = -\sin(k_p z)\frac{k_p}{\kappa_p}\tilde{g}_m J_m'(\kappa_p r)\cos(m\theta - \phi_m), \tag{2.112}$$

$$E_\theta(r,\theta,z) = \sin(k_p z)\frac{k_p}{\kappa_p^2 r}m\tilde{g}_m J_m(\kappa_p r)\sin(m\theta - \phi_m), \tag{2.113}$$

$$E_z(r,\theta,z) = \cos(k_p z)\tilde{g}_m J_m(\kappa_p r)\cos(m\theta - \phi_m), \tag{2.114}$$

$$B_r(r,\theta,z) = \frac{i}{\omega_l}\cos(k_p z)\frac{\kappa_p^2 + k_p^2}{\kappa_p^2 r}m\tilde{g}_m J_m(\kappa_p r)\sin(m\theta - \phi_m), \tag{2.115}$$

$$B_\theta(r,\theta,z) = \frac{i}{\omega_l}\cos(k_p z)\frac{\kappa_p^2 + k_p^2}{\kappa_p}\tilde{g}_m J_m'(\kappa_p r)\cos(m\theta - \phi_m), \tag{2.116}$$

$$B_z(r,\theta,z) = 0, \tag{2.117}$$

which similarly matches the literature.

We now analyse the electrodynamics of the fundamental accelerating mode TM$_{010}$, the transverse deflecting modes TM$_{m10}$ and general TM$_{mnp}$ modes with $n \neq 0$ and $p \neq 0$.

TM$_{010}$

The longitudinal electric field of the TM$_{010}$ mode has the form

$$E_z(r) = \tilde{g}_0 J_0(\kappa_0 r), \tag{2.118}$$

where

$$\kappa_0 = k_l = \frac{j_{01}}{r_0}. \tag{2.119}$$

The longitudinal electric field only has radial dependence and it is visualised in Fig. 2.5 which is a contour plot of E_z where the field is normalised to the maximum value E_0.

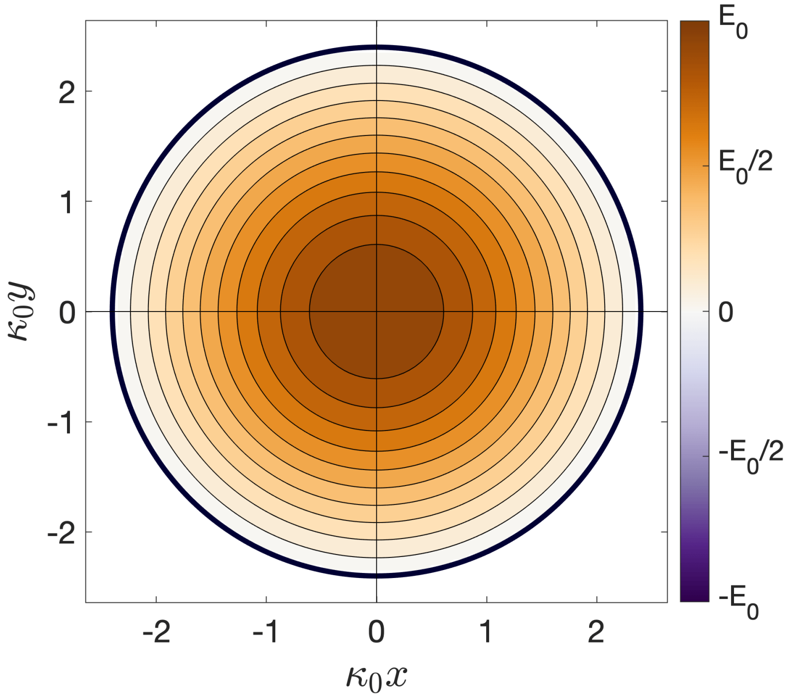

Figure 2.5: Contour plot in wavenumber-scaled Cartesian space showing the longitudinal electric field in the TM$_{010}$ mode supported by a pillbox cavity. The colour denotes the size of the field value relative to the maximum electric field E_0.

The change in longitudinal momentum of a test charge traversing the TM$_{010}$ mode can be calculated by inserting Eqn. 2.118 into Eqn. 2.76 to get

$$\Delta p_z(r, \theta) = \frac{e}{v_z} \cos{(\xi_l)} \tilde{g}_0 J_0(\kappa_0 \delta r) L^0_{\text{eff}}. \tag{2.120}$$

Assuming the test charge enters the cavity at a radial offset δr that is close enough to on-axis that $\kappa_0 \delta r \ll 1$, Eqn. 2.120 becomes

$$\Delta p_z(\delta r, \theta) \simeq \frac{e}{v_z} \cos{(\xi_l)} \tilde{g}_0 L^0_{\text{eff}}, \tag{2.121}$$

where we have used the *small beam approximation*

$$\lim_{x\to 0} J_m(x) = \frac{1}{m!\cdot 2^m} x^m. \tag{2.122}$$

A particle beam that traverses the RF cavity on-axis is therefore accelerated (or decelerated, depending on the phase) by an amount proportional to the monopolar magnitude and the effective cavity length.

The change in transverse momentum of a test charge traversing the TM_{010} mode can be calculated by inserting Eqn. 2.118 into Eqn. 2.96 to get

$$\Delta\vec{p}_\perp(r,\theta) = -\frac{e}{\omega_l}\sin(\xi_l)\tilde{g}_0 \begin{pmatrix} \kappa_0 J_0'(\kappa_0 r) \\ 0 \end{pmatrix} L^0_{\mathrm{eff}}, \tag{2.123}$$

If we again assume the test charge enters close to on-axis, Eqn. 2.123 becomes

$$\Delta\vec{p}_\perp(\delta r,\theta) \simeq \frac{e}{\omega_l}\sin(\xi_l)\tilde{g}_0 \frac{\kappa_0}{2} \begin{pmatrix} \delta r \\ 0 \end{pmatrix} L^0_{\mathrm{eff}}, \tag{2.124}$$

where we have used the small beam approximation

$$\lim_{x\to 0}\frac{dJ_m(x)}{dx} = \begin{cases} -\frac{1}{2}x, & m=0; \\ \frac{1}{(m-1)!\cdot 2^m}x^{m-1}, & m>0. \end{cases} \tag{2.125}$$

A particle beam that traverses the cavity on-axis is therefore focused (or defocused) for all angles by an amount proportional to the monopolar magnitude, the offset and the effective length but inversely proportional to the cavity radius because $\kappa_0 \propto 1/r_0$.

The TM_{010} mode is known as the fundamental accelerating mode because, from Eqn. 2.111, it has the lowest frequency of all the TM modes and accelerates an on-axis particle beam. RF cavities operating in this mode are used close to on-crest for the acceleration of high-β particles.

TM$_{m10}$

The TM$_{m10}$ mode with $m \neq 0$ has a longitudinal electric field of the form

$$E_z(r,\theta) = \tilde{g}_m J_m\left(\kappa_0 r\right)\cos\left(m\theta - \phi_m\right), \tag{2.126}$$

where

$$\kappa_0 = k_l = \frac{j_{m1}}{r_0}. \tag{2.127}$$

The longitudinal electric field of such modes varies with the azimuthal angle θ. This is visible in Fig. 2.6 which shows three contour plots of the longitudinal electric field of the quadrupolar TM$_{210}$ mode for different values of ϕ_m. As ϕ_m simply rotates the field without affecting the physical dimensions of the pillbox, the $m \neq 0$ TM$_{m10}$ modes are degenerate; this is in contrast to the TM$_{010}$ mode which is not.

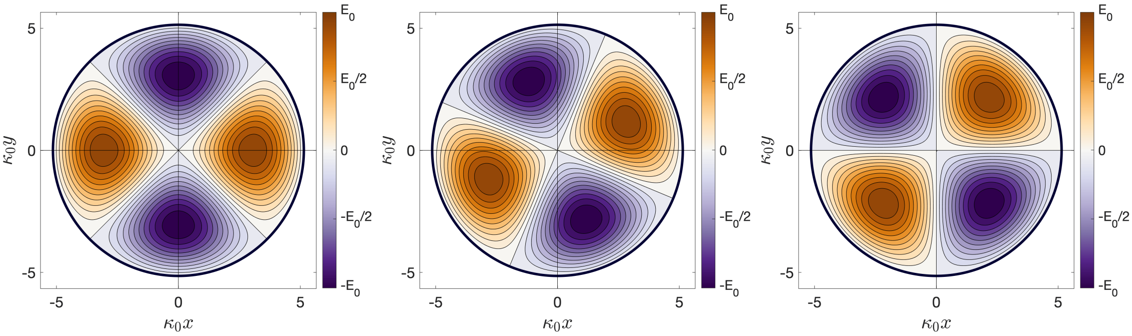

Figure 2.6: Contour plots in wavenumber-scaled Cartesian space showing the longitudinal electric field in the TM$_{210}$ mode for $\phi_2 = 0$ (left), $\phi_2 = \pi/4$ (centre) and $\phi_2 = \pi/2$ (right).

The change in longitudinal momentum of a test charge traversing a TM$_{m10}$ mode can be calculated by inserting Eqn. 2.126 into Eqn. 2.76

$$\Delta p_z(r,\theta) = \frac{e}{v_z}\cos\left(\xi_l\right)\tilde{g}_m J_m(\kappa_0 r)\cos\left(m\theta - \phi_m\right)L^0_{\text{eff}}. \tag{2.128}$$

Assuming the test charge traverses the field at a sufficiently small offset $\kappa_0 \delta r \ll 1$ that the Bessel function can be approximated using Eqn. 2.122, Eqn. 2.128 becomes

$$\Delta p_z(\delta r, \theta) \simeq \frac{q}{v_z} \cos(\xi_l) \tilde{g}_m \frac{\kappa_0^m}{m! \cdot 2^m} \delta r^m \cos(m\theta - \phi_m) L^0_{\text{eff}}. \tag{2.129}$$

A particle beam traversing an $m \neq 0$ TM_{m10} mode on-axis thus experiences an acceleration that varies radial offset as δr^m and the azimuth as $\cos(m\theta - \phi_m)$.

The change in transverse momentum of a test charge traversing a TM_{m10} mode is found by inserting Eqn. 2.126 into Eqn. 2.96 which gives

$$\Delta \vec{p}_\perp(\delta r, \theta) = -\frac{e}{\omega_l} \sin(\xi_l) \tilde{g}_m \begin{pmatrix} \kappa_0 J'_m(\kappa_0 \delta r) \cos(m\theta - \phi_m) \\ -\frac{m}{\delta r} J_m(\kappa_0 \delta r) \sin(m\theta - \phi_m) \end{pmatrix} L^0_{\text{eff}}. \tag{2.130}$$

For small radial offsets $\kappa_0 \delta r \ll 1$ such that the approximation in Eqn. 2.125 can be used, Eqn. 2.130 becomes

$$\Delta \vec{p}_\perp(\delta r, \theta) \simeq -\frac{e}{\omega_l} \sin(\xi_l) \tilde{g}_m \frac{\kappa_0^m}{(m-1)! \cdot 2^m} \delta r^{m-1} \begin{pmatrix} \cos(m\theta - \phi_m) \\ -\sin(m\theta - \phi_m) \end{pmatrix} L^0_{\text{eff}}. \tag{2.131}$$

It is important to note that the form of Eqn. 2.131 has an identical dependence on the radial offset and azimuthal angle to that of an m-pole magnet, as given by Eqn. 1.22. The dynamical effect on a particle beam traversing an $m \neq 0$ TM_{m10} mode on-axis is therefore analogous to the dynamical effect on a particle beam traversing an m-pole magnetic field, provided the assumptions made including that the beam has a sufficiently small transverse size $\Delta r \ll 1/\kappa_0$.

TM$_{mnp}$

The $n \neq 1$ TM$_{mn0}$ modes have the same form of longitudinal electric field as the TM$_{m10}$ modes given in Eqn. 2.126, but the wavenumber is instead

$$\kappa_0 = k_l = \frac{j_{mn}}{r_0}. \tag{2.132}$$

Contour plots of the longitudinal electric field in the $n = 1$, 2 and 3 TM$_{1n0}$ and TM$_{5n0}$ modes are shown in Fig. 2.7. The cavity cross-sections that support the $n = 1$, 2 and 3 modes are graphed in black, blue and cyan respectively. The $n = 1$ modes are typically the optimal choice for acceleration or manipulation as they are the smallest structures.

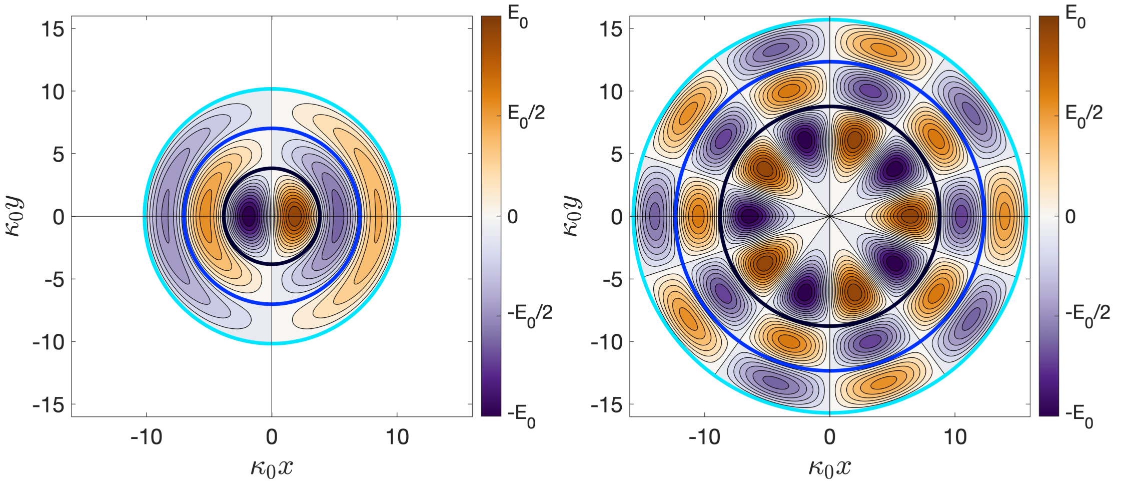

Figure 2.7: Contour plots in wavenumber-scaled Cartesian space of the longitudinal electric field in the TM$_{1n0}$ modes with $\phi_1 = 0$ (left) and TM$_{5n0}$ modes with $\phi_5 = 0$ (right). The $n = 1$, 2 and 3 cross-sections that support these modes are graphed in black, blue and cyan.

The longitudinal electric field of the $p \neq 0$ TM$_{mnp}$ modes is given by Eqn. 2.114 and their resonant frequencies have an explicit dependence on the length of the cavity, as given by Eqn. 2.111. These modes vary in the longitudinal direction and the parameters L^p_{eff} and κ_p capture how this affects the change in longitudinal and transverse momentum of an on-axis particle beam that traverses the mode. For an accelerating

TM_{0np} mode, the change in longitudinal momentum is

$$\Delta p_z(\delta r, \theta) \simeq \frac{e}{v_z} \cos(\xi_l) \tilde{g}_0 L_{\text{eff}}^p, \tag{2.133}$$

which is identical to that of a TM_{0n0} mode except for the generalisation to L_{eff}^p as given by Eqn. 2.81. For a manipulating TM_{mnp} mode, the change in transverse momentum is

$$\Delta \vec{p}_\perp(\delta r, \theta) \simeq -\frac{e}{\omega_l} \sin(\xi_l) \tilde{g}_m \frac{\kappa_p^m}{(m-1)! \cdot 2^m} \delta r^{m-1} \begin{pmatrix} \cos(m\theta - \phi_m) \\ -\sin(m\theta - \phi_m) \end{pmatrix} L_{\text{eff}}^p, \tag{2.134}$$

which is identical to that of an $m \neq 0$ TM_{mn0} mode except for the generalisation to L_{eff}^p and κ_p, where the latter is given by Eqn. 2.111.

2.5 Implementation in Particle Accelerators

We showed in Sec. 2.4 that the modes supported by a closed pillbox cavity are composed of a single multipole m. The $m = 0$ TM_{0np} modes can be used to accelerate a particle beam whereas the $m \neq 0$ TM_{mnp} modes can be used to manipulate a particle beam analogous to an m-pole magnet. In the following Chapter 3, a systematic method is presented for designing closed azimuthally modulated RF cavities that support tailored $\mathrm{TM}_{\{M\}\eta 0}$ modes with a desired multipolar content $\{M\}$.

It should be noted, however, that the actual design of the RF structure for application in a particle accelerator is influenced by the *specification* which includes:

- Purpose of the cavity: for example to accelerate a particle beam, manipulate it, bunch or debunch it, shape it or introduce a synchrotron frequency spread.
- Operation of the cavity: for example normal conducting (NC) or superconducting (SC), standing wave or travelling wave, continuous wave or pulsed mode,

on single bunches or trains of bunches, on a low or large beam current.

- Operating frequency, bandwidth and tuning: for example a fixed or sweeping operating frequency, a narrow or wide bandwidth, the implementation of any tuning mechanisms.
- Beam loading: for example the implementation of any LOM or HOM couplers.
- Limitations and constraints: for example spatial constraints, tolerances in the machining process, peak electromagnetic fields.

Given a specification, the design of an RF structure, including those that are azimuthally modulated, can then be optimised for cost, reliability, operability, maintainability, flexibility, sensitivity to tolerances and, perhaps most importantly, the figures of merit.

2.5.1 Figures of Merit

The figures of merit provide a means with which to evaluate RF structures and we discuss these before looking at common RF structures used in particle accelerators.

Effective Cavity Length and Transit Time Factor

One figure of merit is the actual change in longitudinal and transverse momenta of a beam traversing a harmonic electromagnetic mode. We discussed in Sec. 2.4.2 that the maximum change in momentum occurs when the effective cavity length is maximised. Reproducing Eqn. 2.81 for the effective cavity length here

$$L_{\text{eff}}^{p} = 2\frac{\frac{\omega_l}{v_z}\cos\left(p\pi\right)\sin\left(\frac{\omega_l}{v_z}\frac{L}{2}\right) - \frac{2p\pi}{L}\sin\left(p\pi\right)\cos\left(\frac{\omega_l}{v_z}\frac{L}{2}\right)}{\left(\frac{\omega_l}{v_z}\right)^2 - \left(\frac{2p\pi}{L}\right)^2},$$

we see that it is maximised when

$$\sin\left(\frac{\omega_l}{v_z}\frac{L_\pi}{2}\right) = 1, \qquad \rightarrow \qquad L_\pi = \frac{\beta_z \lambda_l}{2}, \tag{2.135}$$

where L_π denotes the physical cavity length that maximises the effective cavity length and λ_l is the wavelength of the mode. This cavity length ensures that the time taken for the beam to traverse the cavity, $t_\pi = L_\pi / v_z$, equals the time taken for the mode to change phase by π, $t_\pi = \pi/\omega_l$.

Such a cavity length, however, does not maximise the acceleration or manipulation per unit length because the beam spends time traversing the mode when the phase of the mode is off-crest. The acceleration or manipulation efficiency related to this is captured by the transit time factors, as defined in Eqn. 2.78 and Eqn. 2.98. These give the ratio of the voltage experienced by a charged particle traversing the mode as it evolves harmonically with time, to the maximum acceleration or manipulation voltage experienced if the mode remained constant with time. To maximise the acceleration or manipulation efficiency, the length of the RF cavity should be chosen such that the transit time factor is as close to unity as possible.

As an example to illustrate the distribution of the longitudinal and transverse transit time factors, we consider them for the on-axis traversal of a TM_{mn0} mode. In this case, both the longitudinal and transverse transit time factors are

$$T(0,0) = \frac{\lambda_l \beta_z}{\pi}\frac{1}{L}\sin\left(\frac{\pi}{\lambda_l \beta_z}L\right). \tag{2.136}$$

and Fig. 2.8 plots this as a function of $L/\lambda_l\beta_z$. We find $T = 2/\pi$ when the length is L_π and we see that the on-axis transit time factors approach 1 for RF cavities that are short relative to the wavelength and speed of the particle. The maximisation of transit time factors by short RF cavities, however, must be balanced by the fact they have a smaller effective length.

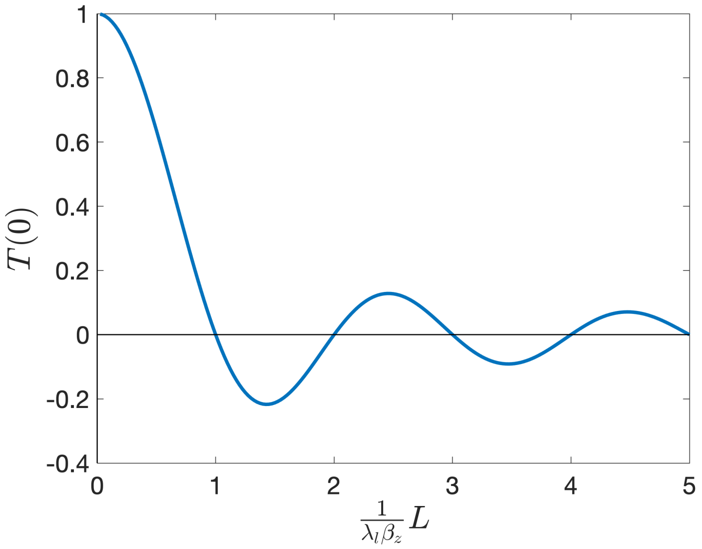

Figure 2.8: Plot of the on-axis transit time factors as a function of $L/\lambda_l\beta_z$.

Peak Electromagnetic Fields

The change in momentum is also proportional to the multipolar magnitudes $\tilde{g}_m$ that are in turn proportional to the peak electric field E_0 and peak magnetic field B_0. The maximum achievable accelerating gradient in NC RF cavities is limited by breakdowns that have been found to scale with the peak surface electric field $E_S^{\max}$ and the modified Poynting vector S_c [22, 68, 69]. The ratios $E_S^{\max}/E_0$ and S_c/E_0 are therefore defined as figures of merit that should be minimised.

The Quality Factor and Geometry Factor

All materials have a surface resistance R_s that cause a resonating RF cavity to dissipate an average power

$$P_s = \frac{1}{2\mu_0^2} \int \int R_s |B|^2 dS, \tag{2.137}$$

on the cavity surface S.

The intrinsic quality factor of a mode Q_0 is defined as the ratio of the stored energy U to the total dissipated average power P during one RF cycle

$$Q_0 = \omega_l \frac{U}{P}. \tag{2.138}$$

As well as dependence upon the cavity geometry, Q_0 has explicit dependence on the surface resistance. This in turn dependent upon many factors external to the geometrical design of the cavity such as the purity of the cavity material, the surface finish of the machined cavity and any heat treatment of the cavity. The geometry factor

$$G = R_s Q_0 = \frac{\omega_l U}{P/R_s}, \tag{2.139}$$

removes this dependence on factors external to the geometry and is a useful figure of merit with which to directly compare cavities of different geometries.

The Shunt Impedance and R/Q_0

The effective shunt impedance is defined as [18]

$$R_z = \frac{(V_z^{\max} T_z(0,0))^2}{2P}, \tag{2.140}$$

and, similarly, the effective transverse shunt impedance as

$$R_\perp = \frac{(V_\perp^{\max} T_\perp(0,0))^2}{2P}. \tag{2.141}$$

Here the word effective indicates the inclusion of the on-axis transit time factors. The shunt impedances measure the effectiveness of accelerating or manipulating a beam for a given power dissipation.

For a given field, the shunt impedances increase linearly with cavity length. To remove this dependence, additional useful quantities are the effective shunt impedances per unit length defined as

$$Z_z = \frac{R_z}{L}, \tag{2.142}$$

and

$$Z_\perp = \frac{R_\perp}{L}. \tag{2.143}$$

Similar to the geometry factor, it is useful to compare cavity geometries independently of any losses. By combining Eqns. 2.140 and 2.141 with 2.138, we can also define

$$\frac{R_z}{Q_0} = \frac{(V_z^{\mathrm{max}} T_z(0,0))^2}{\omega_l U}, \tag{2.144}$$

and

$$\frac{R_\perp}{Q_0} = \frac{(V_\perp^{\mathrm{max}} T_\perp(0,0))^2}{\omega_l U}, \tag{2.145}$$

as figures of merit.

2.5.2 Beam Pipes and Power Couplers

The closed cavities analysed thus far are not suitable for application in particle accelerators. At the very least, there is no way for a particle beam to enter and exit the cavity nor is there any means with which to excite the desired mode. Beam pipes and power couplers must therefore be incorporated into the pillbox cavity design to use it in a particle accelerator.

Beam Pipes

Figure 2.9 shows an implementation of irises and beam pipes of radii r_p into a pillbox cavity.

Incorporating beam pipes means that the end-cap boundary condition is no longer satisfied for $r < r_p$. As such, the condition given by Eqn. 2.34 (which states that the multipolar coefficients $\tilde{e}_m(k)$ and $\tilde{f}_m(k)$ are only non-zero for the specific values

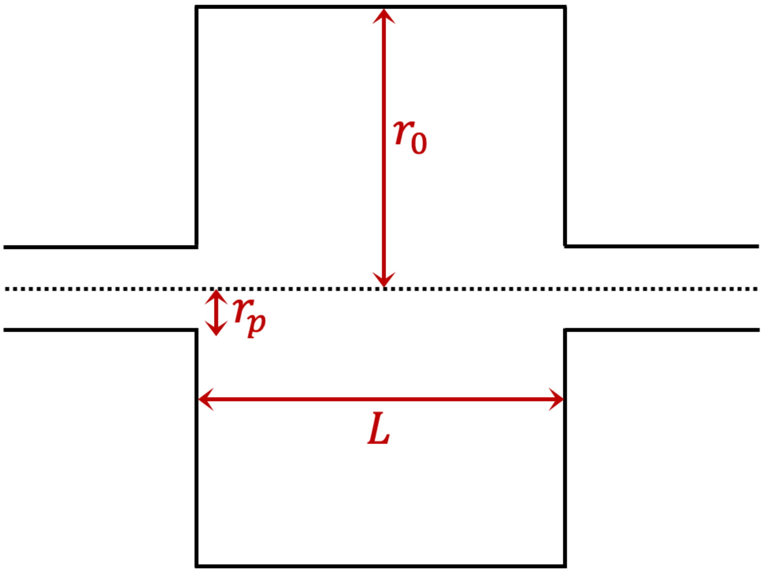

Figure 2.9: Longitudinal cross-section showing beam pipes of radii r_p incorporated into a pillbox RF cavity of radius r_0 and length L.

$k = k_p$) no longer holds and the electromagnetic basis of the mode is therefore more complex. For example, it can be shown using Ref. [64] that the monopolar coefficient describing the electric field of the accelerating mode in the cavity shown in Fig. 2.9 is

$$\tilde{g}_0(k) = \frac{LE_L}{\sqrt{2\pi}J_0(\kappa_l r_p)} \frac{\sin(kL/2)}{kL/2}, \tag{2.146}$$

where the electric field has been assumed constant in the gap as $E_z(r_p, \theta, z) = E_L$. The electric field at any point in the cavity can then be calculated numerically using Eqn. 2.24, but it has no simple analytic expression.

Furthermore, in the case of more realistic cavity designs where, for example, the beam pipe is rounded, the assumption $E_z(r_p, \theta, z) = E_L$ no longer holds and there is no longer any simple analytic expression for the multipolar coefficients. As such, electromagnetic solvers such as CST Studio Suite [70] must be used to calculate the electromagnetic fields in the mode.

Adding a beam pipe to a closed azimuthally modulated cavity thus modifies its electromagnetic modes and this in turn modifies the change in longitudinal and transverse momentum of a particle beam which traverses it. Away from the beam pipe and close to the cavity wall, the electromagnetic mode must approach the basis given by Eqns. 2.66-2.71. Inside the beam pipe, however, it is non-trivial to relate the azimuthal cross-section of the cavity to the multipolar form of E_z, V_z, Δp_z or $\Delta\vec{p}_\perp$ and thus the resultant beam dynamics.

It is noted that the Bessel functions of order m approach x^m as the argument tends to zero (this is the small beam approximation), however, exploring exactly how adding beam pipes to closed azimuthally modulated cavities affects the multipolar forms E_z, V_z, Δp_z and $\Delta\vec{p}_\perp$ is beyond the scope of this thesis.

Power Couplers

Power couplers transfer power into an RF cavity by coupling the electromagnetic field of a power transfer line into the electromagnetic field of the RF cavity. The two main techniques for coupling power are either by incorporating a slot into the cavity design that connects it to a waveguide (typical in NC structures) or by inserting loops and antennas in coaxial couplers into the cavity (typical in SC structures) [71].

Both types of couplers affect the multipolar content of the modes because they alter the azimuthal profile of the RF structure. For example, single-slot couplers give rise to a strong dipole component in the field whereas dual-slot couplers give rise to a strong quadrupole component [72, 73]. Electromagnetic solvers are used to determine their exact effect on the multipolar content of the mode.

The effect of dual-slot couplers on the multipolar composition of a mode is analysed in Chapter 4 and the effect of a single-slot coupler in Chapter 5.

2.5.3 Other Design Considerations

The RF cavity ‘zoo’ of different styles implemented in particle accelerators is vast. Here we touch on a few common modifications and considerations for RF cavity design.

Nose Cones

The LHS of Fig. 2.10 shows the incorporation of a nose cone into an RF structure. The nose cone concentrates the on-axis electric field into a shorter region and allows the transit time factor and shunt impedance to be optimised. This, however, also increases $E_S^{\max}/E_0$ which can limit the maximum accelerating gradient. To reduce this ratio, the sharp edges are rounded off as per the RHS of Fig. 2.10 and such designs are known as re-entrant cavities.

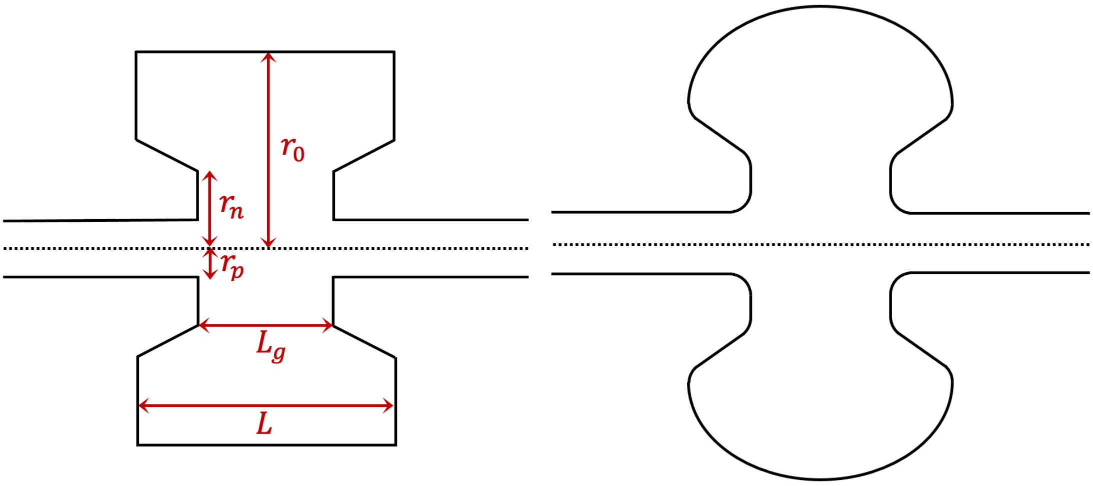

Figure 2.10: Longitudinal cross-sections of a re-entrant cavity before (left) and after (right) the rounding of sharp corners.

LOM and HOM Coupling

Every RF cavity design supports an infinite number of modes. Higher order modes (HOMs) and lower order modes (LOMs) may be excited by a charged particle beam, producing a wakefield that may cause detrimental dynamical effects on subsequent bunches and lead to instabilities and beam loss. Wakefields and their unwanted effects can by mitigated by incorporating LOM and HOM dampers into the cavity design.

SOM Coupling

We showed in Sec. 2.4 that the $m \neq 0$ TM_{mnp} modes are degenerate with same order modes (SOMs). For example, if the azimuthal symmetry is broken by incorporating a power coupler at a horizontal position on the cavity wall, there will be two degenerate $m \neq 0$ TM_{mnp} SOMs (one aligned in the horizontal and the other in the vertical) that have similar frequencies. If unwanted SOMs are excited by the power source or the beam, they may cause detrimental dynamical effects.

The effect of unwanted SOMs can be prevented by sufficiently altering the azimuthal profile of the design such that the unwanted SOM frequencies are far enough away from the wanted SOM frequency that they are not excited or that they can be damped by incorporating a LOM or HOM coupler. Techniques for separating out SOMs in frequency space include incorporating suppressor holes [74, 75], incorporating small longitudinal rods [76] and optimising the power coupler design [77].

Periodic Structures

A series of N RF cavity cells can be coupled together to make a periodic structure, as shown in Fig. 2.11. Using the definition of shunt impedance as given by Eqn. 2.140, the total acceleration voltage for such a periodic structure is

$$V_z^{\max} = N\sqrt{\frac{2P}{N}R_z} = \sqrt{2P(NR_z)}, \tag{2.147}$$

where the power is assumed to be split evenly across the cells. This periodic structure thus has a shunt impedance that is greater by a factor of N relative to a single cavity of the same size, ignoring any transit time factor contributions [78].

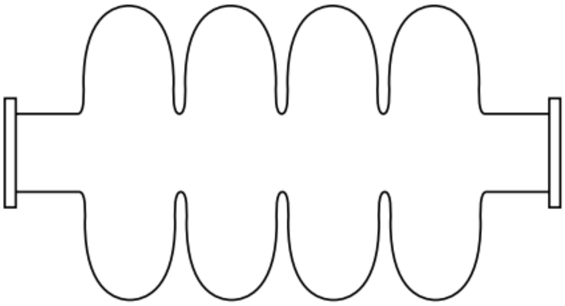

Figure 2.11: Longitudinal cross-section of 4 cavities coupled together. Reproduced from [21].

2.6 Chapter Summary

In this chapter, the basis of harmonic electromagnetic modes in closed azimuthally modulated cavities was derived. The notation $\mathrm{TE}_{\{M\}\eta p}$ and $\mathrm{TM}_{\{M\}\eta p}$ was then introduced to describe their profiles. Subsequently, complementary equations were derived for the changes in the longitudinal and transverse momenta of a high-β charged particle beam that traverses the electromagnetic field of an RF cavity on-axis.

The basis was then used to reproduce the specific form of the TE_{mnp} and TM_{mnp} modes found in pillbox cavities. The electrodynamics of beams traversing such modes was analysed. It was shown that the TM_{0np} modes accelerate on-axis beams whereas the $m \neq 0$ TM_{mnp} modes manipulate on-axis beams in a fashion analogous to m-pole magnets. This motivates the work presented in Chapter 3 where the azimuthal modulation method is outlined for designing azimuthally modulated cavities that support $\mathrm{TM}_{\{M\}\eta 0}$ modes composed of any desired set of multipoles $\{M\}$.

Finally, the figures of merit in RF cavity design were discussed as well as common modifications made to pillbox cavities for their incorporation and application in particle accelerators. Such concepts are particularly relevant in Chapter 4 where the design, fabrication and testing of an azimuthally modulated cavity is presented.

Chapter 3

The Azimuthal Modulation Method

In Chapter 2, we showed that pillbox cavities support TM_{mnp} modes with azimuthal profiles that are described in terms of a single multipolar term of order m. We showed that the $m = 0$ modes accelerate on-axis particle beams whereas the $m \neq 0$ manipulate them similarly to an m-pole magnet. Each TM_{mnp} mode, however, has a distinct frequency and so the multipolar content of a mode, and therefore its application, cannot be tailored beyond monopolar acceleration or m-polar manipulation. In this chapter, we outline and analyse a method for designing azimuthally modulated RF cavities that support bespoke electromagnetic modes composed of any number and magnitude of desired multipoles.

The chapter begins with an analysis of two different methods that can both be used to introduce a desired transverse multipole into an accelerating mode, but with no means to control its magnitude. The first involves designing RF cavities with elliptical cross-sections, analysed in in Sec. 3.1, and the second involves designing RF cavities with nose cones that have a longitudinal modulation, analysed in Sec. 3.2. Such discussions motivate the azimuthal modulation method (AMM) which is outlined in

Sec. 3.3.

The scope and limitation of the AMM for designing realisable cavities is then explored. In Sec. 3.4 and Sec. 3.5, the properties of the azimuthally modulated cavities that support a mode composed of a monopole and single transverse multipole and those that support a mode composed of two transverse multipoles are explored. Different concepts are introduced to describe the properties of modes and the cavities that support them and, in Sec. 3.6, the generalisation of these concepts to modes composed of any number of multipoles is discussed.

3.1 Elliptical Method

Introducing a quadrupole component into accelerating modes by designing circular RF cavities with rectangular irises as well as rectangular RF cavities with circular irises has previously been investigated for application in the high energy collider CLIC [79, 80]. Figure 3.1 shows one such example of a quasi-rectangular cavity with a circular iris. The potential advantages of introducing a quadrupole term into an accelerating field include savings in high-precision permanent magnets and the potential to also use such cavities for both parasitic beam position measurements and Landau damping [81, 82].

The rectangular cross-sections, however, do not provide a means with which to control precisely the magnitude of either the introduced quadrupolar component or other unwanted higher order multipoles. This limits the method, which we illustrate by analysing example cavities with elliptical cross-sections.

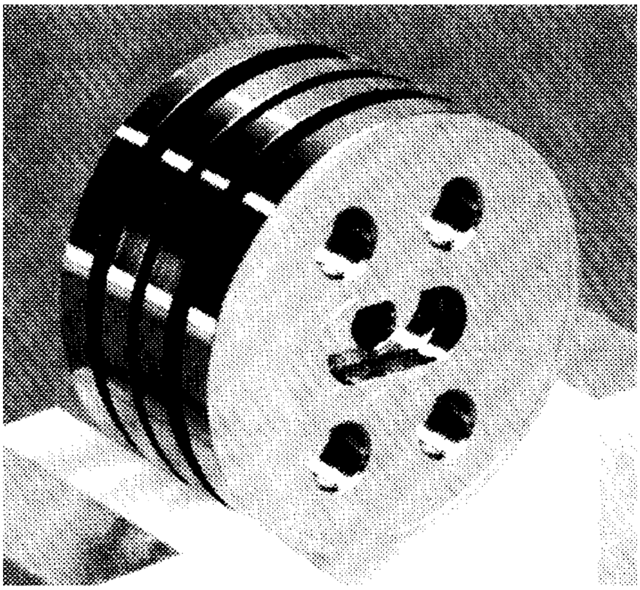

Figure 3.1: A quasi-rectangular cavity with a circular iris. Reproduced from [79].

3.1.1 Cavities with Elliptical Cross-Sections

An elliptical cross-section is defined in polar coordinates as

$$r_0(\theta) = \frac{b}{\sqrt{1-(e\cos(\theta))^2}}, \tag{3.1}$$

where $e = \sqrt{1-b^2/a^2}$ is the eccentricity, and a and b are the semi-major and semi-minor axes.

If a closed RF cavity is created with such a cross-section, it introduces a quadrupole component into the accelerating mode. For example, consider the contour plot on the LHS of Fig. 3.2 which displays the longitudinal electric field in the 3 GHz fundamental accelerating mode of a cavity with an elliptical cross-section where $b = 38.24$ mm and $e = 0.9$. This mode was determined using the electromagnetic solver CST and we note that it does not have any longitudinal variation because it is the fundamental accelerating mode with $p = 0$.

The multipolar content of this mode can be investigated qualitatively by considering its azimuthal variation at a constant radius [83]. For instance, the RHS plot

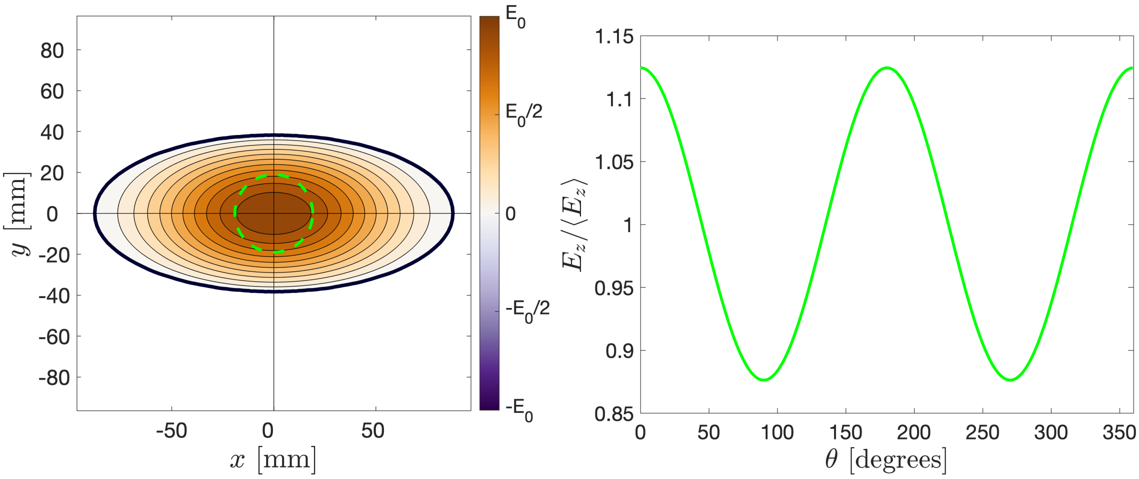

Figure 3.2: Contour plot in Cartesian space of E_z in the 3 GHz fundamental accelerating mode of a closed cavity with an elliptical cross-section of $b = 38.24$ mm and $e = 0.9$ (left). Plot of variation in $E_z/\langle E_z \rangle$, where the angled brackets denote the mean, as a function of azimuthal angle around the dashed green circle (right).

in Fig. 3.2 shows the variation of the longitudinal electric field on the dashed green circle of radius 19 mm as a function of the azimuthal angle. We see the field has a monopolar term because there is a constant offset as well as a quadrupolar term because it has a 2-fold periodic variation.

The multipolar content of the mode can be calculated quantitatively by performing a Helmholtz decomposition of the mode, as outlined in Appendix A. The LHS plot in Fig. 3.3 shows the variation of the first six orders of multipolar magnitudes, $\tilde{g}_m$, in the 3 GHz fundamental accelerating modes as a function of the ellipse eccentricity. We note that due to the orientation of the ellipse, all the multipolar terms are aligned with the horizontal such that $\phi_m = 0$. At $e = 0.9$, the field contains a quadrupolar component $\tilde{g}_2/\tilde{g}_0 = 1.025$ confirming our prior observation, but it also contains higher order, even multipoles including a significant octopolar component of $\tilde{g}_4/\tilde{g}_0 = 0.190$.

Elliptical cross-sections thus introduce a quadrupole component and higher-order, even multipoles into the accelerating mode, and there are not enough degrees of freedom to design the cavity such that it only introduces a quadrupole term. Additionally, the RHS plot in Fig. 3.3 shows that in order to support a 3 GHz accelerating

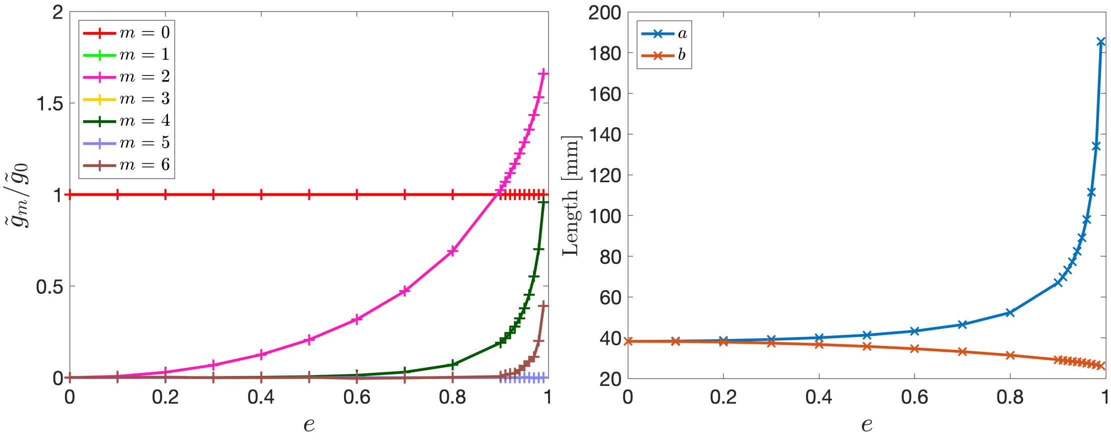

Figure 3.3: Plot of the multipolar composition of the 3 GHz fundamental accelerating modes supported by closed cavities with elliptical cross-sections as a function of the eccentricity e (left). Plot of the corresponding semi-major a and semi-minor b lengths as a function of eccentricity required such that the fundamental accelerating mode resonates at 3 GHz (right).

mode, the semi-major axis of the elliptical cross-section must increase non-linearly with eccentricity whilst the corresponding decrease in the semi-minor axis is far less significant. The structures thus become impractically large along the semi-major axis when pushing for a greater quadrupolar component.

3.1.2 Cavities with Generalised Elliptical Cross-Sections

An $m_1/2$ factor can be introduced into the cosine term in Eqn. 3.1 as

$$r_0(\theta) = \frac{b}{\sqrt{1-(e\cos(m_1\theta/2))^2}}, \tag{3.2}$$

in an attempt to generalise the formula for designing RF cavities that support accelerating modes containing a transverse multipole term of order m_1. Cross-sections created using Eqn. 3.2 are referred to as *generalised elliptical* cross-sections.

Figure 3.4 shows cross-sections given by Eqn. 3.2 for different values of m_1. Helmholtz decompositions of their fundamental accelerating modes showed they contain a monopole and m_1-pole. However, these generalised elliptical designs suffer from the same limitations as the elliptical cross-sections whereby higher order multipoles are also introduced and b increases non-linearly with the magnitude of the multipole of order m_1.

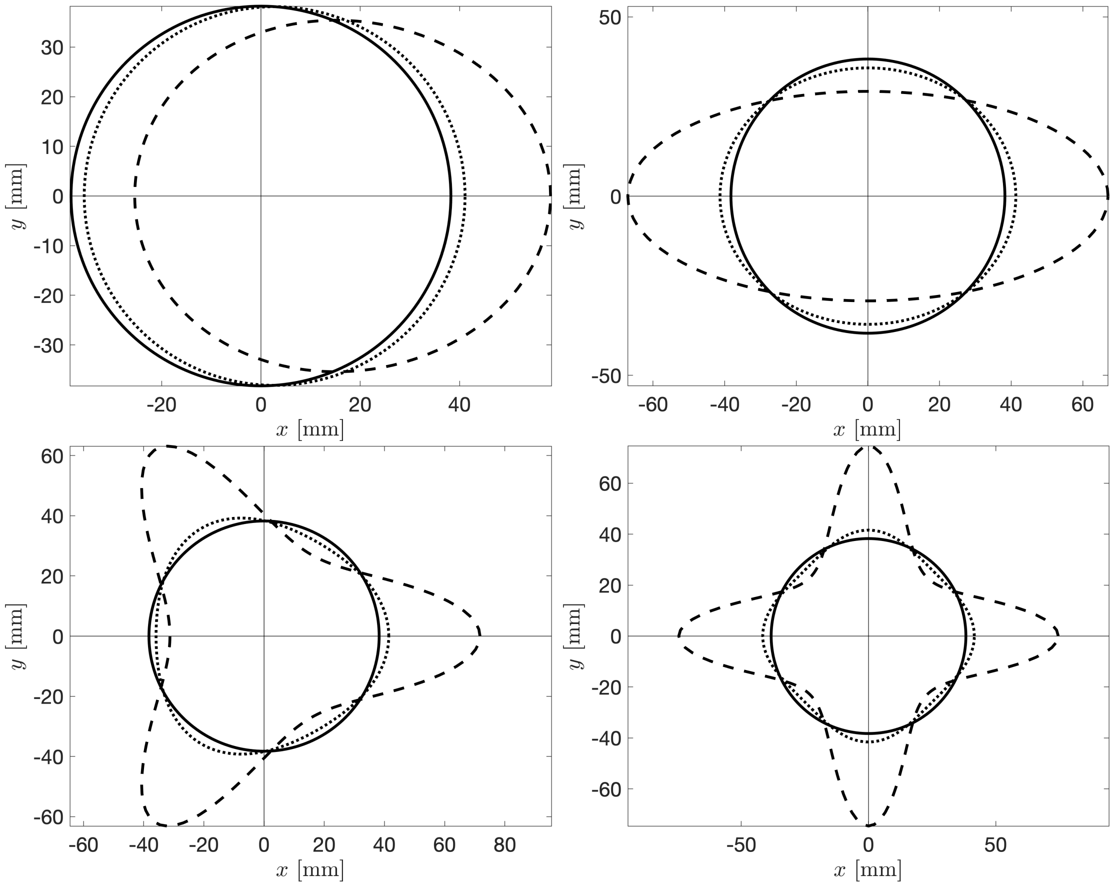

Figure 3.4: Plots in Cartesian space of three cross-sections defined by Eqn. 3.2 for $e = 0$, 0.5, and 0.9 graphed as full, dashed and dotted lines respectively for $m_1 = 1$ (top-left), $m_1 = 2$ (top-right), $m_1 = 3$ (bottom-left) and $m_1 = 4$ (bottom-right). b is set such that the fundamental accelerating mode resonates at 3 GHz.

This generalised elliptical approach thus lacks sufficient degrees of freedom to control the multipolar content of the accelerating mode.

3.2 Longitudinally Modulated Nose Cones

Another method for introducing transverse multipoles into a fundamental accelerating mode is by incorporating a longitudinal modulation into the cavity design such as modulating the nose cone by $z(\theta) = z_0 + z_m(\theta)$, where z_0 is an offset length and $z_m(\theta)$ is a θ-dependent modulating length. An example of such a structure is shown in Fig. 3.5.

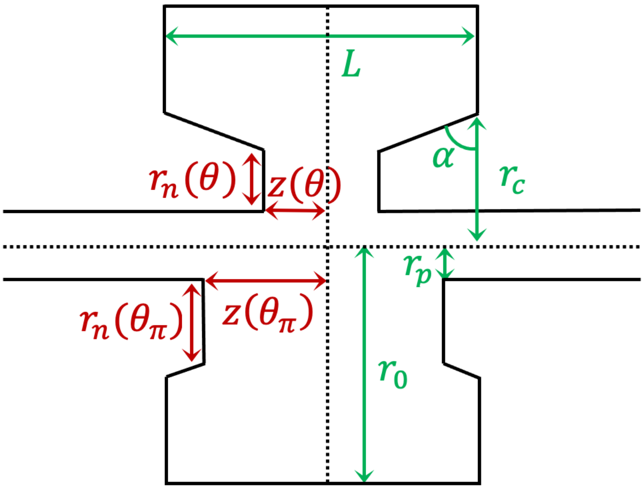

Figure 3.5: Cross-section of a 3D re-entrant cavity with a longitudinally modulated nose cone when cut along a plane orientated at θ. The variables denoted in green are constant for all θ whilst those in red vary. Note that $\theta_\pi = \theta + \pi$.

There is not an analytic equation to model the effect of incorporating a nose cone on the fundamental accelerating mode. As a result, the optimal modulation for introducing the desired multipolar magnitudes and orders into an accelerating mode is not simple to determine.

A sensible choice to try, however, is a modulation of the form $z(\theta) = z_0 + z_m \cos(m\theta)$. RF cavities with these profiles were created and simulated in CST. For example, Fig. 3.6 shows a 3D structure defined by $m = 3$, $L = 10$ mm, $r_0 = 10$ mm, $r_c = 7$ mm, $r_p = 1$ mm, $\alpha = 33.7^{\text{o}}$, $z_0 = 2.5$mm and $z_m = 0.5$ mm. A Helmholtz decomposition of its fundamental accelerating mode gave $\tilde{g}_3/\tilde{g}_0 \sim 20$ but significant higher order multipoles are present too.

This longitudinal modulation method thus suffers from the same problems of the elliptical approach whereby there are insufficient degrees of freedom to control the multipolar content of the accelerating mode.

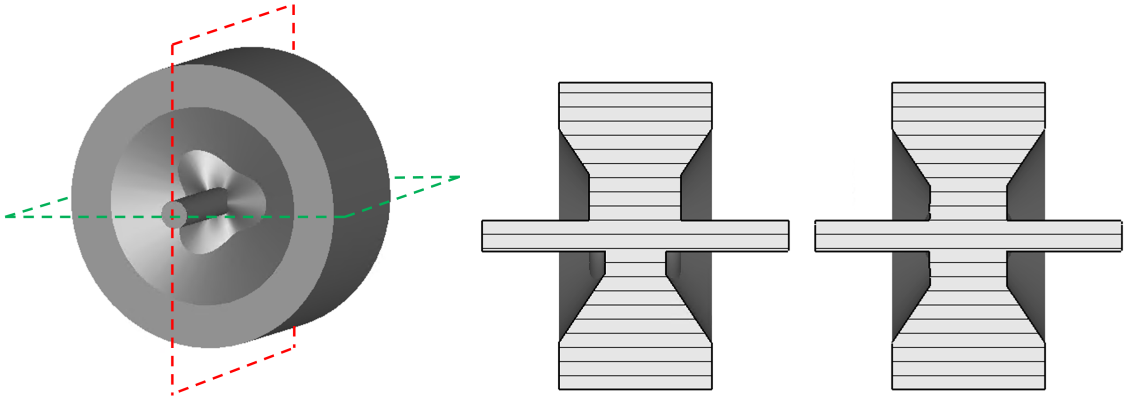

Figure 3.6: Isometric projection of a re-entrant cavity with a longitudinally modulated nose cone incorporated (left). Horizontal and vertical cutting planes are superimposed in green and red respectively and the cavity viewed when cut along the horizontal (centre) and vertical (right) cutting planes are also shown.

3.3 Outline of the Azimuthal Modulation Method

The *azimuthal modulation method* (*AMM*) is a method for tailoring the multipolar content of modes supported by RF cavities. For simplicity, we choose to only present and analyse the method for calculating the azimuthally modulated cavities that support $\mathrm{TM}_{\{M\}\eta 0}$ modes with $p = 0$.[1] The form of these modes, as determined using the basis given by Eqns. 2.66-2.71, is

$$E_r = E_\theta = B_z = 0, \tag{3.3}$$

$$E_z(r,\theta) = \sum_{\{M\}} \tilde{g}_M J_M(kr) \cos\left(M\theta - \phi_M\right), \tag{3.4}$$

$$B_r(r,\theta) = \frac{i}{c} \sum_{\{M\}} \frac{M}{kr} \tilde{g}_M J_M(kr) \sin\left(M\theta - \phi_M\right), \tag{3.5}$$

$$B_\theta(r,\theta) = \frac{i}{c} \sum_{\{M\}} \tilde{g}_M J'_M(kr) \cos\left(M\theta - \phi_M\right), \tag{3.6}$$

---

[1] The method works identically for azimuthally modulated cavities that support $\mathrm{TM}_{\{M\}\eta p}$ modes except that the frequency of the mode also varies with the cavity length.

where we have simplified the notation using

$$\kappa_0 = k_l = \frac{\omega_l}{c} = k. \tag{3.7}$$

The azimuthally modulated cavity cross-sections $r_0^{(\eta)}(\theta)$ that support the $\mathrm{TM}_{\{M\}\eta 0}$ modes that resonate at ω_l and are composed of the set of multipoles $\{M\}$ of multipolar magnitudes $\tilde{g}_M$ and orientations ϕ_M are calculated by determining the *solutions* to the cavity wall boundary condition in Eqn. 3.4. That is

$$0 = \sum_{\{M\}} \tilde{g}_M J_M \left(k r_0^{(\eta)}(\theta) \right) \cos\left(M\theta - \phi_M \right), \tag{3.8}$$

where we include the superscript (η) to denote the order of the solutions. When the cardinality of $\{M\}$ is greater than 1, Eqn. 3.8 cannot be solved analytically for the azimuthally modulated cross-sections $r_0^{(\eta)}(\theta)$. It must instead be computed numerically.

The general properties of $\mathrm{TM}_{\{M\}\eta 0}$ modes and the azimuthally modulated cross-sections that support them can be illuminated by mathematical and graphical analyses of different examples. We therefore apply the azimuthal modulation method to analyse in Secs. 3.4-3.6 respectively: the $\mathrm{TM}_{\{0,m_1\}\eta 0}$ modes solely composed of a monopole and single transverse multipole, the $\mathrm{TM}_{\{m_1,m_2\}\eta 0}$ modes solely composed of two different transverse multipoles and $\mathrm{TM}_{\{M\}\eta 0}$ modes composed of three or more multipoles.

3.4 Monopole and Single Transverse Multipole

From Eqn. 3.4, the $\mathrm{TM}_{\{0,m_1\}\eta 0}$ modes composed of a monopole and a single transverse multipole have a longitudinal electric field of the form

$$E_z(r,\theta) = \tilde{g}_0 J_0(kr) + \tilde{g}_{m_1} J_{m_1}(kr)\cos(m_1\theta - \phi_{m_1}), \tag{3.9}$$

and are supported by the azimuthally modulated cross-sections that solve the cavity wall boundary condition

$$0 = \tilde{g}_0 J_0\left(kr_0^{(\eta)}(\theta)\right) + \tilde{g}_{m_1} J_{m_1}\left(kr_0^{(\eta)}(\theta)\right)\cos(m_1\theta - \phi_{m_1}). \tag{3.10}$$

Properties of these $\mathrm{TM}_{\{0,m_1\}\eta 0}$ modes and their cross-sections can be determined by a general mathematical analysis of Eqns. 3.9-3.10. First, the effect of changing the value of ϕ_{m_1} from $\phi_{m_1}^{(1)}$ to $\phi_{m_1}^{(2)}$ simply rotates both the modes and the corresponding cross-sections by $(\phi_{m_1}^{(2)} - \phi_{m_1}^{(1)})/m_1$. Furthermore, the periodicity of the $\cos(m_1\theta - \phi_{m_1})$ function means that both the modes and cross-sections have m_1-fold rotational symmetry. Additionally, we note that the azimuthally modulated cross-section at $\theta_{2q} = (2q\pi + \phi_{m_1})/m_1$ and $\theta_{2q+1} = ((2q+1)\pi + \phi_{m_1})/m_1$ are turning points of opposite forms, where $q \in \mathbb{Z}$. That is if θ_{2q} is a maximum then θ_{2q+1} is a minimum, or vice versa.

Also, the cosine term in Eqn. 3.10 vanishes at the angles $\theta_q = ((2q+1)\pi + 2\phi_{m_1})/(2m_1)$ such that

$$\tilde{g}_0 J_0\left(kr_0^{(\eta)}(\theta_q)\right) = 0. \tag{3.11}$$

Equation 3.11 is solved by

$$kr_0^{(\eta)}(\theta_q) = j_{0Q}, \tag{3.12}$$

where $Q \in \mathbb{Z}$.[2] Note that q and Q are both used as indices throughout this chapter

---

[2] The reason why $Q \neq \eta$ is discussed in Sec. 3.4.2.

with q used to denote angles and Q used to denote Bessel roots and intervals.

Equation 3.12 relates the frequency of the mode to the radial distance of the cavity wall at the angles θ_q and to the roots of the 0^{th} order Bessel function of the first kind j_{0Q}. It also states that η for the $\text{TM}_{\{0,m_1\}\eta 0}$ modes is the number of poles in E_z specifically along the θ_q radial lines. This can be contrasted with the generality of the interpretation of n in a TM_{mnp} mode as the number of poles along any non-nodal, radial line.

Another property of the $\text{TM}_{\{0,m_1\}\eta 0}$ modes are they are non-degenerate and do not have any SOMs. This is much like the non-degenerate TM_{0np} modes supported by pillbox cavities and is in contrast to the degenerate $m_1 \neq 0$ $\text{TM}_{m_1 np}$ modes discussed in Sec. 2.4.

Furthermore, if the ratio of the transverse multipole to the monopole is zero, $\tilde{g}_{m_1}/\tilde{g}_0 = 0$, the form of the mode is equivalent to that of a TM_{0n0} mode. Such modes are supported by pillbox cavities with circular cross-sections in Sec. 2.4. We therefore expect the azimuthally modulated cross-sections that support $\text{TM}_{\{0,m_1\}\eta 0}$ modes with a small ratio of the transverse multipole to the monopole, $\tilde{g}_{m_1}/\tilde{g}_0 \ll 1$, to be perturbed only slightly from circular. Taking the other extreme whereby the transverse multipole to monopole ratio tends to infinity, $\tilde{g}_{m_1}/\tilde{g}_0 \to \infty$, the azimuthually modulated cross-sections do not tend back to circular. Instead, the cross-sections tend toward unique and non-circular shapes and an example is presented and discussed in 3.4.1. The underlying reason is that the $m_1 \neq 0$ $\text{TM}_{m_1 n0}$ modes are degenerate in a circular pillbox whereas the $\text{TM}_{\{0,m_1\}\eta 0}$ modes are non-degenerate and for all ratios of $\tilde{g}_{m_1}/\tilde{g}_0$.

A final property drawn from mathematical analysis is that the $\text{TM}_{\{0,m_1\}10}$ modes are the fundamental TM modes. This statement is a consequence of the validity of Courant's nodal domain theorem [84] which applies to systems described by a Laplacian operator in a bounded domain in D-dimensional real space that obey the Dirichlet boundary condition that the solutions are zero on the boundary. Courant's nodal domain theorem states that, given the eigenvalues are ordered in a non-decreasing sequence with repetitions according to multiplicities, the eigenfunction that corresponds to the N^{th} eigenvalue will have at most N nodal domains [85]. From this, it follows that the fundamental mode (the 1^{st} eigenvalue) will have at most 1 nodal domain. The fundamental mode therefore is the $\text{TM}_{\{0,m_1\}10}$ mode because it is only zero on the boundary and thus has only a single nodal domain.

Further insight into the properties of the $\text{TM}_{\{0,m_1\}\eta 0}$ modes and the corresponding azimuthally modulated cavities that support them is obtained through graphical analysis. We introduce these techniques by analysing the simple case of the $\text{TM}_{\{0,1\}\eta 0}$ modes and corresponding cross-sections that support them.

3.4.1 $\text{TM}_{\{0,1\}\eta 0}$ Modes

The $\text{TM}_{\{0,1\}\eta 0}$ modes composed of a monopole and a dipole are supported by the azimuthally modulated cross-sections that satisfy the boundary condition

$$0 = \tilde{g}_0 J_0\left(kr_0^{(\eta)}(\theta)\right) + \tilde{g}_1 J_1\left(kr_0^{(\eta)}(\theta)\right)\cos(\theta - \phi_1). \tag{3.13}$$

The LHS contour plots of Figs. 3.7-3.9 show the variation in the longitudinal electric field of the $\eta = 1$, 2 and 3 $\text{TM}_{\{0,1\}\eta 0}$ modes for $\tilde{g}_1/\tilde{g}_0 = 0.1$, 1 and 50 with $\phi_1 = 0$. The azimuthally modulated cross-sections that support the $\eta = 1$, 2 and 3 modes are graphed in black, blue and cyan. We see that each mode and cross-section has 1-fold rotational symmetry, that η is the number of poles along the $\pi/2$ and $3\pi/2$ radial lines and that the cross-sections are slightly perturbed from circular when $\tilde{g}_1/\tilde{g}_0 \ll 1$ whereas they tend to unique, non-circular shapes as $\tilde{g}_1/\tilde{g}_0 \gg 1$.

The RHS plots of Figs. 3.7-3.9 can assist with understanding the properties of the

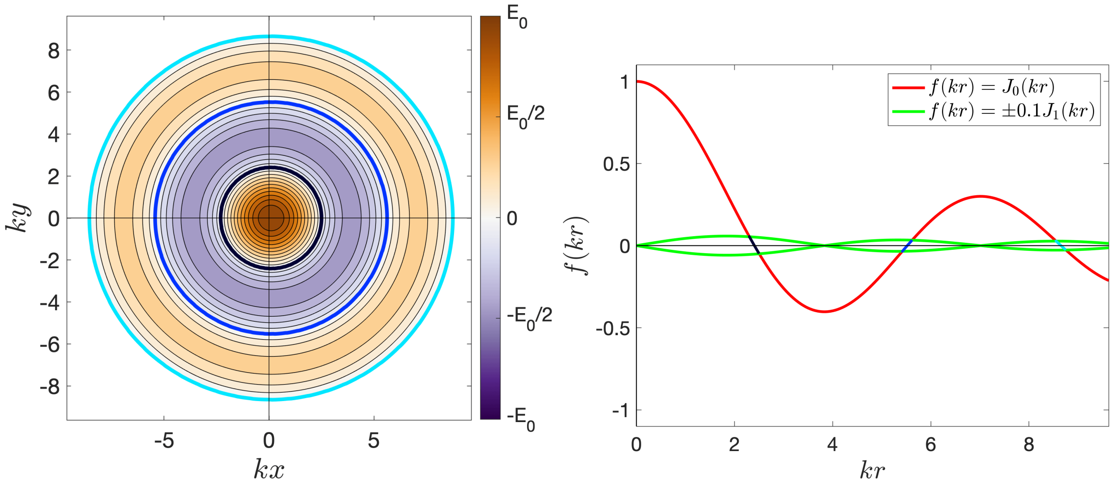

Figure 3.7: Contour plot in wavenumber-scaled Cartesian space of E_z in the TM$_{\{0,1\}\eta 0}$ modes with $\tilde{g}_0 = 1$, $\tilde{g}_1 = 0.1$ and $\phi_1 = 0$ (left). The functions $J_0(kr)$ and $-0.1J_1(kr)\cos(\theta)$ are plotted against kr for $\theta = 0, \pi$ (right). The $\eta = 1$, 2 and 3 solutions are graphed for all θ in black, blue and cyan.

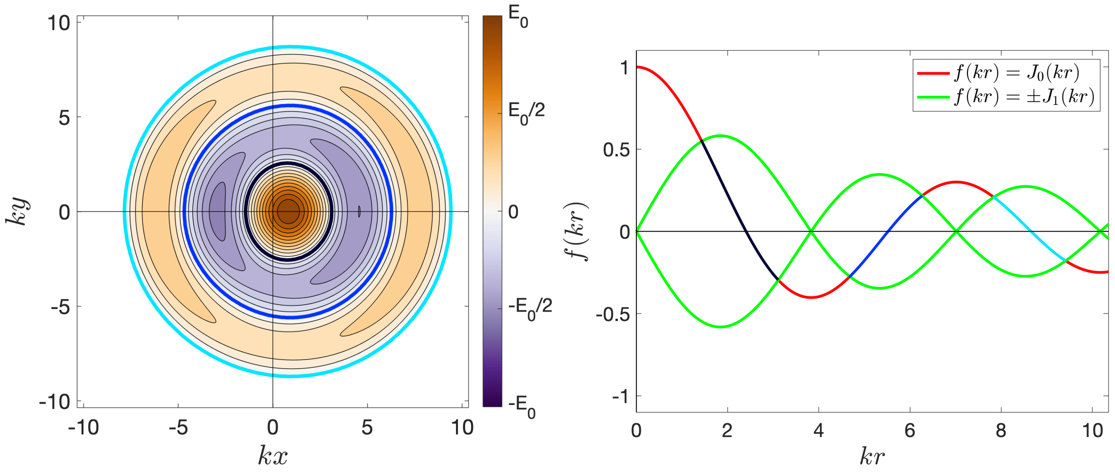

Figure 3.8: Contour plot in wavenumber-scaled Cartesian space of E_z in the TM$_{\{0,1\}\eta 0}$ modes with $\tilde{g}_0 = 1$, $\tilde{g}_1 = 1$ and $\phi_1 = 0$ (left). The functions $J_0(kr)$ and $-J_1(kr)\cos(\theta)$ are plotted against kr for $\theta = 0, \pi$ (right). The $\eta = 1$, 2 and 3 solutions are graphed for all θ in black, blue and cyan.

different modes and cross-sections. If we rearrange Eqn. 3.13 to

$$\tilde{g}_0 J_0\left(kr_0^{(\eta)}(\theta)\right) = -\tilde{g}_1 J_1\left(kr_0^{(\eta)}(\theta)\right)\cos(\theta - \phi_1), \tag{3.14}$$

it is evident that the $r_0^{(\eta)}(\theta)$ solutions at a given θ occur when the monopolar term, $\tilde{g}_0 J_0\left(kr_0^{(\eta)}(\theta)\right)$, equals the negative of the dipolar term, $-\tilde{g}_{m_1} J_1\left(kr_0^{(\eta)}(\theta)\right)\cos(\theta - \phi_1)$.

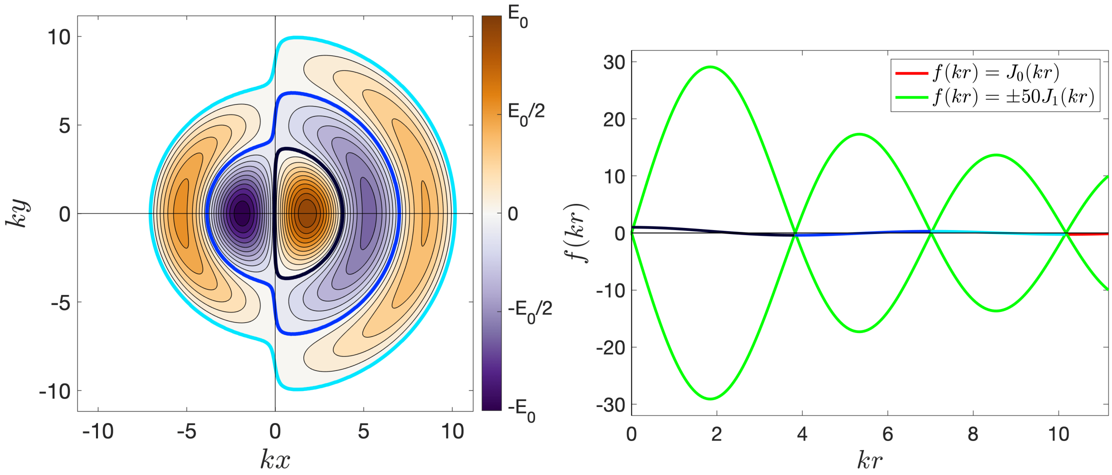

Figure 3.9: Contour plot in wavenumber-scaled Cartesian space of E_z in the TM$_{\{0,1\}\eta 0}$ modes with $\tilde{g}_0 = 1$, $\tilde{g}_1 = 50$ and $\phi_1 = 0$ (left). The functions $J_0(kr)$ and $-50J_1(kr)\cos(\theta)$ are plotted against kr for $\theta = 0, \pi$ (right). The $\eta = 1$, 2 and 3 solutions are graphed for all θ in black, blue and cyan.

Equation 3.14 can therefore be solved graphically for a given θ by plotting the monopolar function $\tilde{g}_0 J_0(kr)$ and dipolar function $-\tilde{g}_1 J_1(kr)\cos(\theta - \phi_1)$ against kr and finding their points of intersection.

We could keep plotting the dipolar function at different θ to calculate the intersections for all θ but this would create a messy plot. Therefore we only plot the dipolar functions $\pm\tilde{g}_1 J_1(kr)$ that correspond to the θ values where $\cos(\theta - \phi_1) = \mp 1$ because the solutions for all other θ values lie between the intersections of $\pm\tilde{g}_1 J_1(kr)$ and $g_0 J_0(kr)$. To explain why, note that the monopolar function does not vary with θ whereas the dipolar function has dependence on a cosine that simply acts as an θ-dependent amplifying term (that is the dipolar function $-\tilde{g}_1 J_1(kr)\cos(\theta - \phi_1)$ simply varies between $\pm\tilde{g}_1 J_1(kr)$ as θ varies between 0 and 2π). The minimum and maximum values of the solutions are therefore found at the angles corresponding to the maximum and minimum values of the cosine term, $\cos(\theta - \phi_1) = \pm 1$, while the remainder of the solution lies within between two extremes.

The RHS plot of Fig. 3.7 shows that the solutions are bound about the region $kr_0^{(\eta)}(\theta) \simeq j_{0\eta} \pm 0.2$ for all θ when $\tilde{g}_1/\tilde{g}_0 = 0.1$. In contrast, the RHS plot of Fig. 3.9

shows that when $\tilde{g}_1/\tilde{g}_0 = 50$, the solution rapidly fluctuates through $kr_0^{(\eta)}(\theta) = j_{0\eta}$ at $\cos(\theta) = 0$ to either $kr_0^{(\eta)}(\theta) \simeq j_{1(\eta-1)}$ if $\cos(\theta) < 0$ or $kr_0^{(\eta)}(\theta) \simeq j_{1\eta}$ if $\cos(\theta) > 0$.

In the case that $\tilde{g}_1/\tilde{g}_0 = \infty$ and $\phi_1 = 0$, the fluctuation is instantaneous and the azimuthally modulated cross-sections become

$$r_0^{(\eta)}(\theta) = \begin{cases} j_{1\eta}, & \cos(\theta) \geq 0, \\ j_{1(\eta-1)}, & \cos(\theta) < 0. \end{cases} \tag{3.15}$$

The LHS plot of Fig. 3.10 shows these azimuthally modulated cross-sections and the $\mathrm{TM}_{1\eta0}$ modes they support. We contrast this with TM_{1n0} modes supported by the circular cross-sections shown on the RHS plot of Fig. 3.10. Both structures impart the same dipolar kick on a particle beam that traverses it on-axis. The practical difference between the two, however, is that the TM_{1n0} modes are degenerate whereas the $\mathrm{TM}_{1\eta0}$ modes are not. It should be noted that the cavity wall of the structure supporting the $\mathrm{TM}_{1\eta0}$ mode passes through the origin and this is an example of a forbidden solution, which are discussed in depth in Sec. 3.5.1.

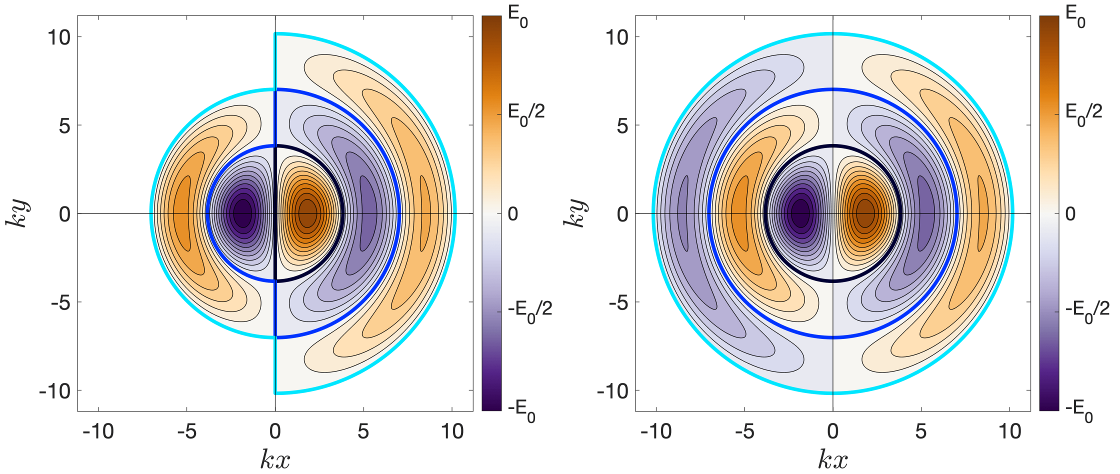

Figure 3.10: Contour plots in wavenumber-scaled Cartesian space of E_z in the $\mathrm{TM}_{1\eta0}$ modes (left) and TM_{1n0} modes (right). The η and $n = 1$, 2 and 3 solutions are graphed for all θ in black, blue and cyan.

Finally, Fig. 3.11 shows the $\mathrm{TM}_{\{0,1\}\eta0}$ modes with $\tilde{g}_1/\tilde{g}_0 = 10$ and $\phi_1 = \pi/2$. We see that a non-zero ϕ_1 simply rotates the mode and the corresponding cross-sections.

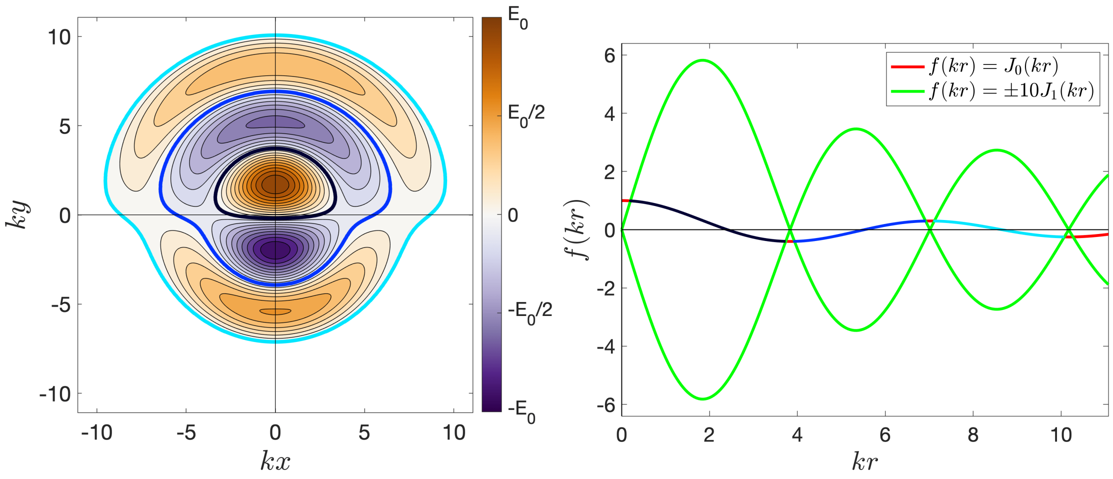

Figure 3.11: Contour plot in wavenumber-scaled Cartesian space of E_z in the $\text{TM}_{\{0,1\}\eta 0}$ modes with $\tilde{g}_0 = 1$, $\tilde{g}_1 = 10$ and $\phi_1 = \pi/2$ (left). The functions $J_0(kr)$ and $-10J_1(kr)\cos(\theta)$ are plotted against kr for $\theta = 0, \pi$ (right). The $\eta = 1$, 2 and 3 solutions are graphed for all θ in in black, blue and cyan.

3.4.2 Conditional Modes and Discontinuous Solutions

A single root of the 1st order Bessel function always fall between the roots of the 0th order Bessel function, that is $j_{1(\eta-1)} < j_{0\eta} < j_{1\eta}$. Consequently, the cross-sections that support the $\text{TM}_{\{0,1\}\eta 0}$ modes are always bound within the interval $kr^{(\eta)}(\theta) = [j_{1(\eta-1)}, j_{1\eta}]$ regardless of the multipolar ratio $\tilde{g}_1/\tilde{g}_0$.

We introduce the term *conditional* to describe the $\text{TM}_{\{0,m_1\}\eta 0}$ modes that have more than one root to the 0th order Bessel function in the $kr = [j_{m_1(Q-1)}, j_{m_1 Q}]$. This has consequences for the corresponding azimuthally modulated cross-sections because they become *discontinuous* when the multipolar ratio $\tilde{g}_{m_1}/\tilde{g}_0$ exceeds a *critical value*. Such discontinuous cross-sections do not exist for all θ and thus cannot be used to support their corresponding $\text{TM}_{\{0,m_1\}\eta 0}$ mode. See, for example, Fig. 3.13 which is discussed in detail in Sec. 3.4.3.

We likewise introduce the term *unconditional* to describe the $\text{TM}_{\{0,m_1\}\eta 0}$ modes that are supported by continuous azimuthally modulated cross-sections for all multipolar ratios $\tilde{g}_{m_1}/\tilde{g}_0$.

The definition of conditionality can also be generalised to any TM$_{\{M\}\eta 0}$ mode of given multipolar content $\{M\}$: such a mode is conditional if any corresponding $r_0^{(\eta)}(\theta)$ solution is discontinuous for any possible combination of magnitudes of the multipolar coefficients. On the other hand, a TM$_{\{M\}\eta 0}$ mode is unconditional if it has a continuous cross-sections for all possible ratios of the multipolar coefficients.

We demonstrate the concepts of conditional modes and discontinuous solutions by analysing the azimuthally modulated cross-sections that support TM$_{\{0,3\}\eta 0}$ modes.

3.4.3 TM$_{\{0,3\}\eta 0}$ Modes

The TM$_{\{0,3\}\eta 0}$ modes composed of a monopole and a sextupole are supported by the azimuthally modulated cross-sections that satisfy the boundary condition

$$0 = \tilde{g}_0 J_0\left(kr_0^{(\eta)}(\theta)\right) + \tilde{g}_3 J_3\left(kr_0^{(\eta)}(\theta)\right)\cos{(3\theta - \phi_3)}. \tag{3.16}$$

Both the TM$_{\{0,3\}10}$ and TM$_{\{0,3\}20}$ modes are conditional because the interval $kr = [0, j_{31}]$ contains the two roots of the 0th order Bessel function j_{01} and j_{02}, as shown in the RHS plots of Figs. 3.12-3.14. In contrast, the $\eta \geq 3$ TM$_{\{0,3\}\eta 0}$ modes are unconditional because all intervals $kr = [j_{3(Q-1)}, j_{3Q}]$ $(Q \geq 2)$ contain the single root of the 0th order Bessel function $j_{0(Q+1)}$.

This is shown by the LHS contour plots of Figs. 3.12-3.14 which visualise the longitudinal electric field of the $\eta = 1$, 2 and 3 TM$_{\{0,3\}\eta 0}$ modes for $\tilde{g}_3/\tilde{g}_0 = 0.95$, 1.5 and 10 with $\phi_3 = 0$. We see that the $\eta = 1$ and 2 solutions become discontinuous and converge on each other when the multipolar ratio increases from 0.95 to 1.5. In contrast the $\eta = 3$ solution remains continuous for all multipolar ratios.

The reason that the $\eta = 1$ and 2 solutions become discontinuous is because the function $-\tilde{g}_3 J_3(kr)\cos{(3\theta)}$ does not intersect the function $\tilde{g}_0 J_0(kr)$ in the interval

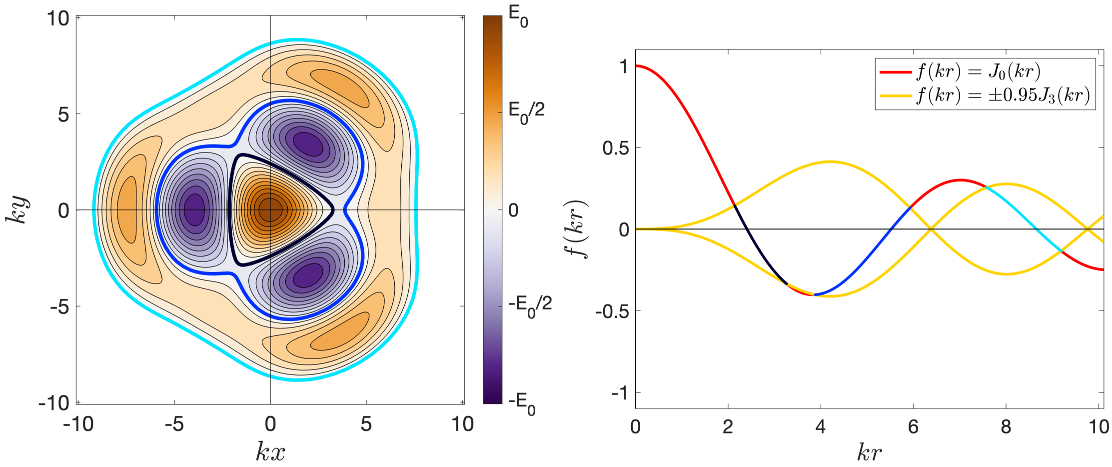

Figure 3.12: Contour plot in wavenumber-scaled Cartesian space of E_z in the $\mathrm{TM}_{\{0,3\}\eta 0}$ modes with $\tilde{g}_0 = 1$, $\tilde{g}_3 = 0.95$ and $\phi_3 = 0$ (left). The functions $J_0(kr)$ and $-0.95 J_3(kr)\cos(3\theta)$ are plotted against kr for $\theta = 0, \pi/3$ (right). The $\eta = 1$, 2 and 3 solutions are graphed for all θ in black, blue and cyan.

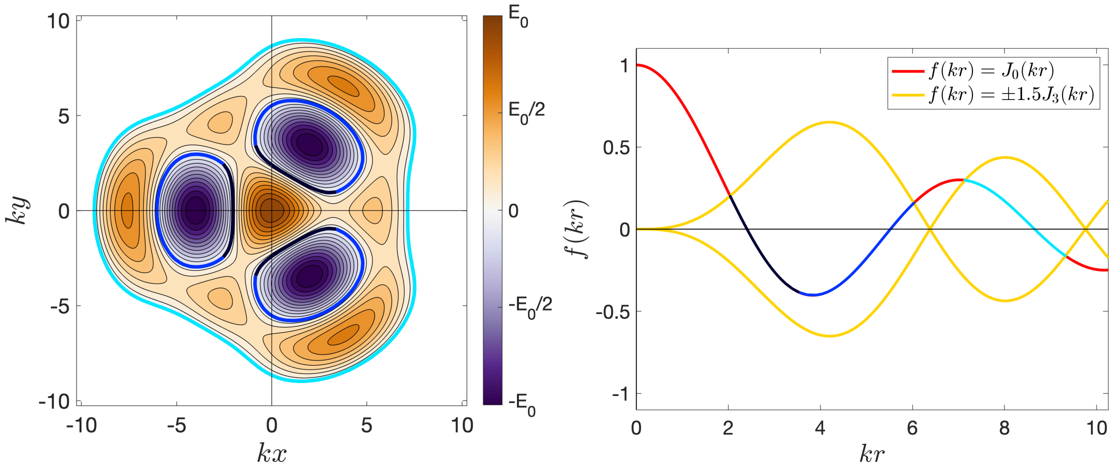

Figure 3.13: Contour plot in wavenumber-scaled Cartesian space of E_z in the $\mathrm{TM}_{\{0,3\}\eta 0}$ modes with $\tilde{g}_0 = 1$, $\tilde{g}_3 = 1.5$ and $\phi_3 = 0$ (left). The functions $J_0(kr)$ and $-1.5 J_3(kr)\cos(3\theta)$ are plotted against kr for $\theta = 0, \pi/3$ (right). The $\eta = 1$, 2 and 3 solutions are graphed for all θ in black, blue and cyan.

$kr = [0, j_{31}]$ when $\tilde{g}_3/\tilde{g}_0 \cos(3\theta) > 0.98$. This loss of intersection can be seen in the RHS plots of Figs. 3.13-3.14. The critical value of these $\eta = 1$ and 2 $\mathrm{TM}_{\{0,3\}\eta 0}$ modes is 0.98 because the cosine function has a maximum amplitude of 1.

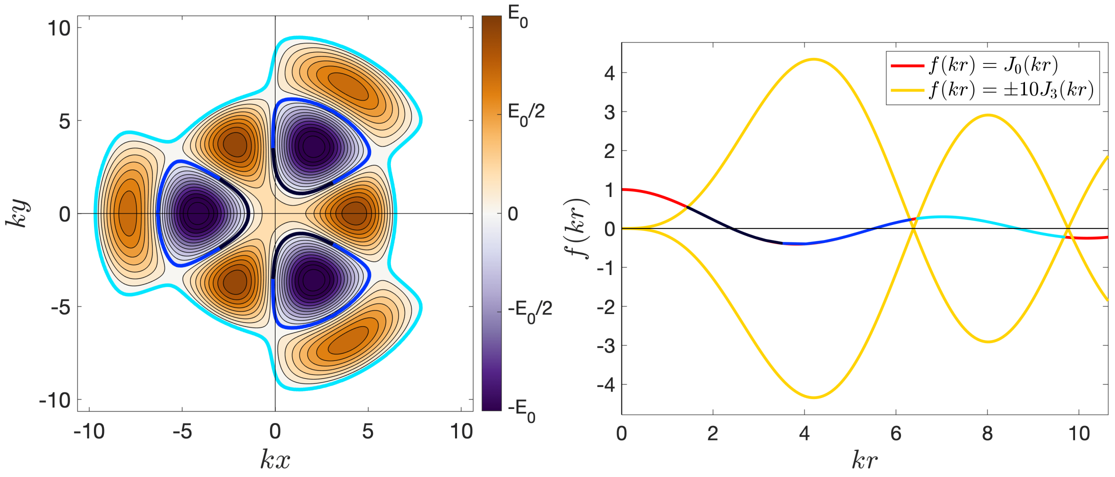

Figure 3.14: Contour plot in wavenumber-scaled Cartesian space of E_z in the $\mathrm{TM}_{\{0,3\}\eta 0}$ modes with $\tilde{g}_0 = 1$, $\tilde{g}_3 = 10$ and $\phi_3 = 0$ (left). The functions $J_0(kr)$ and $-10J_3(kr)\cos(3\theta)$ are plotted against kr for $\theta = 0, \pi/3$ (right). The $\eta = 1$, 2 and 3 solutions are graphed for all θ in black, blue and cyan.

3.4.4 Hybrid Solutions and Hybrid Modes

In certain cases, the set of discontinuous cross-sections $\{\eta\}$ that lie in an interval $kr = [j_{m_1(Q-1)}, j_{m_1 Q}]$ can be connected up continuously to form a *hybrid solution* that supports a $\mathrm{TM}_{\{0,m_1\}\{\eta\}0}$ *hybrid mode*. Such hybrid cross-sections can be formed if at least one solution exists in the interval for all θ and all solutions in the interval can be continuously connected. See, for example, Fig. 3.17 which is discussed in detail in Sec. 3.4.5.

In the case of the hybrid mode, the number of poles along the θ_q radial lines is one of the elements of the set of $\{\eta\}$.

The definition of hybridity can also be generalised: a $\mathrm{TM}_{\{M\}\{\eta\}0}$ hybrid mode is one that is supported by a continuous azimuthally modulated cavity cross-section that transitions continuously across solutions of different orders of η.

We demonstrate hybrid solutions and hybrid modes by analysing the azimuthally modulated cross-sections that support $\mathrm{TM}_{\{0,5\}\eta 0}$ modes.

3.4.5 $\text{TM}_{\{0,5\}\eta 0}$ Modes

The azimuthally modulated cross-sections that support the $\text{TM}_{\{0,5\}\eta 0}$ modes composed of a monopole and a decupole must satisfy the boundary condition

$$0 = \tilde{g}_0 J_0\left(kr_0^{(\eta)}(\theta)\right) + \tilde{g}_5 J_5\left(kr_0^{(\eta)}(\theta)\right)\cos(5\theta - \phi_5). \tag{3.17}$$

The RHS plots of Figs. 3.15-3.17 show the three Bessel roots j_{01}, j_{02} and j_{03} all exist within the interval $kr = [0, j_{51}]$. The LHS contour plots of Figs. 3.15-3.17 show the variation in the longitudinal electric field of the $\eta = 1$, 2, 3 and 4 $\text{TM}_{\{0,5\}\eta 0}$ modes for $\tilde{g}_5/\tilde{g}_0 = 0.9$, 5 and 10 with $\phi_5 = 0$.

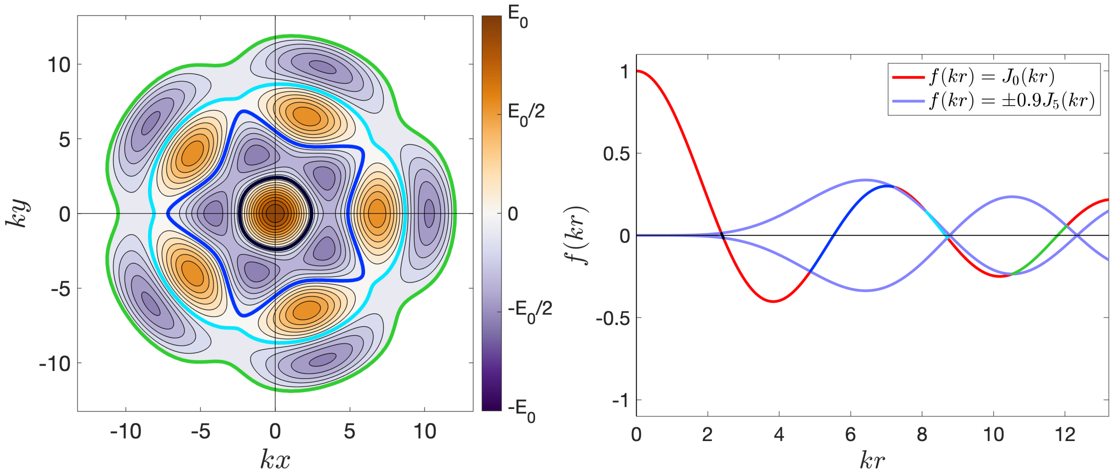

Figure 3.15: Contour plot in wavenumber-scaled Cartesian space of E_z in the $\text{TM}_{\{0,5\}\eta 0}$ modes with $\tilde{g}_0 = 1$, $\tilde{g}_5 = 0.9$ and $\phi_5 = 0$ (left). The functions $J_0(kr)$ and $-0.9J_5(kr)\cos(5\theta)$ are plotted against kr for $\cos(5\theta) = \pm 1$ (right). The $\eta = 1$, 2, 3 and 4 solutions are graphed for all θ in black, blue, cyan and lime.

Looking at Fig. 3.15, we see the solutions are continuous when $\tilde{g}_5/\tilde{g}_0 = 0.9$. As this ratio is increased to 5, however, Fig. 3.16 shows the $\eta = 2$ and 3 cross-sections converge and that they are discontinuous around the $\theta_q = (2q+1)\pi/5$ angles where $\cos(5\theta_q) = -1$. This converged solution, that we denote as $\eta = \{2, 3\}$, is not a hybrid solution because it is discontinuous.

When the ratio is increased to 10, Fig. 3.17 shows that the $\eta = 1$ also converges

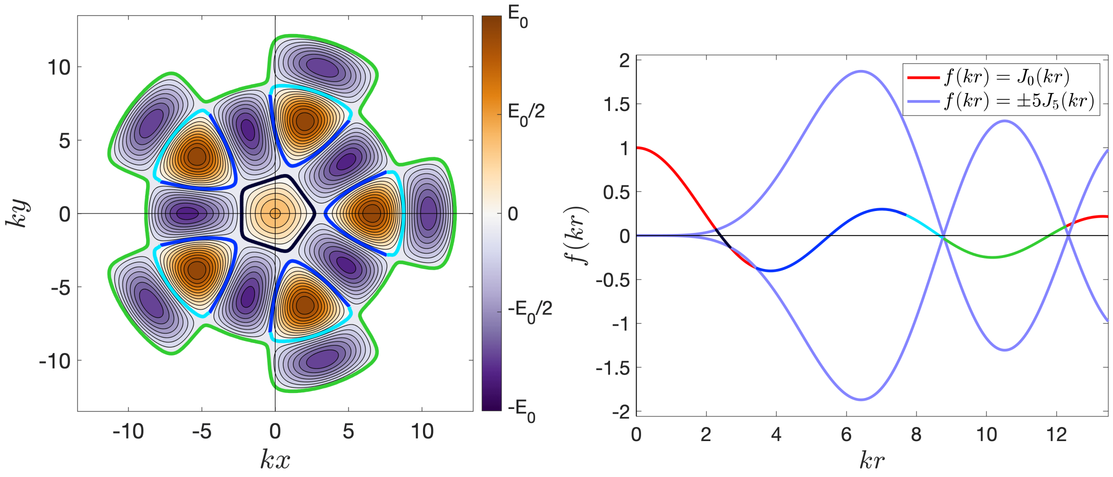

Figure 3.16: Contour plot in wavenumber-scaled Cartesian space of E_z in the $\mathrm{TM}_{\{0,5\}\eta 0}$ modes with $\tilde{g}_0 = 1$, $\tilde{g}_5 = 5$ and $\phi_5 = 0$ (left). The functions $J_0(kr)$ and $-5J_5(kr)\cos(5\theta)$ are plotted against kr for $\cos(5\theta) = \pm 1$ (right). The $\eta = 1$, 2, 3 and 4 solutions are graphed for all θ in black, blue, cyan and lime.

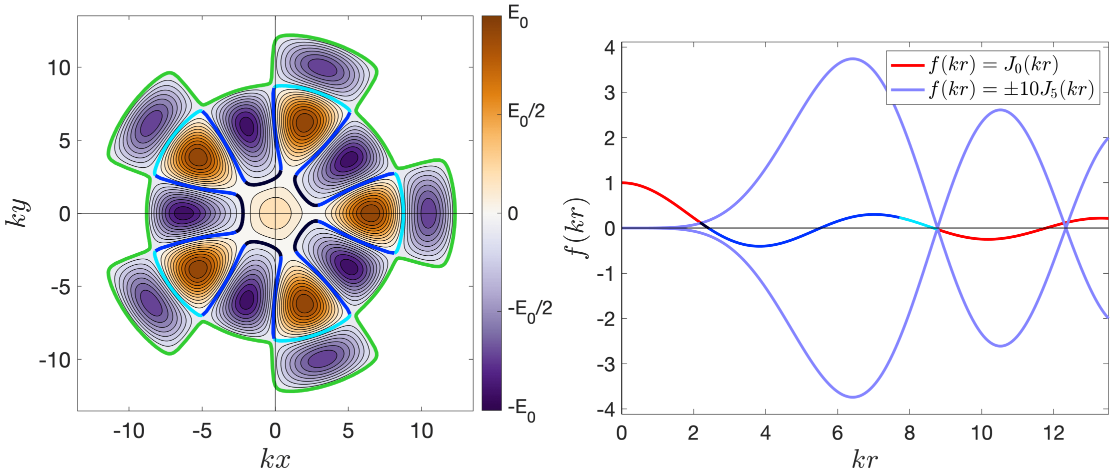

Figure 3.17: Contour plot in wavenumber-scaled Cartesian space of E_z in the $\mathrm{TM}_{\{0,5\}\eta 0}$ modes with $\tilde{g}_0 = 1$, $\tilde{g}_5 = 10$ and $\phi_5 = 0$ (left). The functions $J_0(kr)$ and $-10J_5(kr)\cos(5\theta)$ are plotted against kr for $\cos(5\theta) = \pm 1$ (right). The $\eta = 1$, 2, 3 and 4 solutions are graphed for all θ in black, blue, cyan and lime.

with the $\eta = 2$ solution and that they are both discontinuous about the $\theta_q = 2q\pi/5$ angles where $\cos(5\theta_q) = +1$. Taken together with the $\eta = 3$ solution, however, the resulting converged $\eta = \{1, 2, 3\}$ solution is continuous for all θ and is therefore hybrid. This hybrid cross-section supports a $\mathrm{TM}_{\{0,5\}\{1,2,3\}0}$ hybrid mode.

The reason that a hybrid solution forms is because there is at least one intersection between the functions $-\tilde{g}_5 J_5(kr)\cos(5\theta)$ and $\tilde{g}_0 J_0(kr)$ in the interval $kr = [0, j_{51}]$ for all ratios of $\tilde{g}_5/\tilde{g}_0$. In the cases where $\tilde{g}_5/\tilde{g}_0 > 6.1$, the $\eta = 1$, 2 and 3 solutions can all be continuously connected, as shown on the RHS plot of Fig. 3.17, to form a hybrid solution which supports a hybrid mode.[3] In the cases where $0.9 < \tilde{g}_5/\tilde{g}_0 \leq 6.1$, the $\eta = \{2, 3\}$ converged solution is discontinuous because, first, there is no continuous connection between $\eta = 1$ and $\{2, 3\}$ solutions. Second, no $\eta = 2$ or 3 solutions exist in the interval $kr = [0, j_{51}]$ for angles around $\cos(5\theta_q) = -1$. This is shown on the RHS plot of Fig. 3.16.

To summarise, the $\eta = 1$, 2 and 3 $\mathrm{TM}_{\{0,5\}\eta 0}$ modes are all conditional because their individual solutions are discontinuous when the ratio $\tilde{g}_5/\tilde{g}_0$ increases beyond critical values of 0.9 and 6.1. When the $\eta = 1$ solution becomes discontinuous, however, it converges with the $\eta = 2$ solution to form a hybrid $\eta = \{1, 2, 3\}$ solution that is continuous. The results for this mode are summarised in Table 3.1 where we note that all $\eta \geq 4$ modes are unconditional because the intervals $kr = [j_{5(Q-1)}, j_{5Q}]$ $(Q \geq 2)$ contain just one single $j_{0(Q+2)}$ root.

Ratio Solution	$\tilde{g}_5/\tilde{g}_0 \leq 0.9$	$0.9 > \tilde{g}_5/\tilde{g}_0 \leq 6.1$	$\tilde{g}_5/\tilde{g}_0 > 6.1$
$\eta = 1$	$\mathrm{TM}_{\{0,5\}10}$	$\mathrm{TM}_{\{0,5\}10}$	$\mathrm{TM}_{\{0,5\}\{1,2,3\}0}$
$\eta = 2$	$\mathrm{TM}_{\{0,5\}20}$	Discontinuous	$\mathrm{TM}_{\{0,5\}\{1,2,3\}0}$
$\eta = 3$	$\mathrm{TM}_{\{0,5\}30}$	Discontinuous	$\mathrm{TM}_{\{0,5\}\{1,2,3\}0}$
$\eta \geq 4$	$\mathrm{TM}_{\{0,5\}\eta 0}$	$\mathrm{TM}_{\{0,5\}\eta 0}$	$\mathrm{TM}_{\{0,5\}\eta 0}$

Table 3.1: The realisable mode supported by continuous azimuthally modulated cross-sections $r_0^{(\eta)}(\theta)$ for different ratios of $\tilde{g}_5/\tilde{g}_0$.

---

[3] An interesting consequence is that the hybrid $\mathrm{TM}_{\{0,5\}\{1,2,3\}0}$ cross-section, as shown on the LHS of Fig. 3.17, *tracks back* on itself when transitioning from the $\eta = 1$ to $\eta = 3$ solutions. That is, if the hybrid cross-section is traced anti-clockwise continuously from $\theta = 0$ along the $\eta = 3$ solution, then one traces clockwise along the $\eta = 2$ solution before continuing to trace anti-clockwise along the $\eta = 1$ solution.

3.5 Two Transverse Multipoles

From Eqn. 2.68, the $\mathrm{TM}_{\{m_1,m_2\}\eta 0}$ modes consisting of two transverse multipoles of order m_1 and m_2, where we assume $m_2 > m_1$ without loss of generality, have a longitudinal electric field of the form

$$E_z(\vec{r}) = \tilde{g}_{m_1} J_{m_1}(kr) \cos m_1\theta + \tilde{g}_{m_2} J_{m_2}(kr) \cos(m_2\theta - \phi_{\{m_1,m_2\}}). \tag{3.18}$$

The $\mathrm{TM}_{\{m_1,m_2\}\eta 0}$ modes can be conditional and hybrid, as defined in Sec. 3.4.2 and Sec. 3.4.4 respectively, and they are supported by the azimuthally modulated cross-sections that solve the cavity wall boundary condition

$$0 = \tilde{g}_{m_1} J_{m_1}\left(kr_0^{(\eta)}(\theta)\right) \cos m_1\theta + \tilde{g}_{m_2} J_{m_2}\left(kr_0^{(\eta)}(\theta)\right) \cos(m_2\theta - \phi_{\{m_1,m_2\}}). \tag{3.19}$$

Here, we have set $\phi_{m_1} = 0$ and rewritten ϕ_{m_2} as $\phi_{\{m_1,m_2\}}$ without loss of generality. This allows for a complete exploration of the properties of the $\mathrm{TM}_{\{m_1,m_2\}\eta 0}$ modes because $\phi_{m_1} \neq 0$ simply rotates the modes and cross-sections by ϕ_{m_1}/m_1.

3.5.1 Forbidden Modes, ZRLs and Spiral Solutions

The absence of a monopole term in the $\mathrm{TM}_{\{m_1,m_2\}\eta 0}$ modes adds complexity to the solutions for three reasons.

First, $r_0^{(\eta)}(\theta) = 0$ is a valid solution to Eqn. 3.19 for all θ. A practical RF structure, however, must have $r_0^{(\eta)}(\theta) > 0$. We therefore introduce the term *forbidden* to describe the $\mathrm{TM}_{\{m_1,m_2\}\eta 0}$ modes and solutions that correspond to azimuthally modulated cross-sections that are zero at any angle.

Second, both terms in Eqn. 3.19 have a cosine dependence and so the zeros of different multipolar terms can align with each other. Consequently, the mode can have *zero radial lines* (*ZRLs*). These are radial lines along which the longitudinal electric field is always zero. The ZRLs of a $\mathrm{TM}_{\{m_1,m_2\}\eta 0}$ mode are found at the angles $\theta_{(0)}$ that simultaneously satisfy both

$$\cos\left(m_1\theta_{(0)}\right) = 0, \tag{3.20}$$

$$\cos\left(m_2\theta_{(0)} - \phi_{\{m_1,m_2\}}\right) = 0. \tag{3.21}$$

From Eqns. 3.20-3.21 it follows

$$m_1\theta_{(0)} = \frac{(2q_1+1)}{2}\pi, \tag{3.22}$$

$$m_2\theta_{(0)} - \phi_{\{m_1,m_2\}} = \frac{(2q_2+1)}{2}\pi, \tag{3.23}$$

where $q_1, q_2 \in \mathbb{Z}$. Both Eqns. 3.22-3.23 are only satisfied when

$$\phi_{\{m_1,m_2\}} = \phi^{(0)}_{\{m_1,m_2\}} = \left(m_2(2q_1+1) - m_1(2q_2+1)\right)\frac{\pi}{2m_1}, \tag{3.24}$$

where we introduce the notation $\phi^{(0)}_{\{m_1,m_2\}}$ to indicate the specific orientations that create ZRLs in $\mathrm{TM}_{\{m_1,m_2\}\eta 0}$ modes. Denoting $\{\texttt{e}\}$ as the set of even integers and $\{\texttt{o}\}$ as the set of odd integers, Table 3.2 shows $\phi^{(0)}_{\{m_1,m_2\}}$ for the first 10 orders of m_2.

	m_1								
m_2	1	2	3	4	5	6	7	8	9
2	$\{\texttt{o}\}\frac{\pi}{2}$	$\cdots$	$\cdots$	$\cdots$	$\cdots$	$\cdots$	$\cdots$	$\cdots$	$\cdots$
3	$\{\texttt{e}\}\frac{\pi}{2}$	$\{\texttt{o}\}\frac{\pi}{4}$	$\cdots$	$\cdots$	$\cdots$	$\cdots$	$\cdots$	$\cdots$	$\cdots$
4	$\{\texttt{o}\}\frac{\pi}{2}$	$\{\texttt{o}\}\frac{\pi}{2}$	$\{\texttt{o}\}\frac{\pi}{6}$	$\cdots$	$\cdots$	$\cdots$	$\cdots$	$\cdots$	$\cdots$
5	$\{\texttt{e}\}\frac{\pi}{2}$	$\{\texttt{o}\}\frac{\pi}{4}$	$\{\texttt{e}\}\frac{\pi}{6}$	$\{\texttt{o}\}\frac{\pi}{8}$	$\cdots$	$\cdots$	$\cdots$	$\cdots$	$\cdots$
6	$\{\texttt{o}\}\frac{\pi}{2}$	$\{\texttt{e}\}\frac{\pi}{2}$	$\{\texttt{o}\}\frac{\pi}{2}$	$\{\texttt{o}\}\frac{\pi}{4}$	$\{\texttt{o}\}\frac{\pi}{10}$	$\cdots$	$\cdots$	$\cdots$	$\cdots$
7	$\{\texttt{e}\}\frac{\pi}{2}$	$\{\texttt{o}\}\frac{\pi}{4}$	$\{\texttt{e}\}\frac{\pi}{6}$	$\{\texttt{o}\}\frac{\pi}{8}$	$\{\texttt{e}\}\frac{\pi}{10}$	$\{\texttt{o}\}\frac{\pi}{12}$	$\cdots$	$\cdots$	$\cdots$
8	$\{\texttt{o}\}\frac{\pi}{2}$	$\{\texttt{o}\}\frac{\pi}{2}$	$\{\texttt{o}\}\frac{\pi}{6}$	$\{\texttt{o}\}\frac{\pi}{2}$	$\{\texttt{o}\}\frac{\pi}{10}$	$\{\texttt{o}\}\frac{\pi}{6}$	$\{\texttt{o}\}\frac{\pi}{14}$	$\cdots$	$\cdots$
9	$\{\texttt{e}\}\frac{\pi}{2}$	$\{\texttt{o}\}\frac{\pi}{4}$	$\{\texttt{e}\}\frac{\pi}{2}$	$\{\texttt{o}\}\frac{\pi}{8}$	$\{\texttt{e}\}\frac{\pi}{10}$	$\{\texttt{o}\}\frac{\pi}{4}$	$\{\texttt{e}\}\frac{\pi}{14}$	$\{\texttt{o}\}\frac{\pi}{16}$	$\cdots$
10	$\{\texttt{o}\}\frac{\pi}{2}$	$\{\texttt{e}\}\frac{\pi}{2}$	$\{\texttt{o}\}\frac{\pi}{6}$	$\{\texttt{o}\}\frac{\pi}{4}$	$\{\texttt{o}\}\frac{\pi}{2}$	$\{\texttt{e}\}\frac{\pi}{6}$	$\{\texttt{o}\}\frac{\pi}{14}$	$\{\texttt{o}\}\frac{\pi}{8}$	$\{\texttt{o}\}\frac{\pi}{18}$

Table 3.2: The value of $\phi^{(0)}_{\{m_1,m_2\}}$ that creates ZRLs in the $\mathrm{TM}_{\{m_1,m_2\}\eta 0}$ modes. $\{\texttt{e}\}$ denotes the set of even integers and $\{\texttt{o}\}$ the set of odd integers.

Third, the cross-sections are not necessarily bound within the interval $kr = [j_{m_2(Q-1)}, j_{m_2Q}]$ because solutions can cross j_{m_2Q} boundaries. This requires a number of steps to prove mathematically and starts by considering Eqn. 3.19 at $\theta = 0$

$$0 = \tilde{g}_{m_1} J_{m_1}\left(kr_0^{(\eta)}(0)\right) + \tilde{g}_{m_2} J_{m_2}\left(kr_0^{(\eta)}(0)\right)\cos\phi_{\{m_1,m_2\}}. \tag{3.25}$$

Assuming non-zero solutions only, then it follows that $kr_0^{(\eta)}(0) \neq j_{m_2Q}$ because $J_{m_2}(j_{m_2Q}) = 0$ but $J_{m_1}(j_{m_2Q}) \neq 0$. Therefore $kr_0^{(\eta)}(0) = j_{m_2Q}$ does not satisfy Eqn. 3.25, that is

$$\tilde{g}_{m_1} J_{m_1}(j_{m_2Q}) + \tilde{g}_{m_2} J_{m_2}(j_{m_2Q})\cos\phi_{\{m_1,m_2\}} = \tilde{g}_{m_2} J_{m_2}(j_{m_2Q})\cos\phi_{\{m_1,m_2\}} \neq 0. \tag{3.26}$$

The above therefore shows that the $kr_0^{(\eta)}(0)$ solutions lie within the interval $kr = [j_{m_2(Q-1)}, j_{m_2Q}]$ and not at the j_{m_2Q} boundaries.

We next consider the $\theta_q = (2q+1)\pi/2m_1$ angles that eliminate the multipolar term of order m_1 such that Eqn. 3.25 becomes

$$0 = \tilde{g}_{m_2} J_{m_2}\left(kr_0^{(\eta)}(\theta_q)\right)\cos\left(\frac{m_2}{m_1}(2q+1)\frac{\pi}{2} - \phi_{\{m_1,m_2\}}\right). \tag{3.27}$$

This has two possible solutions. The first is that the cosine term is zero which occurs when $\phi_{\{m_1,m_2\}} = \phi_{\{m_1,m_2\}}^{(0)}$ and is the condition for a ZRL at θ_q. The second is that the Bessel function of order m_2 is zero such that

$$kr_0^{(\eta)}(\theta_q) = j_{m_2Q}. \tag{3.28}$$

Equation 3.28 therefore states $r_0^{(\eta)}(\theta_q)$ lies at a j_{m_2Q} boundary provided $\phi_{\{m_1,m_2\}} \neq \phi_{\{m_1,m_2\}}^{(0)}$.

The next step is to determine whether the solutions cross the lower or upper boundary of a $kr = [j_{m_2(Q-1)}, j_{m_2Q}]$ interval at these θ_q angles. This can be determined by calculating the gradient of the cross-section with respect to θ. Specifically, the solutions cross the lower limit if the gradient is negative at θ_q and the upper limit if it is positive. Differentiating Eqn. 3.25 gives

$$k\frac{dr_0^{(\eta)}(\theta)}{d\theta} = \frac{J_{m_1}(kr_0^{(\eta)}(\theta))\tilde{g}_{m_1} m_1 \sin(m_1\theta) + J_{m_2}(kr_0^{(\eta)}(\theta))\tilde{g}_{m_2} m_2 \sin(m_2\theta - \phi_{\{m_1,m_2\}})}{J'_{m_1}(kr_0^{(\eta)}(\theta))\tilde{g}_{m_1} \cos(m_1\theta) + J'_{m_2}(kr_0^{(\eta)}(\theta))\tilde{g}_{m_2} \cos(m_2\theta - \phi_{\{m_1,m_2\}})}, \tag{3.29}$$

and substituting in Eqn. 3.28 and using $\cos(m_1\theta_q) = 0$ gives

$$\left.\frac{dr_0^{(\eta)}(\theta)}{d\theta}\right|_{\theta_q} = \frac{m_1}{k}\frac{\tilde{g}_{m_1}}{\tilde{g}_{m_2}}\frac{J_{m_1}(j_{m_2Q})(-1)^q}{J'_{m_2}(j_{m_2Q})\cos(m_2\theta_q)}. \tag{3.30}$$

Equation 3.30 can be numerically evaluated at every θ_q to determine the sign of the gradient at every boundary j_{m_2Q}. If the number of times the upper limit is crossed equals the number of times the lower limit is crossed, the solution will lie in the interval $kr = [j_{m_2(Q-\zeta)}, j_{m_2Q}]$, where $(\zeta+1)$ is numerically calculated and equal to the number of boundaries crossed. In the case where $\zeta \geq Q$, the TM$_{\{m_1,m_2\}\eta 0}$ modes that initially lie in the $kr = [j_{m_2(Q-1)}, j_{m_2Q}]$ interval are forbidden because there are angles where the cross-section is zero.

If, however, the number of times the gradient is positive does not equal the number of times the gradient is negative (that is the number of times the upper boundary of an interval is crossed does not equal the total number of times the lower boundary of an interval is crossed) then $r^{(\eta)}(0)$ will lie in a different interval to $r^{(\eta)}(2\pi)$. This means $r^{(\eta)}(0) \neq r^{(\eta)}(2\pi)$ and we define such solutions as *spiral*.

These findings are summarised in Table 3.3 which shows the η value of the first non-forbidden TM$_{\{m_1,m_2\}\eta 0}$ mode when $\phi_{\{m_1,m_2\}} \neq \phi^{(0)}_{\{m_1,m_2\}}$ as well as the first non-forbidden mode when $\phi_{\{m_1,m_2\}} = \phi^{(0)}_{\{m_1,m_2\}}$. It also indicates the multipolar values of the spiral modes.

We now analyse the TM$_{\{2,4\}\eta 0}$ modes to illustrate the concepts of forbidden modes

	m_1								
m_2	1	2	3	4	5	6	7	8	9
2	2, 1	$\cdots$	$\cdots$	$\cdots$	$\cdots$	$\cdots$	$\cdots$	$\cdots$	$\cdots$
3	$\nexists$, 1	3, 2	$\cdots$	$\cdots$	$\cdots$	$\cdots$	$\cdots$	$\cdots$	$\cdots$
4	2, 1	2, 1	4, 3	$\cdots$	$\cdots$	$\cdots$	$\cdots$	$\cdots$	$\cdots$
5	$\nexists$, 1	3, 2	$\nexists$, 2	5, 4	$\cdots$	$\cdots$	$\cdots$	$\cdots$	$\cdots$
6	2, 1	$\nexists$, 1	2, 1	3, 2	6, 5	$\cdots$	$\cdots$	$\cdots$	$\cdots$
7	$\nexists$, 1	3, 2	$\nexists$, 2	3, 2	$\nexists$, 3	7, 6	$\cdots$	$\cdots$	$\cdots$
8	2, 1	2, 1	4, 3	2, 2	4, 3	4, 3	8, 7	$\cdots$	$\cdots$
9	$\nexists$, 1	3, 2	$\nexists$, 1	3, 2	$\nexists$, 2	3, 2	$\nexists$, 4	9, 8	$\cdots$
10	2, 1	$\nexists$, 1	4, 3	3, 2	2, 1	$\nexists$, 2	4, 3	5, 4	10, 9

Table 3.3: The η values of the first non-forbidden $\mathrm{TM}_{\{m_1,m_2\}\eta 0}$ mode shown for the case $\phi_{\{m_1,m_2\}} \neq \phi^{(0)}_{\{m_1,m_2\}}$ (left of comma) and $\phi_{\{m_1,m_2\}} = \phi^{(0)}_{\{m_1,m_2\}}$ (right of comma). $\nexists$ denotes a spiral mode.

and ZRLs before analysing $\mathrm{TM}_{\{1,3\}\eta 0}$ modes to illustrate the concept of spiral solutions.

3.5.2 $\mathrm{TM}_{\{2,4\}\eta 0}$ Modes

The azimuthally modulated cross-sections that support the $\mathrm{TM}_{\{2,4\}\eta 0}$ modes composed of an octupole and a quadrupole must satisfy the boundary condition

$$0 = \tilde{g}_2 J_2\left(kr_0^{(\eta)}(\theta)\right)\cos(2\theta) + \tilde{g}_4 J_4\left(kr_0^{(\eta)}(\theta)\right)\cos(4\theta - \phi_{\{2,4\}}). \tag{3.31}$$

The LHS contour plots of Figs. 3.18-3.20 show the variation in the longitudinal electric field of the $\eta = 1$, 2 and 3 $\mathrm{TM}_{\{2,4\}\eta 0}$ modes for $\tilde{g}_4/\tilde{g}_2 = 0.1$, 1 and 10 with $\phi_{\{2,4\}} = 0$. We see that the field visually changes from appearing more quadrupolar when $\tilde{g}_4/\tilde{g}_2 = 0.1$ to appearing more octupolar when $\tilde{g}_4/\tilde{g}_2 = 10$. We also see there are no ZRLs which is expected because Table 3.2 predicts the mode only has ZRLs when $\phi_{\{2,4\}} = \phi^{(0)}_{\{2,4\}} = \{\mathtt{o}\}\frac{\pi}{2} = \pi/2, 3\pi/2$. Furthermore, only the $\eta = 1$ solution is forbidden which is expected from Table 3.3 and the RHS plots of Figs. 3.18-3.20 show that each $r_0^{(\eta)}(\theta)$ solution is bound within the interval $kr = [j_{4(\eta-2)}, j_{4\eta}]$.

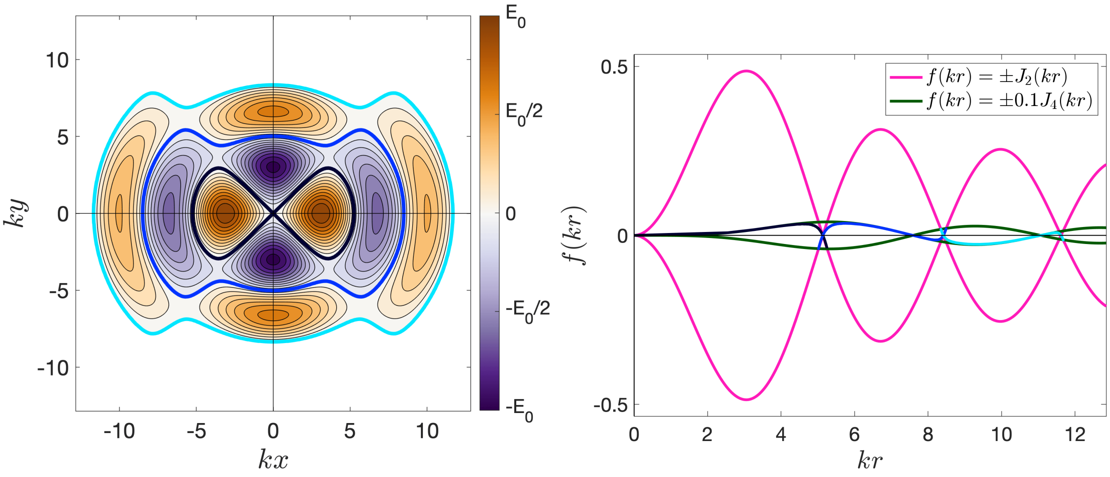

Figure 3.18: Contour plot in wavenumber-scaled Cartesian space of E_z in the $\mathrm{TM}_{\{2,4\}\eta 0}$ modes with $\tilde{g}_2 = 1$, $\tilde{g}_4 = 0.1$ and $\phi_{\{2,4\}} = 0$ (left). The functions $\pm J_2(kr)$ and $\pm 0.1 J_4(kr)$ are plotted against kr (right). The $\eta = 1$, 2 and 3 solutions are graphed for all θ in black, blue and cyan.

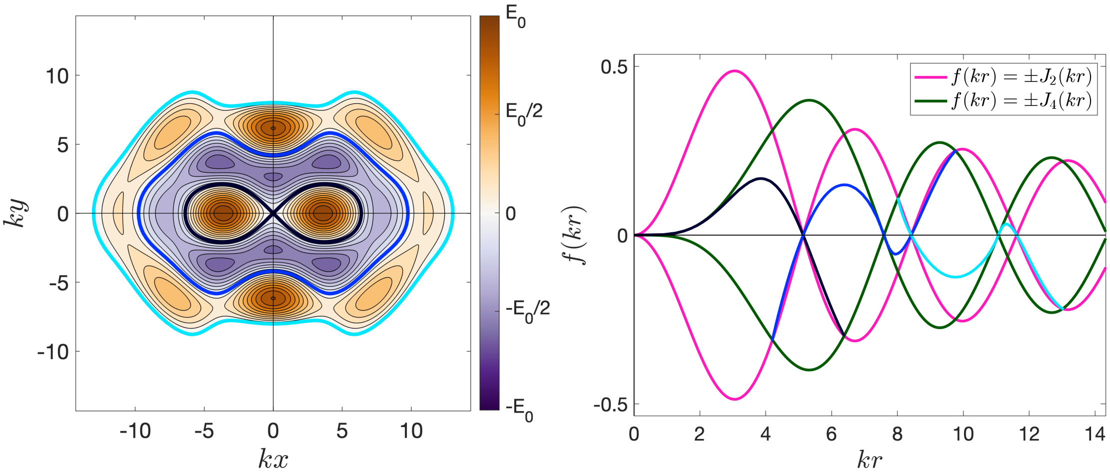

Figure 3.19: Contour plot in wavenumber-scaled Cartesian space of E_z in the $\mathrm{TM}_{\{2,4\}\eta 0}$ modes with $\tilde{g}_2 = 1$, $\tilde{g}_4 = 1$ and $\phi_{\{2,4\}} = 0$ (left). The functions $\pm J_2(kr)$ and $\pm J_4(kr)$ are plotted against kr (right). The $\eta = 1$, 2 and 3 solutions are graphed for all θ in black, blue and cyan.

We next consider the LHS contour plot of Fig. 3.21 which shows the $\mathrm{TM}_{\{2,4\}\eta 0}$ modes and solutions when $\tilde{g}_4/\tilde{g}_2 = 1$ and $\phi_{\{2,4\}} = \phi^{(0)}_{\{2,4\}} = \pi/2$. As expected, we now observe ZRLs because $\phi_{\{2,4\}} = \pi/2$ and we see they are orientated at $\theta_{(0)} = (2q+1)\pi/4$. There are no forbidden solutions and the RHS plot shows that each solution is bound within the interval $kr = [j_{4(\eta-1)}, j_{4\eta}]$.

It should be noted that ZRLs obscure the definition of η with respect to the

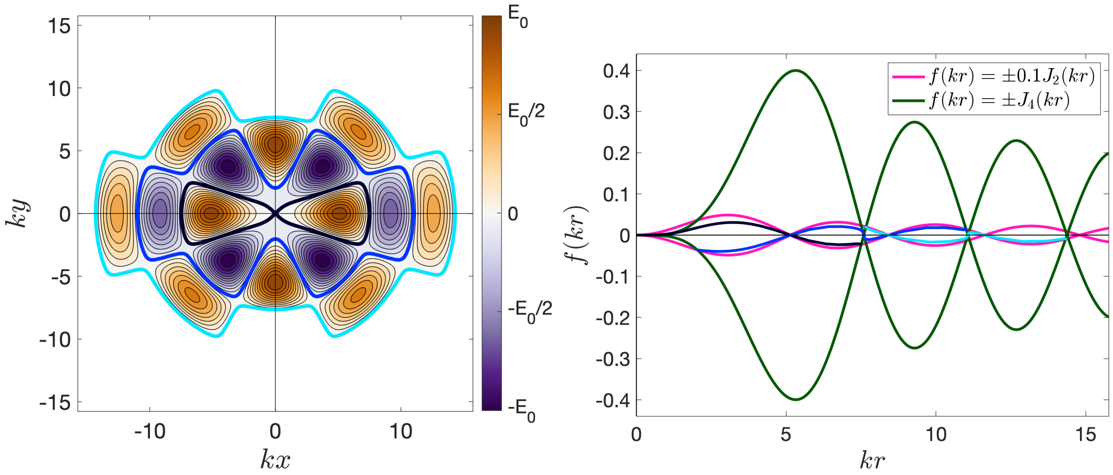

Figure 3.20: Contour plot in wavenumber-scaled Cartesian space of E_z in the $\mathrm{TM}_{\{2,4\}\eta 0}$ modes with $\tilde{g}_2 = 0.1$, $\tilde{g}_4 = 1$ and $\phi_{\{2,4\}} = 0$ (left). The functions $\pm 0.1 J_2(kr)$ and $\pm J_4(kr)$ are plotted against kr (right). The $\eta = 1$, 2 and 3 solutions are graphed for all θ in black, blue and cyan.

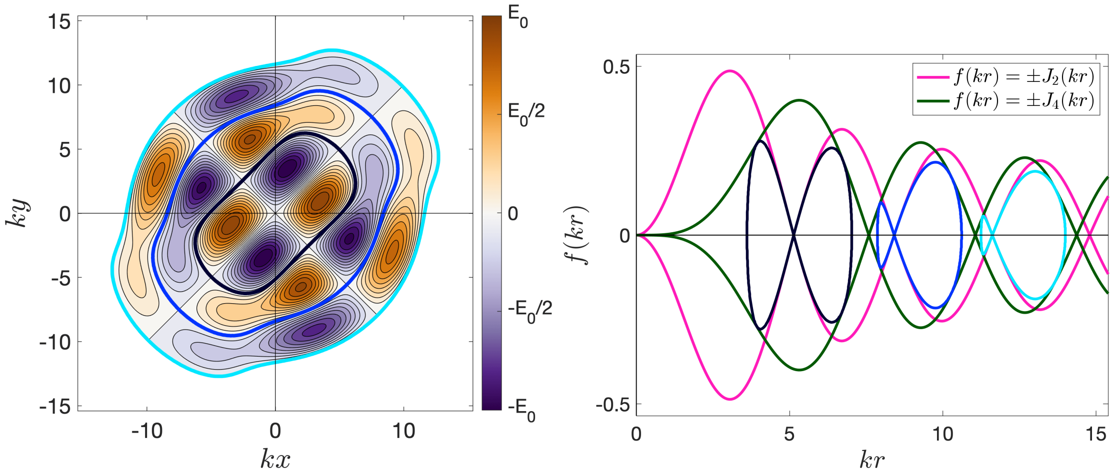

Figure 3.21: Contour plot in wavenumber-scaled Cartesian space of E_z in the $\mathrm{TM}_{\{2,4\}\eta 0}$ modes with $\tilde{g}_2 = 1$, $\tilde{g}_4 = 1$ and $\phi_{\{2,4\}} = \pi/2$ (left). The functions $\pm J_2(kr)$ and $\pm J_4(kr)$ are plotted against kr (right). The $\eta = 1$, 2 and 3 solutions are graphed for all θ in black, blue and cyan.

azimuthally modulated cross-sections. This is because the mode is zero all along the ZRL and so the solution can take any value along it, $kr_0^{(\eta)}(\theta_{(0)}) \in \mathbb{R}$. The azimuthally modulated cross-sections can therefore instantaneously fluctuate between any order of solutions along the ZRL and examples of such cross-sections are plotted in the LHS contour plot of Fig. 3.10 that shows the $\mathrm{TM}_{1\eta 0}$ modes. Here and in the following, we use η to exclusively denote the modes that do not instantaneously fluctuate along the

ZRLs.

3.5.3 $\mathrm{TM}_{\{1,3\}\eta 0}$ Modes

The azimuthally modulated cross-sections that support the $\mathrm{TM}_{\{1,3\}\eta 0}$ modes composed of a dipole and a sextupole must satisfy the boundary condition

$$0 = \tilde{g}_1 J_1 \left(k r_0^{(\eta)}(\theta) \right) \cos(3\theta) + \tilde{g}_3 J_3 \left(k r_0^{(\eta)}(\theta) \right) \cos(\theta - \phi_{\{1,3\}}). \tag{3.32}$$

Figure. 3.22 shows the $\mathrm{TM}_{\{1,3\}\eta 0}$ modes for $\tilde{g}_3/\tilde{g}_0 = 1$ and $\phi_{\{1,3\}} = 0$. As expected from Tables 3.2-3.3, there are ZRLs orientated at $\theta_{(0)} = (2q+1)\pi/2$ and there are no forbidden modes because $\phi_{\{1,3\}}^{(0)} = \{\mathtt{e}\}\pi/2$.

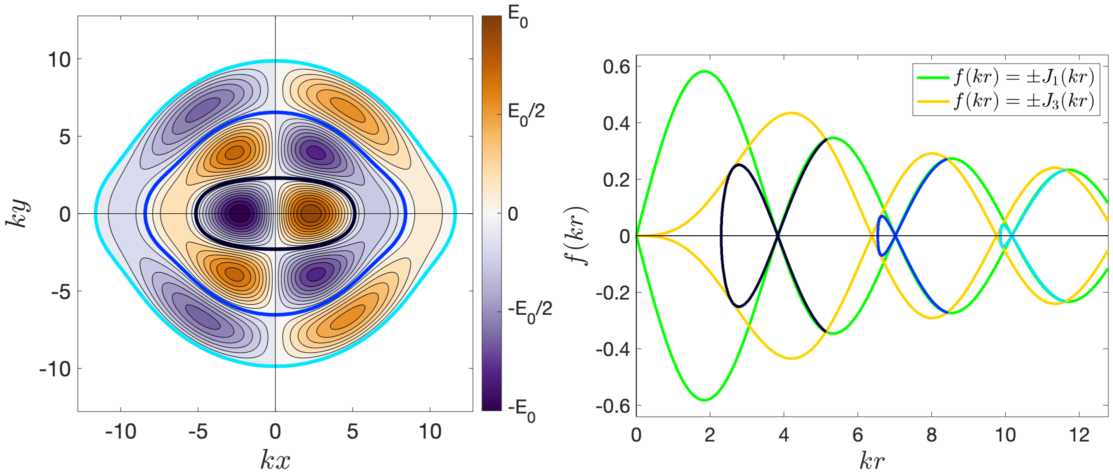

Figure 3.22: Contour plot in wavenumber-scaled Cartesian space of E_z in the $\mathrm{TM}_{\{1,3\}\eta 0}$ modes with $\tilde{g}_1 = 1$, $\tilde{g}_3 = 1$ and $\phi_{\{1,3\}} = 0$ (left). The functions $\pm J_1(kr)$ and $\pm J_3(kr)$ are plotted against kr (right). The $\eta = 1$, 2 and 3 solutions are graphed for all θ in black, blue and cyan.

In contrast, we expect spiral solutions when $\phi_{\{1,3\}}^{(0)} \neq \{\mathtt{e}\}\pi/2$ and Fig. 3.23 shows the mode and solutions when $\phi_{\{1,3\}} = \pi/40$ with $\tilde{g}_3/\tilde{g}_1 = 1$. We see there are no ZRLs and that the solutions rapidly fluctuate to a higher value close to the angles $\theta = \pi/2, 3\pi/2$. The solutions do not return to their original values as θ is varied from 0 to 2π and so a single, continuous spiral solution forms. This is not a realisable design for an RF cavity because, not only is it forbidden, but it also has infinite length. Figure 3.24 shows the mode and solution when the orientation is increased to $\pi/2$. This changes the orientation of the rapid fluctuation to the angles $\theta = 3\pi/4, 7\pi/4$.

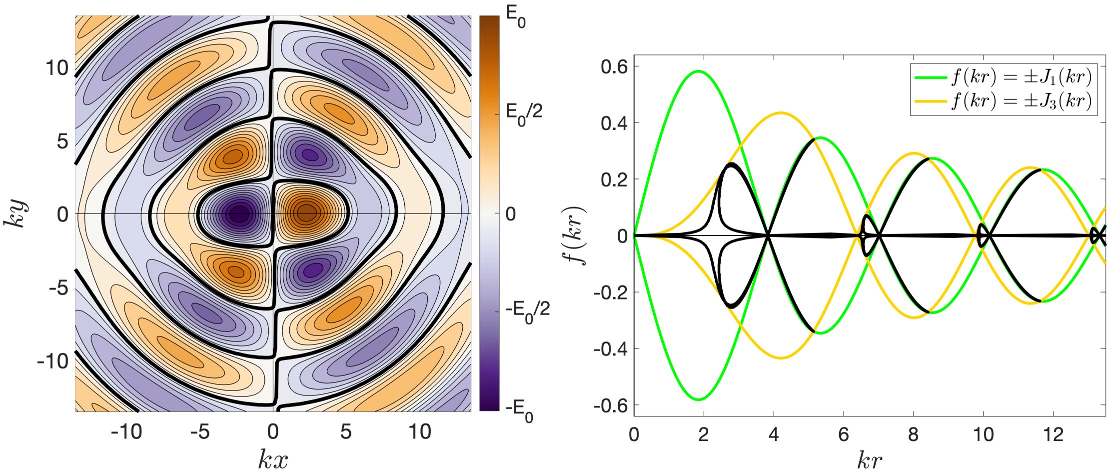

Figure 3.23: Contour plot in wavenumber-scaled Cartesian space of E_z in the $\mathrm{TM}_{\{1,3\}\eta 0}$ modes with $\tilde{g}_1 = 1$, $\tilde{g}_3 = 1$ and $\phi_{\{1,3\}} = \pi/40$ (left). The functions $\pm J_1(kr)$ and $\pm J_3(kr)$ are plotted against kr (right). The spiral solution is graphed for all θ in black.

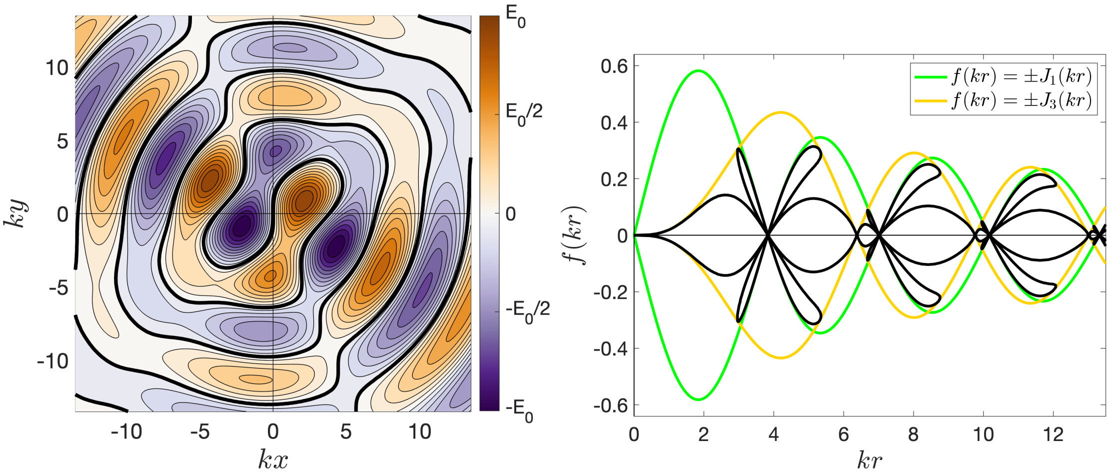

Figure 3.24: Contour plot in wavenumber-scaled Cartesian space of E_z in the $\mathrm{TM}_{\{1,3\}\eta 0}$ modes with $\tilde{g}_1 = 1$, $\tilde{g}_3 = 1$ and $\phi_{\{1,3\}} = \pi/2$ (left). The functions $\pm J_1(kr)$ and $\pm J_3(kr)$ are plotted against kr (right). The spiral solution is graphed for all θ in black.

3.6 Three or More Multipoles

General mathematical and graphical analysis for modes with three or more multipoles is difficult because they have at least three, free parameters describing the mode. However, the concepts of conditional, hybrid, forbidden and spiral modes and solutions can be used to understand the scope and limitations of azimuthally modulated cross-sections that support $\mathrm{TM}_{\{M\}\eta 0}$ modes.

Here we present an example analysis of the $\mathrm{TM}_{\{0,1,3\}\eta 0}$ modes.

3.6.1 $\mathrm{TM}_{\{0,1,3\}\eta 0}$ Modes

The azimuthally modulated cross-sections that support $\mathrm{TM}_{\{0,1,3\}\eta 0}$ modes composed of a monopole, dipole and sextupole must solve the boundary condition

$$0 = \tilde{g}_0 J_0\left(kr_0^{(\eta)}(\theta)\right) + \tilde{g}_1 J_1\left(kr_0^{(\eta)}(\theta)\right)\cos(\theta-\phi_1) + \tilde{g}_3 J_3\left(kr_0^{(\eta)}(\theta)\right)\cos(\theta-\phi_3). \tag{3.33}$$

This has dependence on three variables: $\tilde{g}_1/\tilde{g}_0$, $\tilde{g}_3/\tilde{g}_0$ and $(\phi_3-\phi_1)$. We note that there are no forbidden solutions because a monopole term is present.

To understand the properties of these modes and their solutions, we proceed with an analysis for specific parameter values. The top-left contour plot in Fig. 3.25 shows that the $\eta = 1, 2, 3$ and 4 solutions are all continuous when $\tilde{g}_0 = \tilde{g}_1 = \tilde{g}_3$ and $\phi_1 = \phi_3 = \pi$. This is an interesting contrast to the $\mathrm{TM}_{\{0,3\}10}$ and $\mathrm{TM}_{\{0,3\}20}$ modes analysed in Sec. 3.4.3 that became discontinuous when the critical limit $\tilde{g}_3/\tilde{g}_0 = 0.98$ was exceeded. Introducing a dipole component, as per this example, allows this critical limit to be exceeded and the top-right plot in Fig. 3.25 shows the solutions are still continuous even when $\tilde{g}_3/\tilde{g}_0 = 2$.

Discontinuous solutions, however, are still found for a large enough $\tilde{g}_3/\tilde{g}_0$ ratio. The bottom-left contour plot in Fig. 3.25 shows the $\eta = 1$ and 2 solutions are discontinuous when $\tilde{g}_3/\tilde{g}_0 = 5$ and $\tilde{g}_1/\tilde{g}_0 = 1$. We thus conclude that the $\mathrm{TM}_{\{0,3\}10}$ and

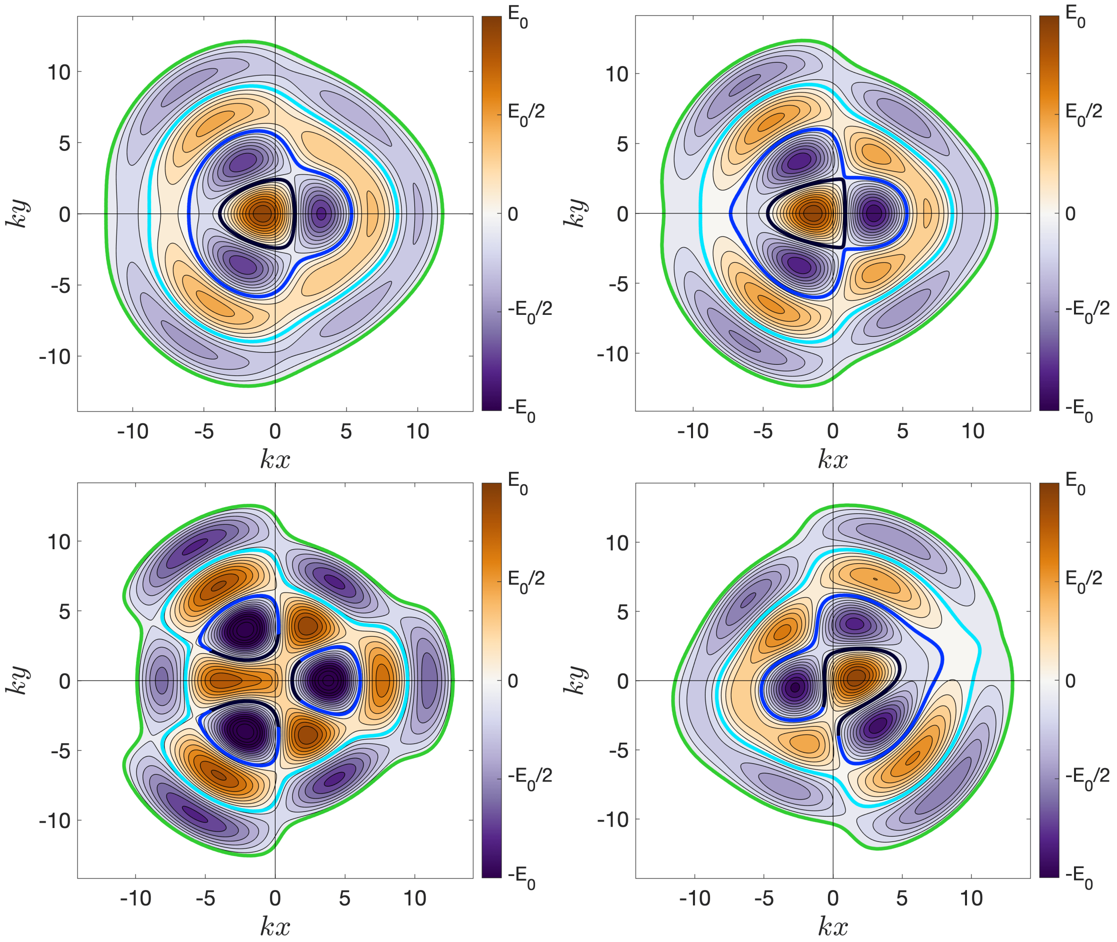

Figure 3.25: Contour plots in wavenumber-scaled Cartesian space of E_z in the $\mathrm{TM}_{\{0,1,3\}\eta 0}$ modes with $\tilde{g}_0 = 1$, $\tilde{g}_1 = 1$, $\tilde{g}_3 = 1$, and $\phi_1 = \phi_3 = \pi$ (top-left), with $\tilde{g}_0 = 1$, $\tilde{g}_1 = 2$, $\tilde{g}_3 = 2$, and $\phi_1 = \phi_3 = \pi$ (top-right), $\tilde{g}_0 = 1$, $\tilde{g}_1 = 1$, $\tilde{g}_3 = 5$, and $\phi_1 = \phi_3 = \pi$ (bottom-left) and $\tilde{g}_0 = 1$, $\tilde{g}_1 = 3$, $\tilde{g}_3 = 3$, $\phi_1 = 0$, and $\phi_3 = \pi/5$ (bottom-right). The $\eta = 1$, 2, 3 and 4 solutions are graphed in black, blue, cyan and lime.

$\mathrm{TM}_{\{0,3\}20}$ modes are conditional.

Varying the orientations of the dipole and sextupole components affects the properties of the mode too. The bottom-right contour plot in Fig. 3.25 shows the mode and solutions when $\tilde{g}_3/\tilde{g}_1 = 3$ and $\tilde{g}_3/\tilde{g}_0 = 1$, $\phi_1 = 0$ and $\phi_3 = \pi/5$. We see the $\eta = 1$ and 2 solutions converge together to form a discontinuous solution that is somewhat similar to a spiral solution. As the ratios of $\tilde{g}_3/\tilde{g}_0$ and $\tilde{g}_1/\tilde{g}_0$ increase, more and more η solutions converge together in a spiral-like fashion. However, the presence of the monopole component stops all solutions converging and spiralling indefinitely.

As such continuous, non-spiralling solutions can always be found at high enough η, regardless of the values of $\tilde{g}_1/\tilde{g}_0$, $\tilde{g}_3/\tilde{g}_0$ and $(\phi_3 - \phi_1)$.

3.6.2 Finding Unconditional Modes

One final consideration is whether unconditional modes can be found for any mode provided η is sufficiently large. If so, this would guarantee that a cavity can always be realised that supports a mode composed of any multipolar content.

We first note that such modes must contain a monopole term to ensure the solutions do not spiral. Then we consider McMahon's Expansion for Large Zeros [86] which states that

$$j_{mn} \sim \beta - \frac{\mu - 1}{8\beta} - \frac{4(\mu - 1)(7\mu - 31)}{3(8\beta^3)} - \frac{32(\mu - 1)(83\mu^2 - 982\mu^2 + 3779)}{15(8\beta^5)} - \cdots , \tag{3.34}$$

provided $n \gg m$ and where $\beta = (n + m/2 - 1/4)\pi$ and $\mu = 4m^2$. From this, we see that

$$\lim_{n \to \infty} \left\{ j_{mn} - j_{m(n-1)} \right\} = \pi, \tag{3.35}$$

and so the roots of every order of Bessel function thus become asymptotically periodic for large arguments. From this it follows that for a sufficiently large η, intervals $kr = [j_{m_h(Q-1)}, j_{m_h Q}]$ (where m_h is the highest order in the set of multipoles) can be found where the set of Bessel functions $\{M\}$ all have a single root. Hence, we conclude that unconditional $\mathrm{TM}_{\{M\}\eta 0}$ modes can always be found at large enough η values for any set $\{M\}$ of multipolar magnitudes which contain a monopole.

3.7 Chapter Summary

In this chapter, we first discussed two methods for designing RF cavities which introduce a transverse multipole of specified order into the fundamental accelerating mode. Both methods modelled the cavity shapes with simple equations, the first involved designing RF cavities with elliptical cross-sections defined by an eccentricity and semi-minor axis length and the second incorporated a longitudinally modulated nose cone defined by an offset and a modulating length into a pillbox cavity. In both methods, however, higher order multipoles were also introduced and the magnitude of the wanted transverse multipole could not be related to any parameters used to define the cavity shape. Consequently, these approaches cannot be used to tailor or fine-tune the multipolar content of a cavity mode.

In contrast, the AMM can be used to both tailor and fine-tune the multipolar content of a cavity mode. After outlining the AMM for designing RF structures that support tailored modes of specified multipole content, we discussed the scope and limitation of using it to design realisable azimuthally modulated cavities. By analysing the $\mathrm{TM}_{\{0,m_1\}\eta 0}$ and $\mathrm{TM}_{\{m_1,m_2\}\eta 0}$ modes, we derived the concepts of conditional modes as well as hybrid, forbidden and spiral modes and solutions. We presented several examples to illustrate these.

Finally, we discussed how these concepts can be generalised to understanding the azimuthally modulated cavities that support $\mathrm{TM}_{\{M\}\eta 0}$ modes composed of any number of multipoles. We also presented an example analysis of a mode composed of three multipoles.

The ability to fine-tune an electromagnetic mode has numerous applications, with several examples presented and analysed in the following chapters.

Chapter 4

Experimental Test of an Azimuthally Modulated RF Cavity

In this chapter, the process for designing, machining and testing an azimuthally modulated RF cavity that supports a 3 GHz $\mathrm{TM}_{\{0,2\}20}$ mode is presented. This work was undertaken with three goals in mind. First, to validate experimentally the AMM presented in Chapter 3 and show it is practical for designing and fabricating RF cavities for use in particle accelerators. Second, to investigate the feasibility of creating an azimuthally modulated cavity that supports a bespoke $\mathrm{TM}_{\{M\}\eta 0}$ mode of specified multipolar content even when power couplers and beam pipes are incorporated into the design. Third, to show that the bead pull technique can be used to verify that a $\mathrm{TM}_{\{M\}\eta 0}$ mode composed of numerous multipoles of specified magnitudes is as designed.

The chapter begins in Sec. 4.1 by outlining the bead pull technique that is used to measure the electromagnetic field of machined cavities. This experimental technique motivated the design choices made regarding the frequency and multipolar content of the mode to test, which is discussed in Sec. 4.2. Simulation results presented in Sec. 4.3 show how the AMM can be used to incorporate couplers into the design such that the supported mode still has the desired multipolar content. In Sec. 4.4, the final design in CAD and the machined prototype are presented. Also, the results from characterising the prototype are compared to simulation. Finally, the experimental bead pull measurements of the prototype are presented and analysed in Sec. 4.5.

4.1 Bead Pull Theory

The bead pull technique is an experimental method for measuring the electromagnetic field inside an RF cavity. The method relies on the relationship between the electromagnetic field at the location of a small, perturbing object and the corresponding change in resonant frequency of the field that it causes.

4.1.1 Cavity Perturbation Theory

Placing a dielectric or soft ferromagnetic material inside a resonating RF cavity modifies its electromagnetic field. Slater's theorem states that the change in resonant frequency of a cavity perturbed by an object which causes a change in permittivity $\Delta\varepsilon$ and a change in permeability $\Delta\mu$ is [87]

$$\frac{\omega_\mathrm{p} - \omega_0}{\omega_\mathrm{p}} = -\frac{\iiint \Big(\Delta\varepsilon \vec{E}_\mathrm{p}(\vec{r},t) \cdot \vec{E}_0^*(\vec{r},t) + \Delta\mu \vec{H}_\mathrm{p}(\vec{r},t) \cdot \vec{H}_0^*(\vec{r},t)\Big)\, dV_p}{\iiint \Big(\varepsilon \vec{E}_\mathrm{p}(\vec{r},t) \cdot \vec{E}_0^*(\vec{r},t) + \mu \vec{H}_\mathrm{p}(\vec{r},t) \cdot \vec{H}_0^*(\vec{r},t)\Big)\, dV}. \tag{4.1}$$

Here ω_p, $\vec{E}_p(\vec{r})$ and $\vec{H}_p(\vec{r})$ are the resonant frequency, electric field and magnetic H-field of the perturbed cavity. The ω_0, $\vec{E}_0(\vec{r})$ and $\vec{H}_0(\vec{r})$ are the resonant frequency, electric field and magnetic H-field of the unperturbed cavity. The integrals are over the entirety of the perturbing object's volume V_p and the asterisk denotes the complex conjugate of the field.

Equation 4.1 provides a relation between the change in resonant frequency caused by the perturbing object and the electromagnetic fields in the RF cavity in both the perturbed and unperturbed cases. Generally one has no knowledge of the perturbed fields in the cavity. In the limit where the perturbing material has a sufficiently small effect on the electromagnetic field, however, both the perturbed fields and resonant frequency can be approximated by the unperturbed values such that Eqn. 4.1 becomes

$$\frac{\Delta\omega}{\omega_0} \simeq -\frac{\iiint \left(\Delta\varepsilon \left|\vec{E}_0(\vec{r})\right|^2 + \Delta\mu \left|\vec{H}_0(\vec{r})\right|^2\right) dV_{\mathrm{p}}}{\iiint \left(\varepsilon \left|\vec{E}_0(\vec{r})\right|^2 + \mu \left|\vec{H}_0(\vec{r})\right|^2\right) dV}. \tag{4.2}$$

Here $\Delta\omega = \omega_{\mathrm{p}} - \omega_0$ is the change in resonant frequency caused by the perturbing object.

Equation 4.2 gives a relation between the change in resonant frequency of the cavity, which can be measured, and its electromagnetic fields in the unperturbed case, which we would like to know. It can be further simplified by noting

$$U = \iiint \left(\varepsilon \left|\vec{E}_0(\vec{r})\right|^2 + \mu \left|\vec{H}_0(\vec{r})\right|^2\right) dV, \tag{4.3}$$

is the stored energy in the unperturbed cavity.

4.1.2 The Bead Pull Technique

The bead pull technique involves pulling a *bead* (a small perturbing object) through an RF cavity whilst the resonant frequency of the structure is continuously measured. The magnitude and orientation of the electric and magnetic fields can be calculated independently of each other by using perturbing objects of different shapes and material properties [87, 88].

In the case where the longitudinal component of the electric field is much larger than the transverse, $E_z(\vec{r}) \gg E_\perp(\vec{r})$, and the perturbing object is made out of a non-magnetic ($\Delta\mu = 0$), dielectric material with a relative permittivity ε_r, Eqn. 4.2

becomes

$$\Delta\omega \simeq -\omega_0 \frac{\iiint \Delta\varepsilon \left|\vec{E}_z(\vec{r})\right|^2 dV_\mathrm{p}}{U}. \tag{4.4}$$

In the limit that the perturbing object is physically small enough such that the electric field can be approximated as constant throughout its volume, Eqn. 4.4 becomes

$$\Delta\omega \simeq -\omega_0 \frac{V_p \Delta\varepsilon}{W} \left|\vec{E}_z(\vec{r}_\mathrm{p})\right|^2, \tag{4.5}$$

where $\vec{r}_\mathrm{p}$ is the position of the object. We note that the volume of the perturbing object, unperturbed resonant frequency and stored energy are all constant.

Equation 4.5 is the bead pull equation. It provides a simple proportionality relation between the change in resonant frequency caused by the perturbing object at a position $\vec{r}_\mathrm{p}$ and the longitudinal electric field at that position. Thus the absolute value of the longitudinal electric field can be determined by measuring the change in resonant frequency of the RF cavity.

4.1.3 S-Parameters

The resonant frequency of an RF cavity can be determined by measuring its scattering parameters (S-parameters) over a range of frequencies. S-parameters describe the input-output relationships between power waves that are incident on and reflected from an N-port network. They are used to analyse electrical systems at microwave frequencies because incident and reflected power can be easily measured with directional couplers, in contrast to direct measurements of voltages and currents which is difficult [66].

S-parameters can be used to analyse any N-port network connected to an unknown electrical network that can be modelled with lumped elements such as resistors, capacitors and inductors. For example, Fig. 4.1 shows a two-port network comprised of port 1 and port 2 which is connected to an electrical network. The S-parameter matrix that relates the incident and reflected power waves on the network is

$$\begin{pmatrix} b_1 \\ b_2 \end{pmatrix} = \begin{pmatrix} S_{11} & S_{12} \\ S_{21} & S_{22} \end{pmatrix} \begin{pmatrix} a_1 \\ a_2 \end{pmatrix}, \tag{4.6}$$

where a_i and b_i are the incident and reflected power waves respectively. The individual elements of the matrix are the S-parameters: S_{11} is the port 1 reflection coefficient, S_{12} is the port 1 to port 2 transmission, S_{21} is the port 2 to port 1 transmission and S_{22} is the port 2 reflection coefficient.

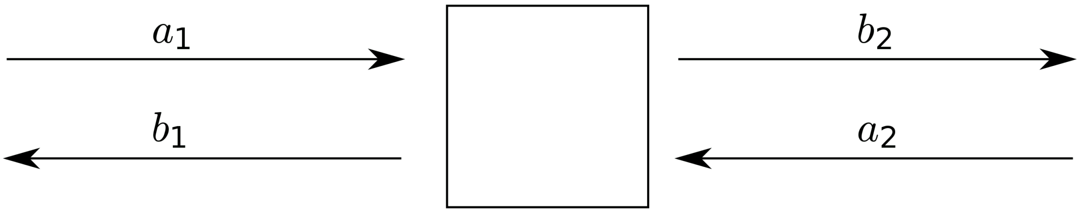

Figure 4.1: A two-port network.

4.1.4 Characterising an RF Cavity System

To relate the S-parameters to the resonant frequency of an RF cavity, we model the RF cavity system (comprised of transmission lines, couplers and the RF cavity itself) using a lumped element model. Figure 4.2 shows a single RF port connected to the RF cavity system [89].

The impedance of the RF cavity itself is

$$Z_c = \frac{1}{i\omega L + \frac{i}{\omega C} + \frac{1}{R_s}} = \frac{R_s}{1 + iQ_0\left(\frac{\omega}{\omega_0} - \frac{\omega_0}{\omega}\right)}, \tag{4.7}$$

where ω is the *driving frequency* (the frequency of the signal emitted from the RF port), L, C and R_s are the inductance, capacitance and shunt impedance of the RF

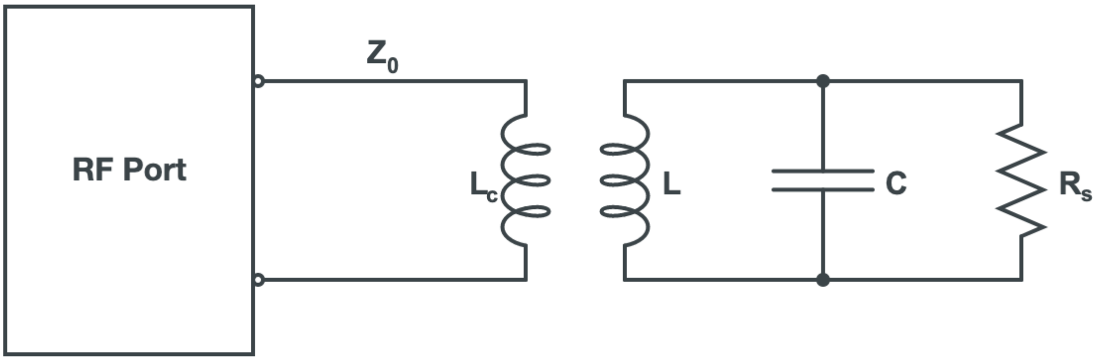

Figure 4.2: A lumped element model of an RF cavity system.

cavity, $\omega_0^2 = 1/LC$ is its resonant frequency and $Q_0 = R_s/(\omega_0 L)$ its intrinsic Q-factor.

Taking into account the transmission lines and the transformer-like inductive coupling between the waveguide and cavity, the impedance of the system is

$$Z = Z_0 + \frac{L_c}{L} Z_c = Z_0 + \frac{L_c R_s}{L\left(1 + iQ_0\left(\frac{\omega}{\omega_0} - \frac{\omega_0}{\omega}\right)\right)}, \tag{4.8}$$

where we substitute Eqn. 4.9 for Z_c. Taking the approximations $Z_0 \ll R_s$ and $L_c \ll L$, Eqn. 4.8 becomes

$$Z \simeq \frac{\beta Z_0}{1 + iQ_0 \xi}, \tag{4.9}$$

where we have introduced the normalised detuning factor

$$\xi = \frac{\omega}{\omega_0} - \frac{\omega_0}{\omega} = (\omega^2 - \omega_0^2)/\omega\omega_0, \tag{4.10}$$

and the coupling factor

$$\beta = \frac{R_s}{Z_0}\frac{L_c}{L} = \frac{Q_0}{Q_e}, \tag{4.11}$$

where $Q_e = Z_0/\omega_0 L_c$ is the external Q-factor.

The reflection coefficient can be derived by considering the reflection of the electromagnetic wave on the system as

$$S_{11} = \frac{Z - Z_0}{Z + Z_0} = \frac{(\beta - 1)(\beta + 1) - Q_0^2\xi^2 - i2\beta Q_0\xi}{(\beta + 1)^2 + Q_0^2\xi^2}. \tag{4.12}$$

By taking the absolute value of Eqn. 4.12, one finds that $|S_{11}|$ is minimised when the driving frequency equals the resonant frequency.

The resonant frequency ω_0 of an RF cavity can therefore be measured experimentally by taking a *frequency sweep* (a measurement over a range of frequencies) of S_{11} and measuring the frequency that corresponds the minimum of $|S_{11}|$.

In addition to the resonant frequency, the RF cavity can be further characterised from the frequency sweep data by calculating the coupling constant using

$$S_{11}(\omega_0) = \frac{Q_e - Q_0}{Q_e + Q_0} = \frac{1 - \beta}{1 + \beta}. \tag{4.13}$$

A cavity is undercoupled if $\beta < 1$, critically coupled if $\beta = 1$ and overcoupled if $\beta > 1$. The return loss is also commonly used in microwave engineering as a measure of the amount of incident power reflected and it is defined as

$$RL = -20 \log_{10}(|S_{11}(\omega_0)|). \tag{4.14}$$

Q_0 can then be calculated by minimising the error in a fit of Eqn. 4.12 to the frequency sweep data. Finally, the extrinsic Q_e can be calculated using

$$Q_e = \frac{Q_0}{\beta}. \tag{4.15}$$

4.1.5 Bead Pull Measurement

The practical technique for taking a bead pull measurement is to take a *time sweep* (a measurement over a range of time) of S_{11} at the driving frequency. To show why, consider the phase of Eqn. 4.12

$$\tan\left(\arg\left(S_{11}\right)\right) = \frac{2\beta Q_0 \xi}{(1-\beta)(1+\beta) + Q_0^2 \xi^2}. \tag{4.16}$$

In the limit of a sufficiently small normalised frequency detuning

$$Q_0^2 \xi^2 \ll |(1-\beta)(1+\beta)|, \tag{4.17}$$

Eqn. 4.16 then becomes

$$\tan\left(\arg\left(S_{11}\right)\right) \simeq \frac{2\beta Q_0 \xi}{(1-\beta)(1+\beta)}. \tag{4.18}$$

If we additionally assume the limit of a small change in frequency $\Delta\omega \ll \omega_0$ such that the normalised detuning factor given by Eqn. 4.10 becomes

$$\xi \simeq \frac{2\Delta\omega}{\omega_0}, \tag{4.19}$$

Eqn. 4.18 becomes

$$\tan\left(\arg\left(S_{11}\right)\right) \simeq \frac{4\beta Q_0}{(1-\beta)(1+\beta)\omega_0} \Delta\omega. \tag{4.20}$$

Taking a time sweep of the phase of S_{11} when the RF cavity is driven at the unperturbed resonant frequency thus gives a quantity which is proportional to the change in resonant frequency. Numerous papers [88, 90, 91, 92] use Eqn. 4.20 to measure the electric field of an RF cavity.

We also note here that the negative of S_{11} in Eqn. 4.12 transforms back to an impedance as

$$Z^- = Z_0 \frac{1 + (-S_{11})}{1 - (-S_{11})} = \frac{Z_0}{\beta}(1 + iQ_0\xi). \tag{4.21}$$

By defining the change in impedance as

$$\Delta Z = Z^{-} - Z^{-}(\omega_0), \tag{4.22}$$

where $Z^{-}(\omega_0)$ is called the *baseline impedance*, we find

$$|\Delta Z| \simeq \frac{2Z_0Q_0}{\beta\omega_0}\Delta\omega. \tag{4.23}$$

This is valid in the limit of a small change in frequency $\Delta\omega \ll \omega_0$.

4.2 Mode Specification

The bead pull technique can be used to measure the longitudinal electric field in a machined, azimuthally modulated RF cavity prototype and show that the AMM is practical for designing RF cavities for application in particle accelerators. There is choice over the frequency and multipolar content of the $\mathrm{TM}_{\{M\}\eta 0}$ mode to be tested and here we outline the reasoning for testing a 3 GHz $\mathrm{TM}_{\{0,2\}20}$ mode with a multipolar ratio of $\tilde{g}_2/\tilde{g}_0 = 5$.

The frequency of 3 GHz was chosen for two main reasons. First, it is close to the standard EU S-Band frequency of 2.99855 GHz and so the machined RF structure is a realistic prototype of a component that could be implemented in a particle accelerator. Second, the resultant structure is on the order of 10s of cm in size and so the materials and machining process was within budget.

The multipolar content of the mode was chosen to be just a monopole and a normal quadrupole because such a mode and its corresponding azimuthally modulated structures have horizontal and vertical symmetry. Testing this symmetry with the bead pull technique thus gives evidence as to whether the prototype is supporting the desired mode.

It is best to take bead pull measurements along the poles of a mode because the field is maximal, which improves the signal to noise ratio, and its transverse derivative is zero in all directions, which minimises spatial errors. The $\eta = 2$ mode was therefore chosen as a compromise between size, whereby higher-orders are larger and thus more costly to build, and the number of poles, whereby higher-orders have more poles.

This leaves the ratio $\tilde{g}_2/\tilde{g}_0$ to be chosen. The contour plots in Fig. 4.3 show the variation in the longitudinal electric field of the $\mathrm{TM}_{\{0,2\}20}$ mode for different values of $\tilde{g}_2/\tilde{g}_0$. We see that there are five poles in the field when $\tilde{g}_2/\tilde{g}_0 \leq 2$ and six poles and one saddle when $\tilde{g}_2/\tilde{g}_0 > 2$.

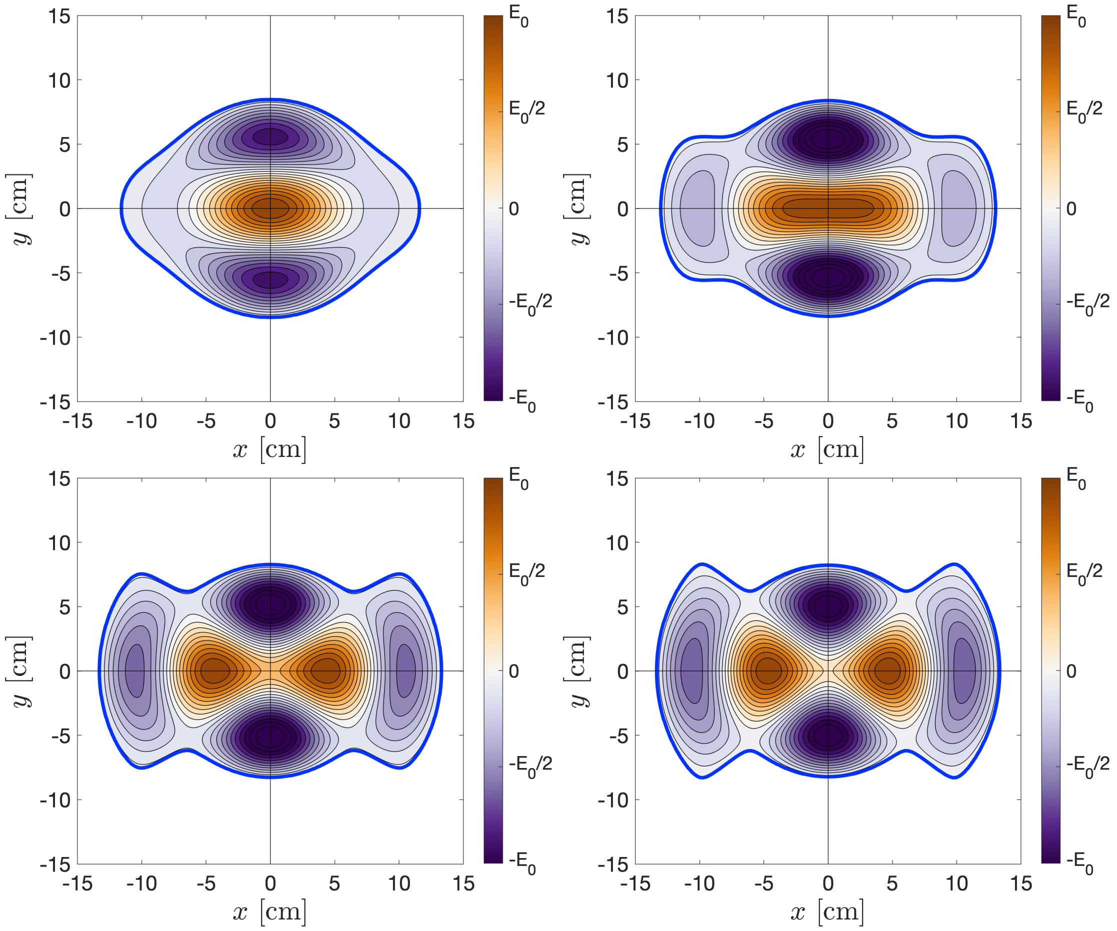

Figure 4.3: Contour plots in Cartesian space of E_z in the 3 GHz $\mathrm{TM}_{\{0,2\}20}$ modes with $\phi_2 = 0$ and $\tilde{g}_2/\tilde{g}_0 = 1.08$ (top-left), $\tilde{g}_2/\tilde{g}_0 = 2$ (top-right), $\tilde{g}_2/\tilde{g}_0 = 5$ (bottom-left) and $\tilde{g}_2/\tilde{g}_0 = 10$ (bottom-right).

The cavity was designed with $\tilde{g}_2/\tilde{g}_0 > 2$ to maximise the number of poles. In this case, three of the six poles are distinct and we name the inner poles on the x-axis as *inner-x*, the outer poles on the x-axis as *outer-x* and the poles along the y-axis as y. We also name the saddle at the origin as *on-axis*.

The ratio of the electric field along the i pole located at (r_i, θ_i) to the on-axis field can be calculated using Eqn. 3.9 as

$$\frac{E_z(r_i, \theta_i)}{E_z(0,0)} = \frac{E_z^i}{E_z^0} = J_0(kr_i) + \frac{\tilde{g}_2}{\tilde{g}_0} J_2(kr_i) \cos(2\theta_i). \tag{4.24}$$

These ratios are plotted as a function of $\tilde{g}_2/\tilde{g}_0$ in blue in Fig. 4.4. The ratio of the radial distance to the pole, r_i, to the radial distance to the cavity wall, $r_0^{(2)}(\theta_i)$, is also plotted in red.

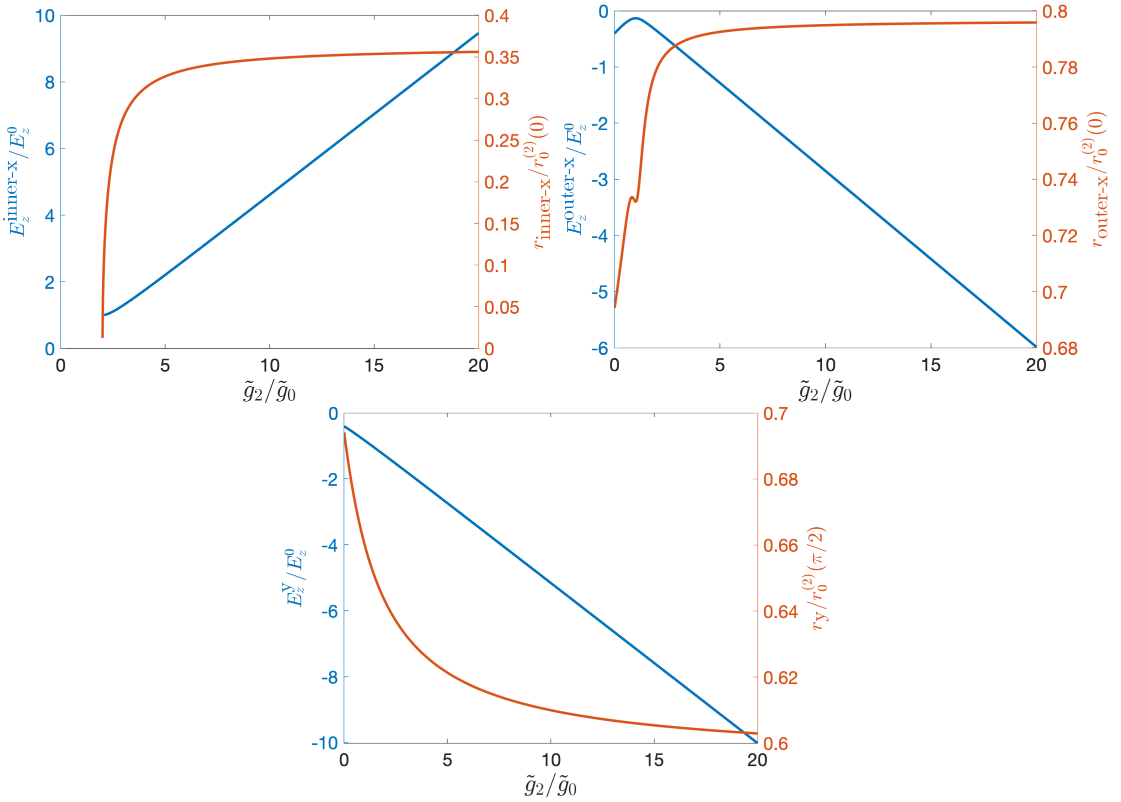

Figure 4.4: Plots showing the ratio of E_z at the inner$-x$ (top-left), outer$-x$ (top-right) and y (bottom) poles to E_z on-axis as a function of the multipolar ratio $\tilde{g}_2/\tilde{g}_0$ (blue) and the ratio of the radial distance to the cavity wall (red).

A flatter gradient of $r_i/r_0^{(2)}(\theta_i)$ with respect to $\tilde{g}_2/\tilde{g}_0$ means that the multipolar ratio of the mode is more sensitive to machining errors. Choosing a greater multipolar ratio and showing that the electric field is as intended would therefore better demonstrate that the AMM is practical for designing RF cavities in the presence of machining tolerances. Increasing the multipolar ratio, however, requires a greater range of electric fields to be measured. This can be problematic for bead pull measurements because they have a limited dynamic range. In particular, the resolution error in the measurement of S_{11} limits the smallest electric fields that can be measured whilst the breakdown of the linearity assumptions in Eqn. 4.17 and Eqn. 4.19 limits the largest electric fields that can be measured.

As a sensible compromise between these two factors, it was chosen to use the bead pull technique to test a $\mathrm{TM}_{\{0,2\}20}$ mode with a quadrupole to monopole ratio of $\tilde{g}_2/\tilde{g}_0 = 5$.

4.3 Design Simulations

Figure 4.5 shows the initial CAD design of an azimuthally modulated cavity of longitudinal length 34.036 mm with waveguides, apertures and couplers all incorporated. In the absence of any couplers, this azimuthally modulated cross-section supports a 3 GHz $\mathrm{TM}_{\{0,2\}20}$ mode with $\tilde{g}_2/\tilde{g}_0 = 5$.

This structure was modelled using the 3D electromagnetic solver CST [70]. The RF port, shown in red, couples RF power into the structure and is the reference plane from where measurements were taken. The edges of the entire structure were rounded as necessary for the machining and simulations showed the rounding had a negligible effect on the mode.

WR284 rectangular waveguides were incorporated into the design with a T junction that transfers equal magnitudes of power to both slots [66]. WR284 waveguides have a cross-sectional area of 72.136 mm × 34.036 mm and are suitable power transfer

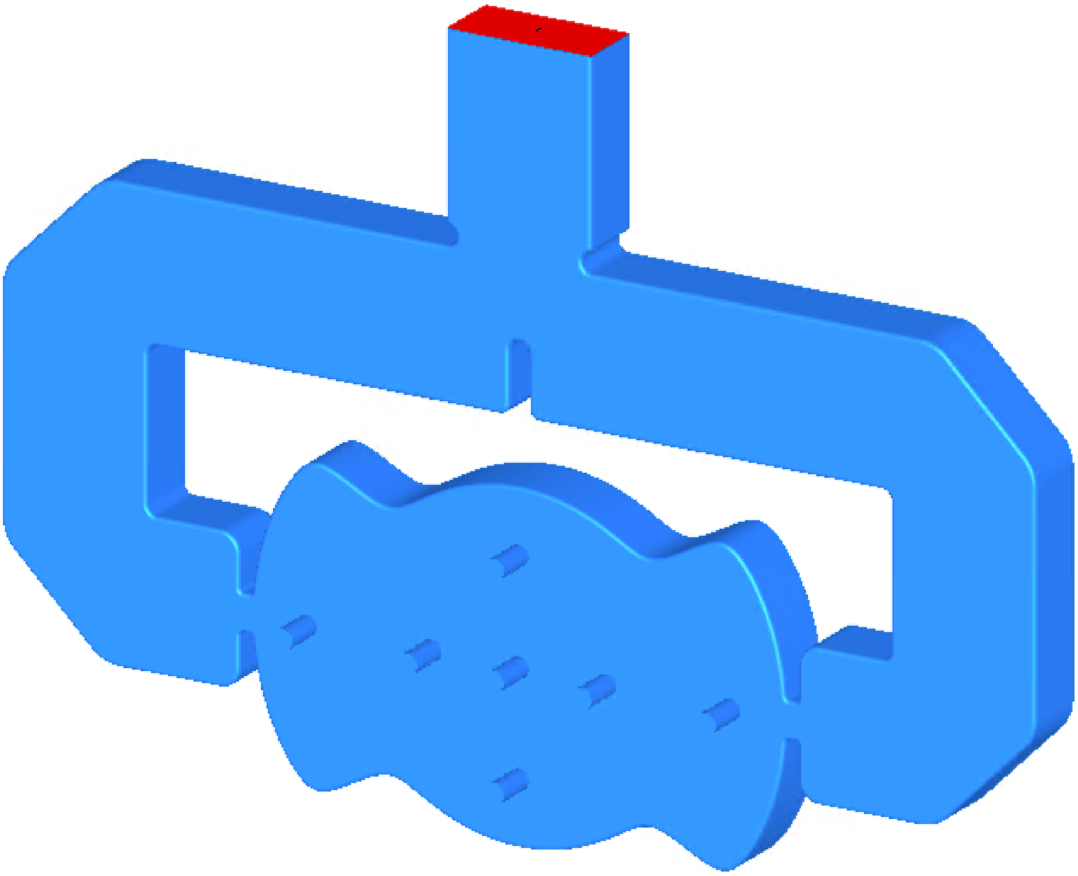

Figure 4.5: 3D design of an RF structure incorporating an RF port, WR284 waveguides, dual-port couplers and the azimuthally modulated RF cavity that supports a 3 GHz $\mathrm{TM}_{\{0,2\}20}$ mode with $\tilde{g}_2/\tilde{g}_0 = 5$.

lines for RF with a wavelength of 3 GHz [93].

Apertures with a radius of 5 mm and longitudinal length of 21.082 mm were also incorporated at the locations of the poles to allow for bead pull measurements. The inclusion of apertures means the azimuthally modulated cavity is no longer closed with flat end-caps and this affects the longitudinal electric field, as discussed in Sec. 2.5.2. The aim of this experiment, however, is to determine the multipolar content of the mode on a global scale and this is achieved by taking measurements at distances much greater than the diameter than the apertures. Subsequent bead pull experiments that probe the field on the local scale within the beam pipe would be valuable, however, this is outside the scope of this thesis.

Dual-slot couplers were incorporated at the locations where the cavity walls intersect the x-axis. The slot widths were optimised such that at least 90% of the power at resonant frequency ($RL < -20$ dB) was coupled from the RF port into the cavity. This optimisation was undertaken assuming the structure was machined out of copper and operated in vacuum, as would be typical for a cavity used in a particle accelerator.

Dual-slot couplers were chosen over a single-slot coupler because the latter would introduce a dipole component which would significantly affect the multipolar content of the $\mathrm{TM}_{\{0,2\}20}$ mode we want to measure [72, 73]. Dual-slot couplers do, however, enhance the quadrupole component and introduce higher-order, even multipoles into the mode. This must be compensated for and so the multipole ratio $\tilde{g}_2/\tilde{g}_0$ used to calculate the closed azimuthally modulated cross-sections was varied until the corresponding structure modelled in CST supported the desired 3 GHz mode with $\tilde{g}_2/\tilde{g}_0 = 5$.

Table 4.1 shows the variation in the measured multipolar ratio $\tilde{g}_2^{\mathrm{m}}/\tilde{g}_0^{\mathrm{m}}$, resonant frequency, slot width, return loss and higher-order multipoles for structures designed with azimuthally modulated cross-sections of different $\tilde{g}_2/\tilde{g}_0$ values. The penultimate row shows that incorporating the dual-slots into the structure shown in Fig. 4.5 increased the quadrupolar component by 30%. It should be noted that the multipolar composition of the mode is determined by excluding the field in the apertures and by using a flat Helmholtz decomposition. This ignores any longitudinal dependence of the multipolar coefficients, as discussed in Appendix A.

Table 4.1 also shows the odd transverse multipoles in the field are negligible which is expected due to the 2-fold symmetry of the structure. The octupolar component, however, is non-zero (and so are higher-order even multipoles such as $\tilde{g}_6^m/\tilde{g}_0^m = 0.25$) and the effect of this non-zero octupole term is discussed in Sec. 4.5.4.

$\tilde{g}_2/\tilde{g}_0$	$\tilde{g}_2^{\mathrm{m}}/\tilde{g}_0^{\mathrm{m}}$	f_0 [GHz]	s_w [mm]	RL [dB]	$\tilde{g}_1^{\mathrm{m}}/\tilde{g}_0^{\mathrm{m}}$	$\tilde{g}_3^{\mathrm{m}}/\tilde{g}_0^{\mathrm{m}}$	$\tilde{g}_4^{\mathrm{m}}/\tilde{g}_0^{\mathrm{m}}$
3.8	4.64	3.00013	17.98	-44.68	0.00	0.00	-0.06
4	4.93	3.00009	17.74	-48.14	0.00	0.00	-0.06
4.2	5.24	2.99997	17.61	-55.64	0.00	0.00	-0.07
4.4	5.54	2.99989	17.47	-54.28	0.00	0.00	-0.07
4.6	5.86	2.99980	17.35	-64.65	0.00	0.00	-0.08
4.8	6.16	2.99975	17.22	-48.21	0.00	0.00	-0.08
5	6.51	2.99962	17.20	-40.59	0.00	0.00	-0.09
4.032	4.99	3.00000	17.82	-38.32	0.00	0.00	-0.06

Table 4.1: The measured multipolar components, resonant frequency and optimised slot width and return loss of the $\mathrm{TM}_{\{0,2\}20}$ mode of the RF structure in Fig. 4.5 for different values of $\tilde{g}_2/\tilde{g}_0$.

By performing a linear fit between $\tilde{g}_2/\tilde{g}_0$ and $\tilde{g}_2^{\mathrm{m}}/\tilde{g}_0^{\mathrm{m}}$, an azimuthally modulated cavity with a multipolar ratio of $\tilde{g}_2/\tilde{g}_0 = 4.032$ was predicted to give a final design with $\tilde{g}_2^{m}/\tilde{g}_0^{m} = 5$. The final row of Table 4.1 shows this prediction was sufficiently accurate and so this was settled on as the final design. A contour plot of the longitudinal electric field in the RF cavity and waveguides is shown in Figure 4.6.

4.4 Characterising the Prototype

Figure 4.7 shows the final design in CAD and the machined prototype. The prototype was made out of aluminium instead of copper to save costs and was machined to a tolerance of 10 µm. L-brackets were incorporated into the design to add stability and the structure was machined as two identical halves that could be sealed together using 36 M12 bolts. The latter decision was made because each half weighed under 20 kg, which allowed for easier manoeuvrability, and the structure could be assembled and disassembled relatively quickly.

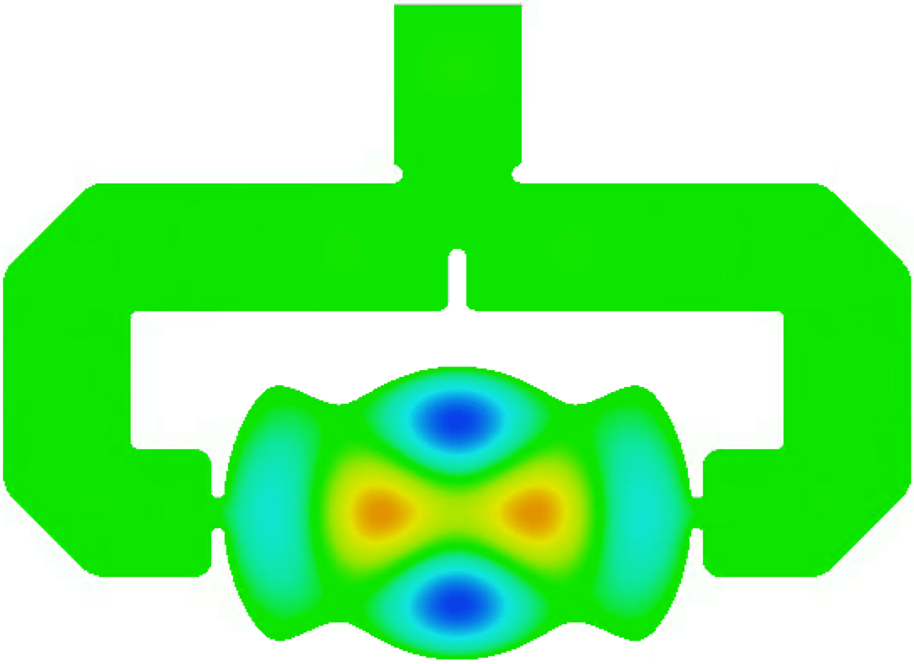

Figure 4.6: Contour plot of E_z at the longitudinal center of the final design. Blue is a minimum in the field, orange a maximum and green zero.

4.4.1 Simulation of the Prototype

To simulate the prototype accurately, several factors must be accounted for. First, the conductivity of the material that the RF structure is built from affects the impedance of the intrinsic Q-factor of the cavity. Simulations therefore need to be undertaken with the structure built out of aluminium. It should be noted that the optimal slot width for maximum power transfer is dependent upon Q_0 and so the prototype was undercoupled as the slot-widths were optimised for copper. Second, any surface roughness on the material increases resistive losses because the effective surface area of the cavity increases [94]. The RMS surface roughness of the milled structure was measured with a white light interferometer to be $0.33\,\mu\text{m}$. Third, any background material inside the RF cavity system changes the permittivity and permeability of the structure and thus the resonant frequency of the cavity, as per Slater's theorem in Eqn. 4.1. The prototype measurements were taken under normal atmospheric conditions, not vacuum.

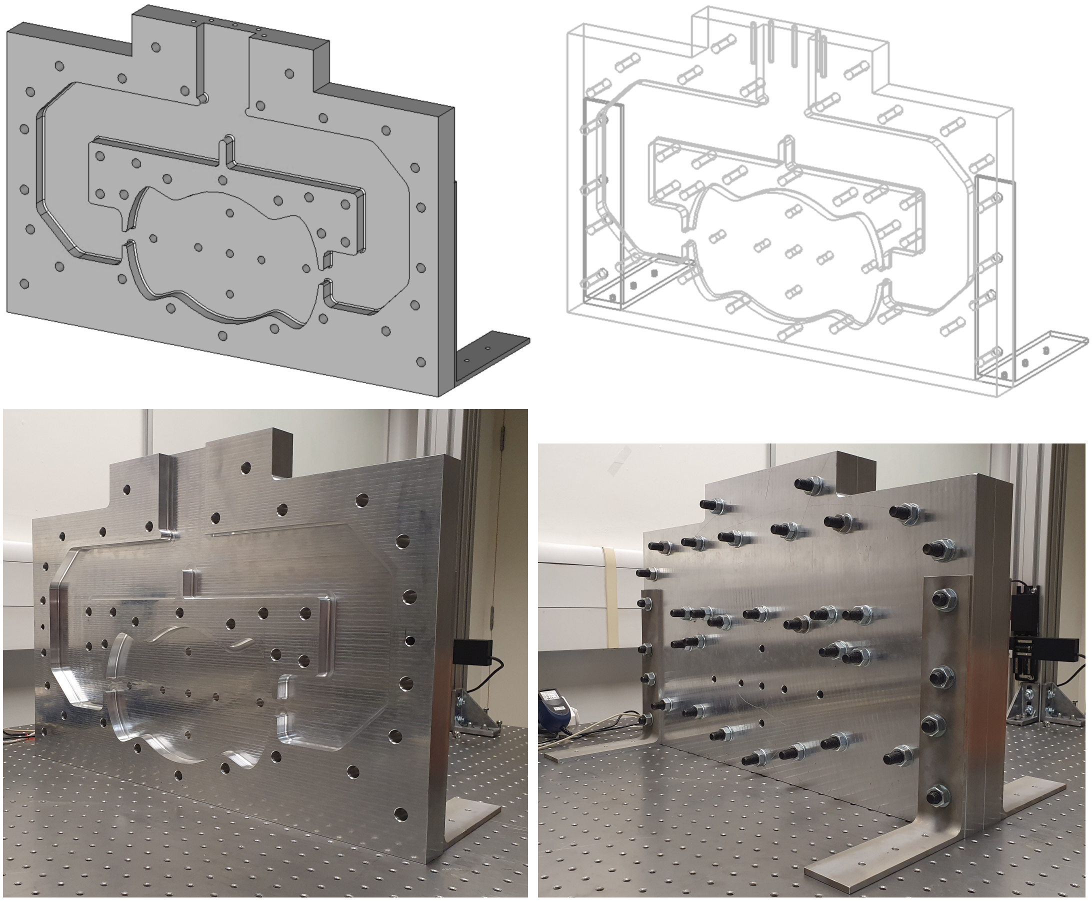

Figure 4.7: One half of the final design in a CAD material view (top-left), a CAD wireframe view (top-right), when machined (bottom-left) and when the two halves are sealed together (bottom-right).

Table 4.2 displays f_0, S_{11}, β, Q_0 and Q_e as calculated from simulations of the final design under different conditions. The results agree with expectations: the change of background has little effect on the Q-factors but shifts the resonant frequency. In contrast, changing the material leaves the resonant frequency unchanged whilst the intrinsic Q-factor drops significantly. Adding a RMS surface roughness of 0.33 µm also further decreases the intrinsic Q-factor.

The final row of Table 4.2 was assumed as the best representation of the machined prototype. Henceforth, any reference to ‘simulation data’ should be assumed to be taken from the simulation of the prototype in air and with a surface roughness of 0.33 µm.

Material	SR [µm]	Background	f_0 [GHz]	RL [dB]	β	Q_0	Q_e
Cu	0	Vacuum	3.00000	-38.32	1.025	20790	20290
Cu	0	Air	2.99911	-38.16	1.025	20690	20190
Al	0	Vacuum	2.99998	-20.13	0.821	16630	20260
Al	0	Air	2.99910	-20.16	0.821	16690	20320
Al	0.33	Air	2.99901	-16.87	0.749	15150	20220

Table 4.2: The variation in resonant frequency, return loss, the coupling constant and Q-factors for simulations of the final design made of different materials, placed in different backgrounds and with a 0.33 µm surface roughness added.

4.4.2 Experimental Setup and Calibration

A Vector Network Analyser (VNA) was used to measure the S-parameters of the prototype. The port of the VNA was connected to coaxial cable (coax) that was in turn connected to an N-type to WR284 adaptor via an N-type to SMA adaptor. The N-type to WR284 adaptor was secured to the top of the prototype using 12 1/4" bolts.

The simulations undertaken in CST measured S-parameters from the top of the RF cavity system and so do not include any effects from the cables and adaptors that transfer the signal from the VNA to the prototype. In the ideal case, these experimental components are matched and lossless and so have no effect on the measurement of S_{11} except for a phase shift. In reality, however, the components are neither perfectly matched nor lossless and their effects need to be accounted for via calibration.

Figure 4.8 shows the experimental setup used for calibration. Access was only available to an N-type calibration kit (cal kit) and so the calibrated electrical short, load and open could only shift the reference plane of the measurements to the start of the N-type to WR284 adaptor.

A calibration of the WR284 adaptor would be required to shift the reference plane of the measurements to the top of the prototype and match simulation. This requires a WR284 cal kit which consists of a waveguide short, a waveguide load and a waveguide open (which is a quarter wave spacer connected to a waveguide short).

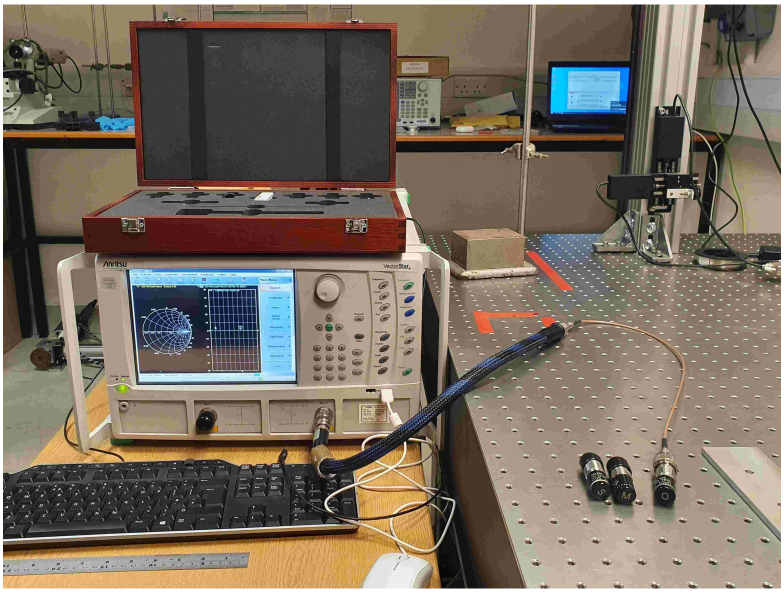

Figure 4.8: The setup for calibrating the coax and SMA to N-type adaptor using an N-type cal kit.

The effect of the uncalibrated N-type to WR284 adaptor on measurements could, however, be investigated by clamping an aluminium plate flush to it and replicating a waveguide short. Figure 4.9 shows the measured impedance and S_{11} when an electrical short is connected to the calibrated coax, and when the WR284 adaptor is connected to the calibrated coax and shorted by clamping an aluminium plate to it. The maximum magnitude of the difference between the two impedance measurements is 0.2 Ω. This discrepancy in Z is of the order of 100 times smaller than both the frequency sweep measurements used for calculating Q-factors and the time sweep bead pull measurements of impedance used to calculate the electric field, as later discussed in Sec. 4.4.3 and Sec. 4.5.3. The calculated Q_e is also similar between simulations and experimental measurements with the adaptor, as discussed in Sec. 4.4.3. The manufacturer of the adaptor also 'guarantees' it to have a VSWR better than 1.15, which corresponds to it reflecting less than 0.5% of incident power [95].

It is difficult to state with certainty, however, the exact effect of the adaptor on characterisation measurements. It should therefore be noted that the subsequent

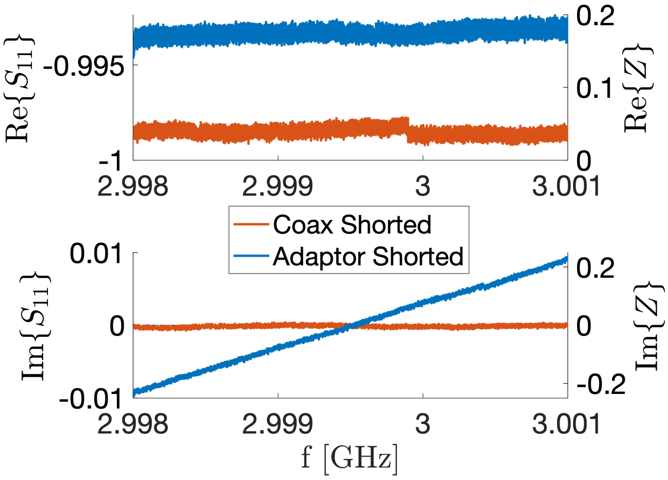

Figure 4.9: Plots showing the impedance and S_{11} measurements, as functions of driving frequency, taken when the calibrated coax was shorted and when the waveguide adaptor was attached to the calibrated coax and shorted by clamping an aluminum plate to it.

characterisation measurements of the prototype were taken from a reference plane at the N-type end of the WR284 adaptor, and not at the top of the prototype. Additionally, the assembly of the structure has a significant effect on the characterisation of the prototype and is also discussed later in Sec. 4.4.3.

4.4.3 Experimental Measurements

Figure 4.10 shows the experimental setup used to obtain frequency sweep data of the prototype. Frequency sweeps composed of 5001 S_{11} measurements between 2.998 and 3.001 GHz were taken to compare the prototype to that of simulation by calculating the characterisation parameters f_0, β and Q_0.

Figure 4.11 visualises the frequency sweep data by plotting the absolute value of S_{11} obtained from experiment and from simulation against the driving frequency. As per the discussion in Sec. 4.1.4, f_0 corresponds to the minimum value of $|S_{11}|$ and is easily measured. The coupling constant β is subsequently calculated using Eqn. 4.13 and Q_0 is calculated by minimising the error in a fit about the range $f_0 \pm 0.05$ MHz of the absolute value of Eqn. 4.12 to the measured $|S_{11}|$ data. The calculated values are

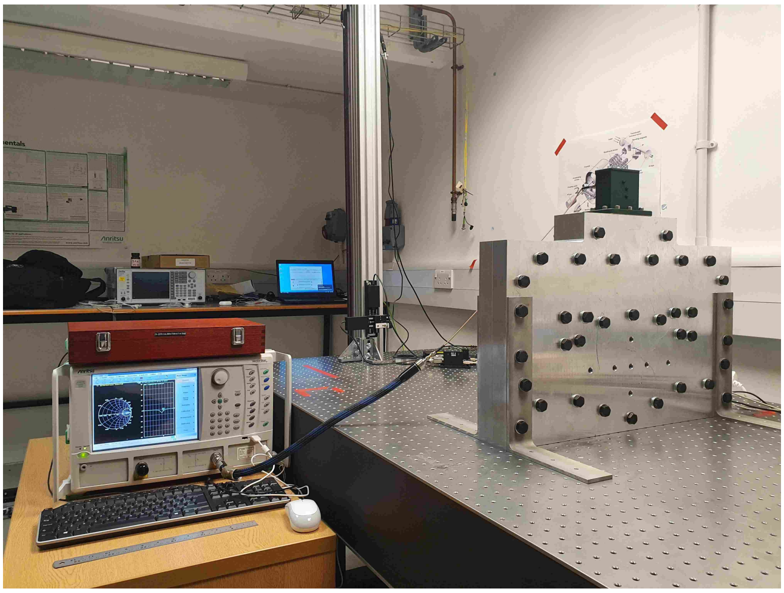

Figure 4.10: The experimental setup for taking a frequency sweep of the prototype.

displayed in Table 4.3 and the dashed lines in Fig. 4.11 model the data by plotting the absolute value of Eqn. 4.12 using these calculated values. The model fits the data well around the resonance but diverges at greater frequencies. This is expected because the assumption in the model that Q_e and Q_0 are independent of driving frequency begins to breakdown.

Before comparing the characterisation of the cavity between simulation and experiment, we further analyse the frequency sweep data and determine the presence of any electrical delays. Electrical delays shift the phase of the measurement of S_{11} and, although they do not affect the calculation of f_0, β and Q_0, they must be accounted for in order to use Eqn. 4.21 and in turn the impedance bead pull measurement given by Eqn. 4.23. Electrical delays can be visualised using a Smith Chart which is a convenient method for visualising and interpreting frequency sweep data [96]. The Smith Chart uses the transformation given in Eqn. 4.12 to transform the complex impedance plane onto the complex S_{11} plane, with lines of constant resistance and constant reactance in the impedance plane mapped to circles in the S_{11} plane.

The experimental and frequency sweep data is plotted on a Smith Chart in

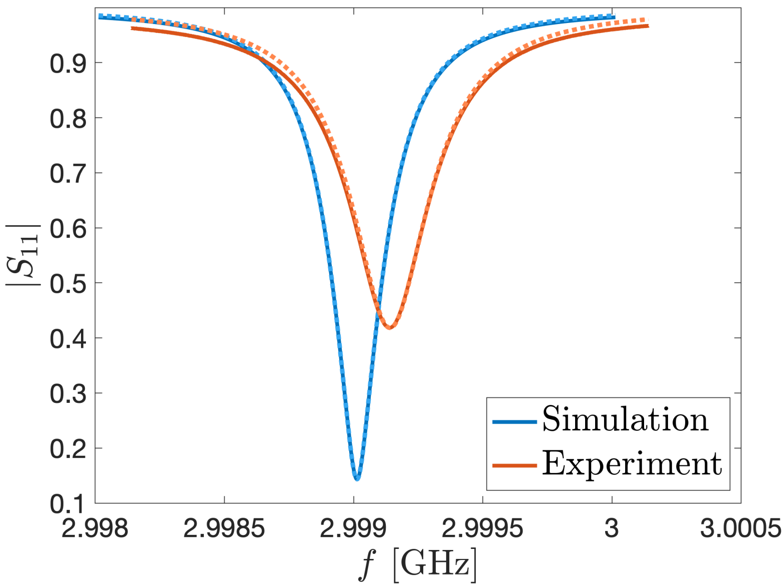

Figure 4.11: Plot of the absolute value of S_{11} against driving frequency in the range $f_0 \pm 1$ MHz. Data obtained from simulation and experiment is compared and the dashed lines model the data using Eqn. 4.12.

Fig. 4.12. We see that there is an approximately π (it is sheer coincidence it is so close to π) phase difference between the frequency sweep data and that obtained by modelling with Eqn. 4.12. This phase difference needs to be exactly π to use Eqn. 4.21, and so the S_{11} data was multiplied by a phase term $e^{i\psi}$ which was varied until the data lines up with a circle of constant reactance on the Smith Chart. The phase was calculated as $\psi = -0.32\ ^\circ$ for the experimental data and the phase term is included in the subsequent bead pull measurements discussed in Sec. 4.5.

Table 4.3 compares the characterisation of the cavity between simulation and experiment. It shows that the resonant frequency of the prototype is in good agreement with simulation and within error when the temperature dependence of the permittivity of air, the thermal expansion of aluminium and mesh errors from simulation are accounted for. The structure, however, is significantly undercoupled ($\beta = 0.410$) compared to simulations ($\beta = 0.749$).

One of the potential causes of this discrepancy in the measurement of the coupling constant is RF leakage through an *air gap* which results from the imperfect seal

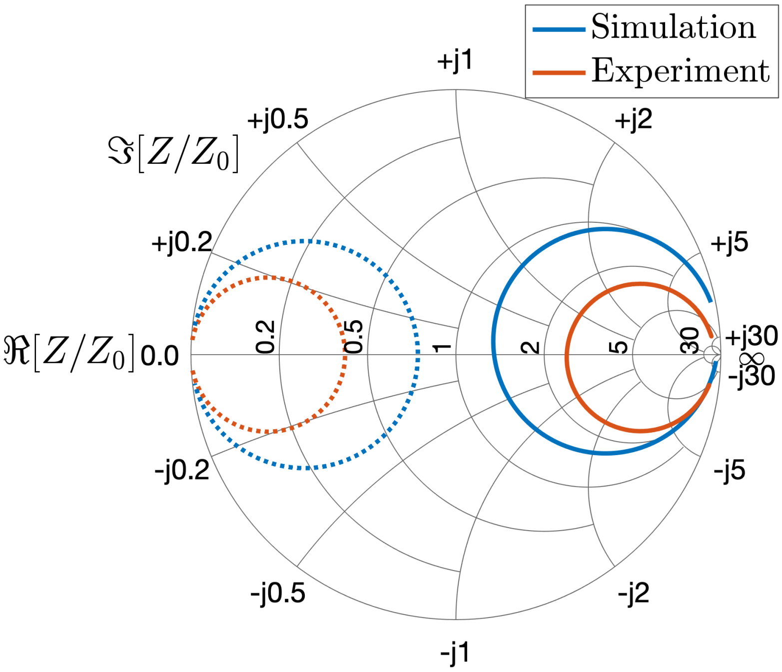

Figure 4.12: Frequency sweep data of the prototype from simulation and experiment plotted in the range $f_0 \pm 1$ MHz on a Smith Chart. The dashed lines model the frequency sweeps using Eqn. 4.12.

Setup	f$_0$ [GHz]	RL [dB]	β	Q_0	Q_e	Q_0/Q_0^{sim}
Simulation	2.99901	-16.87	0.749	15150	20220	—
Experimental	2.99914	-7.57	0.410	9120	22230	0.60
Experimental with In wire	2.99969	-8.54	0.456	9830	21570	0.65

Table 4.3: The variation in the measured resonant frequency, return loss, coupling constant and the Q-factors when frequency sweeps of the unperturbed prototype are taken with and without an indium wire seal. The final column compares the measured intrinsic Q-factor to that of simulation.

between the two halves of the structure. Such an air gap will be highly non-uniform across the structure and its effect is difficult to quantify and simulate. Under the assumption of a uniform air gap, however, simulations showed that uniformly displacing the two halves from each other by 3.5 µm is sufficient to explain the coupling constant discrepancy.

To try and investigate the significance of the air gap on the experimental characterisation of the prototype, indium wire with a 1 mm diameter was placed around one half of the milled structure, as shown in Fig. 4.13. Indium wire is very malleable so can be used to fill any gaps between the two halves as they are compressed together. Table 4.3, however, shows the indium wire only marginally improved the coupling by 10%. Naively, one may conclude this measurement implies that any air gap between the two halves in the absence of the indium wire is insufficient to explain the discrepancy between simulation and experiment. It should be noted, however, that the air gap likely has a more significant effect than the indium wire measurement suggests because, not only is the effect of a non-uniform gap very difficult to quantify, but the quality of the seal cannot be measured. On this latter point, there will be points at which the compressed indium wire encroaches into the cavity and points at which it does not fill the gap.

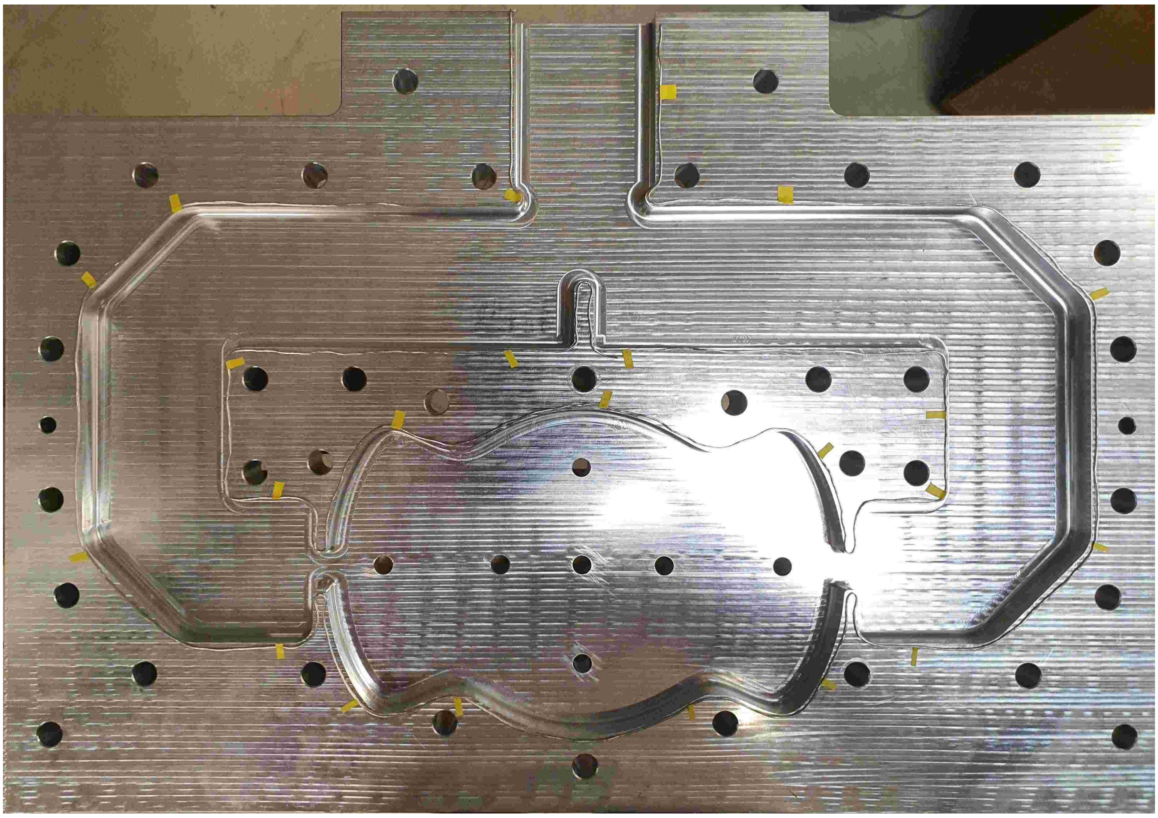

Figure 4.13: 1 mm diameter indium wire placed around the edges of the milled structure. Note that the yellow tape was used to help hold the indium wire in place initially. It was removed before the two halves were sealed together.

There are also additional mechanisms that could contribute to the discrepancy. For example, errors in the manufactured slot-width would change the coupling. The prototype was machined to a 10 µm tolerance, however, and simulations showed that the coupling constant was very stable with respect to slot width changes up to 100 µm. Additionally, only a small sample of the prototype was measured to determine an RMS surface roughness. There could be large cracks or regions of larger surface roughness generated by the milling process that are unaccounted for and cause additional losses. Furthermore, an aluminium oxide layer on the cavity surface would prevent a good electrical contact between the prototype halves, reducing the conductivity and lowering Q_0. Finally, the N-type to waveguide adaptor is not calibrated and it may cause additional losses.

Although the prototype is significantly undercoupled with $\beta = 0.410$, the mismatch does not affect the multipolar composition of the $\mathrm{TM}_{\{0,2\}20}$ mode that the prototype is designed to support. We now discuss the bead pull measurements taken of the prototype's electric field and compare the results to simulation.

4.5 Bead Pull Measurements

4.5.1 Experimental Setup

Figure 4.14 shows two views of the experimental setup for taking bead pull measurements on-axis. Spherical, Toho seed beads (typically used in jewellery, these are made out of soda-lime glass which has a relative permittivity of 7.2 at 25 °C [97]) with diameters of 1.5 mm (coloured cyan), 2.2 mm (blue) and 3 mm (red) were used as the perturbing objects. As per Eqn. 4.5, beads of greater volume cause greater changes in resonant frequency and so different sized beads were used to investigate and maximise the dynamic range of the measurements.

One bead of each size was knotted onto a thread of mono-filament wire (typically

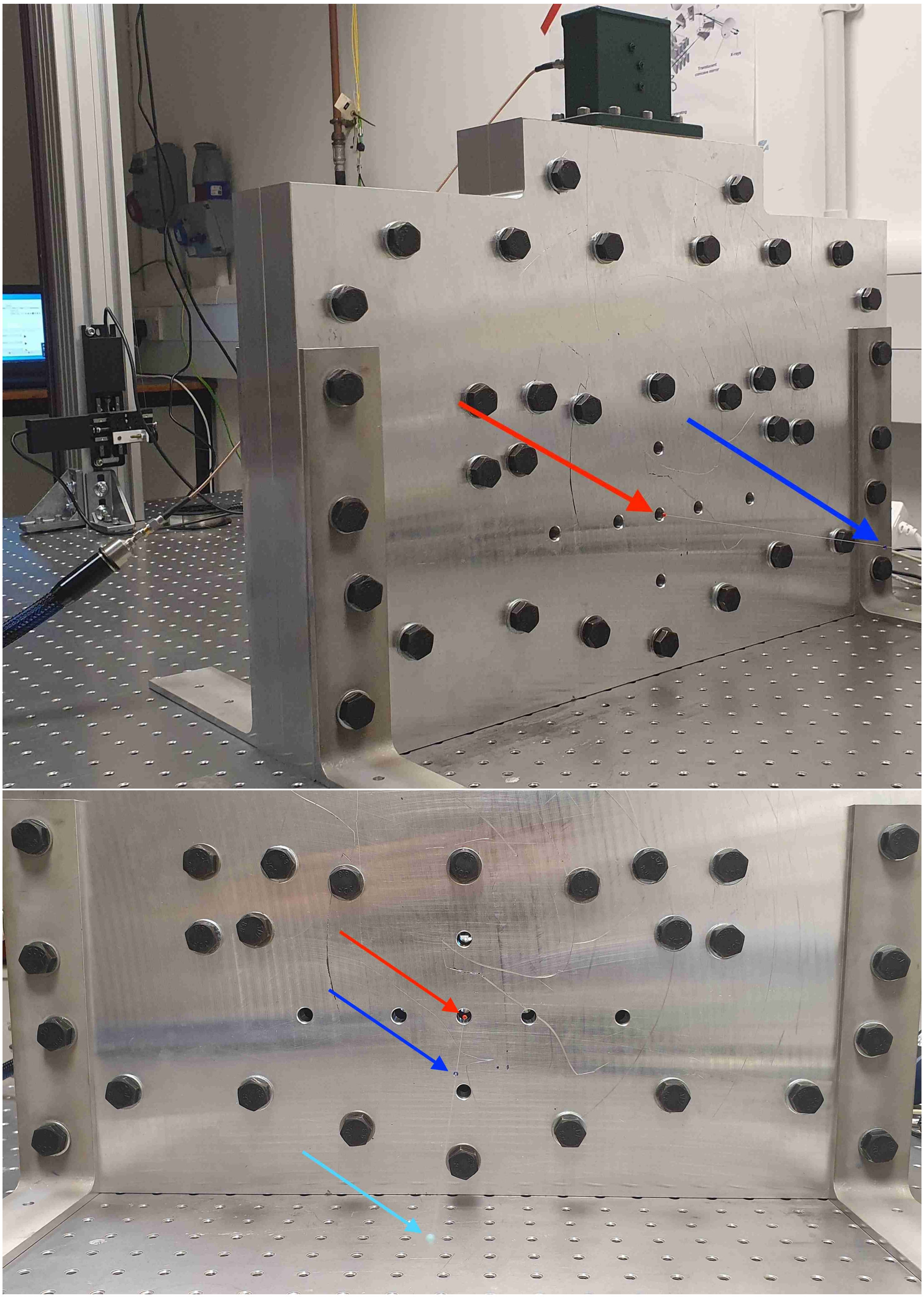

Figure 4.14: An isometric (top) and head-on (bottom) view of the experimental setup for taking on-axis bead pull measurements. Arrows point to the different beads used.

used for fishing, this is made out of nylon which has a relativity permittivity between 3.2 and 5 depending upon the exact composition and temperature [98]). The beads were separated by a distance greater than the longitudinal length of the prototype such that independent measurements could be taken with each bead acting as the perturbing object while using the same thread.

The thread was passed through opposite apertures and through two compact motorised translation stages positioned either side of the prototype. These were used to position the thread transversely. One end of the thread was attached to a weight to provide tension and minimise any drooping of the wire. The other end was attached to a linear servo motor that was used to pull the beads through the prototype at a constant speed.

Before taking a measurement with a given bead, the bead was aligned by eye using the transverse motors so that it passed through the centre of both apertures. The apertures were all centred where the transverse derivatives of the electric field is zero. This minimises errors from misalignment and also from the drooping of the thread and bead as it passes through the cavity. The significance of these errors was investigated by taking measurements with the 2.2 mm diameter bead deliberately misaligned the bead across the apertures. The maximum error when the bead was maximally misaligned within the aperture was found to be approximately 10% for the on-axis saddle measurement, 2% for the y pole measurements and 1% for both inner-x and outer-x pole measurements.

To take a bead pull measurement, the servo motors were used to pull the beads through the prototype at a constant rate. Simultaneously, a time sweep of the change in S_{11} was measured at the driving frequency equal to the unperturbed resonant frequency.

4.5.2 Calculating the Electric Field

We showed in Sec. 4.1.5 that both the change in the phase of S_{11} and the absolute value of ΔZ are linearly proportional to the change in resonant frequency of the prototype, but only within a certain range. In particular, both require that $\Delta\omega \ll \omega_0$ whilst the phase of S_{11} also requires $Q_0^2\xi^2 \ll |(1-\beta)(1+\beta)|$.

Figure 4.15 compares frequency sweep data of the unperturbed prototype when plotted as $\tan(\arg(S_{11}))$ and $|\Delta Z|$. The dashed lines are linear fits between the respective parameter and f, fitted to and extrapolated from small Δf. The 2.2 mm diameter perturbing bead caused a maximum change in resonant frequency of $|\Delta f| = 0.079$ MHz and both insets zoom in on this region. The insets show that $\tan(\arg(S_{11}))$ deviates from linear by up to 20% whereas $|\Delta Z|$ varies linearly with driving frequency to within 0.3%. As the red bead has a larger volume, it causes a greater change in resonant frequency and so this deviation is greater. The opposite is true for the smaller cyan bead.

The electric field at a location $\vec{r_p}$ was therefore determined by measuring the change in impedance caused by the bead at that position and using

$$|E_0(\vec{r_p})| \propto \sqrt{\Delta Z}. \tag{4.25}$$

4.5.3 Processing the Data

For the time sweep measurements, the VNA was set to output an RF signal at the unperturbed resonant frequency of $f = 2.99914$ GHz and to measure S_{11} at a sample rate of 150 points per second. The servo motor was set to pull the bead through at a speed of 3 mm/s.

Figure 4.16 is an example of the raw data measured when the 1.5 mm cyan bead is pulled along one of the y poles. For approximately the first 2000 records, there is no change in the measured data because the bead has not yet been pulled into

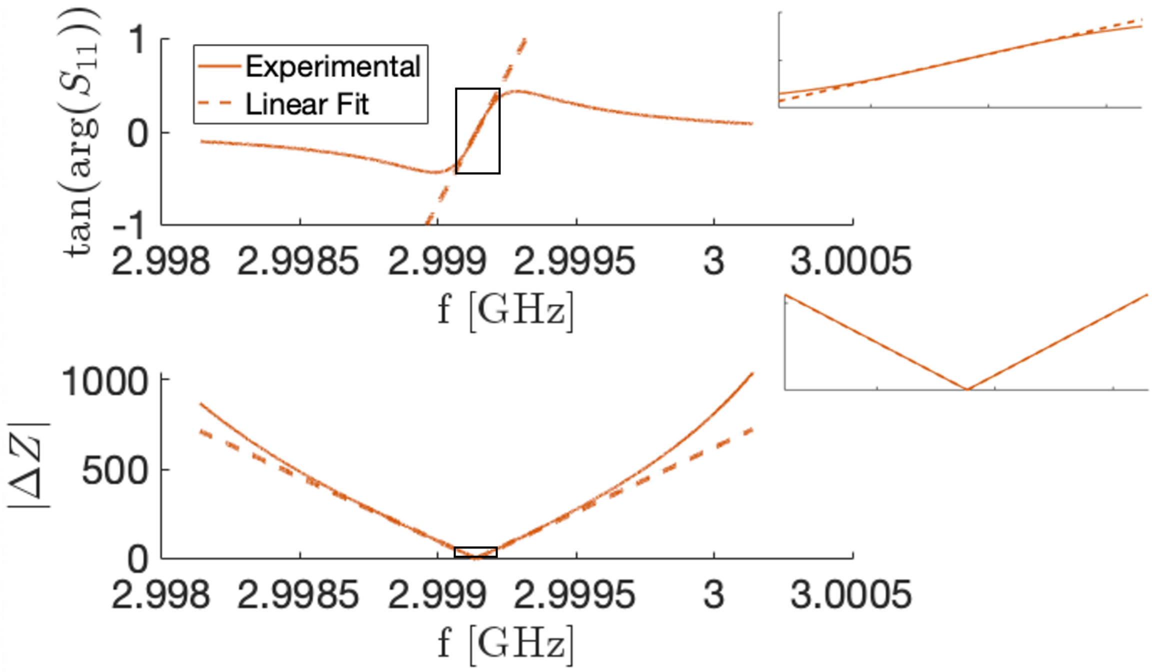

Figure 4.15: Plots showing the measured variation in $\tan(\arg(S_{11}))$ (top) and $|\Delta Z|$ (bottom) as a function of the driving frequency. The insets zoom in on the regions outlined by the black rectangles.

the cavity. At around record 2100 the measurement rises rapidly, corresponding to the bead entering the cavity and perturbing the mode. At around record 3900 the measurement falls rapidly, corresponding to the bead exiting the cavity.

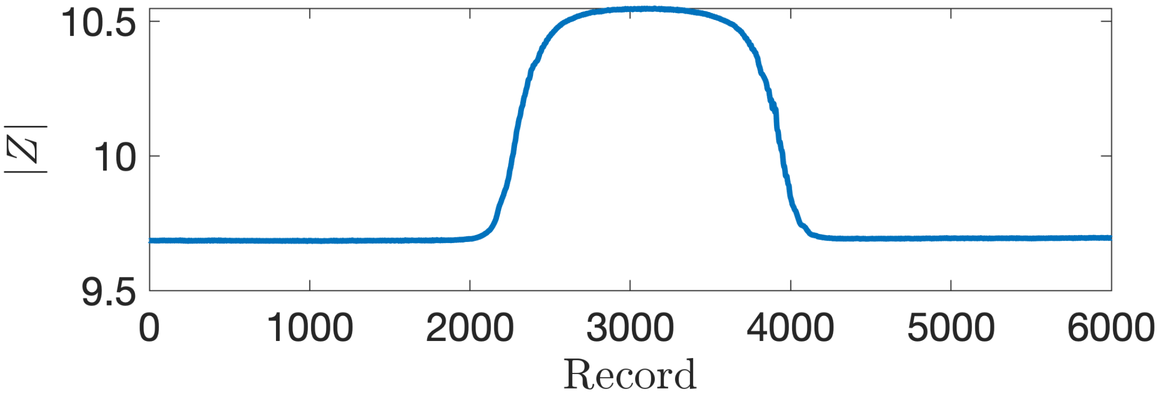

Figure 4.16: Plot of the raw $|Z|$ data, against record number, measured from a time sweep of the cyan bead pulled along one of the y poles.

The record number N can be converted to a longitudinal position relative to the centre of the prototype by using the known sample rate (150 s^{-1}) and motor speed

(3 mm/s) as $z = (N - N_c) \times 3/150$ mm, where N_c is the record number corresponding to the centre of the peak in Fig. 4.16. Any data recorded when the bead is outside the prototype, $|z| > 38.1$ mm, can be ignored.

The blue trace on Fig. 4.17 shows this time sweep in a Smith Chart with the measurements outside the prototype ignored. The bead pull Eqn. 4.25 states, however, that it is the change in impedance relative to a baseline measurement that is proportional to the electric field. One option is to use the first impedance measurement at $z = -38.1$ mm as the baseline and the corresponding change in impedance is plotted in red in Fig. 4.18. We see that there is a drift between the first and last measurements as the bead traverses the prototype. Potential sources of this drift include an asymmetry in the drooping of the thread resulting from different sized beads knotted at each end and any changes in temperature over the time scale of the measurement.

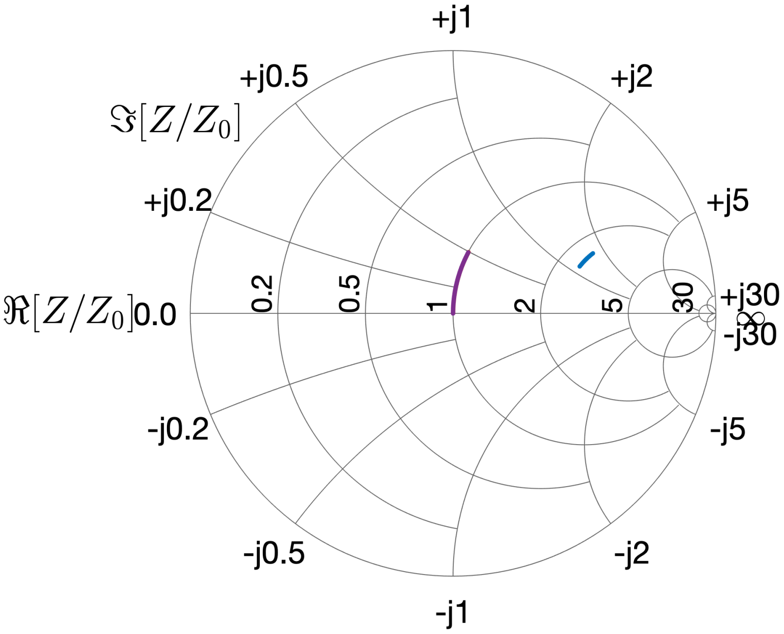

Figure 4.17: The raw Z data (blue) and the ΔZ data with a line of best fit used as the baseline (purple) measured from a time sweep of the cyan bead pulled along one of the y poles.

This drift was removed by assuming it is linear and calculating the line of best fit between the first and last 50 measurement points in the time sweep (corresponding to the bead being in the first and last 1 mm of the prototype). Lines of best fit were made to both the real and imaginary components independently. The corresponding change in impedance that results from using this complex line of best fit as the baseline is plotted in purple in Figs. 4.17-4.18. We see this accounts for the drift.

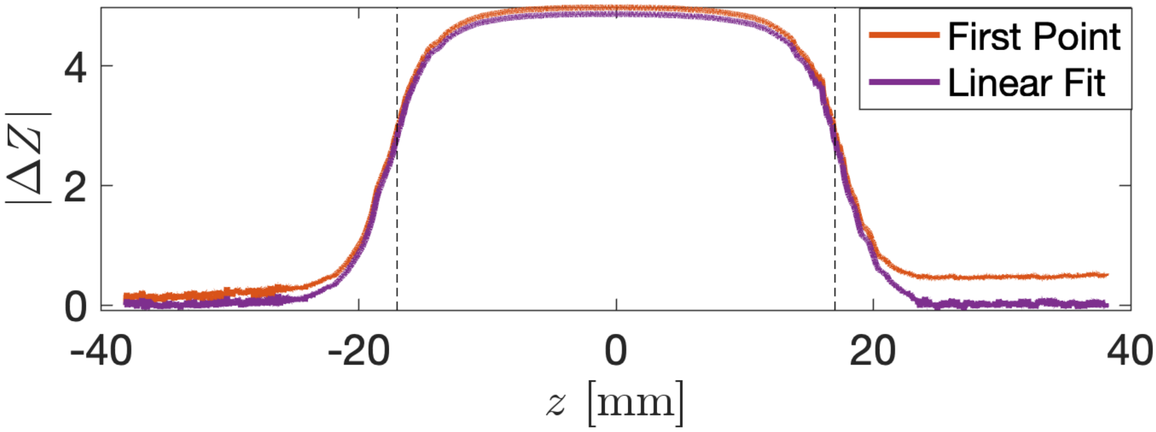

Figure 4.18: Plot of the absolute change in impedance against bead position, as measured from a time sweep of the cyan bead pulled along a y pole. The legend indicates the two different baselines used to calculate the change in impedance. The dashed lines indicate the longitudinal extent of the RF cavity, outside of these lines the bead is in the beam pipe of the prototype.

4.5.4 Results and Comparison to CST Simulation and Theory

Figure 4.19 compares the electric field between bead pull measurements using the 1.5 mm diameter cyan bead (dashed lines) to simulation (full lines). Here the simulation measurement was obtained by exporting the longitudinal electric field exactly along each of the poles.

The simulation data of the electric field on-axis (blue) and along the inner$-x$ (red), outer$-x$ (green) and y (black) poles is normalised by dividing by the maximum on-axis electric field. As expected, the electric field is the same across both inner$-x$ poles, across both outer$-x$ poles and across both y poles because the mode has 2-fold azimuthal rotational symmetry.

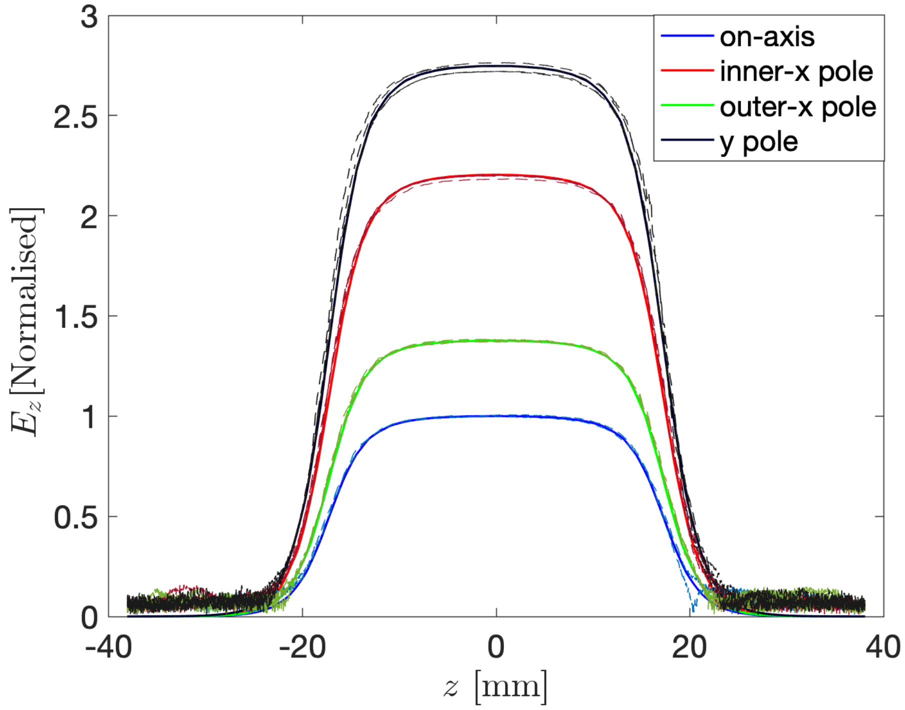

Figure 4.19: Plot of the electric field along each of the poles (normalised to the mean maximum field on-axis) against longitudinal position. The simulation measurements and the bead pull measurements using the 1.5 mm diameter bead are plotted as full and dashed lines respectively.

The experimental measurement of the longitudinal electric field is calculated using the process outlined in Sec. 4.5.3 and assuming that $E_0 = E_z$. It is plotted with dashed lines for the cyan bead travelling in both longitudinal directions along each pole. All measurements are normalised by the mean measurement of the on-axis field along both directions and in the central 6 mm of the cavity.

The data in Fig. 4.19 shows good agreement between simulation and experiment. There is consistency between experimental measurements of the bead travelling in opposite directions and also of measurements between duplicate poles. This indicates that the prototype supports a mode with the expected symmetry in the horizontal, vertical and longitudinal directions.

The agreement is quantitatively shown in Table 4.4 which compares the mean measurement of the data in the central 6 mm of the RF cavity. The given error states the maximum deviations from the mean value also in the central 6 mm of the RF cavity. This range is taken to reflect the misalignment error resulting from the realignment of the thread for each bead pull measurement. The data shows that the experimental measurements made using the cyan bead are consistent with all simulation results within error. From this, we conclude that the bead pull technique verifies the multipole composition of the $\text{TM}_{\{0,2\}20}$ mode is $\tilde{g}_2/\tilde{g}_0 = 4.99$ as designed.

	Simulation	1.5 mm cyan	2.2 mm blue	3 mm red
on-axis	1.000	$1.000 \pm^{0.009}_{0.008}$	$1.000 \pm^{0.005}_{0.005}$	$1.000 \pm^{0.007}_{0.008}$
outer$-x$ pole	1.377	$1.377 \pm^{0.009}_{0.009}$	$1.373 \pm^{0.006}_{0.009}$	$1.368 \pm^{0.007}_{0.007}$
inner$-x$ pole	2.204	$2.195 \pm^{0.009}_{0.017}$	$2.185 \pm^{0.004}_{0.005}$	$2.171 \pm^{0.004}_{0.004}$
y pole	2.747	$2.736 \pm^{0.028}_{0.023}$	$2.725 \pm^{0.030}_{0.026}$	$2.707 \pm^{0.037}_{0.037}$

Table 4.4: Comparison of the mean electric field in the central 6 mm of the RF cavity along each aperture when normalised to the mean of the on-axis field between simulation and bead pull measurements.

Table 4.1 also shows the experimental results are less consistent with simulation when the 2.2 mm diameter blue and 3 mm diameter red beads were used. In particular, all measurements are outside the stated error when the red bead was used. This is an expected consequence of the beads being bigger because, first, the assumption that the electric field is constant throughout their volume is weaker and, second, they cause a greater change in resonant frequency and the linearity discussed with regards to Fig. 4.15 breaks down.

The measured electric field along the poles can also be compared to that predicted using the AMM. To do so, Eqn. 4.24 is generalised to

$$\frac{E_z(r_i, \theta_i)}{E_z(0,0)} = J_0(kr_i) + \sum_{\{m\}} \frac{\tilde{g}_m}{\tilde{g}_0} J_m(kr_i) \cos(m\theta_i), \tag{4.26}$$

which gives the AMM expected electric field at each i pole. Table 4.5 compares the predicted field at each pole when successively higher-order multipoles are included in Eqn. 4.26. We see the higher-order terms have a notable effect on the predicted field and, in particular, the non-zero octupole and duodecupole term have significant effect on the outer$-x$ and y pole measurements because they are further away from the origin and the multipole terms vary as $J_m(kr)$.

	Simulation	$\tilde{g}_2/\tilde{g}_0 = 4.99$	$\tilde{g}_4/\tilde{g}_0 = -0.06$	$\tilde{g}_6/\tilde{g}_0 = -0.25$
on-axis	1.000	1	1	1
outer$-x$ pole	1.377	1.283	1.298	1.375
inner$-x$ pole	2.204	2.201	2.195	2.193
y pole	2.747	2.734	2.744	2.740

Table 4.5: Comparison of the electric field between simulation and that predicted using Eqn. 4.26 when successively higher multipole orders are included.

These octupole, duodecupole and other higher-order multipoles do not affect the conclusion of this chapter whereby the AMM has been used to successfully design and test a structure which supports a mode with the desired quadrupole to monopole ratio. However, it should be noted that, if so desired, these higher-order multipoles could be negated by additional use of the AMM. The method for doing is outlined, analysed and discussed in Chapter 5.

4.6 Chapter Summary

In this chapter, we detailed cavity perturbation theory and derived a bead pull equation. We outlined the bead pull technique which can be used to measure the electric field in RF cavities and we discussed the specification of a $\mathrm{TM}_{\{M\}\eta 0}$ mode that would be sensible to test with it. The 3 GHz $\mathrm{TM}_{\{0,2\}20}$ mode with $\tilde{g}_2/\tilde{g}_0 = 5$ was settled on as a sensible choice.

The azimuthally modulated cavity that supports this mode can be calculated using the AMM. Power couplers need to be incorporated into the design to use the bead pull technique to measure the electromagnetic mode but they affect the multipolar content of the mode. For example, we showed that dual-slot couplers increase the

$\tilde{g}_2/\tilde{g}_0$ ratio by 30% in the azimuthally modulated cavity designed to support the specified mode. By using the AMM, the multipoles introduced by the power coupler could be compensated for and we showed the final design of an azimuthally modulated structure with power couplers and apertures incorporated that supports a 3 GHz $\mathrm{TM}_{\{0,2\}20}$ with $\tilde{g}_2/\tilde{g}_0 = 4.99$.

From this design, a prototype was machined. When characterising the prototype, a discrepancy was found when comparing the measured intrinsic Q-factor and coupling factor to simulation results. Various experiments were undertaken to investigate the cause of the discrepancy but the cause could not be determined conclusively.

This discrepancy does not affect the composition of the mode, however. The experimental setup used to measure the electric field in the prototype was outlined alongside the method for processing the data. We showed that the experimental results of the electric field were in agreement with simulation, concluding that the bead pull technique can be used to verify the multipole composition of azimuthally modulated cavities.

Chapter 5

Multipole Compensation in RF Cavities

Incorporating power couplers into RF cavity designs and tuning RF cavities post-fabrication both introduce unwanted transverse multipoles into the desired mode. In this chapter, we discuss how the AMM outlined in Chapter 3 can be used to mitigate these unwanted multipoles.

We begin in Sec. 5.1, by detailing a systematic method for correcting the unwanted transverse multipoles introduced by N-slot power couplers. As a proof of principle, the process for negating the transverse multipoles in a 3 GHz TM_{010} accelerating mode with a single-slot coupler incorporated is demonstrated. In Sec. 5.2, the multipolar components generated using 1-way tuning pins are determined. Two different azimuthally modulated designs that can be used to anticipate and minimise the transverse multipolar components introduced by such tuning are then discussed and analysed.

5.1 Power Couplers

Power couplers that transfer electromagnetic energy from a power source into an RF cavity to drive the desired mode are an essential part of RF cavity design. Couplers, however, change the azimuthal profile of a cavity design and generate unwanted multipoles that can cause undesirable beam dynamics and beam loss. To mitigate the generation of such multipoles, RF cavities have been designed with symmetric couplers that minimise both unwanted components. For example, a compact X-band TM_{01} mode launcher with a fourfold symmetry has been designed in order to minimise the generation of any dipole and quadrupole components [99].

An alternative method for minimising these unwanted multipoles is to apply the AMM. Here, a systematic method is presented and applied for negating the unwanted multipoles introduced by incorporating N-slot power couplers into an RF cavity design.

5.1.1 Negating Transverse Multipoles from Slots

Consider an RF cavity design with an azimuthally modulated cross-section, which we denote as $r_0(\theta)$ specifically in the absence of any couplers, that has N-slot power couplers incorporated into it. The latter have widths s_w that are optimised for coupling power into the fundamental accelerating mode and the design has been scaled such that this mode resonates at the desired frequency f_0. The N-slots have introduced a set of unwanted transverse multipoles $\{\alpha\}$ of magnitudes $\tilde{g}_{\{\alpha\}}/\tilde{g}_0$ and orientations $\phi_{\{\alpha\}}$ into the mode.

As a first pass attempt for removing these unwanted multipoles, we solve for the azimuthally modulated cross-section $r_0^1(\theta)$ that supports a mode with the same transverse multipoles as those introduced by the N-slots but of opposite of sign. As per Eqn. 3.8, this can be calculated by solving the boundary condition on the longitudinal electric field

$$0 = \tilde{g}_0 J_0(kr_0^1(\theta)) - \sum_{\{\alpha\}} \tilde{g}_\alpha J_\alpha \left(kr_0^1(\theta)\right) \cos\left(\alpha\theta - \phi_\alpha\right). \tag{5.1}$$

This new cross-section is then incorporated into the design and the coupler widths are reoptimised to maximise power transfer.

Changing the slot widths, however, changes both the resonant frequency and multipolar content of the mode. To negate the unwanted transverse multipoles completely, an iterative process is followed whereby the i^{th} iteration is designed with a wavenumber

$$k^i = \frac{f_0}{f_0^i} k^{i-1}, \tag{5.2}$$

and a cross-section that solves

$$0 = \tilde{g}_0^i J_0(k^i r_0^i(\theta)) - \sum_{\{\beta\}} \tilde{g}_\beta^i J_\beta \left(k^i r_0^i(\theta)\right) \cos\left(\beta\theta - \phi_\beta\right), \tag{5.3}$$

where

$$\tilde{g}_\beta^i = \sum_{j=0}^{i} \tilde{g}_\alpha^j. \tag{5.4}$$

This process is repeatedly applied until the fundamental mode resonates at the desired frequency and the unwanted transverse multipoles are sufficiently small.

5.1.2 Coupler Compensation in a Pillbox Cavity

As an example, this iterative method is applied to design an RF cavity with a single-slot coupler that supports a 3 GHz TM_{010} mode with no transverse multipoles. The first step is to determine the radius of the pillbox that supports a 3 GHz TM_{010} mode using Eqn. 2.111 as

$$r_0 = \frac{c}{\omega} j_{01}. \tag{5.5}$$

Substituting in a resonant frequency of 3 GHz gives $r_0 = 38.25$ mm.

For the first iteration ($i = 0$), a pillbox cavity of this radius and length 34.036 mm was modelled in the 3D electromagnetic solver CST. This cavity was coupled to a rectangular WR284 waveguide of height 100 mm, length 34.036 mm and width 72.136 mm via a single slot of height 6 mm, length 34.036 mm and variable width s_w, as per the LHS of Fig. 5.1.

The slot width is defined as optimised when $RL < -20$ dB. To do this optimisation, an RF port was added to the end of the waveguide (visible in red on the LHS of Fig. 5.1) and this initial structure was found to be optimised for a slot width of $s_w = 14.44$ mm. With this width, the accelerating mode had a resonant frequency of $f_0 = 2.98829$ GHz and the power transfer was $RL = -38.25$ dB.

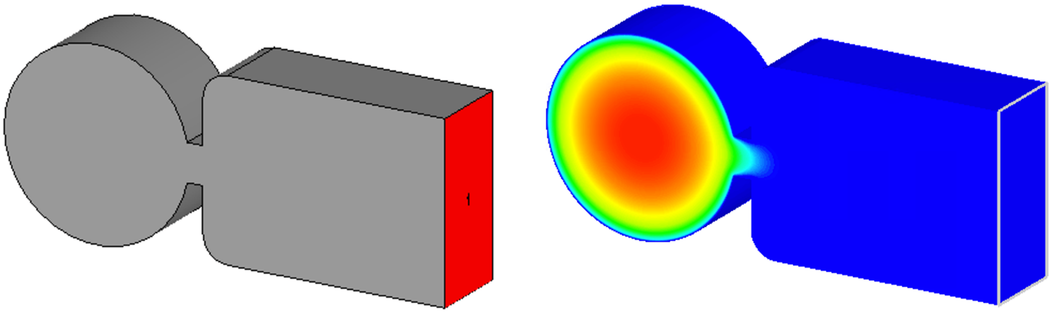

Figure 5.1: Schematic of a pillbox cavity coupled to an RF input port via a single-slot (left) and a contour log plot of the longitudinal electric field in its fundamental accelerating mode (right).

The fundamental accelerating mode of the optimised structure was then solved for and it is shown on the RHS of Fig. 5.1. The presence of transverse multipoles is evidenced by the field seeping into the waveguide through the single-slot. Undertaking a Helmholtz decomposition of the mode returned $\tilde{g}_1/\tilde{g}_0 = 0.0182$, $\tilde{g}_2/\tilde{g}_0 = 0.0217$, $\tilde{g}_3/\tilde{g}_0 = 0.0464$ and $\tilde{g}_4/\tilde{g}_0 = 0.139$, in addition to higher orders that are ignored. The iterative method was then applied to bring the resonant mode back to the desired frequency and to mitigate the unwanted transverse multipoles of all orders.

Table 5.1 presents the results of applying this iterative process. It shows that each iteration brought the resonant frequency closer to the desired frequency as well as reducing the transverse multipoles by approximately 10%. After 4 iterations, a design that has the desired resonant frequency and negated transverse multipoles was created, where negated is defined to be < 5e-5.

Iteration	f_0 [GHz]	$\tilde{g}_1/\tilde{g}_0$	$\tilde{g}_2/\tilde{g}_0$	$\tilde{g}_3/\tilde{g}_0$	$\tilde{g}_4/\tilde{g}_0$
i = 0	2.98829	0.0187	0.0227	0.0476	0.1422
i = 1	2.99879	0.0021	0.0021	0.0059	0.0210
i = 2	2.99982	0.0004	0.0004	0.0010	0.0039
i = 3	2.99992	<5e-5	0.0002	0.0001	0.0002
i = 4	3.00000	<5e-5	<5e-5	<5e-5	<5e-5
Pillbox	3.00000	0.0188	0.0224	0.0480	0.1423

Table 5.1: The resonant frequency and multipolar content of the fundamental accelerating mode in iterative pillbox cavity designs that systematically reduce the effects of incorporating a single-slot coupler.

Table 5.1 also shows the multipolar content of a pillbox cavity with a single-slot coupler incorporated which is scaled such that the fundamental accelerating mode resonates at a frequency of 3 GHz. The cross-sections of this pillbox and the $i = 4$ design are compared in Fig. 5.2. The differences in their cross-sections are on the order of hundreds of microns. A machining tolerance on the order of tens of microns or below will therefore generate machining errors that are significantly smaller than the difference in cross-section required to negate the transverse multipoles.

5.2 Tuning

There are many factors that contribute to an RF structure requiring tuning after fabrication such that it has the desired resonant frequency. Example factors include any imperfections arising due to the finite tolerances in the machining process, any physical deformations resulting from the assembly and installation, and any environmental conditions differing from those used in simulations. Tuning can be done in

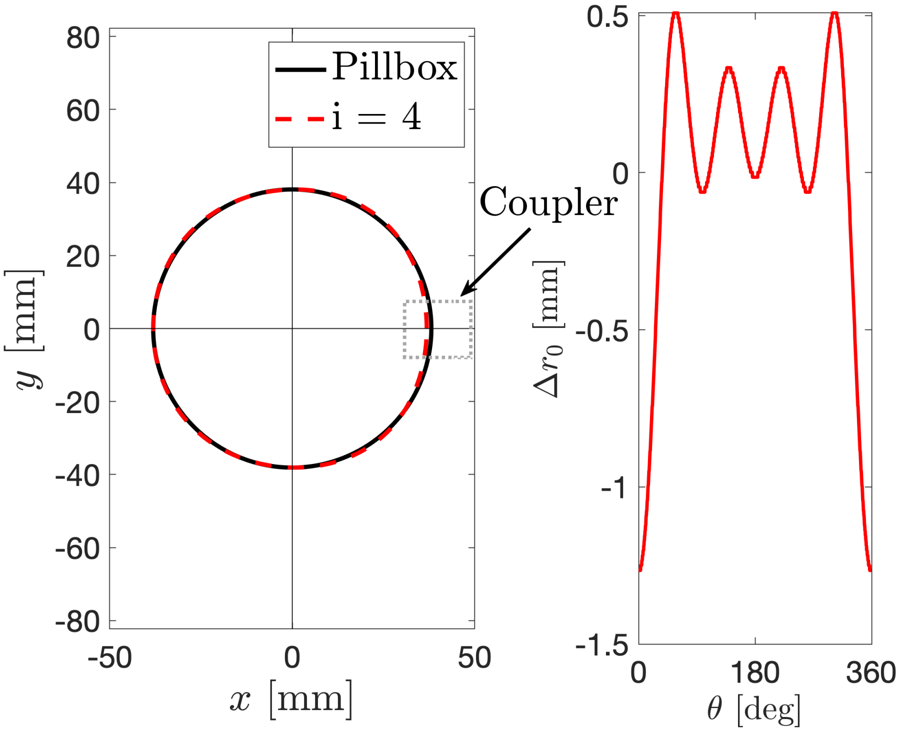

Figure 5.2: The pillbox and $i = 4$ designs in Table 5.1 plotted in Cartesian space with the location where the coupler attaches indicated (left). The difference in their cross-sections plotted as a function of angle (right).

many different ways [21, 100, 101]. Many modify the azimuthal profile of the cavity and this introduces unwanted transverse multipolar components.

Here, we investigate using the AMM to anticipate and mitigate the unwanted multipoles generated using 1-way tuning pins.

5.2.1 1-Way Tuning Pins

1-way tuning pins compensate for manufacturing errors by physically deforming the RF cavity. This reduces the volume in the outer, magnetic field region and thus increases the resonant frequency of the mode.

If the tolerance on the manufacturing process is $\pm\,\delta$ and the cavities are machined without accounting for this, 1-way tuning pins will only be able to tune the fabricated cavities that are machined too large. To overcome this, the design can be oversized by

δ. If we assume that the tolerance causes manufacturing errors that can be modelled as a truncated Gaussian distribution like that shown in Fig. 5.3, then the average fabricated cavity will be δ too large after manufacture. Such average cavities will require an average amount of deformation from the tuning pins to bring the mode to resonance.

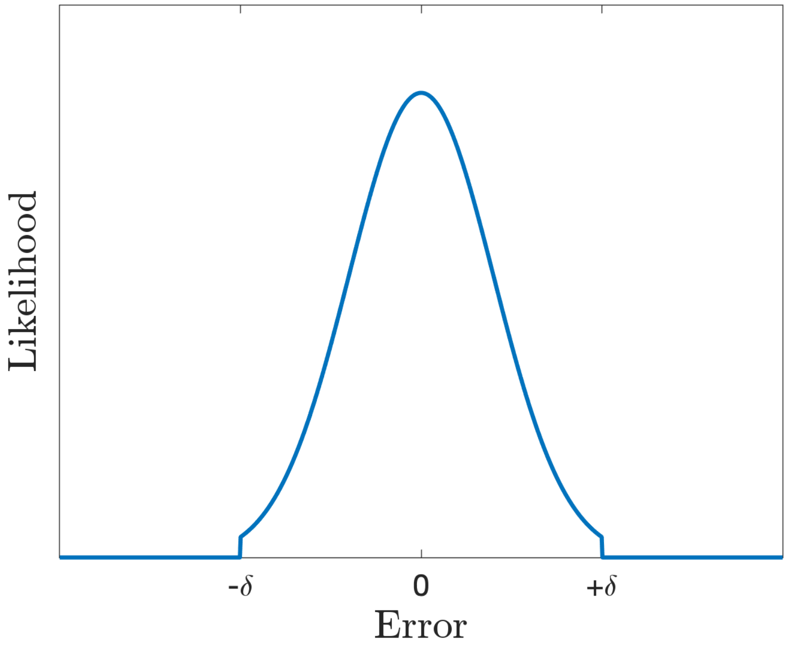

Figure 5.3: Plot of likelihood against machining error to give an example of the probability distribution of a machining error. The error is modelled by a truncated Gaussian with $\mu = 0$, $\sigma = 0.4\delta$ and truncated at $\pm\delta$.

Not all cavities will have this average error. At one extreme, the fabricated cavity will be 2δ too large and require a maximum deformation from the tuning pins. At the other extreme, the fabricated cavity will be manufactured such that the mode is on resonance and this will require no deformation from the tuning pins.

The deformations created by tuning pins introduce unwanted multipoles and so we can apply the AMM to minimise the multipoles created by the tuning pins in the average or extreme cases.

1-Way Tuning Pin Compensation

As an example, consider the fabrication of a single-slot cavity machined to a tolerance of ±50 µm. The transverse multipoles introduced when the fundamental accelerating mode is tuned to 3 GHz using two 1-way tuning pins are compared for three different designs:

- Pillbox — A pillbox cavity with a single-slot coupler that supports a 3 GHz fundamental accelerating mode. For fabrication, it is oversized by 50 µm.
- Extreme Azimuthal — An azimuthally modulated RF cavity with a single-slot coupler that supports a 3 GHz fundamental accelerating mode with negated transverse multipoles up to fourth order. For fabrication, it is oversized by 50 µm.
- Expected Azimuthal — An azimuthally modulated RF cavity with a single-slot coupler that supports a 3 GHz fundamental accelerating mode with negated transverse multipoles up to fourth order when oversized by 50 µm and tuned to resonance. For fabrication, it is oversized by 50 µm.

The transverse multipoles generated in each design were analysed for three different manufacturing errors:

- Zero — The fabrication process does not add any net machining error. The average fabricated structure is simply oversized by 50 µm and requires average insertion of the pins to bring it to resonance.
- Maximum Negative — The fabrication process negates the 50 µm oversizing. The fabricated structure requires minimum insertion of the tuning pins to bring it back to resonance.
- Maximum Positive — The fabrication process oversizes the cavity by a further

50 µm. The fabricated structure requires maximum insertion of the tuning pins to bring it back to resonance.

Simulations were undertaken to determine the transverse multipoles introduced by the tuning process for each design fabricated with the three different manufacturing errors. To model the tuning process, it was assumed that two 1-way tuning pins were pushed against the longitudinal centre of the RF cavity and at right angles to the single-slot. Although these pins are relatively small, they cause the cavity to cave in around the point where they are pressed. This deformation was modelled as a hemisphere of 5 mm that encroaches into the cavity by a distance equal to the depth of the tuning pin, as shown Fig. 5.4.

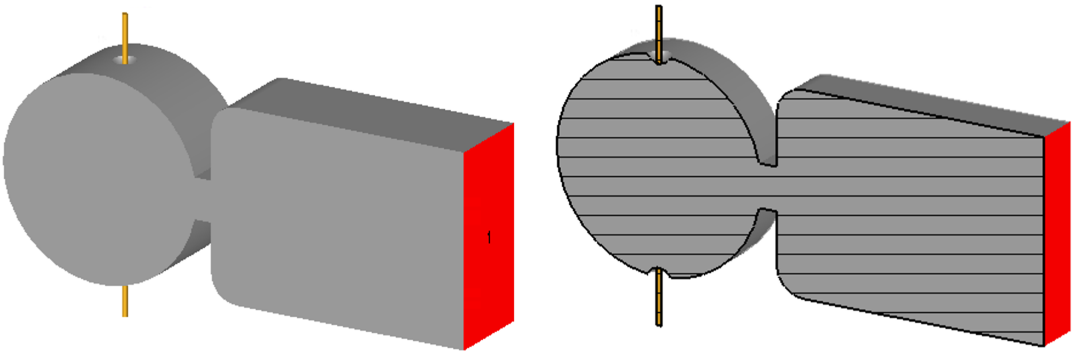

Figure 5.4: Schematics showing an isometric view (left) and longitudinal cutting plane view (right) of the deformation caused by two 1-way tuning pins incorporated perpendicularly to the single-slot being inserted into 3 mm into the cavity.

The distance of encroachment was varied until the mode was tuned to the desired frequency of 3 GHz. A flat Helmholtz decomposition was then undertaken to determine the transverse multipoles in the fundamental accelerating mode. It should be noted that the tuning pin deformation introduces a longitudinal asymmetry to the structure and mode. However, the flat Helmholtz decomposition is justified because the deformation is small and so has a small effect on the mode.

Table 5.2 shows the transverse multipoles generated by the tuning process for each of the three different designs under the three different manufacturing errors. As expected from the 2-fold rotational symmetry of the deformation, the tuning process only generates quadrupole and octupole components. We see that the quadrupole to monopole ratio consistently increases by approximately 0.007 across all three designs as the tuning pin depth is varied from minimal (the Maximum Negative case) to average (Zero) and to maximal (Maximum Positive). In contrast, the octupolar ratio decreases by approximately 0.050.

Design	Fabrication Error	$\tilde{g}_1/\tilde{g}_0$	$\tilde{g}_2/\tilde{g}_0$	$\tilde{g}_3/\tilde{g}_0$	$\tilde{g}_4/\tilde{g}_0$
Pillbox	Maximum Negative	0.019	0.023	0.048	0.142
	Zero	0.019	0.030	0.047	0.088
	Maximum Positive	0.019	0.037	0.048	0.036
Extreme Azimuthal	Maximum Negative	0.000	0.000	0.000	0.000
	Zero	0.000	0.007	0.000	-0.050
	Maximum Positive	0.000	0.015	0.000	-0.100
Expected Azimuthal	Maximum Negative	0.000	-0.007	-0.001	0.051
	Zero	0.000	0.000	0.000	0.000
	Maximum Positive	0.000	0.007	0.000	-0.049

Table 5.2: The multipolar magnitudes introduced by the tuning of the three different designs for three different fabrication errors.

Under the assumption of a truncated Gaussian distribution for the manufacturing error, the Expected Azimuthal design is the best choice for minimising the transverse multipoles. Not only does this design minimise the transverse multipoles for the average fabricated cavity, but it also minimises the maximum deviation of the transverse multipoles in the cases of extreme fabrication error.

This shows that the AMM can be used to anticipate average multipoles that may be introduced by a tuning process post fabrication and compensate for them as part of the design process.

5.3 Chapter Summary

In this chapter, an iterative method for negating the transverse multipoles introduced into the fundamental accelerating mode by N-slot couplers was presented. The method was applied to design an RF cavity with a single-slot coupler that supports a 3 GHz TM_{010} mode free of transverse multipoles and after 4 iterations the magnitudes of the dipole, quadrupole, sextupole and octupole components were all negligible. This shows that the AMM can be used to precisely control and fine-tune the multipolar content when power couplers are incorporated.

The effect of using 1-way tuning pins on the multipolar composition of the mode was also analysed. An azimuthally modulated cavity design that anticipated the average multipoles introduced by 1-way tuning pins was presented and simulations of the structure showed it minimised the unwanted multipoles caused by the deformation.

Chapter 6

Tailoring the Field Off-Axis

A particle beam may pass through components in a particle accelerator at different transverse positions. This may be an integral part of the acceleration mechanism that is accounted for in the design process (for example, higher energy beams in cyclotrons circulate at a larger radius) or may result from random errors (for example, errors in the alignment of components). In this chapter, we show how the AMM may be used to tailor a mode in anticipation of off-axis traversal.

The chapter begins in Sec. 6.1 with an analysis of how the multipolar content of a mode transforms as a TM_{m10} mode is traversed off-axis. This motivates Sec. 6.2 where the AMM is applied to designing azimuthally modulated cavities that support flat modes that contain a single multipolar term whose magnitude remains constant as the mode is traversed off-axis. As an example, the method is applied to design an optimally flat accelerating field under a spatial constraint for application in a cyclotron. Finally, the generalisation of the AMM for designing more bespoke off-axis fields is discussed briefly in Sec. 6.3.

6.1 Off-axis Traversal of TM_{m10} Modes

In Chapter 2, we showed that the electric field in the fundamental accelerating mode of a pillbox cavity is

$$E_z(r) = \tilde{g}_0 J_0(kr), \tag{6.1}$$

as per Eqn. 2.118. This mode accelerates (or decelerates) and focuses (or defocuses) an on-axis particle beam. We also analysed the $m_1 \neq 0$ $\mathrm{TM}_{m_1 10}$ modes and showed they manipulate on-axis beams in a fashion analogous to an m_1-pole magnet.

If a beam travels a TM_{m10} mode off-axis, the electrodynamics differ. For instance, consider without loss of generality a beam that traverses a TM_{m10} mode off-axis at the position $(x_b, 0)$, where $x_b < r_0$ and r_0 is the radius of the pillbox. Defining the translated coordinate system (r', θ') as the coordinate system with the beam centroid at the origin, then the circular cross-section of the pillbox cavity in the original coordinate system transforms to

$$r'_0(\theta) = x_b \cos(\theta) + \sqrt{r_0^2 - x_b^2 \sin^2(\theta)}. \tag{6.2}$$

An off-axis particle beam therefore sees the pillbox cross-section as azimuthally modulated. The multipolar composition of the mode is therefore different in the translated coordinate system and the beam experiences different electrodynamics.

To analyse the transformation, we define the electric field in the translated coordinate system as

$$E'_z(r', \theta') = \tilde{g}'_0 J_0(kr') + \sum_{m_1=1}^{\infty} \tilde{g}'_{m_1} J_m(kr') \cos(m\theta' - \phi'_{m_1}), \tag{6.3}$$

where $\tilde{g}'_m$ and ϕ'_m are the transformed multipolar magnitudes and orientations respectively. It should be noted that throughout this chapter the off-axis traversal is along the horizontal and we allow the transformed magnitudes $\tilde{g}'_m$ to be negative which simply corresponds to the orientation $\phi'_{m_1} = \pi$.

These transformed multipoles can be determined numerically for a given field. For example, consider a beam traversing a TM$_{010}$ mode off-axis. The transformed multipolar coefficients at a position $(x_b, 0)$ can be calculated by performing a Helmholtz decomposition of

$$E_z(r,\theta) = \tilde{g}_0 J_0\left(\sqrt{(R\cos(\theta) + x_b)^2 + y^2}\right), \tag{6.4}$$

where R is the radius of the circle along which the decomposition is performed. The multipoles are independent of the radius in all coordinate systems and so the choice of R simply depends on the numerical accuracy desired.

Figure 6.1 shows the values of $\tilde{g}'_m/\tilde{g}_0$ as a function of x_b/r_0 which is the ratio of the beam offset along the horizontal to the pillbox cavity radius. It shows that the beam experiences a decreasing acceleration the further it traverses the cavity off-axis, which is expected because the electric field varies as $\tilde{g}_0 J_0(kr)$. It also shows, however, the $\tilde{g}'_1/\tilde{g}_0$ grows up to $x_b/r_0 \simeq 0.75$ whilst other higher order multipoles continually grow.

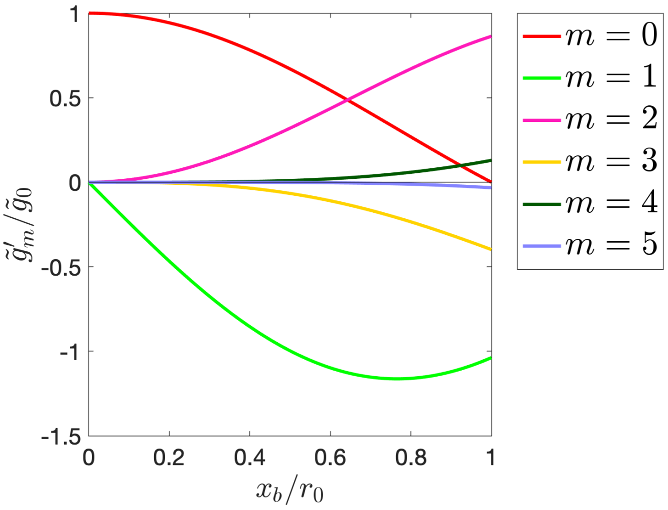

Figure 6.1: Plot showing the multipolar content at different offsets x_b in the TM$_{010}$ mode of a pillbox cavity of radius r_0.

A similar method can be used to determine the transformed multipolar components as $m_1 \neq 0$ TM$_{m_1 10}$ modes are traversed off-axis. For example, the LHS plot of Fig. 6.2 shows the transformed multipoles in the TM$_{110}$ modes as a function of x_b/r_0. We see that the dipole decreases with the offset, and thus particles experience a decreasing dipole kick, until approximately half-way through the cavity when the kick changes sign. Furthermore, Fig. 6.2 shows other multipole terms vary significantly with the offset. Similar observations but for a quadrupole instead of dipole are made for a beam traversing a TM$_{210}$ mode off-axis, as shown in the RHS plot of Fig. 6.2.

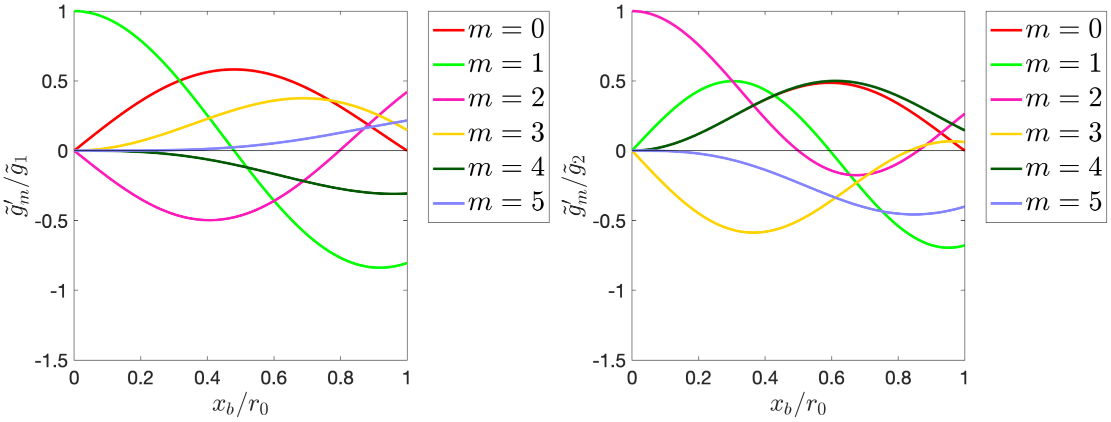

Figure 6.2: Plots showing the multipolar contents at different offsets x_b in the TM$_{110}$ mode (left) and TM$_{210}$ mode (right) of a pillbox cavity of radius r_0.

This analysis of the pillbox cavity shows that the magnitude of a desired multipole of order $\tilde{g}_m$ does not remain constant, or *flat*, as the beam traverses the TM$_{m10}$ mode off-axis. In Sec. 6.2, the AMM is applied to design azimuthally modulated cavities that support modes with optimally flat fields that vary as x^m along the horizontal. Such flat fields would, for example, minimise the change in acceleration or change in dipole kick experienced as a particle traverses a cavity off-centre. The discussion is also extended to the design of other bespoke horizontal fields in Sec. 6.3.

The analysis of the pillbox cavity also shows that undesired multipoles become non-zero as the beam traverses the TM$_{m10}$ modes off-axis. For example, an increasing dipole kick is seen as a particle traverses the TM$_{010}$ mode off-axis. The detailed study of the effects of these unwanted multipoles on the electrodynamics of a beam with finite vertical size is outside the scope of this thesis.

6.2 Flat Fields

6.2.1 Flat Accelerating Fields

In Chapter 2, we derived the basis of the $\mathrm{TM}_{\{M\}\eta 0}$ modes in azimuthally modulated cavities as

$$E_z(r,\theta) = \sum_{\{M\}} \tilde{g}_M J_M(kr) \cos\left(M\theta - \phi_M\right). \tag{6.5}$$

Equation 6.5 therefore gives the form of the $\mathrm{TM}_{\{0,2\}\eta 0}$ modes with $\tilde{g}_2/\tilde{g}_0 = \gamma_2$ and $\phi_2 = 0$ as

$$E_z(r,\theta) = \tilde{g}_0 \left[J_0(kr) + \gamma_2 J_2(kr)\cos\left(2\theta\right)\right]. \tag{6.6}$$

If we consider this field along the horizontal and use Eqn. 2.19 to expand the Bessel functions into polynomial form, we find

$$\begin{aligned} E_z(r,0) = \tilde{g}_0 \Bigg(& \frac{1}{0!0!} - \left(\frac{1}{1!1!} - \frac{\gamma_2}{0!2!}\right)\left(\frac{kr}{2}\right)^2 + \left(\frac{1}{2!2!} - \frac{\gamma_2}{1!3!}\right)\left(\frac{kr}{2}\right)^4 - \\ & \left(\frac{1}{3!3!} - \frac{\gamma_2}{2!4!}\right)\left(\frac{kr}{2}\right)^6 + \left(\frac{1}{4!4!} - \frac{\gamma_2}{3!5!}\right)\left(\frac{kr}{2}\right)^8 \cdots \Bigg). \end{aligned} \tag{6.7}$$

Setting $\gamma_2 = 2$ thus cancels the quadratic term and flattens the accelerating field along the horizontal to

$$\begin{aligned} E_z(r,0) = \tilde{g}_0 \Bigg(& \frac{1}{0!0!} + \left(\frac{1}{2!2!} - \frac{2}{1!3!}\right)\left(\frac{kr}{2}\right)^4 - \\ & \left(\frac{1}{3!3!} - \frac{2}{2!4!}\right)\left(\frac{kr}{2}\right)^6 + \left(\frac{1}{4!4!} - \frac{2}{3!5!}\right)\left(\frac{kr}{2}\right)^8 \cdots \Bigg). \end{aligned} \tag{6.8}$$

The LHS contour plot of Fig. 6.3 visualises this field as given by Eqn. 6.6 with $\gamma_2 = 2$. The η = 1, 2 and 3 azimuthally modulated cross-sections that support such a field are also graphed. Comparing these solutions to the pillbox cavities that support the TM_{0n0} modes, as shown on the RHS contour plot of Fig. 6.3, we see the azimuthally modulated cross-sections are stretched in the horizontal but slightly shrunk in the vertical.

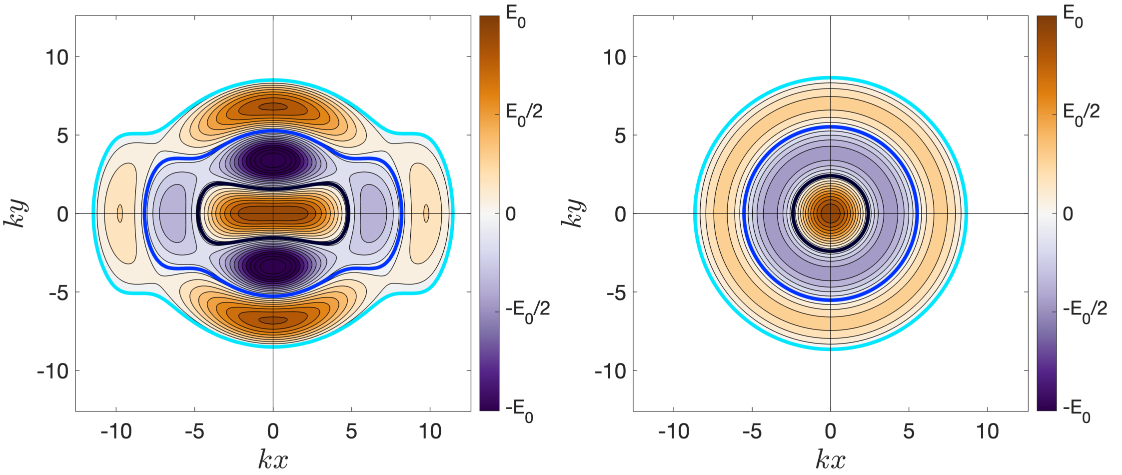

Figure 6.3: Contour plots in wavenumber-scaled Cartesian space of E_z in the $\mathrm{TM}_{\{0,2\}\eta 0}$ modes with $\tilde{g}_2/\tilde{g}_0 = 2$ and $\phi_2 = 0$ (left) and the TM_{0n0} modes (right). The η and n = 1, 2 and 3 solutions are graphed for all θ on both plots in black, blue and cyan.

Comparing the flatness of the cavities, the acceleration only drops by 1% and 14% at $kr_0/2$ and kr_0 in the $\mathrm{TM}_{\{0,2\}10}$ mode compared to 33% and 100% in the TM_{010} mode (where kr_0 is the wavenumber-scaled radius of the pillbox cavity). This, however, is at the expense of the $\eta = 1$ azimuthally modulated cavity being roughly twice the size along the horizontal, although it is roughly a third smaller along the vertical.

The field can be flattened further by adding more even multipolar terms to Eqn. 6.9 because the expansion of

$$E_z(r,\theta) = \tilde{g}_0 \left(J_0(kr) + 2 \sum_{m=1}^{N} J_{2m}(kr) \cos(2m\theta) \right), \tag{6.9}$$

is

$$E_z(r,0) = \tilde{g}_0 \left(1 + O\left(r^{2(N+1)}\right)\right). \tag{6.10}$$

For example, the contour plot in Fig. 6.4 shows the $\eta = 1$, 2 and 3 $\text{TM}_{\{0,2,4,6,8\}\eta 0}$ modes as given by Eqn. 6.9 with $N = 4$. Comparing to Fig. 6.6, we see that the $\eta = 1$ cross-section is still approximately a third smaller along the vertical than the corresponding pillbox cavity despite the increase in N, but it is now 4.7 times larger along the horizontal. Its accelerating field is very flat, dropping by under 0.001% at kr_0.

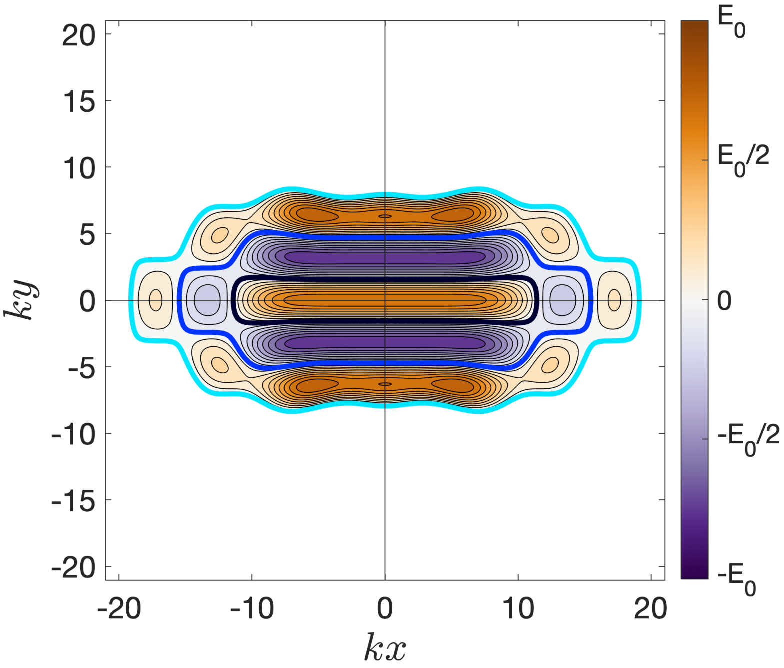

Figure 6.4: Contour plot in wavenumber-scaled Cartesian space of E_z in the $\text{TM}_{\{0,2,4,6,8\}\eta 0}$ modes with $\tilde{g}_2/\tilde{g}_0 = \tilde{g}_4/\tilde{g}_0 = \tilde{g}_6/\tilde{g}_0 = \tilde{g}_8/\tilde{g}_0 = 2$ and $\phi_2 = \phi_4 = \phi_6 = \phi_8 = 0$. The $\eta = 1$, 2 and 3 solutions are graphed for all θ in black, blue and cyan.

As $N \to \infty$, the accelerating field becomes completely flat and the $\eta = 1$ solution converges to that of two parallel plates. This is what one would intuitively expect because the cavity shape must remain constant under a horizontal translation for the field to remain flat too.

6.2.2 Flat Transverse Fields

A similar method can be utilised to design azimuthally modulated cavities that support m-polar fields that remain flat as a particle beam traverses off-axis by noting

$$\frac{1}{1!}\left(\frac{kr}{2}\right) = \sum_{m=0}^{\infty}(2m+1)J_{2m+1}(kr), \tag{6.11}$$

$$\frac{1}{2!}\left(\frac{kr}{2}\right)^2 = \sum_{m=0}^{\infty}(m+1)^2 J_{2m+2}(kr), \tag{6.12}$$

$$\frac{1}{3!}\left(\frac{kr}{2}\right)^3 = \sum_{m=0}^{\infty}\frac{(m+1)(m+2)(2m+3)}{6}J_{2m+3}(kr), \tag{6.13}$$

and increasingly complex formulae for higher orders.

As an example, a flat dipole field that varies linearly along the horizontal can be created using

$$E_z(r,\theta) = \tilde{g}_1 \sum_{m=0}^{N}(2m+1)J_{2m+1}(kr)\cos\left((2m+1)\theta\right), \tag{6.14}$$

such that

$$E_z(r,0) = \tilde{g}_1\left(\frac{kr}{2} + O\left(r^{2(N+1)}\right)\right). \tag{6.15}$$

The LHS contour plot in Fig. 6.5 shows the $\eta = 1$, 2, 3 and 4 $\mathrm{TM}_{\{1,3,5,7,9\}\eta 0}$ modes as given by Eqn. 6.9 with $N = 4$. Interestingly there is an $\eta = \{3,4\}$ hybrid solution. The $\eta = 1$ cross-section has horizontal and vertical dimensions that are 3.3 and 0.4 times the size of the pillbox that supports the TM_{110} mode. Comparing the flatness of the dipole terms, it is found that $\tilde{g}_1'/\tilde{g}_1$ does not deviate from constant by more than 0.5% at kr_0. In contrast, the transformed dipole term in the TM_{010} mode, as shown in Fig. 6.2, oscillated significantly within the same range.

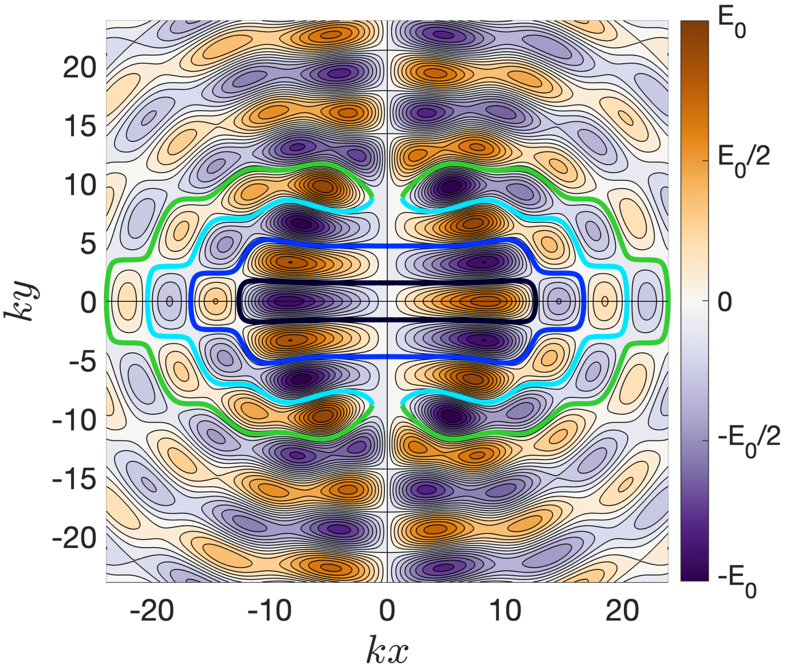

Figure 6.5: Contour plot in wavenumber-scaled Cartesian space of E_z in the $\mathrm{TM}_{\{1,3,5,7,9\}\eta 0}$ modes with $\tilde{g}_3/\tilde{g}_1 = 3$, $\tilde{g}_5/\tilde{g}_1 = 5$, $\tilde{g}_7/\tilde{g}_1 = 7$, $\tilde{g}_9/\tilde{g}_1 = 9$ and $\phi_1 = \phi_3 = \phi_5 = \phi_7 = \phi_9 = 0$. The $\eta = 1$, 2, 3 and 4 solutions are graphed for all θ in black, blue, cyan and lime.

6.2.3 Optimising the Flatness with Constraints

Equation 6.9 and Eqn. 6.14 remove polynomial terms up to the orders $2N$ and $(2N+1)$ respectively to make flatter accelerating and dipole fields along the horizontal. Similar equations could be derived to make flatter m-pole fields of any order.

With these equations, however, the azimuthally modulated cavities become physically bigger as the field is made flatter. This is a problem because RF cavities must satisfy frequency and spatial constraints for application in a particle accelerator.

An example procedure is therefore outlined for finding the mode of frequency f which has the flattest accelerating field over a distance d under the constraint of being supported by a cavity that is no larger than a distance x_0 in the horizontal direction:

- First, a set $\{X\}$ of N higher order terms are introduced to Eqn. 6.1 such that it becomes

$$E_z(r,\theta) = \tilde{g}_0 \left[J_0(kr) + \sum_{\{X\}} \gamma_X J_X(kr) \cos{(X\theta)} \right] . \tag{6.16}$$

- Next, it is assumed that the flattest field is found when the solution is lowest order ($\eta = 1$) and when the cavity has the maximal horizontal dimension x_0.
- Then, the space of azimuthally modulated solutions $r_0^{(1)}(\theta)$ that satisfy the boundary condition $E_z(x_0, 0) = 0$ is determined:
  - To do so, the following is solved

    $$0 = \tilde{g}_0 \left[J_0(kx_0) + \sum_{\{X\}} \gamma_X J_X(kx_0) \right] . \tag{6.17}$$

    This constrains the values of γ_X.
  - Next, the following is solved with the constrained values of γ_X

    $$0 = \tilde{g}_0 \left[J_0 \left(kr_0^{(1)}(\theta) \right) + \sum_{\{X\}} \gamma_X J_X \left(kr_0^{(1)}(\theta) \right) \cos{(X\theta)} \right] . \tag{6.18}$$

    This determines the space of solutions $r_0^{(1)}(\theta)$.
- Next, the solutions that exceed any other spatial constraints are removed.
- Finally, the optimum solution with the minimal flatness over the distance d is determined.

A computer script can be run to carry out this procedure.[1]

To illustrate this flatness optimisation process, an example application is presented for designing RF cavities that support optimally flat accelerating fields whilst fitting

---

[1] It should be noted that increasing N (the number of higher-order terms) improves the flatness of the optimum field that can be found but also increases the complexity of the optimisation process.

within the space constraints of the isochronous ring cyclotron at the High Intensity Proton Accelerator facility, PSI [102].

The PSI Cyclotron

The PSI cyclotron accelerates protons from 72 MeV at an injection radius of 2.1 m to 590 MeV at an extraction radius of 4.5 m. Within the cyclotron, there are 4 accelerating structures held by a support structure of dimensions 3.9 m × 5.6 m × 0.1 m [103, 104]. The cavities operate at 50.4 MHz and their design, as shown in Fig. 6.6, is optimised for the maximum shunt impedance.[2]

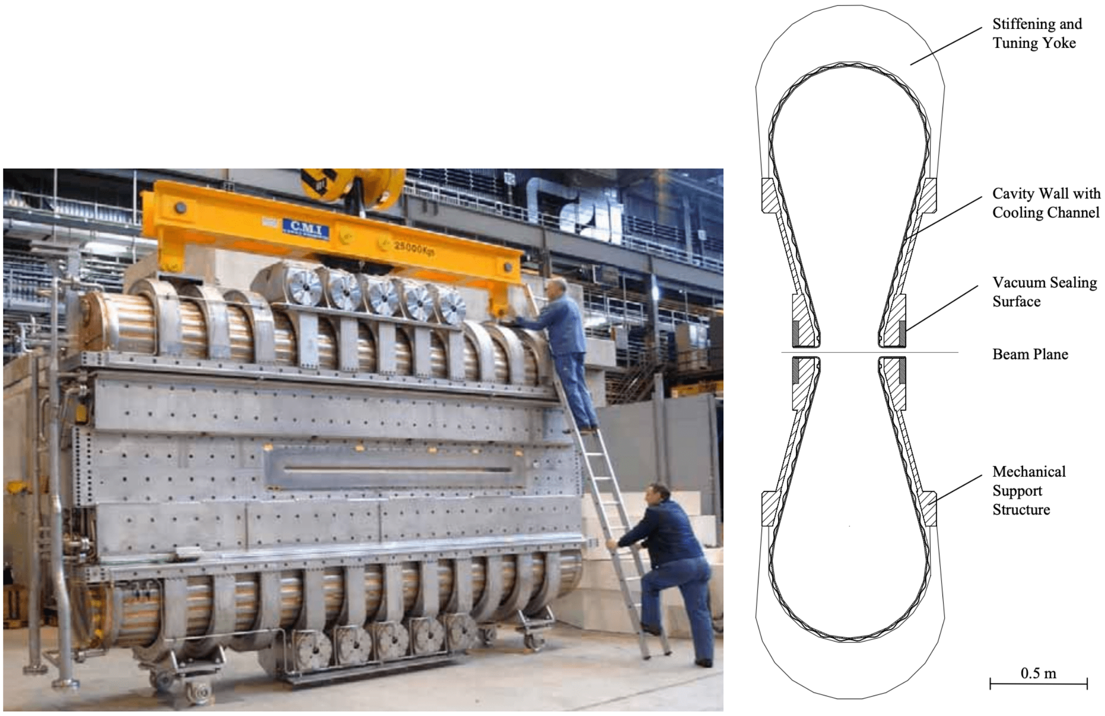

Figure 6.6: The fabricated cavity and support structure installed in the PSI cyclotron (left) and the design of cavity cross-section (right). Reproduced from [103] and [104].

Access to the model of the PSI cavity was unavailable and so the AMM could

---

[2] It should be noted that protons at these energies are non-relativistic and thus the transverse electrodynamics analysis undertaken in Sec. 2.3 may not apply well. In this example, however, the application of the AMM is demonstrated for tailoring the longitudinal electric field off-axis and optimising the flatness of the acceleration. The resultant effect on transverse beam dynamics is not analysed (it is noted, however, that flattening the longitudinal electric field along the horizontal also minimises the transverse magnetic field along the horizontal).

not be applied directly to the PSI cavity model in order to optimise its flatness. Instead, the AMM was used to design optimally flat structures that fit within the space constraints of the PSI cyclotron and these were benchmarked against a closed, cuboid cavity of dimensions 2.85 m × 5.2 m × 0.1 m. The flatness of the fields between the AMM and cuboid structures were compared using the parameter Δ, defined as the maximum deviation of the field between the injection and extraction points compared to the centre. An injection radius of -1.25 m and extraction radius of 1.25 m was assumed and it should be noted that beam pipes were not incorporated into the models.

The cuboid structure supports a 60 MHz fundamental accelerating mode and a contour plot of the mode is shown on the LHS of Fig. 6.7. The cavity is horizontally symmetric and so the longitudinal electric field is the same at injection and extraction. The RHS plot of Fig. 6.7 shows the variation in the longitudinal electric field from the centre to the cavity wall. The dashed line indicates the injection/extraction distance and we see that $\Delta = 27.2\%$ for this structure.[3]

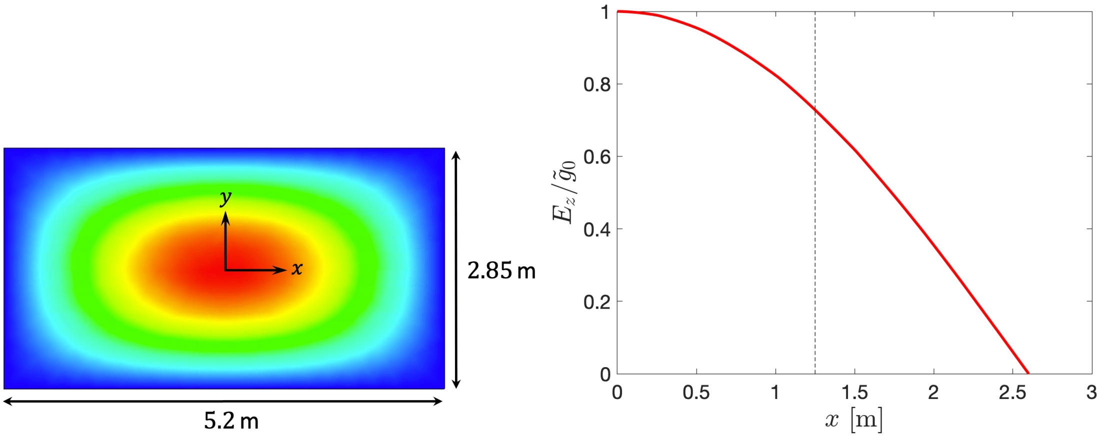

Figure 6.7: Contour plot of the longitudinal electric field in a rectangular cavity, where red is a maximum and blue is zero (left). Plot of the normalised longitudinal electric field against offset (right).

---

[3] As an additional benchmark, the pillbox cavity with a radius of 1.91 m that supports a 60 MHz accelerating field can be considered. With the same injection/extraction radius of 1.25 m, its deviation from flatness is $\Delta = 52.9\%$.

The flatness optimisation procedure is now demonstrated for desinging a series of azimuthally modulated cavities with a maximum horizontal dimension of 5.2 m that support 60 MHz fields of the form given by Eqn. 6.16 when $N = 1$, 2 and 3 higher order terms are included.

To begin, consider Eqn. 6.17 with just a non-zero quadrupole term. As γ_2 is the sole free-variable in Eqn. 6.17 (the wavenumber is constrained by the frequency $f = 60$ MHz and the size by the maximum horizontal dimension $x_0 = 5.2$ m), the sole solution is $\gamma_2 = 0.70$. Therefore there is only a single solution for $r_0^{(1)}(\theta)$ and its resulting mode has a flatness deviation of $\Delta = 35.2\%$. This is almost 10% larger than the cuboid model.

Next, consider Eqn. 6.17 with just non-zero quadrupole and octupole terms

$$0 = \tilde{g}_0 \left[J_0(kx_0) + \gamma_2 J_2(kx_0) + \gamma_4 J_4(kx_0) \right]. \tag{6.19}$$

Here both γ_2 and γ_4 are free-variables and Fig. 6.8 shows the 1D solution space of γ_2 and γ_4 values that satisfy the Eqn. 6.19 (blue). The corresponding Δ for each of the solved γ_2 and γ_4 values are also plotted (red). We see the minimum deviation from flatness is $\Delta = 2.8\%$, achieved when $\gamma_2 = 2.37$ and $\gamma_4 = -4.71$. This is significantly smaller than the flatness of the cuboid model.[4]

The LHS contour plot of Fig. 6.9 shows the azimuthally modulated cross-sections that support the 60 MHz mode with $\gamma_2 = 2.37$ and $\gamma_4 = -4.71$. We see that the cavity cross-section is a minimum along $\theta = 0$ and reaches a maximum of approximately 8 m in the vertical. Although the field is significantly flatter along the horizontal

---

[4] These optimal values can be understood by considering the 0th order Bessel term expanded into polynomial form. As shown in Eqn. 6.9, the deviation from flatness in the TM_{010} mode is mostly affected by the quadratic term. Adding a 2nd order Bessel function with magnitude $\gamma_2 > 0$ can correct for this but it increases the horizontal size and it also enhances the quartic term if $\gamma_2 > 2/3$. Both the increased horizontal size and enhanced quartic term can be compensated for by introducing a 4th order Bessel function with magnitude $\gamma_4 < 0$. We therefore expect the optimal value of $\gamma_2 \approx 2$ such that it mostly corrects for the quadratic term and $\gamma_4 \lesssim -1$ to reduce the horizontal size and mostly correct for the enhanced quartic.

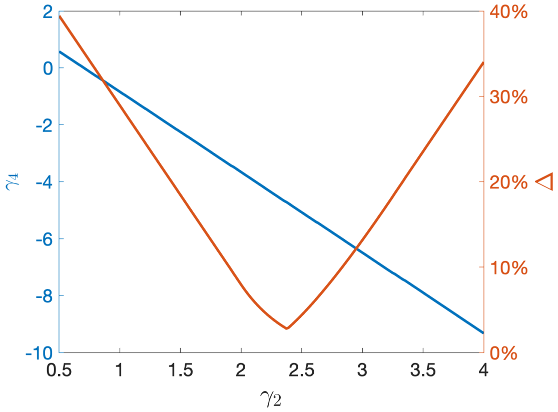

Figure 6.8: Plot of the γ_4 values that satisfy the Eqn. 6.19 (blue) and the corresponding flatness for each solution (red) as functions of γ_2.

than the cuboid cavity, as shown in the RHS plot, the design is impractical due to its large size in all other directions. The underlying reason for its large size is that the first continuous solution is an $\eta = \{1, 2, 3\}$ hybrid solution, as graphed on the LHS contour plot of Fig. 6.9.

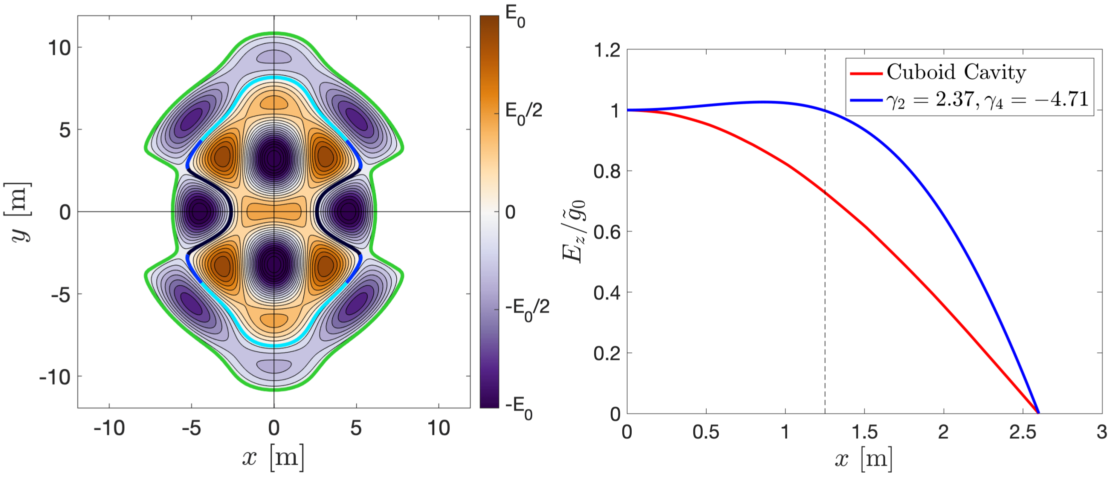

Figure 6.9: Contour plot in Cartesian space of the electric field given by Eqn. 6.16 with $\gamma_2 = 2.37$ and $\gamma_4 = -4.71$ and the η = 1, 2, 3 and 4 solutions graphed in black, blue, cyan and lime (left). A comparison of the variation in the field along the horizontal between the hybrid structure and the cuboid cavity is shown (right).

The optimisation procedure was subsequently carried out under the additional constraint that the structure must be smaller than 5.2 m in all θ directions. This requires $\gamma_2 \leq 1.15$ and Fig. 6.8 shows that the optimum flatness occurs at the edge of this limit when $\gamma_2 = 1.15$ and $\gamma_4 = -1.26$. The LHS contour plot in Fig. 6.10 shows the azimuthally modulated cross-sections for these values and we see that the $\eta = 1$ and 2 solutions are at the limit of converging and forming a discontinuous structure. The RHS plot of Fig. 6.10 compares the fields between this structure and the cuboid cavity and we see that the field is flatter across the structure with $\Delta = 25.8\%$ compared to $\Delta = 27.2\%$ for the cuboid cavity.[5]

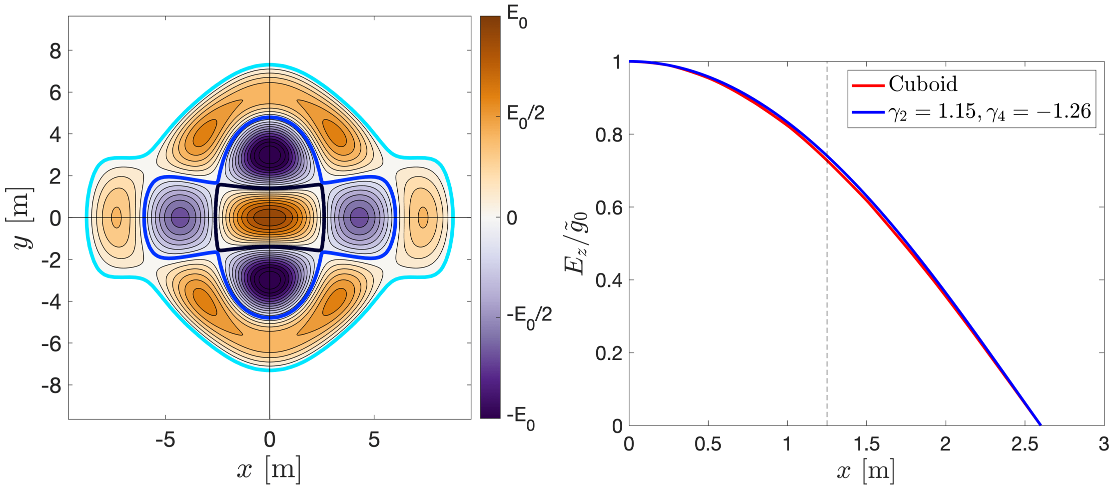

Figure 6.10: Contour plot in Cartesian space of the electric field given by Eqn. 6.16 with $\gamma_2 = 1.15$ and $\gamma_4 = -1.26$ and the $\eta = 1$, 2 and 3 cross-sections that support it graphed in black, blue and cyan (left). A comparison of the variation in the field along the horizontal between this structure and the cuboid cavity is shown (right).

Additional even multipolar terms can be added into Eqn. 6.16 to create flatter fields (odd multipolar terms should not be added because they result in an horizontally asymmetric cavity and field). It is expected that the structure of optimal flatness under the PSI spatial constraint occurs for $\gamma_2 \simeq 1.15$ and $\gamma_4 \simeq -1.26$ with smaller corrections from higher order even multipoles. This is evident when adding a dodecupole term alongside a quadrupole and octupole which returned $\Delta = 25.4\%$ for $\gamma_2 = 1.18$, $\gamma_4 = -1.62$ and $\gamma_6 = 2.49$.

---

[5] Trying a similar optimisation but with a quadrupole and a dodecupole term returned $\Delta = 30.7\%$ when $\gamma_2 = 0.89$ and $\gamma_6 = -5.00$. This is a larger deviation from flatness than when optimising with a quadrupole and octupole and is expected because there is no correction to the quartic term by the 6th order Bessel function, which instead first corrects for the sextic term.

The field flatness therefore improves from $\Delta = 35.2\%$ when there is just a monopole and quadrupole term, to 25.8% when also including an octupole, to 25.4% when further including a dodecupole. It is therefore expected that the minimum deviation from flatness would be around 25% if a full optimisation is done with many more multipolar terms.

Interestingly, this is only about a 10% improvement over the simple model of a 60 MHz cuboid cavity. There are, however, several benefits to the AMM in this application space to highlight. First, the height and width of the cuboid cavity must be varied in a parameter scan to attain the desired frequency whereas the AMM guarantees the desired frequency of a closed cavity. Second, if a more complex structure is designed, such as the PSI cavity that is optimised for maximum shunt impedance, the flatness may not necessarily be so close to optimal. The AMM and the outlined optimisation process can therefore be used to fine-tune the multipolar content of the mode in order to optimise for flatness. This can be done in similar iterative means to the process outlined in Chapter 5. Third, the AMM can be used more generally to optimise a structure for supporting more bespoke horizontal fields, and is not just limited to optimising for flatness.

6.3 Bespoke Off-Axis Fields

The AMM can also be used for bespoke tailoring of the off-axis field. For example, the design of an azimuthally modulated cavity that supports a mode consisting of a flat accelerating and dipole component along the horizontal could be considered by solving

$$E_z(r,\theta) = \tilde{g}_0 \left(J_0(kr) + 2\sum_{m=1}^{N} J_{2m}(kr)\cos(2m\theta) \right) + \\ \tilde{g}_1 \left(\sum_{m=0}^{N} (2m+1) J_{2m+1}(kr)\cos((2m+1)\theta) \right), \quad (6.20)$$

which becomes

$$E_z(r,\theta) = \tilde{g}_0 + \tilde{g}_1 \frac{kr}{2} + O\left(r^{2(N+1)}\right). \quad (6.21)$$

Then, if there are spatial constraints, a similar optimisation process to that outlined in Sec. 6.2 could be run to determine the optimal field.

6.4 Chapter Summary

In this chapter, it has been shown that the profile of a mode can be tailored off-axis by applying the AMM which was derived and outlined in Chapter 3.

Specifically, it was shown how that the AMM can be used to design RF cavities that support perfectly flat m-pole fields of specified frequency. This, however, is at the expense of a large dimension along the horizontal and particle accelerators impose constraints on the size of RF cavities. An optimisation process based on the AMM was therefore outlined for finding the azimuthally modulated cavity shape which supports the flattest mode given a spatial constraint. An example application of this process was demonstrated to determine the flattest accelerating field that could be fit within the spatial constraints of the PSI cyclotron with an accelerating field. The deviation from flatness was found to be under 25.4% between an injection and extraction radius which is flatter than a cuboid cavity that had a flatness deviation of 27.2%.

Finally, the scope for extending the method beyond designing flat fields to more complex fields was briefly discussed.

Chapter 7

Public Engagement Activity

This chapter outlines a public engagement activity, the *Funky Drums and Particle Accelerators* outreach workshop, that was inspired by the research presented in this thesis. I created, designed, led and evaluated this project which was delivered to over 300 11-14 year-old students in 4 different Oxfordshire schools. It was funded by a £4,000 award that I obtained from the University of Oxford's Public Engagement with Research Seed Fund.

The chapter begins in Sec. 7.1 by detailing the relationship between musical drums and azimuthally modulated RF cavities. Three different azimuthally modulated drums that were manufactured for the workshop are presented and their different frequency spectra are analysed. Then, in Sec. 7.2, the goals and achievements of the project are detailed alongside an outline of how the workshop met the aims.

7.1 Drums and RF Cavities

7.1.1 Vibrations of Simple Drums

The initial inspiration for the Funky Drums and Particle Accelerators workshop was the parallel between the equations that govern the electromagnetic modes in an azimuthally modulated RF cavity and the vibrational modes of an azimuthally modulated drum.

The vibrations of a *simple* musical drumhead with a uniform thickness which is negligibly thin compared to its transverse size can be modelled by the vibrations of an elastic membrane. Denoting the longitudinal displacement of the drumhead at a time t and position (r, θ) as $u(r, \theta, t)$, the vibrational modes must satisfy the homogeneous wave equation

$$\nabla^2 u - \frac{1}{c^2}\frac{\partial^2 u}{\partial t^2} = 0, \tag{7.1}$$

where c is the transverse speed of wave propagation [105]. This relates to the physical properties of the drum as

$$c = \sqrt{\frac{T}{\sigma}}, \tag{7.2}$$

where we assume the drumhead to have a uniform surface tension T and mass density σ.

If the drumhead is clamped to an azimuthally modulated frame with a cross-section $r_0(\theta)$, the vibrational modes must also satisfy the boundary condition

$$u(r_0(\theta), \theta, t) = 0. \tag{7.3}$$

Assuming Eqns. 7.1-7.3 are satisfied by an infinite number of harmonic standing wave solutions l of distinct frequencies ω_l, Eqn. 7.1 for a given mode l becomes

$$\frac{\partial^2 u}{\partial r^2} + \frac{1}{r}\frac{\partial u}{\partial r} + \frac{1}{r^2}\frac{\partial^2 u}{\partial \theta^2} + k_l^2 u = 0, \tag{7.4}$$

where $k_l = \omega_l / c$. Note that the z-dimension is neglected such that $\partial u/\partial z = 0$ because the drumhead has negligible thickness compared to its transverse dimensions.

Equation 7.4 is the plane polar component of Eqn. 2.2 while Eqn. 7.3 is an identical boundary condition to Eqn. 2.61. The equations that govern the vibrational modes of simple azimuthally modulated drums are therefore identical to those that govern the longitudinal electric field of the $p = 0$ TM modes in azimuthally modulated cavities. The analysis presented in Chapter 3 regarding $\mathrm{TM}_{\{M\}\eta 0}$ modes is thus applicable to the vibrations of drumheads too. The vibrational modes of azimuthally modulated drums are thus denoted by ({M},η).

7.1.2 Simple Circular Drums

The frequency spectrum of a simple circular drum is given by

$$\omega_{mn} = \frac{j_{mn}}{r_0} c, \tag{7.5}$$

where r_0 is its radius. This is identical to the spectra of the TM_{mn0} modes in a circular pillbox of radius r_0 given by Eqn. 2.111 in Chapter 2.

The frequency spectrum of a simple circular drum relative to the fundamental frequency starts 1 : 1.59 : 2.14 : 2.30 : 2.65 : 2.92 : 3.16 : 3.50 : 3.65, corresponding to the excitement of the (0,1), (1,1), (2,1), (0,2), (3,1), (1,2), (4,1), (2,2) and (5,1) modes respectively. This spectrum is nonharmonic because it does not solely consist of overtones that are integer multiples of a fundamental frequency. The sound produced by such a drum therefore has indefinite pitch because a harmonic spectrum is essential for a listener to hear a sound of definite pitch.

Harmonic Circular Drums

There are circular drums that can be played to produce sounds of definite pitch. One such example is the kettledrum shown in Fig. 7.1 that consists of a, typically, 84 cm diameter drumhead stretched across the the opening of a copper bowl. When the drumhead is struck at a distance roughly two-thirds from the centre to the rim, it produces a sound with a frequency spectra that closely approximates the integer sequence 2 : 3 : 4 : 5 : 6 [106]. This corresponds to the excitation of the (1,1), (2,1), (3,1), (4,1) and (5,1) modes respectively. This spectrum is a so-called missing fundamental spectrum because the overtones imply a fundamental frequency which the sound does not contain. The nonharmonic (0,1) and (0,2) modes contribute little to the sound because their monopole nature makes them efficient at radiating sound and so they decay rapidly [106]. Furthermore these, alongside other nonharmonic modes, are deemphasised by the offset striking position.

Figure 7.1: A kettledrum. Reproduced from [107].

The kettledrum design exploits four different physical mechanisms in order to bring the equivalent, nonharmonic frequency spectrum of a simple circular drum, which is 2 : 2.68 : 3.33 : 3.96 : 4.58, to harmonicity. One is air-mass loading whereby the resonant frequencies are lowered due to the weight of the air on the motion of the drumhead. This has the most significant effect on the (1,1) mode. A second is the interaction of the air enclosed within the bowl with the individual drumhead modes. Particularly, the enclosed air has resonances of its own that can interact with the drumhead modes of similar frequency. A third is the resistance of the drumhead to shearing forces which increases the frequencies of the higher harmonics. And a fourth is the use of a pedal, or other tuning mechanism, to change the tension in the drumhead [106].

7.1.3 Azimuthally Modulated Drums

Another mechanism with which to change the frequency spectrum of a drum is to change its cross-section. Investigating this forms the basis of the Funky Drums and Particle Accelerators workshop where students are tasked with measuring the different frequencies produced by different azimuthally modulated, or *funky*, drums.

Azimuthally modulated drums are bespoke so the manufacturing of these drums was contracted to an external company. A first prototype based on the Irish bodrhán drum is shown on the LHS of Fig. 7.2. Here the drumhead has been stretched directly over the azimuthally modulated frame. This caused it to pinch in the convex regions of the drum as it dried, however, significantly increasing the tension and effectively changing the shape of the drum. To prevent this pinching whilst attempting the preserve the desired boundary condition, the drumskin was glued firmly to an extension that made the frame concave for all angles. This final design is shown on the RHS of Fig. 7.2. A red line is superimposed on the image to help identify the frame extension.

The three different funky drum designs are shown in Fig. 7.3. The smallest drum (called FD1) had a cross-section that supports a ({0,2},1) mode with $\tilde{g}_2/\tilde{g}_0 = 4.032$. The next largest (FD2) had a cross-section that supports a ({0,2},2) mode with $\tilde{g}_2/\tilde{g}_0 = 4.032$ and the largest (FD3) had a cross-section that supports a ({0,3},2) mode with $\tilde{g}_3/\tilde{g}_0 = 0.95$. The drums were all scaled such that the modes of interest resonate at the same frequency.

The measured frequency spectra of the three different drums when struck on and off centre is shown in Fig. 7.4. We see that the fundamental frequency of FD1 is

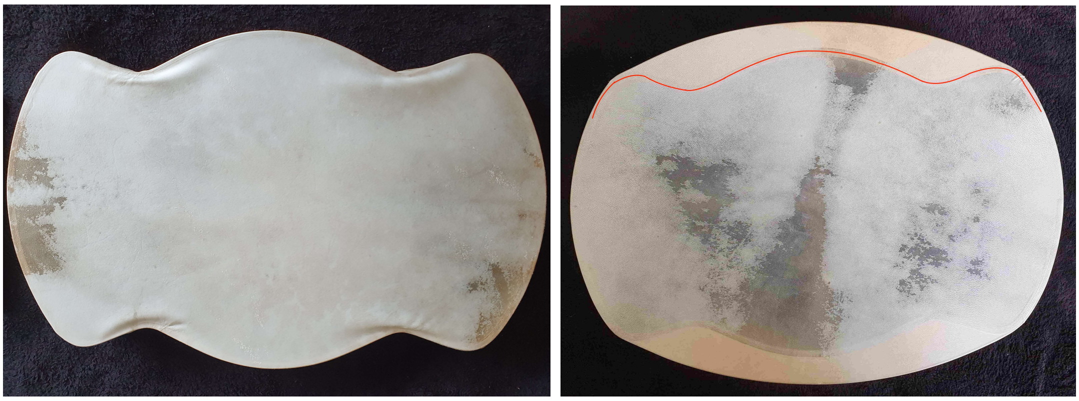

Figure 7.2: The first prototype funky drum made (left) and the corresponding final design (right).

Figure 7.3: The three different funky bodrhán drums.

higher than FD2 and FD3, as expected because it is physically smaller. Beyond the fundamental frequency, however, there are no significant peaks in the FD1 spectra. FD1 was a particularly poor build for a drum because its small size makes it difficult to strike and the drumhead does not ring for long when struck.

The sound produced by FD2 and FD3 was much clearer and their different excitations are visible in Fig. 7.4. We also see that the amplitudes of the different

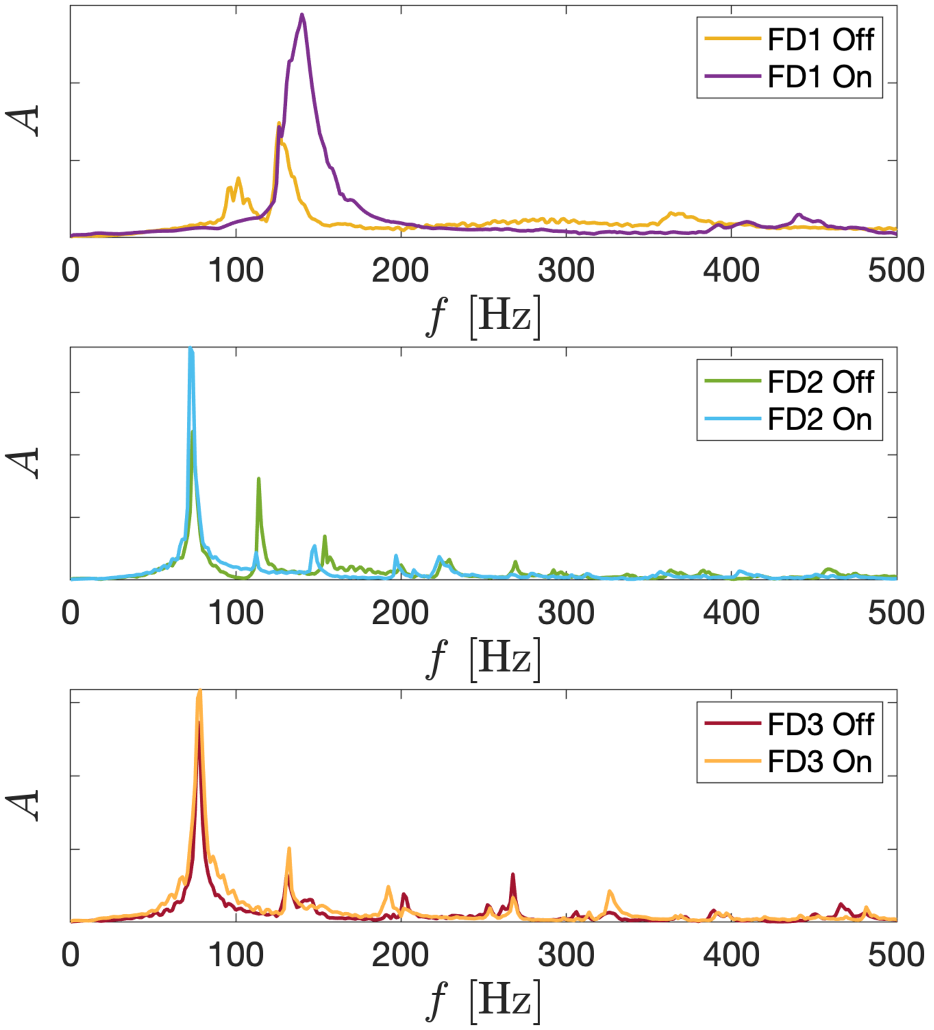

Figure 7.4: Frequency spectra of the different drums when hit on and off centre.

frequencies depend on where the drum is struck. Attempts to correlate the measured frequency spectra of the funky drums with the simulated frequency spectra of the equivalent azimuthally modulated RF cavities were unsuccessful. This discrepancy is because air-mass loading is not accounted for and the drumhead is made out of goatskin that is glued to the extension. The latter means that the assumptions of uniform thickness, mass density, tension and a perfectly clamped boundary condition on the desired azimuthally modulated shape all break down. This variation in the drumhead is even visible in Figs. 7.2-7.3 as parts of the drumhead are translucent.

7.2 The Funky Drums and Particle Accelerators Outreach Workshop

7.2.1 Aim

The aim of the Funky Drums and Particle Accelerators workshop was to build the *science capital* of 11-14 year-old school students and encourage an uptake in post-16 STEM study.

Science capital is a concept similar to cultural and social capital that is used to explain "differential patterns of aspiration and educational participation among young people" [108]. It has been framed around 8 key dimensions that capture the sum of all the science-related knowledge, attitudes, experiences, and resources an individual has:

- Scientific literacy,
- Science-related attitudes, values and dispositions,
- Knowledge about the transferability of science,
- Talking about science in everyday life,
- Knowing people in science-related roles,
- Family science skills, knowledge and qualifications,
- Science media consumption,
- Participation in out-of-school science learning contexts.

Although lower levels of science capital are linked to lower participation in science post-16, which can lead to a significant loss of future opportunities, one's science capital constantly evolves and can grow [109].

The first 5 dimensions of science capital as listed above can be improved by an outreach workshop that is fun, provides hands-on experimentation with bespoke scientific equipment and relates the physics of musical drums to the physics of azimuthally modulated RF cavities. This is the basis for the Funky Drums and Particle Accelerators workshop in which students explore how the modes of drums, Chladni plates and RF cavities all have dependence on the cross-section.

7.2.2 Outline

The workshop itself is split into three different workstands.

Funky Drums

The aim of the Funky Drums workstand is for the students to determine the dominant frequencies excited when different azimuthally modulated drums are struck at different locations. This link between the vibrational modes of musical drums and the electromagnetic modes of RF cavities provides a very accessible means with which to engage pre-GCSE students with our research. Nearly all 11-14 year-old students would have seen, heard and played musical drums whilst having very little or no familiarity with RF cavities and particle accelerators.

Chladni Plates

The aim of the Chladni Plates workstand is for the students to find different vibrational patterns, such as those shown in Fig. 7.5, that are produced when different azimuthally modulated Chladni plates are driven at different resonant frequencies.

Chladni plates are thin, rigid surfaces whose vibrational modes can be visualised by scattering small particles such as table salt onto the plate's surface before driving it at a resonant frequency. This causes the particles to bounce around the surface until they either fall off the plate or settle along one of the nodal lines where the plate

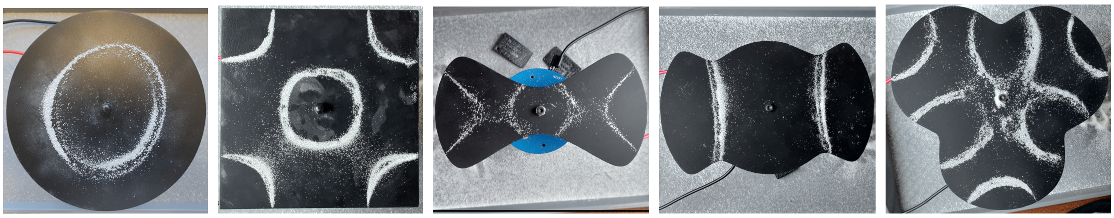

Figure 7.5: Example vibrational modes formed on each of the five different Chladni plates. From left to right: the nodal structure at 260 Hz on the circular Chladni plate, at 470 Hz on the rectangular plate, at 880 Hz on the FD1 plate, at 200 Hz on the FD2 plate and at 1510 Hz on the FD3 plate.

does not vibrate. Over time, the particles therefore concentrate along the nodal lines.

Unlike the drumheads analysed in Sec. 7.1, the vibrational modes of the rigid plates obey the biharmonic equation

$$\nabla^2\nabla^2 u = k^2 W. \tag{7.6}$$

Here k is

$$k^4 = \frac{\sigma\omega^2}{D}, \tag{7.7}$$

where σ is the mass density per unit area of the plate, ω the angular frequency of the mode and D the flexural rigidity of the plate defined as

$$D = \frac{h^2 E}{12(1-\nu^2)}, \tag{7.8}$$

where h is its thickness, E is its Young's modulus and ν is its Poisson's ratio [110]. The Chladni plates also have different boundary conditions compared to the clamped drumheads because their boundary is free.

Accelerators

The aim of the Accelerators workstand is for students to observe and analyse different particle tracks inside a cloud chamber, before developing an understanding of how azimuthally modulated RF cavities could be used to both accelerate and manipulate particles. The 3D printed RF cavities shown in Fig. 7.6 were used to help explain how the electromagnetic fields in an RF cavity depend upon its azimuthal cross-section.

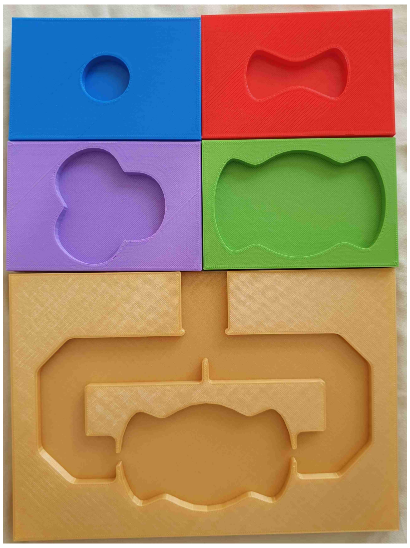

Figure 7.6: 3D printed RF cavities.

7.2.3 Evaluation

Positive written feedback was received after delivering the workshop including comments from teachers that “[the students] were more interested and animated than I have seen them before so it clearly hit the spot” and “[the workshop] generated quite a few questions in my next lesson”. Comments from students included “very interactive and I would love to do it again” and “I liked doing the experiments”. Additionally, a basic questionnaire was filled out by the students and over 75% of students agreed or strongly agreed (under 9% disagreed or strongly disagreed) that ‘the workshop was fun’ while over 58% agreed or strongly agreed (under 6% disagreed or strongly disagreed) that they ‘understood how particle accelerators and funky drums are linked’.

Although these percentages are positive in the majority, the negative responses are important to note too. Furthermore, there were students who were visibly disengaged during the workshop and, in particular, 23% of attending students disagreed or strongly disagreed that ‘the workshop made them think more that scientists are people like me’. I found that, with enough effort, even the least enthusiastic students could be sufficiently engaged with the equipment and experiments. However, this was not always possible, especially given the time constraints of the workshop whereby the students swapped workstands every 15 minutes and the large group sizes of nine or more students per workstand.

Overall, I think the equipment made and experiments designed for the Funky Drums and Particle Accelerators workshop are effective outreach tools for engaging the public. The kit could also be used in other outreach environments. To improve future workshops, I would introduce an additional hands-on experiment to the Accelerators workstand to demonstrate the ability of azimuthally modulated RF cavities to accelerate and manipulate simultaneously. I would also limit the class size to a maximum of six students per workstand to better engage the students of the lowest science capitals and enthusiasms.

7.3 Chapter Summary

In this chapter, the underlying physics that links the vibrational modes of azimuthally modulated drums to the electromagnetic modes of azimuthally modulated RF cavities has been detailed. In particular, we showed that the AMM can be used to design drums with azimuthally modulated cross-sections that support ($\{\mathrm{M}\}$,η) modes. The frequency spectra of the three different azimuthally modulated drums created for the Funky Drums and Particle Accelerators workshop were analysed.

This activity was developed to engage the public with our scientific research and build the science capital of its 11-14 year-old target audience. This workshop has been delivered to over 300 students so far and can continue to be delivered in the future with little extra cost as the equipment required for the workshop is now complete.

Chapter 8

Conclusions

This thesis has described the development, testing and application of a method for precisely controlling the multipolar content of the electromagnetic fields in RF cavities.

The basis of the electromagnetic modes in closed azimuthally modulated cavities with a cross-section $r_0(\theta)$ was derived from Maxwell's equations. The modes were shown to be either TE or TM and the radial, azimuthal and longitudinal profile of the mode was denoted by $\{M\}\eta p$. Here $\{M\}$ is the set of integers that denotes the multipolar content of the mode, η the integer that denotes the radial order and p the integer that denotes the longitudinal dependence. By defining the desired form of a TM mode, one can apply the boundary condition that the tangential electric field is zero on the cavity wall to determine the azimuthally modulated cross-section that supports it. This is the so-called azimuthal modulation method (AMM).

The scope and limitations of using the AMM for designing closed azimuthally modulated cavities that support $\mathrm{TM}_{\{M\}\eta 0}$ modes of any number of multipole terms of specified magnitudes and orientations was outlined. It was found that there are situations where the azimuthally modulated cross-section is not physically realisable. For example, the cavity radius may become zero or discontinuous for certain angles or the radius may be continuous but not closed such that it forever spirals.

These results were used to explore the application space of using the AMM to design RF cavities for use in particle accelerators. For example, the $\mathrm{TM}_{\{0,2\}\eta 0}$ modes that simultaneously accelerate and focus a beam can be used for parasitic beam position measurements and Landau damping as well as acceleration. It was shown that the AMM can be used to design a cavity with dual-slot couplers incorporated that supports a desired 3 GHz $\mathrm{TM}_{\{0,2\}20}$ mode of $\tilde{g}_2/\tilde{g}_0 = 5$. The dual-slot couplers introduced a significant quadrupole term and so the design process required repeated use of the AMM to scan through different design ratios of $\tilde{g}_2/\tilde{g}_0$ until the desired measured ratio was obtained. Subsequent experimental tests of a prototype based on this design showed manufacturing errors did not have a significant effect on the mode and that bead pull testing can be used to verify the mode is as designed. In this case, a variation on the standard bead pull measurement was required because the prototype was significantly undercoupled. Using the absolute value of impedance rather than the change in phase of S_{11} significantly improved the dynamic range of the bead pull measurements.

The AMM can also be used to minimise unwanted multipoles generated by power couplers, LOM and HOM couplers and deformations from tuning pins that may otherwise be significant enough to influence design choices. Dual-slot couplers, for example, may be used instead of single-slot to prevent the generation of an unwanted dipole component. A systematic method was presented that uses the AMM to negate unwanted transverse multipoles caused by N-slot power couplers. This was applied to designing an azimuthally modulated cavity with a single-slot coupler incorporated that supports an accelerating mode free of dipole, quadrupole, sextupole and octupole components. In addition, another cavity design was presented which anticipates and compensates for the multipoles introduced by deformation using tuning pins. These results have major implications for future RF cavity designs because the preservation of emittance and longer beam lifetimes both rely on the minimisation of such multipolar terms.

Additionally, the AMM can be used for tailoring the off-axis profile of a mode. For example, accelerating modes that remain as flat as possible along the horizontal are desirable in cyclotrons because they minimise the number of turns needed for acceleration. A process was presented that uses the AMM to optimise the flatness of the accelerating field and found that, under the spatial constraints of the PSI cyclotron, an optimal azimuthally modulated structure had a 10% better flatness than a simple cuboid cavity. Although this gain is marginal, it is a proof of concept that the AMM can be used to systematically improve the flatness of a field and the benefits of this method may be much more significant in more complex cavity designs. Furthermore, such optimisation processes can be generalised to the design of more bespoke fields along the horizontal that, for example, are flat in the monopole and dipole terms.

Finally, the AMM applies to musical drums too as they are governed by the same equations of motion. This similarity inspired the creation and delivery of an outreach workshop Funky Drums and Particle Accelerators designed to engage 11-14 year old students with science.

8.1 Future Work

Applying the AMM to real-world cavity designs in order to determine the benefits (and drawbacks) of its utilisation on the multipolar content of modes would be a natural next step. Some examples could include: designing an azimuthally modulated TM_{01} mode launcher and comparing it to the fourfold symmetric structure analysed in [99], using the AMM to minimise transverse multipoles introduced by HOM dampers in the CLIC accelerating structures [10], or applying the AMM to fine-tune the flatness of the exact PSI cyclotron cavity design [103].

The electrodynamics of the $\text{TM}_{\{M\}\eta p}$ modes were also analysed under strict assumptions including small, high-β beams and thin, closed cavities. Undertaking beam dynamics studies of beams traversing azimuthally modulated cavities would therefore be useful, particularly to understand how the incorporation of beam pipes and the violation of the small beam limit affects the application of the AMM. Such beam dynamics studies could also be used to precisely quantify the effects and advantages of using simultaneous accelerating and manipulating modes supported by azimuthally modulated cavities.

Furthermore, determining systematic methods for optimising the figures of merit within azimuthally modulated RF cavities whilst preserving the desired multipole content would be useful. For example, verifying that nose cones can be incorporated into an azimuthally modulated cavity and the shunt impedance optimised without significantly affecting the desired multipolar content of the mode.

Additionally, the AMM has so far been used to design RF cavities that support TM and not TE modes. The latter do, however, find useful applications such as compensating emittance growth in superconducting cavities [67], and the AMM could be similarly utilised for designing azimuthally modulated cavities that support bespoke TE modes.

Finally, this thesis has focused on the application of the AMM in NC cavities because SC cavities are very much limited by the peak surface magnetic field. A detailed analysis of how the peak surface magnetic field varies with the multipolar content of $\text{TM}_{\{M\}\eta p}$ modes would determine the scope for utilising azimuthally modulated SC cavities.

Appendix A

The Helmholtz Decomposition

The Helmholtz decomposition is a method developed in Ref. [64] for calculating the normal $\tilde{e}_m(k)$ and skew $\tilde{f}_m(k)$ Helmholtz coefficients of a given longitudinal electric field distribution supported by an RF structure.

A.1 The General Case

The general solution for the longitudinal electric field in cylindrical coordinates is derived in Ref. [64] as

$$E_z(\vec{r}) = \int_{-\infty}^{\infty} \frac{dk}{\sqrt{2\pi}} e^{ikz} \left\{ \tilde{e}_0(k) R_0(k,r) + \sum_{m=1}^{\infty} R_m(k,r) \left[\tilde{e}_m(k) \cos m\theta + \tilde{f}_m(k) \sin m\theta \right] \right\}, \tag{A.1}$$

where

$$R_m(k,r) = \begin{cases} J_m(\kappa_l r), & k^2 < k_l^2; \\ I_m(\kappa_l r), & \text{otherwise}, \end{cases} \tag{A.2}$$

and

$$\kappa_l^2 = |k^2 - k_l^2|. \tag{A.3}$$

Given the longitudinal electric field, $E_z(R,\theta,z)$, on the surface of a cylinder of radius R within an RF structure, a Helmholtz decomposition is undertaken by carrying out a Fourier transform. This obtains the Fourier decomposition of the harmonic modes as

$$\tilde{e}_m(k) = \frac{1}{R_m(k,R)} \int_{-\infty}^{\infty} \frac{dz}{\sqrt{2\pi}} e^{-ikz} \int_0^{2\pi} \frac{d\theta}{\sqrt{2\pi}} E_z(R,\theta,z) \cos{(m\theta)}, \tag{A.4}$$

$$\tilde{f}_m(k) = \frac{1}{R_m(k,R)} \int_{-\infty}^{\infty} \frac{dz}{\sqrt{2\pi}} e^{-ikz} \int_0^{2\pi} \frac{d\theta}{\sqrt{2\pi}} E_z(R,\theta,z) \sin{(m\theta)}. \tag{A.5}$$

These calculated Helmholtz coefficients are independent of the radial coordinate r and can be used to determine the longitudinal electric field at any point within the cavity via Eqn. A.1.

A.2 The Flat Helmholtz Decomposition

It is derived in Chapter 2 that closed, azimuthally modulated structures support longitudinal electric fields of distinct frequency that can be written in the form

$$E_z(r,\theta)\cos{(k_p z)} = \cos{(k_p z)} \left\{ \tilde{e}_0 J_0(\kappa_{lp} r) + \sum_{m=1}^{\infty} J_m(\kappa_{lp} r) \left[\tilde{e}_m \cos{(m\theta)} + \tilde{f}_m \sin{(m\theta)} \right] \right\}, \tag{A.6}$$

as given by 2.39, and where

$$\kappa_{lp} = \sqrt{k_l^2 - k_p^2} = \sqrt{k_l^2 - \left(\frac{2p\pi}{L}\right)^2}, \tag{A.7}$$

as given by Eqn.2.40.

By definition, if such a field as given by Eqn. A.6 is decomposed, then the Helmholtz coefficients are non-zero for just a single-value of $k = k_p$

$$\tilde{e}_m(k_p) = \frac{L}{J_m(\kappa_{lp} r)} \int_0^{2\pi} E_z(R,\theta) \cos{(m\theta)} d\theta, \tag{A.8}$$

$$\tilde{f}_m(k_p) = \frac{L}{J_m(\kappa_{lp} r)} \int_0^{2\pi} E_z(R,\theta) \sin{(m\theta)} d\theta, \tag{A.9}$$

because

$$\int_{-\infty}^{\infty} e^{-ikz} e^{ik_p z} dz = \delta(k - k_p) 2\pi L. \tag{A.10}$$

For any given electric field with a longitudinal dependence that is not necessarily $\cos{(k_p z)}$, we define the *flat* Helmholtz decomposition as

$$\tilde{e}_m(0) = \frac{1}{J_m(k_l R)} \int_{-L/2}^{L/2} \int_0^{2\pi} E_z(R,\theta,z) \cos{(m\theta)} d\theta dz, \tag{A.11}$$

$$\tilde{f}_m(0) = \frac{1}{J_m(k_l R)} \int_{-L/2}^{L/2} \int_0^{2\pi} E_z(R,\theta,z) \sin{(m\theta)} d\theta dz. \tag{A.12}$$

This calculates the *flat* Helmholtz coefficients for $k = 0$ only and so the flat Helmholtz decomposition does not calculate the Helmholtz coefficients for any other values of k.

A.3 Simulation and Analysis of an RF Cavity

3D simulations of RF structures have been undertaken and analysed as part of this thesis research for a multitude of reasons. This includes verifying theoretical predictions and optimising structures for experimental testing. A step-by-step process for simulating a 3D RF structure using the electromagnetic solver CST and analysing a mode by a flat Helmholtz decomposition is as follows:

- The RF structure is created using CST's CAD software, as per Fig. A.1
- Discrete cylindrical surfaces of various radii are created within the structure, as per Fig. A.2.
- The density of the computation mesh is set, as per Fig. A.3.
- The mode of interest is solved for by running CST's eigenmode solver, as per Fig. A.4.

- The longitudinal electric field at every point comprising the discrete cylindrical surfaces is exported for analysis.
- The flat Helmholtz coefficients are calculated using Eqns. A.11-A.12 and analysed, as per Fig. A.5.

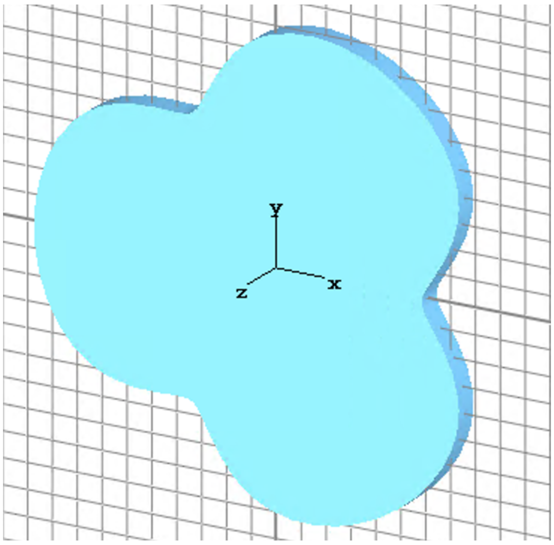

Figure A.1: The closed azimuthally modulated structure that supports a 3 GHz $\text{TM}_{\{0,3\}20}$ mode with $\tilde{g}_3/\tilde{g}_0 = 0.95$ created in CST, as per Point 1. The longitudinal length of the structure is 10 mm and the structure is made out of PEC and evacuated.

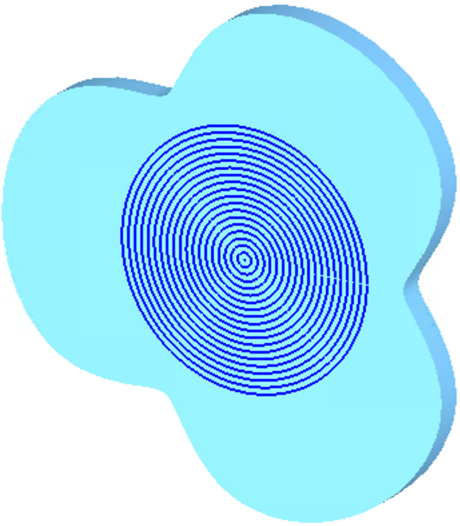

Figure A.2: 30 discrete cylindrical surfaces composed of 720 azimuthal points at 10 regularly spaced longitudinal intervals are created with radii between 0.1 mm and 47.5 mm, as per Point 2.

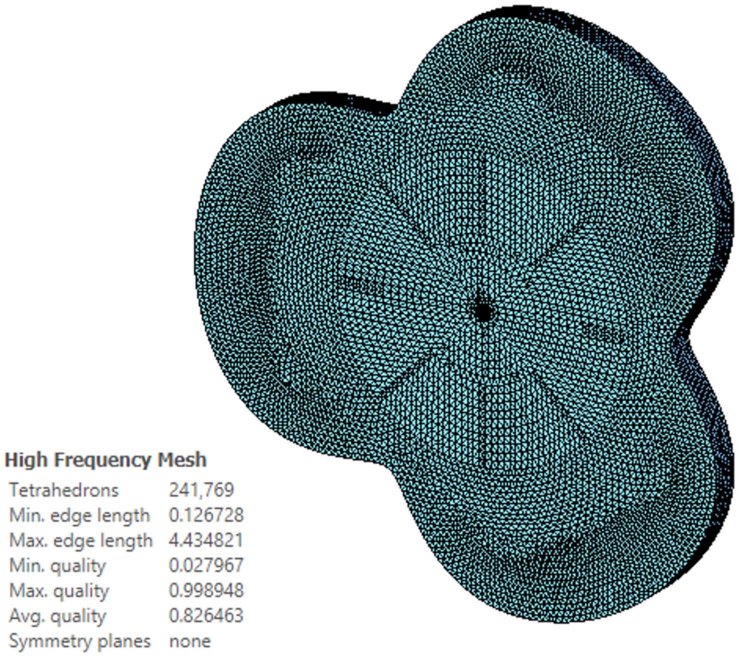

High Frequency Mesh

Tetrahedrons	241,769
Min. edge length	0.126728
Max. edge length	4.434821
Min. quality	0.027967
Max. quality	0.998948
Avg. quality	0.826463
Symmetry planes	none

Figure A.3: The mesh is defined, as per Point 3. In this example, a 'mesh bomb' has been created whereby the mesh has vertices at all points of the discrete cylindrical surfaces.

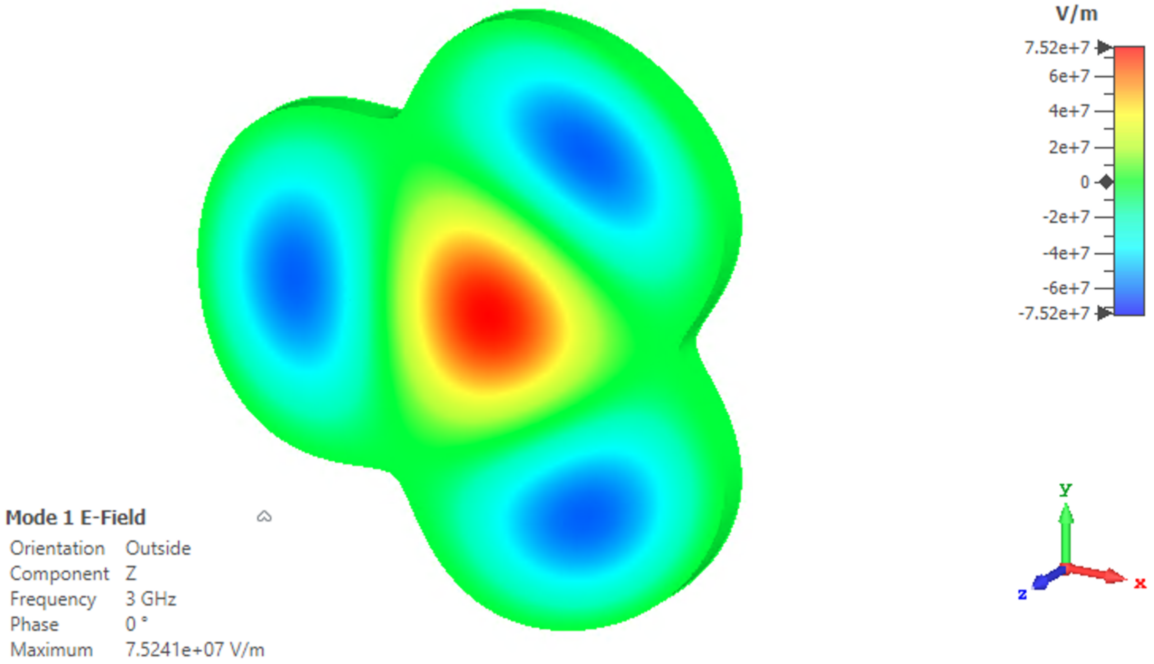

Mode 1 E-Field

Orientation	Outside
Component	Z
Frequency	3 GHz
Phase	0 °
Maximum	7.5241e+07 V/m

Figure A.4: The longitudinal component of the 3 GHz electric field, solved for as per Point 4, is visualised using a contour plot.

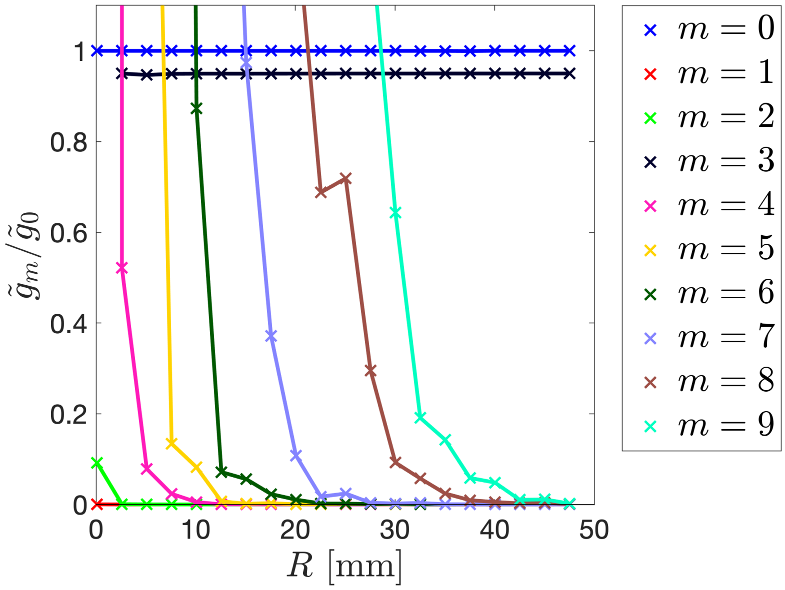

Figure A.5: Plot showing the variation in the magnitude of the flat Helmholtz coefficients, $\tilde{g}_m$, normalised to $\tilde{g}_0$ as determined by decompositions along discrete cylindrical surfaces of different radii R within the azimuthally modulated structure shown in Fig. A.1.

The example structure shown in Fig. A.1 was designed to support a 3 GHz $\mathrm{TM}_{\{0,3\}20}$ mode with $\tilde{g}_3/\tilde{g}_0 = 0.95$. Figure A.3 shows that the field has the desired frequency. The multipolar magnitudes calculated by the Helmholtz decomposition are plotted in Fig. A.5. This shows that the mode has the desired form because $\tilde{g}_3/\tilde{g}_0 = 0.95$ for all radii whilst all other multipolar terms are zero, within error. On this latter point, we observe in Fig. A.5 that all multipoles diverge from null as $r \to 0$. This is because $J_m(x) \to 0$ as $x \to 0$ when $m \geq 1$ and the electric field data must be divided by $J_m(k_l R)$ to determine the flat Helmholtz coefficients as per Eqns. A.11-A.12. Any simulation errors arising from the finite errors of the mesh or the discrete nature of the cylindrical surfaces are therefore amplified for smaller radii and larger multipolar order.

Bibliography

[1] J. D. Cockcroft and E. T. S. Walton, "Experiments with high velocity positive ions. (i) further developments in the method of obtaining high velocity positive ions," *Proc. R. Soc. London, Ser. A*, vol. 136, no. 830, pp. 619–630, 1932.

[2] J. D. Cockcroft and E. T. S. Walton, "Experiments with high velocity positive ions. (ii) the disintegration of elements by high velocity protons," *Proc. R. Soc. London, Ser. A*, vol. 137, no. 831, pp. 229–242, 1932.

[3] F. Frommberger, "Particle accelerators around the world." http://www-elsa.physik.uni-bonn.de/accelerator_list.html, 2022.

[4] O. S. Brüning *et al.*, "LHC Design Report," Tech. Rep. CERN-2004-003-V1, CERN, Geneva, 2004.

[5] S. Widodo *et al.*, "Policy review on research, development, and applications of particle accelerator in indonesia," in *AIP Conf. Proc.*, vol. 2381, p. 020106, 2021.

[6] T. Feder, "Accelerator school travels university circuit," *Phys. Today*, vol. 63, no. 2, pp. 20–22, 2010.

[7] S. Gourlay, T. Raubenheimer, and V. Shiltsev, "Challenges of future accelerators for particle physics research," *Front. Phys.*, vol. 10, p. 920520, 2022.

[8] J. D. Lykken, “Beyond the Standard Model,” *arXiv e-prints*, 2010. arXiv:1005.1676.

[9] M. Benedikt *et al.*, “FCC-ee: The Lepton Collider: Future Circular Collider Conceptual Design Report Volume 2. Future Circular Collider,” Tech. Rep. CERN-ACC-2018-0057, CERN, Geneva, 2019.

[10] M. Aicheler *et al.*, “A Multi-TeV Linear Collider Based on CLIC Technology: CLIC Conceptual Design Report,” Tech. Rep. CERN-2012-007, CERN, Geneva, 2012.

[11] T. Behnke *et al.*, “The International Linear Collider Technical Design Report,” Tech. Rep. CERN-ATS-2013-037, CERN, Geneva, 2013.

[12] The CEPC Study Group, “CEPC conceptual design report: Volume 1 - accelerator,” Tech. Rep. IHEP-CEPC-DR-2018-01, IHEP, Beijing, 2018.

[13] E. Zubizarreta *et al.*, “Need for radiotherapy in low and middle income countries – the silent crisis continues,” *Clinical Oncology*, vol. 27, no. 2, pp. 107–114, 2015.

[14] E. Zubizarreta, J. Van Dyk, and Y. Lievens, “Analysis of global radiotherapy needs and costs by geographic region and income level,” *Clinical Oncology*, vol. 29, no. 2, pp. 84–92, 2017.

[15] Atun, Rifat and others, “Expanding global access to radiotherapy,” *Lancet Oncol.*, vol. 16, no. 10, pp. 1153–1186, 2015.

[16] M. Dosanjh, “Access to Effective Cancer Care in Low- Middle Income Countries Requires Sophisticated Linear Accelerator Based Radiotherapy,” in *Proc. IPAC’22*, pp. 3147–3151, JACoW Publishing, Geneva, Switzerland, 2022.

[17] A. W. Chao *et al.*, *Handbook of Accelerator Physics and Engineering*. Singapore: World Scientific Publishing Company, 2nd ed., 2013.

[18] S. Y. Lee, *Accelerator Physics* . Singapore: World Scientific Publishing Company, 4th ed., 2018.

[19] F. Hinterberger, "Electrostatic accelerators," in *CERN Accelerator School: Small Accelerators*, pp. 95–112, 2006.

[20] W. D. Kilpatrick, "Criterion for vacuum sparking designed to include both rf and dc," *Rev. Sci. Instrum.*, vol. 28, no. 10, pp. 824–826, 1957.

[21] T. P. Wangler, *RF Linear Accelerators.* New Jersey: Wiley, 2nd ed., 2008.

[22] A. Grudiev, S. Calatroni, and W. Wuensch, "New local field quantity describing the high gradient limit of accelerating structures," *Phys. Rev. ST Accel. Beams*, vol. 12, p. 102001, 2009.

[23] J. Paszkiewicz, A. Grudiev, and W. Wuensch, "Local power coupling as a predictor of high-gradient breakdown performance," *arXiv e-prints*, 2022. arXiv:2209.15291.

[24] A. Grudiev and W. Wuensch, "Design of the CLIC Main Linac Accelerating Structure for CLIC Conceptual Design Report," in *Proc. LINAC'10*, pp. 211–213, JACoW Publishing, Geneva, Switzerland, 2010.

[25] E. Wilson, *An Introduction to Particle Accelerators.* Oxford: Oxford University Press, 2001.

[26] N. G. Burnet *et al.*, "Proton beam therapy: perspectives on the national health service england clinical service and research programme," *The British Journal of Radiology*, vol. 93, no. 1107, p. 20190873, 2020.

[27] Paul Emmanuel Goethals, *Cyclotrons used in Nuclear Medicine Report & Directory.* MEDraysintell, 2020.

[28] E. D. Courant, M. S. Livingston, and H. S. Snyder, “The strong-focusing synchroton—a new high energy accelerator,” *Phys. Rev.*, vol. 88, pp. 1190–1196, 1952.

[29] D. Alesini, “Linac,” *arXiv e-prints*, 2021. arXiv:2103.16500.

[30] L. Arnaudon *et al.*, “Linac4 Technical Design Report,” Tech. Rep. CERN-AB-2006-084, CERN, Geneva, 2006.

[31] SLC Working Group, “SLAC Linear Collider Conceptual Design Report,” Tech. Rep. SLAC-R-0229, SLAC, California, 1980.

[32] E. D. Bloom *et al.*, “High-energy inelastic $e - p$ scattering at 6° and 10°,” *Phys. Rev. Lett.*, vol. 23, pp. 930–934, 1969.

[33] A. Wolski, “Maxwell’s Equations for Magnets,” *arXiv e-prints*, 2010. arXiv:1103.0713.

[34] H. Wiedemann, *Particle accelerator physics.* Berlin: Springer, 3rd ed., 2007.

[35] A. Wolski, *Introduction to Beam Dynamics in High-Energy Electron Storage Rings.* 2053-2571, Morgan & Claypool Publishers, 2018.

[36] J. Seeman *et al.*, *Design and Principles of Linear Accelerators and Colliders*, pp. 295–336. Cham: Springer International Publishing, 2020.

[37] S. Guiducci, “Chromaticity,” in *CERN Accelerator School: Course on General Accelerator Physics*, pp. 191–206, 1992.

[38] J. Gareyte, J.-P. Koutchouk, and F. Ruggiero, “Landau damping dynamic aperture and octupole in LHC,” Tech. Rep. CERN-LHC-Project-Report-91, CERN, Geneva, 1997.

[39] W. Herr, "Introduction to Landau Damping," *arXiv e-prints*, 2014. arXiv:1601.05227.

[40] Y. Papaphilippou *et al.*, "Correction Systems Upgrade for the SNS Ring," in *Proc. PAC'01*, vol. 3, pp. 1670–1672, JACoW Publishing, Geneva, Switzerland, 2001.

[41] D. Neuffer, "Multipole Correction in Synchrotrons," in *Proc. PAC'89*, pp. 1432–1435, JACoW Publishing, Geneva, Switzerland, 1989.

[42] A. Ijspeert *et al.*, "Test results of the prototype combined sextupole - dipole corrector magnet for LHC," *IEEE Trans. Appl. Supercond.*, vol. 3, pp. 773–776, 1993.

[43] Y. Chen *et al.*, "Designs and measurements of gradient dipole magnets for the upgrade of pohang light source," *Nucl. Instrum. Methods Phys. Res., Sect. A*, vol. 682, pp. 85–89, 2012.

[44] L. Dallin *et al.*, "Gradient Dipole Magnets for the Canadian Light Source," in *Proc. EPAC'02*, p. 2340, JACoW Publishing, Geneva, Switzerland, 2002.

[45] M. Pont, E. Boter, and M. L. Lopes, "Magnets for the Storage Ring ALBA," in *Proc. EPAC'06*, p. 2562, JACoW Publishing, Geneva, Switzerland, 2006.

[46] H. Hahn and H. J. Halama, "Design of the deflector for the rf beam separator at the brookhaven ags," *Rev. Sci. Instrum.*, vol. 36, no. 12, pp. 1788–1796, 1965.

[47] O. H. Altenmueller, R. R. Larsen, and G. A. Loew, "Investigations of traveling-wave separators for the stanford two-mile linear accelerator," *Rev. Sci. Instrum.*, vol. 35, no. 4, pp. 438–442, 1964.

[48] A. Citron *et al.*, "First operation of a superconducting rf-particle separator," *Nucl. Instrum. Methods*, vol. 155, no. 1, pp. 93–96, 1978.

[49] S. Belomestnykh *et al.*, “Deflecting cavity for beam diagnostics at cornell erl injector,” *Nucl. Instrum. Methods Phys. Res., Sect. A*, vol. 614, no. 2, pp. 179 – 183, 2010.

[50] P. Emma, Z. Huang, K.-J. Kim, and P. Piot, “Transverse-to-longitudinal emittance exchange to improve performance of high-gain free-electron lasers,” *Phys. Rev. ST Accel. Beams*, vol. 9, p. 100702, 2006.

[51] M. Borland, “Simulation and analysis of using deflecting cavities to produce short x-ray pulses with the advanced photon source,” *Phys. Rev. ST Accel. Beams*, vol. 8, p. 074001, 2005.

[52] P. Emma *et al.*, “A transverse rf deflecting structure for bunch length and phase space diagnostics,” *LCLS Technical Note*, vol. 12, 2000.

[53] B. Marchetti *et al.*, “Experimental demonstration of novel beam characterization using a polarizable x-band transverse deflection structure,” *Sci. Rep.*, vol. 11, p. 3560, 2021.

[54] R. B. Palmer, “Energy scaling, crab crossing and the pair problem,” *eConf*, vol. C8806271, pp. 613–619, 1988.

[55] R. Calaga, “Crab Cavities for the High-Luminosity LHC,” in *Proc. SRF’17*, pp. 695–699, JACoW Publishing, Geneva, Switzerland, 2017.

[56] Y. Funakoshi, “Operational experience with crab cavities at KEKB,” *arXiv e-prints*, 2014. arXiv:1410.4036.

[57] K. Akai *et al.*, “Commissioning and Beam Operation of KEKB Crab RF System,” in *Proc. SRF’07*, JACoW Publishing, Geneva, Switzerland, 2007.

[58] I. Béjar Alonso *et al.*, “High-Luminosity Large Hadron Collider (HL-LHC): Technical Design Report,” Tech. Rep. CERN-2020-010, CERN, Geneva, 2020.

[59] S. Verdú-Andrés *et al.*, “Crab cavities for colliders: past, present and future,” *Nucl. Part. Phys. Proc.*, vol. 273-275, pp. 193 – 197, 2016. 37th International Conference on High Energy Physics (ICHEP).

[60] CERN, “Crab cavity diagram.” https://home.cern/news/news/accelerators/crab-cavities-colliding-protons-head, 2017.

[61] A. Grudiev, “Radio frequency quadrupole for Landau damping in accelerators,” *Phys. Rev. Accel. Beams*, vol. 17, no. 1, p. 011001, 2014.

[62] M. Abramowitz and I. Stegun, *Handbook of Mathematical Functions: With Formulas, Graphs, and Mathematical Tables.* Applied mathematics series, New York: Dover Publications, 1965.

[63] G. Dome, “Basic RF theory, waveguides and cavities,” in *CERN Accelerator School: RF Engineering for Particle Accelerators*, pp. 1–96, 1991.

[64] D. T. Abell, “Numerical computation of high-order transfer maps for rf cavities,” *Phys. Rev. ST Accel. Beams*, vol. 9, p. 052001, 2006.

[65] W. K. H. Panofsky and W. A. Wenzel, “Some considerations concerning the transverse deflection of charged particles in radio-frequency fields,” *Rev. Sci. Instrum.*, vol. 27, no. 11, pp. 967–967, 1956.

[66] D. M. Pozar, *Microwave engineering.* New Jersey: Wiley, 4th ed., 2012.

[67] V. Volkov and D. Janssen, “Applications of cavity transverse modes in accelerators,” *Phys. Rev. ST Accel. Beams*, vol. 11, p. 061302, 2008.

[68] W. Wuensch *et al.*, “A demonstration of high-gradient acceleration,” in *Proc. PAC’03*, JACoW Publishing, Geneva, Switzerland, 2003.

[69] S. A. Barengolts *et al.*, “Mechanism of vacuum breakdown in radio-frequency accelerating structures,” *Phys. Rev. Accel. Beams*, vol. 21, p. 061004, 2018.

[70] Dassault Systemes, “CST Studio Suite.” www.3ds.com., 2021.

[71] D. Alesini, “Power coupling,” *ArXiv e-prints*, 2011. arXiv:1112.3201.

[72] V. Shemelin *et al.*, “Dipole-Mode-Free and Kick-Free 2-Cell Cavity for the SC ERL Injector,” in *Proc. PAC’03*, vol. 3, pp. 2059–2061, JACoW Publishing, Geneva, Switzerland, 2003.

[73] D. Alesini *et al.*, “New technology based on clamping for high gradient radio frequency photogun,” *Phys. Rev. ST Accel. Beams*, vol. 18, p. 092001, 2015.

[74] O. H. Altenmueller, R. R. Larsen, and G. A. Loew, “Investigations of Traveling-Wave Separators for the Stanford Two-Mile Linear Accelerator,” *Rev. Sci. Instrum.*, vol. 35, no. 4, pp. 438–442, 1964.

[75] J. Shi *et al.*, “A 3-cell deflecting rf cavity for emittance exchange experiment at anl,” *Nucl. Instrum. Methods Phys. Res., Sect. A*, vol. 598, no. 2, pp. 388–393, 2009.

[76] D. Alesini *et al.*, “Rf deflector design and measurements for the longitudinal and transverse phase space characterization at sparc,” *Nucl. Instrum. Methods Phys. Res., Sect. A*, vol. 568, no. 2, pp. 488–502, 2006.

[77] R. J. England *et al.*, “X-Band Dipole Mode Deflecting Cavity for the UCLA Neptune Beamline,” in *Proc. PAC’05*, pp. 2627–2629, JACoW Publishing, Geneva, Switzerland, 2005.

[78] E. Jensen, “RF Cavity Design,” *arXiv e-prints*, 2014. arXiv:1601.05230.

[79] I. H. Wilson and H. Henke, “Transverse focussing strength of CLIC slotted iris accelerating structures,” Tech. Rep. CLIC-Note-62, CERN, Geneva, 1988.

[80] W. Schnell and I. H. Wilson, “The possibility of introducing additional focusing caused by the circular irises in iris loaded accelerator sections,” in *Conference*

Record of the 1991 IEEE Particle Accelerator Conference, vol. 5, (San Francisco, California, US), pp. 3237–3239, 1991.

[81] H. Henke, “Rf focussing in the high energy linac,” Tech. Rep. CLIC-Note-48, CERN, Geneva, 1987.

[82] H. Henke, “Study work on the CERN Linear Collider (CLIC),” Tech. Rep. CLIC-Note-100, CERN, Geneva, 1989.

[83] G. Burt. Private communication, 2019.

[84] I. Chavel, B. Randol, and J. Dodziuk, *Eigenvalues in Riemannian Geometry*, vol. 115 of *Pure and applied mathematics*. San Diego: Elsevier Science & Technology, 1984.

[85] G. Alessandrini, “On courant’s nodal domain theorem,” *Forum Mathematicum*, vol. 10, no. 5, pp. 521–532, 1998.

[86] J. McMahon, “On the roots of the bessel and certain related functions,” *Ann. Math.*, vol. 9, no. 1/6, pp. 23–30, 1894.

[87] L. C. Maier and J. C. Slater, “Field strength measurements in resonant cavities,” *J. Appl. Phys.*, vol. 23, no. 1, pp. 68–77, 1952.

[88] B. Hall, *Designing the four rod crab cavity for the high-luminosity LHC upgrade.* PhD thesis, Lancaster University, 2012.

[89] T. Weis, “Interaction between rf-system, rf-cavity and beam.” TU Dortmund, Germany, Delta Internal Report 05-02, 2005.

[90] R. Ainsworth *et al.*, “Bead-pull Test Bench for Studying Accelerating Structures at RHUL,” in *Proc. IPAC’11*, pp. 187–189, JACoW Publishing, Geneva, Switzerland, 2011.

[91] S. Ghosh *et al.*, "Bead-pull Measurement using Phase-Shift Technique in Multicell Elliptical Cavity," in *Proc. IPAC'11*, pp. 280–282, JACoW Publishing, Geneva, Switzerland, 2011.

[92] I. V. Konoplev *et al.*, "Experimental studies of 7-cell dual axis asymmetric cavity for energy recovery linac," *Phys. Rev. Accel. Beams*, vol. 20, p. 103501, 2017.

[93] Everything RF, "WR284 Rectangular Waveguide." www.everythingrf.com/tech-resources/waveguides-sizes/wr284.

[94] S. P. Morgan, "Effect of surface roughness on eddy current losses at microwave frequencies," *J. Appl. Phys.*, vol. 20, no. 4, pp. 352–362, 1949.

[95] Flann, "Flann Microwave N-Type Adapters Series 093/094 NX." www.flann.com/products/adapters/n-type-adapters-series-093-094-nx/.

[96] F. Caspers, "RF engineering basic concepts: the Smith chart," *arXiv e-prints*, 2012.

[97] Vidrasa, "Permittivity of Soda-Lime Glass." www.vidrasa.com/eng/products/arglas/arglas_pf.html, 2022.

[98] RF Cafe, "Permittivity of Nylon." www.rfcafe.com/references/electrical/dielectric-constants-strengths.htm, 2022.

[99] G. Castorina *et al.*, "A TM01 mode launcher with quadrupole field components cancellation for high brightness applications," *J. Phys.: Conf. Ser.*, vol. 1067, no. 8, p. 082025, 2018.

[100] M. Liepe, W. D. Moeller, and S. N. Simrock, "Dynamic Lorentz Force Compensation with a Fast Piezoelectric Tuner," in *Proc. PAC'01*, vol. 2, pp. 1074–1076, JACoW Publishing, Geneva, Switzerland, 2001.

[101] N. C. Shipman *et al.*, "Ferro-Electric Fast Reactive Tuner Applications for SRF Cavities," in *Proc. IPAC'21*, pp. 1305–1310, JACoW Publishing, Geneva, Switzerland, 2021.

[102] J. Grillenberger, C. Baumgarten, and M. Seidel, "The High Intensity Proton Accelerator Facility," *SciPost Phys. Proc.*, p. 002, 2021.

[103] H. Fitze *et al.*, "Developments at PSI (Including New RF Cavity)," in *Proc. Cyclotrons'04*, p. 67, JACoW Publishing, Geneva, Switzerland, 2003.

[104] H. Fitze and others and, "Development of a New High Power Cavity for the 590 MeV Ring Cyclotron at PSI," in *Proc. PAC'99*, vol. 2, pp. 795–797, JACoW Publishing, Geneva, Switzerland, 1999.

[105] N. H. Asmar, *Partial differential equations with Fourier series and boundary value problems.* Upper Saddle River: Pearson Prentice Hall, 2nd ed., 2005.

[106] T. D. Rossing, "The physics of kettledrums," *Scientific American*, vol. 247, no. 5, pp. 172–179, 1982.

[107] B. Blik, "Percussion musical instrument timpani isolated on white background." www.depositphotos.com/197377060/stock-photo-percussion-musical-instrument-timpani-isolated.html, 2022.

[108] L. Archer *et al.*, "Science capital: A conceptual, methodological, and empirical argument for extending bourdieusian notions of capital beyond the arts," *Journal of Research in Science Teaching*, vol. 52, no. 7, pp. 922–948, 2015.

[109] S. Godec, H. King, and L. Archer, "The science capital teaching approach: Engaging students with science, promoting social justice," tech. rep., UCL, 2017.

[110] A. Leissa, *Vibration of Plates.* New York: Acoustical Society of America, 1993.